

ABSTRACT

STANO, KELLY LYNN. Atomic Layer Deposition on Carbon Nanotubes and their Assemblies. (Under the direction of Philip D. Bradford and Jesse S. Jur).

Global issues related to energy and the environment have motivated development of advanced material solutions outside of traditional metals ceramics, and polymers. Taking inspiration from composites, where the combination of two or more materials often yields superior properties, the field of organic-inorganic hybrids has recently emerged. Carbon nanotube (CNT)-inorganic hybrids have drawn widespread and increasing interest in recent years due to their multifunctionality and potential impact across several technologically important application areas. Before the impacts of CNT-inorganic hybrids can be realized however, processing techniques must be developed for their scalable production.

Optimization in chemical vapor deposition (CVD) methods for synthesis of CNTs and vertically aligned CNT arrays has created production routes both high throughput and economically feasible. Additionally, control of CVD parameters has allowed for growth of CNT arrays that are able to be drawn into aligned sheets and further processed to form a variety of aligned 1, 2, and 3-dimensional bulk assemblies including ribbons, yarns, and foams. To date, there have only been a few studies on utilizing these bulk assemblies for the production of CNT-inorganic hybrids. Wet chemical methods traditionally used for fabricating CNT-inorganic hybrids are largely incompatible with CNT assemblies, since wetting and drying the delicate structures with solvents can destroy their structure. It is therefore necessary to investigate alternative processing strategies in order to advance the field of CNT-inorganic hybrids.

In this dissertation, atomic layer deposition (ALD) is evaluated as a synthetic route for the production of large-scale CNT-metal oxide hybrids as well as pure metal oxide architectures utilizing CNT arrays, ribbons, and ultralow density foams as deposition templates. Nucleation and growth behavior of alumina was evaluated as a function of CNT surface chemistry. While highly graphitic and defect-free CNTs were shown to produce alumina beads on their surfaces, plasma-treated CNTs with a high concentration of oxygen-

containing functional groups on their surface promoted conformal film formation. Furthermore, it was determined that ultrahigh aspect ratio CNT assemblies could be uniformly coated throughout the cross-section by orienting the CNT axes parallel to the direction of precursor flow, as well as by removing any barriers to the pump/purge process such as growth substrates or non-porous sample holders.

Heat treatment of CNT-alumina hybrids in air not only led to the crystallization of alumina, but also oxidative removal of CNTs from the core-shell structure. In the case of CNT arrays, this resulted in a weak array of alumina nanotubes. When the same process was applied to alumina-coated CNT foams (CNTFs) however, a robust and resilient aerogel-like material remained post-calcination. Further inspection of this novel material revealed that the foam was made up of a three-dimensional network of interconnect alumina nanotubes resulting from the direct templating of alumina on the CNTF structure. With an average density of 1.2 mg cm^{-3} , it is an order of magnitude lower than the lowest density alumina aerogel reported to date, and is among the lowest density for any inorganic aerogel reported to date as well.

The structure, and therefore, properties of these novel foams could be easily tuned by varying the thickness of the alumina coating. Evaluation of the compressive behavior of all foams revealed that their mechanical properties exceed those of various foams with similar densities. This was found to be a result of efficient load transfer through the structure due to good connectivity among nanotube ligaments. This connectivity also provided unprecedented elastic recoverability following compression, particularly for thin-walled samples with CNTFs still intact. Structural stability to liquid infiltration and drying increased with the number of ALD cycles, as well as thermal insulation ability.

© Copyright 2015 Kelly L. Stano

All Rights Reserved

Atomic Layer Deposition on Carbon Nanotubes and their Assemblies

by
Kelly Lynn Stano

A dissertation submitted to the Graduate Faculty of
North Carolina State University
in partial fulfillment of the
requirements for the Degree of
Doctor of Philosophy

Fiber and Polymer Science

Raleigh, North Carolina

2015

APPROVED BY:

Philip D. Bradford
Committee Co-Chair

Jesse S. Jur
Committee Co-Chair

Russell E. Gorga

Yuntian Zhu

DEDICATION

To my parents Lynn and Gene, my sister Meg, and my husband, Tyler.

BIOGRAPHY

Kelly Lynn Stano was born in Anchorage, Alaska on June 26, 1987 to Gene and Lynn Stano. She is the older of two children, having a younger sister, Megan. In 1995, Kelly's family moved to Little Switzerland in the mountains of North Carolina where she spent her childhood. After graduating from Mitchell High School in 2005, she enrolled at North Carolina State University to pursue her B.S. in Textile Engineering. Under the direction of Dr. Russell Gorga, she participated in undergraduate research where she worked with many aspects of the electrospinning process in the development of polymer-carbon nanotube (CNT) composite nanofibers. In 2007, Kelly had the opportunity to travel abroad to the University of Cambridge as a Visiting Scientist where she worked in the Macromolecular Materials Group, led by Professor Alan Windle. While there she studied the mechanical properties of CNT yarns formed via their patented continuous spinning technique. It was here that her fascination with CNTs was ignited, as well as her desire to pursue a career in research.

In the summer of 2010 she began her M.S. in Textile Engineering at North Carolina State University as a Research Assistant in the Carbon Nanotube Textiles Group under the direction of Dr. Philip Bradford. Here she helped to build and optimize a CNT growth reactor and also developed a novel synthetic method for production of aligned CNT – copper nanocomposites. In 2011, Kelly was awarded the National Science Foundation's Graduate Research Fellowship for her proposal on CNT reinforced – ceramic composites prepared using atomic layer deposition (ALD). She went on to pursue her Ph.D. in Fiber and Polymer Science under the guidance of both Dr. Philip Bradford and Dr. Jesse Jur of the Nano-Extended Textiles (next) Group, where she investigated the use of ALD to coat CNT assemblies for fabrication of CNT-inorganic hybrid materials and ultralow density inorganic aerogels.

After finishing her Ph.D., Kelly will be moving to Waynesboro, Virginia with her husband, Tyler, her dog, Bailey, and her cat, Bodie. There she will be joining the Research and Development team at INVISTA as a Material, Polymer, and New Product Development Scientist.

ACKNOWLEDGMENTS

I would first like to thank my (not one, but two!) advisors, Dr. Philip Bradford and Dr. Jesse Jur. Dr. Bradford provided me the opportunity to start my graduate career in his group, and further encouraged me to apply for the NSF Graduate Research Fellowship which has supported the duration of my Ph.D. I am truly grateful for the time, effort, and trust you have invested in me over the last five years. I am also thankful for Dr. Jur's willingness to welcome me to his group and co-advise my research. This work would not have been possible without your support, guidance, and enthusiasm. You have both been invaluable contributors in my development as a researcher and scientist.

Next I would like to acknowledge my committee members—Dr. Russell Gorga and Dr. Yuntian Zhu. Dr. Gorga inspired me to become involved in undergraduate research almost 10 years ago, and I have never looked back since. Thank you for not only serving on my committee, but also being a lifelong mentor and friend. Without Dr. Zhu, this dissertation might very well not exist...A brief glance at my “academic genealogy” would reveal that Dr. Zhu is in fact my grand-advisor, so for that I am doubly thankful.

I am incredibly fortunate to have had the camaraderie and friendship of two lab groups. A huge thank you to all of my current and former lab mates in the Bradford and Jur Research Groups. I have been here so long that I literally run out of room on this page before I can list everyone off!! This work would not have been possible without the support and assistance of so many: Dr. Quan Shi and Dr. Marian McCord, Junjie Zhao and Parsons' Research Group, Amanda Padbury, Birgit Anderson, Judy Elson, the AIF crew—Chuck Mooney, Fred Stevie, Yang Liu, Elaine Zhou, BB Chung, Roberto Garcia, Christina Rost, Ed Mily, and JP Maria, Liz Bradford, Xin Wang and Zhu Research Group.

I would like to thank my Mom, Dad, Meg, Grandma and Grandpa Edwards, Grandma Stano, my wonderful in-laws, and the rest of my family for their support and encouragement throughout my endeavors. Finally, I would like to thank my husband, Tyler, for his unwavering patience and love which have made the completion of this dissertation possible.

TABLE OF CONTENTS

LIST OF TABLES.....	ix
LIST OF FIGURES.....	x
1 Introduction.....	1
2 Literature Review	5
2.1 Carbon Nanotubes and their Assemblies	5
2.1.1 Chemical Vapor Deposition of Carbon Nanotube Arrays	5
2.1.1.1 Normal Arrays	6
2.1.1.2 Compressible Arrays	9
2.1.1.3 Spinnable Arrays	10
2.1.1.4 Carbon Nanotube Assemblies Made from Spinnable Arrays.....	14
2.2 Carbon Nanotube – Inorganic Hybrid Materials.....	18
2.2.1 Functionalization.....	19
2.2.2 Synthesis of CNT-Inorganic Hybrids	20
2.2.3 Characteristics of Atomic Layer Deposition.....	20
2.2.3.1 Atomic Layer Deposition of Aluminum Oxide.....	25
2.2.3.2 Atomic Layer Deposition of Zinc Oxide.....	26
2.2.3.3 Atomic Layer Deposition of Titanium Dioxide	29
2.2.4 Coating Carbon Nanotubes Using Atomic Layer Deposition.....	31
2.2.4.1 Al ₂ O ₃ Atomic Layer Deposition on Carbon Nanotubes.....	31
2.2.4.2 ZnO Atomic Layer Deposition on Carbon Nanotubes	34
2.2.4.3 TiO ₂ Atomic Layer Deposition on Carbon Nanotubes.....	38
2.2.5 Properties and Applications of Carbon Nanotube – Metal Oxide Hybrids	39
2.2.5.1 Photocatalysis	40
2.2.5.2 Gas Sensing	48
2.2.5.3 Batteries and Capacitors	51
2.3 Cellular Solids	53
2.3.1 Alumina-Based Aerogels and Foams.....	54
2.3.2 Sol-Gel Synthesis.....	55
2.3.3 Template-Based Methods	58
2.4 Critical Summary	61
3 Experimental	63
3.1 Materials and Methods.....	63
3.1.1 Aligned CNT Growth	63
3.1.2 Growth of Spinnable CNT Arrays	63

3.1.3	Fabrication of CNT Ribbons.....	63
3.1.4	Fabrication of CNT Foams	64
3.1.5	CNT Surface Modification	64
3.1.6	Atomic Layer Deposition.....	65
3.2	Characterization	66
3.2.1	Microstructure Analysis.....	66
3.2.2	Chemical Analysis	66
3.2.3	Thermal Analysis.....	67
3.2.4	Mechanical Analysis.....	67
4	Conformal Atomic Layer Deposition of Alumina on Millimeter Tall, Vertically- Aligned Carbon Nanotube Arrays	68
4.1	Introduction	69
4.2	Materials and Methods	71
4.2.1	Aligned MWCNT Growth	71
4.2.2	MWCNT Surface Modification	72
4.2.3	ALD of Al ₂ O ₃	73
4.2.4	Characterization	73
4.3	Results and Discussion.....	74
4.3.1	Conformal Coating of MWCNTs	74
4.3.2	Al ₂ O ₃ Distribution in VACNT Arrays	82
4.4	Conclusions	92
4.5	Supplemental Information.....	93
5	Chemical and Structural Characterization of ALD-Deposited Alumina on Carbon Nanotube Foams.....	101
5.1	Introduction	101
5.2	Experimental	102
5.2.1	Materials and Methods.....	102
5.2.2	Characterization	102
5.3	Results and Discussion.....	103
5.3.1	Analysis of As-Deposited and Calcinated Alumina	103
5.3.2	High Temperature Thermal Annealing.....	106
5.4	Conclusions	109
6	Interconnected Metal Oxide Nanotube Networks for Ultralight Aerogels.....	111
6.1	Introduction	111
6.2	Experimental	114
6.2.1	Materials and Methods.....	114
6.2.1.1	Growth of Spinnable CNT Arrays.....	114

6.2.1.2	Preparation of Aligned CNT Foam Templates.....	114
6.2.1.3	CNT Foam Functionalization.....	115
6.2.1.4	Synthesis of Metal Oxide Nanotube Foam.....	115
6.2.2	Characterization.....	115
6.2.2.1	Structure and Morphology.....	115
6.2.2.2	Humidity Sensing.....	116
6.2.2.3	Flame Testing.....	118
6.3	Results and Discussion.....	118
6.4	Conclusions.....	125
6.5	Supplemental Information.....	126
7	Strong and Resilient Alumina Nanotube and CNT/Alumina Hybrid Foams with Tuneable Elastic Properties	130
7.1	Introduction.....	130
7.2	Experimental.....	133
7.2.1	Materials and Methods.....	133
7.2.1.1	Preparation of ACNT Foam Templates.....	133
7.2.1.2	Synthesis of Alumina/CNT Hybrid Foams.....	134
7.2.1.3	Synthesis of Pure Alumina Nanotube Foams.....	134
7.2.2	Characterization.....	134
7.3	Results and Discussion.....	135
7.3.1	Compression Testing.....	139
7.3.2	Wetting Behavior and Liquid Absorption Capacity.....	145
7.3.3	Thermal Stability.....	147
7.4	Conclusions.....	148
8	Final Conclusions.....	154
9	Items of Interest and Future Work.....	156
9.1	Resilient and Hydrophobic PyC-Alumina Nanotube Foams.....	156
9.2	Synthesis of Carbon Nanotubes on Alumina-Coated CNTFs.....	160
9.3	Future Work.....	161
	REFERENCES.....	164

LIST OF TABLES

Table 1.	Average compressive modulus and strength values for ALD coated and uncoated VACNTs.....	90
-----------------	---	----

LIST OF FIGURES

Figure 2.1	Schematics depicting the (a) “template-assisted” growth model for CNT array growth on mesoporous silica, and (b) aligned nanotube growth and orientation on porous Si wafer via “self-supported growth” technique. Reproduced from (15, 17), respectively.....	7
Figure 2.2	TEM images showing MWCNTs grown using chlorine mediated CVD with (a) no chlorine gas added, and (b) with chlorine gas. Reproduced from (51).....	11
Figure 2.3	SEM images of CNT forests grown for 3 min (a-e), 9 min (f-j), and 60 min (k-o). All scale bars represent 1 μm . Reproduced from (56).....	13
Figure 2.4	SEM images of the cross-sections of biscrolled yarns. (A, B) 70% Ti@MWNT yarn fabricated by electron beam evaporation and symmetrical twist insertion in liquid. (C, D) 93% TiO ₂ @MWNT yarn made by filtration based deposition and symmetrical twist insertion in liquid. (E, F) TiO ₂ @MWCNT yarn made by aerosol based deposition and twist insertion in air. (G, H) TiO ₂ @MWNT yarn made by patterned filtration-based deposition on MWNT sheets and asymmetrical twist insertion in liquid. Reproduced from (83).....	17
Figure 2.5	Schematic of ALD cycle. Step 1: Pulse of precursor A leading to its absorption on the substrate surface. Step 2: Purge of the unreacted precursor A and byproducts. Step 3: Pulse of precursor B, which reacts with the surface species created by precursor A. Step 4: Purge of the unreacted precursor B and byproducts. Reproduced from (100, 101).....	22
Figure 2.6	Growth per cycle as a function of (a) pulse time and (b) temperature for different growth modes.....	23
Figure 2.7	Top-view SEM images of ZnO films deposited on p-type Si(100) substrates at various temperatures of (a) 70, (b) 90, (c) 110, and (d) 150 °C. Films deposited at 70 and 90 °C have strong (002) <i>c</i> -axis preferred orientations due to the cylindrical and columnar structures oriented normal to the substrate. Films deposited at 110 and 150 °C show wedge-shaped crystal structures with <i>a</i> -axis directions parallel to the substrate. Reproduced from (128).....	28
Figure 2.8	SEM images of TiO ₂ films deposited on (a) water plasma treated and (b) as-received polycarbonate. Both films were deposited for 50 cycles at 80 °C. Reproduced from (147).....	31

Figure 2.9	Raman spectrum of CNTs before (a) and after (b) ALD of ZnO. The inset depicts additional peaks due to presence of ZnO on ZnO-coated CNTs. Reproduced from (171).....	36
Figure 2.10	Photoresponse curves of MWCNT-ZnO UV photodetectors obtained after (a) 50 and (b) 150 ALD cycles. Reproduced from (173).....	38
Figure 2.11	UV-vis spectra of core-shell MWCNT/TiO ₂ , acid-treated MWCNTs and anatase TiO ₂ . Reproduced from (191).....	42
Figure 2.12	(A) A series of TEM images of CNT/TiO ₂ coaxial nanocables with increasing deposition time, showing oxide behaviors on CNTs spun from nanotube arrays. (B) Low and (C) high resolution TEM images of the nanostructures in a CNT/TiO ₂ film. Reproduced from (69).....	45
Figure 2.13	(A) Raman spectra of a CNT sheet (a) and a CNT/TiO ₂ film (b). (B) XPS spectra of a 2 min deposited CNT/TiO ₂ film (a) and a TiO ₂ film prepared by oxidative removal of the CNTs in a CNT/TiO ₂ film at 500 °C in air (b), and High-resolution XPS spectra of the Ti2p peaks for the two films. Reproduced from (69).....	46
Figure 4.1	TEM micrographs taken after 100 cycles of Al ₂ O ₃ ALD on (a) VACNT_100 and (b) PyC+O ₂ _100 (PyC deposited and plasma functionalized) MWCNTs.....	76
Figure 4.2	XPS spectra (a) survey and high resolution scans of the (b) O 1s and (c) C 1s collected for pristine, PyC deposited, and plasma treated MWCNT arrays. Only the C 1s peak is visible for non-plasma treated arrays, but O 1s and F 1s peaks are found in PyC+O ₂	80
Figure 4.3	Raman spectra were collected from post-treated VACNT arrays with (b) and without (a) plasma functionalization treatments to characterize changes in defect density.	81

Figure 4.4	EDS analysis at the top, middle, and bottom of each ALD coated array and the atomic % of Al was measured through the thickness as a function of experimental set up. In (a), the MWCNT axes were aligned perpendicular to the flow of ALD precursor and the array remained on the quartz growth substrate. This resulted in a high concentration of Al at the top of the array, which rapidly decreased through the thickness. (b) The array mounted to the quartz was then rotated 90° so that the MWCNT axes were oriented parallel to precursor flow. (c) Finally, Al was homogeneously dispersed throughout the MWCNT array which was both removed from the quartz growth substrate and rotated.	83
Figure 4.5	SEM micrographs of pre-treated VACNT arrays after 500 cycles of Al ₂ O ₃ ALD at (a) low and (b) high magnification. Both images were taken from the middle section of the coated array.	85
Figure 4.6	(a) TGA and (b) dTGA plots show improvement in oxidation resistance of all alumina ALD coated CNT samples compared to as-grown.	86
Figure 4.7	VACNTs were removed via oxidation to leave behind a vertically aligned network of alumina nanotubes with high porosity and high surface area.....	88
Figure 4.8	Compressive stress – strain curves for ALD coated and uncoated VACNTs. Arrays which underwent surface activation prior to ALD coating (PyC+O ₂ _100 and PyC+O ₂ _500) exhibited a larger enhancement in compressive properties compared to uncoated and non-functionalized arrays (Pristine, PyC, VACNT_100).	90
Figure 4.9	Pristine VACNT arrays are superhydrophobic due to high surface roughness and low CNT density in the array. After 100 cycles of Al ₂ O ₃ ALD, the surface energy of the coating dominates over the physical structure and the arrays wet.....	91
Figure S4.10	Experimental apparatus used to mount MWCNT array with CNT axes parallel to precursor flow in ALD chamber.....	93
Figure S4.11	SEM images of VACNT array cross section at (a) low and (b) high magnification. Inset shows TEM image of typical MWNT used in experiments.	94
Figure S4.12	EDS spectrum from an as-grown array shows that the level of impurity is very low, with only 0.96 at% and 0.42 at% oxygen and iron, respectively.....	94

Figure S4.13	TEM images of alumina nucleation on as-grown CNTs after (a) 25, (b) 75, and (c) 100 ALD cycles.	95
Figure S4.14	TEM images after 100 cycles of alumina ALD on (a,b) graphitized and (c,d) PyC coated CNTs.....	96
Figure S4.15	TEM images after 100 cycles alumina ALD on (a,b) VACNT+O ₂ /CF ₄ , (c,d) VACNT+G+O ₂ /CF ₄ , and VACNT+PyC+O ₂ /CF ₄ (e,f).....	97
Figure S4.16	Cross-sectional SEM and accompanying EDS measurements taken from top to bottom throughout the ALD-coated array for (a) pristine VACNTs and (b) VACNT+O ₂ /CF ₄	98
Figure S4.17	Cross-sectional SEM and accompanying EDS measurements taken from top to bottom throughout the ALD-coated array for (a) graphitized VACNTs and (b) G+O ₂ /CF ₄	99
Figure S4.18	Cross-sectional SEM and accompanying EDS measurements taken from top to bottom throughout the ALD-coated array for (a) PyC deposited VACNTs and (b) PyC+O ₂ /CF ₄	100
Figure 5.1	(a) XRD spectra of pure CNTFs, as-deposited alumina on CNTFs, and calcinated alumina nanotubes. The peak signature of the alumina nanotubes, along with (b) TEM showing lattice fringes in alumina walls indicates that crystallization began during calcination, to form metastable η -Al ₂ O ₃	104
Figure 5.2	High resolution XPS spectra of the O1s and Al2p peaks taken from pure CNTFs (only O1s), and CNTFs coated with alumina for 20, 100, and 500 cycles, as well as calcinated alumina nanotubes.....	105
Figure 5.3	(a) SEM and (b,c) TEM micrographs of CNTF coated for 20 ALD cycles with alumina, and then annealed for 1 hour in Ar at 1200 °C. The alumina coating was found to remain intact during heat treatment, and evidence of lattice fringes shown in (c) indicate crystallization.	108
Figure 5.4	XRD spectra of pure CNTF, as-deposited alumina on CNTF, and alumina-coated CNTFs after high temperature annealing in Ar gas after 1 and 2 hours. While as-deposited alumina was found to be amorphous, 1 hour of annealing yielded a mixture of θ and α -Al ₂ O ₃ polymorphs. After 2 hours of treatment, all alumina was fully converted to α -Al ₂ O ₃	109

Figure 6.1	Illustration of the processing steps used to synthesize ultralow density aligned Al ₂ O ₃ aerogels. PyC coating of CNTs creates physical crosslinks at CNT junctions which provide elastic response. Oxygen plasma treatment functionalizes the CNTF surface, which allows for very thin yet conformal Al ₂ O ₃ films to be deposited, creating a core-shell structure. The CNTF is easily removed from the Al ₂ O ₃ shell via calcination in air, to leave behind an interconnected network of aligned Al ₂ O ₃ nanotubes.	113
Figure 6.2	Schematic of humidity sensor testing apparatus.	117
Figure 6.3	Analysis of sample morphology. Photographs, SEM, and TEM micrographs of a-c) CNTF template with significant surface roughness from PyC coating, d-f) CNTF template with 2.5 nm thick Al ₂ O ₃ coating, and g-i) Al ₂ O ₃ aerogel and hollow Al ₂ O ₃ nanotubes following removal of CNTF template via calcination.	119
Figure 6.4	Structural characterization and translation of process to other materials. a) Photographs of foams before, during and after compression to 50% strain. Al ₂ O ₃ foams exhibit slight permanent deformation, but all samples recover elastically due to c,d) encapsulation of junctions by ALD coating. b) CNTF wound on quartz rod creates low density insulating layer following ALD coating and calcination. e) XRD spectra showing amorphous nature of ALD alumina and crystallization following calcination. f,g) Photograph and SEM micrograph of ZnO nanofiber foam, made using same process. h) XRD spectra showing as-deposited wurtzite ZnO on CNTF and improvement in crystal structure and grain growth that occurs during calcination. For XRD plots, peaks corresponding to the CNTF and sample holder are depicted by * and + symbols, respectively.	120
Figure 6.5	Demonstrations of multifunctionality. a-c) Photographs showing different wetting behaviors among un-coated, coated and calcinated foams. d) Humidity-time (top) and Resistance-time (bottom) plots for a commercial humidity sensor and Al ₂ O ₃ nanotube sensor (shown in inset), respectively. e) Photograph depicting high temperature insulating ability of Al ₂ O ₃ aerogel which effectively protects the flower from a propane flame. f) Plot describing temperature rise of the top surface of the Al ₂ O ₃ aerogel over time.	123
Figure S6.6	Photographs depicting (a) drawing of aligned CNT sheets from a spinnable array which are continuously collected on rotating parallel glass rods. (b) Many layers of stacked CNT sheets accumulated on glass rods.	126
Figure S6.7	Photograph illustrating the translucent optical behavior of a thick Al ₂ O ₃ nanotube aerogel due to its nanoscale features and high porosity.	127

Figure S6.8	TEM micrograph of hollow Al ₂ O ₃ nanotubes after CNTF removal. Lattice fringes seen in the tube walls indicate that the amorphous Al ₂ O ₃ began to crystallize during calcination.	128
Figure S6.9	Thermogravimetry plot shows that minimal mass loss occurs in either foam until 650 °C, when un-coated CNTFs begin to oxidize. The onset of decomposition for ALD coated foams is shifted slightly higher, indicating good conformality of the coating.	129
Figure S6.10	Resistance-time curve of the Al ₂ O ₃ nanotube sensor exposed to 5 cycles of switching relative humidity from 10% to 30%.	129
Figure 7.1	Analysis of sample morphology. Photographs and SEM micrographs of (a) CNTF+20AO, (b) 20AO, (c) CNTF+100AO, (d) 100AO, (e) CNTF+500AO, and (f) 500AO. TEM micrographs depicting hollow and interconnected alumina nanotube structures for (g) 20AO, (h) 100AO, and (i) 500AO.....	137
Figure 7.2	(a) Linear dependence of CNTF/alumina and alumina foam density on # of ALD cycles. (b) Mass loss as a function of temperature for CNTFs coated for 0, 20, 100, and 500 cycles of ALD.	139
Figure 7.3	Compressive stress – strain curves from first cycle of testing (a) alumina/CNT foams and (b) alumina nanotube foams in both transverse and longitudinal directions. Schematic provided in (c) to illustrate nanotube alignment relative to direction of compressive load.	140
Figure 7.4	Cyclic compression behaviour for CNTF+100AO in (a) transverse, and (b) longitudinal directions as well as 100AO in (c) transverse, and (d) longitudinal directions.	142
Figure 7.5	Evaluation of mechanical properties. (a) Modulus and (b) strength as a function of density for CNT/alumina and alumina nanotube samples in transverse and longitudinal directions. (c) To benchmark the materials produced in this study, modulus as a function of density for other foams with similar densities was also plotted.	144
Figure 7.6	Anisotropic wetting behaviour is shown for (a) CNTF+20AO and (b) 20AO foams. (c) Densified 20AO foam remains intact and forms a film. Fully saturated (d) CNTF+100AO and (e) 100AO foams.	146
Figure 7.7	Thermal insulating performance was evaluated by measuring the temperature rise over time for 20, 100, and 500 cycle alumina nanotube foams subjected to 5 minutes of continuous firing from a 1000 °C flame.	148

Figure 9.1 (a) Alumina nanotube foams made from 500 ALD cycles (left) and 20 cycles (right) before PyC deposition. (b) After 30 minutes of PyC treatment, the foams turned black from deposition of carbon. (c) PyC coated alumina foams exhibited hydrophobic wetting behavior and mechanical resilience. 157

Figure 9.2 (a,b) SEM and (c-f) TEM micrographs showing morphology of CNTs grown on thin-walled alumina nanotubes. Graphitic PyC layers deposited on alumina nanotubes are particularly visible in images d-f. 159

Figure 9.3 SEM characterization of CNTs grown on CNTFs coated with 100 cycles of alumina..... 161

1 Introduction

The field of materials research has undergone a drastic and exciting expansion since the advent of nanomaterials and nanotechnology. Gone are the days where a solitary metal, ceramic, or polymer is employed to solve a singular problem. The complex technological challenges facing society are instead met with advanced engineered material solutions which are multifunctional, smart, and energy saving. Composite materials exhibit properties superior to their individual constituents due to additive interactions between matrix and reinforcement phases. As the size scale of these phases has decreased to the nano-regime a new class of material known as hybrids has emerged (1). Carbon nanotube (CNT) – inorganic hybrids are a class of functional materials which has drawn widespread and increasing interest in recent years (2). As opposed to nanocomposites where the phases are combined via mechanical means, CNT-inorganic hybrids are characterized by CNTs which are coaxially coated with thin layers of inorganic material. Due to interfacial charge transfer processes and size domain effects, the CNT-inorganic hybrids are expected to exhibit a synergistic set of enhanced physical properties.

There are many emerging applications where nanoscale metal oxide coatings on CNTs are desired. CNTs are an interesting substrate for inorganic materials, not only because of their high surface area, but also their inherently high electrical conductivity which allows them to be utilized as contact electrodes for many applications. For this reason core-shell coating morphologies are popular for photodetectors, transistors, sensors, solar cells, and other optoelectronic applications. In this scenario, a Schottky barrier is formed at the interface between the CNT and metal oxide thin film. This serves as a charge rectifier and can thus preferentially stream electrons for the desired application performance. A large issue in these applications is the complicated and highly technical sample preparation involved for the nanoscale manipulation of individual CNTs. In some cases a dispersion of CNTs may be cast on a substrate followed by inorganic deposition. Then electron beam lithography is used to mill out unwanted areas and produce patterns for devices utilizing individual coated CNTs. Electrodes are applied to contact the device using sputtering or evaporation.

While these methods are necessary for the production of nanoscale transistors, there are many scaled up applications that may not require such precision or accuracy. For such cases, CNT assemblies, rather than individual CNTs, can be synthesized and applied. A CNT assembly is a general classification for a macroscale 1, 2, or 3-dimensional bulk CNT architecture (3). Examples include fibers and yarns, vertically aligned arrays, ribbons, foams, and buckypapers among others. Within these examples are varying degrees of CNT alignment, density, and mechanical integrity. For the purpose of this dissertation CNT assemblies produced from spinnable vertically aligned carbon nanotube (VACNT) arrays will be the focus; specifically to include ultralow density CNT foams (CNTFs) and the arrays themselves.

Before the challenges of device fabrication can be met, there are many significant fundamental aspects of achieving conformal coatings on CNTs themselves as well as their assemblies), which must be addressed. Atomic layer deposition (ALD) is a versatile technique used to conformally deposit a wide variety of multifunctional materials onto complex micro- and nano-sized structures with atomic scale precision. Successful coating of MWCNTs has been demonstrated in the literature, though it is generally agreed upon that these MWCNTs likely had high defect densities due to poor graphitic quality and/or inadvertent oxidation during synthesis. Likewise, discontinuous and bead-like coatings have also been shown in experiments where MWCNTs were known to have high graphitic quality and low defect density. In the latter scenario, functionalization treatments were used to increase nucleation density and thus promote conformal growth. Many common functionalization techniques rely on wet chemical processes and are therefore unsuitable for CNT assemblies as they will cause CNT agglomeration, densification, and entanglement upon drying. Gas-phase techniques should be explored for suitability and effectiveness in achieving conformal ALD growth.

The extent of capabilities of ALD for depositing on a variety of CNT assemblies has not yet been explored. In Chapter 4, the deposition of alumina on high aspect ratio CNT arrays is demonstrated. The role of CNT surface/defect chemistry and their effects on nucleation and growth of ALD films was explored and optimized to promote conformal coating without sacrificing the structural integrity of the CNTs within the array, or the array itself. Furthermore,

unprecedented uniformity in coating distribution was achieved for 1.5 mm tall CNT arrays through identification and mitigation of barriers to ALD precursor diffusion.

The interactions between CNTs and inorganic coatings, especially those deposited via ALD, are presently not well understood. This relationship is important to explore since the electrical, optical, chemical, thermal, and mechanical properties of the hybrid are innately tied to chemical composition, microstructure, and presence of interfacial bonding. To this extent, Chapter 5 examines the chemical bonding environment of as-deposited alumina on plasma-treated CNTFs, and also investigates how the nature of bonding changes as a function of film thickness (controlled by varying the number of ALD cycles). Additionally, the crystallization behavior is studied for as-deposited samples as well as those having undergone varying degrees of post-deposition heat treatment in both air and argon atmospheres.

One emerging application for the ALD process is the preparation of porous metal oxides that are high surface area and low density (4). These cellular solids have applications in catalysis (either as the active species itself, or as a catalyst support), sensors, filters or membranes, and energy conversion or storage. In this technique, ALD is used to deposit a film on a template, which may or may not be removed through further processing. This method has been explored as an alternative to sol-gel chemistry, which is traditionally used to prepare high surface area aerogels. There are numerous drawbacks to aerogels produced using sol-gel methods, as well as the sol-gel process itself. Some examples include the difficulty in controlling pore size or pore size distribution, non-uniform and cracked aerogel monoliths, poor mechanical properties, as well as experimental complexity and long process times. Templating techniques show promise in addressing many of these issues, but selecting the appropriate template is crucial as it will affect not only the form factor and morphology of the final material, but it should also be able to be produced in bulk quantities with useful and customizable dimensions.

For this reason, CNTFs were explored as a template material for the production of low density aerogel-like materials. In Chapter 6, ultrathin (2.5 nm) conformal films are grown on plasma-treated CNTFs made from pyrolytic carbon (PyC) deposition on aligned stacks of continuously drawn CNTs. Removal of the aligned CNTF template via calcination in air

resulted in the creation of a free-standing alumina nanotube aerogel-like material with an average density of 1.2 mg cm^{-3} , which is an order of magnitude lower than the lowest value previously reported for an alumina aerogel, as well as among the lowest density for any inorganic material (5). Due to conformal coating of CNT-CNT junctions within the foam, the alumina nanotubes possessed a highly unique three-dimensional and interconnected morphology, which was shown to provide mechanical resilience. The humidity sensing behavior of films made from these foams was explored, as well as their thermal insulating ability. Finally, the same processing technique was used to prepare ZnO nanofiber foams, demonstrating the ease in translation and customization associated with using ALD templating.

In Chapter 7, the compressive mechanical properties, thermal insulation behavior, and liquid absorption capacity of CNT/alumina and pure alumina nanotube foams were evaluated as a function of foam density. It was demonstrated that foam density could be controlled by varying the coating thickness through varying the number of ALD cycles. Foams produced in this work are unique in that they possess a high level of preferential alignment among the ligaments or struts. This was shown to provide anisotropic mechanical properties when compressive load was applied parallel or perpendicular to the direction of nanotube axes. Benchmarking of moduli measured for our foams against foams with similar densities revealed that longitudinally-loaded alumina nanotube foams exceeded previously reported values by an order of magnitude. Strength values of alumina nanotube foams also outperformed commercially-available aluminum foams that were twice as dense. Furthermore, thin-walled pure alumina and hybrid specimens, particularly when loaded in the transverse direction were found to exhibit elastic recovery in cyclic compression testing.

2 Literature Review

2.1 Carbon Nanotubes and their Assemblies

Carbon nanotubes are widely regarded as being one of the most potentially revolutionary materials in modern technology. A great deal of research has focused on their synthesis, purification, functionalization, sorting, and isolation in order to effectively incorporate them into current technological materials to best take advantage of their stellar physical properties. The successful realization of these properties in macroscale applications, however, remains a hurdle for researchers the world-over. For this reason, interest has shifted toward the use of bulk assemblies of CNTs in devices and composites. This shift was brought about by developments in CNT synthesis which allow for the quick and easy manufacture of bulk CNT architectures using a variety of dry processing techniques.

There are generally two routes for manufacturing CNT assemblies via dry processing. In the first case, CNTs are synthesized in such a manner that they form entangled networks inside the reactor using a technique called floating catalyst chemical vapor deposition (FCCVD) (6). The CNTs are then forced to a collection zone using a carrier gas where they can be continuously taken up as a flat ribbon or a yarn, depending on the post-processing technique (7–10). Alternatively, CNT arrays or forests can be grown to produce spinnable arrays, from which thin ribbons can be drawn to form a sheet, ribbon, or yarn (11, 12). In either case the CNTs are assembled into an aligned morphology without the need for liquid based processing like acid functionalization, suspension, or wet spinning, and are therefore referred to as dry-processable CNTs (3).

2.1.1 Chemical Vapor Deposition of Carbon Nanotube Arrays

In the simplest form, CVD of CNTs proceeds via catalytic thermal decomposition of gaseous carbon feedstock by a metal nanoparticle. Upon decomposition, active carbon atoms diffuse through the catalyst particle to the high surface energy step edges. This occurs until a critical saturation of carbon in the metal is reached, at which point the carbon precipitates out to form a carbon nanotube (13, 14). Common catalysts include Fe, Ni, Co, and Mo, while

carbon monoxide, methane, ethane, acetylene, and ethylene are the most widely used carbon sources. A typical growth, carried out at a temperature range of 600-850 °C, results in the synthesis of a fine black powder, where the CNTs are randomly oriented, aggregated, and entangled. If the appropriate growth parameters are selected however, CNT arrays or forests may be grown where the CNTs are vertically aligned, evenly distributed, and minimally aggregated. Although these arrays are an interesting CNT assembly all on their own, further refinement of the growth parameters can yield spinnable arrays, where the vertically aligned CNTs can easily be drawn into horizontally aligned sheets. These arrays, both spinnable and non-spinnable, are the building block for all CNT assemblies used in this dissertation, and as such, their synthesis will be discussed in greater detail.

2.1.1.1 Normal Arrays

Large-scale CNT arrays were first grown on mesoporous silica substrates (15). In these experiments a sol-gel technique was used to form a silica substrate covered in evenly spaced, cylindrical pores which were generally oriented perpendicular to the substrate and filled with Fe nanoparticles, as depicted in Figure 2.1a. The CNTs then grew along the axes of these pores, their alignment aided by the templating effect provided by the substrate. After 2-5 hours the resulting arrays were 50-100 μm long. Further optimization of substrate preparation yielded array heights approaching 2 mm grown over the course of 48 hours (16).

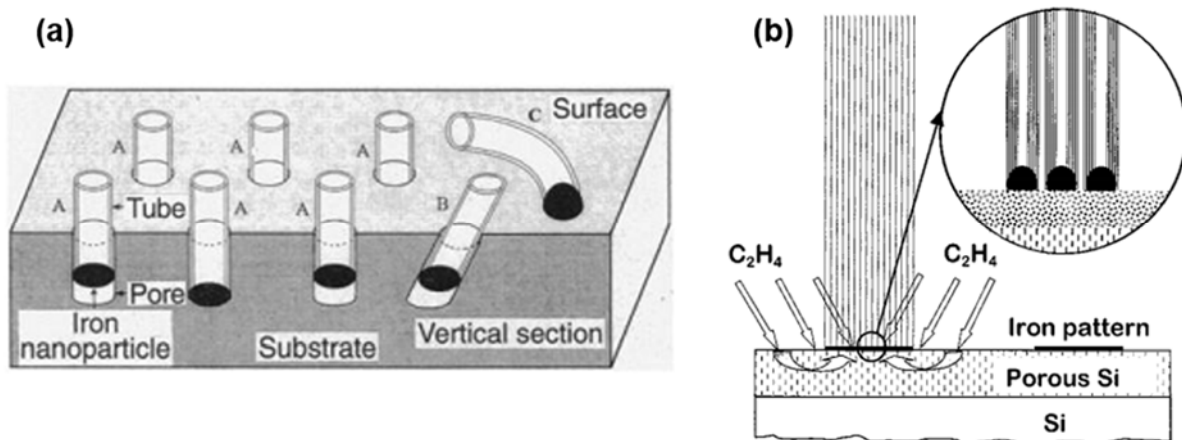


Figure 2.1 Schematics depicting the (a) “template-assisted” growth model for CNT array growth on mesoporous silica, and (b) aligned nanotube growth and orientation on porous Si wafer via “self-supported growth” technique. Reproduced from (15, 17), respectively.

Template-assisted growth of aligned CNTs was quickly replaced by self-oriented growth methods. In 1998 Ren et al. demonstrated the growth of well-aligned arrays on Ni-coated glass using plasma-enhanced CVD (18). It was shown that thinner catalyst films resulted in smaller diameter CNTs, as well as decreasing quality of alignment. The growth and alignment mechanisms were further investigated by Fan et al. (17). Here, Fe catalyst films were evaporated onto porous Si, and then oxidized in air to form densely packed iron oxide nanoparticles. During synthesis, a CNT grew from each nanoparticle normal to the substrate plane. Due to their close proximity, the CNTs interacted with their nearest neighbors via van der Waals forces, which resulted in a mutual stiffening effect. Where individual CNTs would normally be too flexible and thus collapse to the substrate, the self-supported array did not. This mechanism is illustrated in Figure 2.1b.

There were several other important findings from this study due to differences in arrays grown on porous and non-porous Si substrates. First, arrays grown on porous substrates grew more rapidly than those grown on regular Si. This was attributed to the ability of ethylene molecules to easily permeate into the highly porous catalyst support, thus enhancing catalytic activity. Moreover, annealing the catalyst film during pre-treatment formed iron oxide

nanoparticles with a narrow size distribution due to strong interactions between the catalyst and porous support. The strong interactions also prevented particle sintering upon heating (17).

As such, it has become the norm to first deposit a buffer layer to the growth substrate before depositing the catalyst layer. Naturally, CNT array growth is linked to the choice of catalyst support (19). An alumina buffer layer in combination with Fe catalyst has been demonstrated as a reliable system for aligned CNT array growth due to increased CNT nucleation density (20). This is a result of limited surface mobility of Fe on alumina due to strong catalyst-substrate interactions (21, 22).

There have been many useful advancements in array growth since these early examples. Hata et al. demonstrated “super-growth” of high purity SWCNT arrays by adding water to the CNT reaction (23). Water was chosen to act as a weak oxidizer, which etched away amorphous carbon from catalyst particles, thus allowing for prolonged catalyst lifetime as well as enhanced catalytic activity (24). Using this technique arrays measuring 2.5 mm were grown in 10 minutes.

Reactor optimization has also led to high impact developments with implications for scaled-up synthesis technologies. Hata et al. designed and built a vertically oriented CVD reactor with a showerhead type precursor injection system. This configuration allows for uniform growth of 1 cm tall arrays on small substrates (1 cm square), and uniform array growth on substrates the size of A4 paper (25). Reactors have also been designed where CNT arrays can be continuously grown on 2D and 3D substrates in an assembly line style process. After tuning growth and process parameters, 1 mm tall arrays could be grown on substrates moving at 2.4 mm/sec (26, 27).

Due to their large aspect ratios, CNTs exhibit extreme anisotropy of physical properties along their axes. As such, VACNT arrays are an attractive material not only because of their lack of bundling and agglomeration, but also their preferential orientation. This morphology allows for easy utilization in a wide variety of applications. For example, VACNT arrays (28) and their composites (29, 30) have been investigated as thermal management materials due to their high thermal conductivity resulting from ballistic phonon transport along the CNT axis. Alternatively VACNT arrays have also been evaluated as structural reinforcement in polymer

(31), metal (32), and ceramic matrix composites (33). The ideal morphology nanocomposite is one where a high volume fraction of high quality, aligned, collinear, and continuous CNTs are homogeneously dispersed in a matrix without voids or defects. Here again, VACNT arrays make an ideal starting material for the fabrication of such a composite. Finally, due to their high surface area and anisotropic electrical conductivity, VACNT arrays have been evaluated as electrode materials for a variety of energy-related devices including batteries (34), solar cells (35), supercapacitors (36), electrocatalysts (37), and even piezoelectric generators (38).

2.1.1.2 Compressible Arrays

In 2005, Cao et al. reported super-compressible foam-like behavior from free-standing VACNT arrays (39). CNTs simultaneously exhibit good mechanical strength as well as high elasticity, and therefore can be repeatedly bent without structural failure. When a compressive load is applied to a VACNT array, individual CNTs act as support struts and the space between CNTs acts as interconnected open-air cells. The dense CNT array makes it difficult for CNTs to buckle in a random fashion upon compression due to the close proximity of nearest neighbors. Instead, cooperative buckling occurs resulting in the creation of a long-range wave-like morphology that folds on itself for very high compressive strains.

Catalyst pre-treatments were shown to affect whether or not a particular array exhibited foam-like properties (40). Longer pre-treatment times caused coarsening of the catalyst particles and resulting arrays were found to have an undulating structure where the CNT curvature increased with pre-treatment time. It was hypothesized that long pre-treatment times led to a wide distribution of catalyst particles sizes. Small diameter CNTs grow at a faster rate than large diameter ones, but since the tops of all CNTs within an array are bound together by van der Waals interactions, the small diameter CNTs must adopt a wavy morphology to match the height of the surrounding neighbors. No explanation on the recovery mechanism was provided in this study or the aforementioned.

Bradford et al. fabricated foams from CNT arrays with tunable mechanical compressibility using a post-growth treatment (41). CVD of pyrolytic carbon (PyC) on CNTs resulted in radial growth of CNT diameter as well as increased surface roughness. Added

roughness reduced van der Waal interactions among neighboring CNTs, while larger diameter CNTs increased their resistance to buckling under compression and thus compressive strength. When resistance to buckling overpowered van der Waal interactions, CNT arrays exhibited foam-like recovery upon removal of compressive load. This same method has also been utilized as a stabilization technique to allow liquid infiltration into VACNT arrays without destruction of their aligned structure upon drying (32).

2.1.1.3 Spinnable Arrays

Spinnable arrays occupy a unique subset within general CNT arrays. The first report on the ability continuously draw strands of horizontally aligned strands of CNTs from vertically aligned CNT arrays was by Jiang and co-workers in 2002 (11). Furthermore, these continuous strands could be twisted much like a traditional textile yarn to form strong and flexible thread-like structures (42). The question of what makes a particular array able to be spun or drawn into sheets remains a topic of intense research, though there are some generally accepted notions on what conditions must exist for a spinnable array to be synthesized. Irrelevant of the growth method used, a critical issue is the areal distribution density of catalyst particles, as well as particle size uniformity. Densely nucleated CNTs of uniform diameter result in a highly aligned and straight CNT array, which may result in spinnability (43). This is commonly achieved by using pre-deposited buffer-catalyst layered substrates such as Fe/SiO₂/Si or Fe/Al₂O₃/SiO₂/Si, where the Al₂O₃ buffer layers have been shown to resist catalyst particle aggregation and diffusion (42, 44–47).

CVD techniques which eliminate the exhaustive pre-deposition steps have also been developed. In chlorine mediated CVD (CM CVD), the catalyst, iron (II) chloride (FeCl₂), reacts directly with the carbon source (acetylene), in the gaseous phase to nucleate Fe nanoparticles from which CNTs grow (48). CM CVD may be carried out at atmospheric pressure, but high concentrations of either FeCl₂ or acetylene causes early termination of growth. Alternatively, Inoue et al. found that operating in low vacuum yielded significant improvement in regulating relative FeCl₂-acetylene concentrations, and therefore enhanced

CNT array growth rate and length (49). After 20 minutes of growth arrays measured 2.1 mm tall with MWCNTs of 20-50 nm diameter.

The greatly enhanced growth rate is a result of the dual catalytic activity of FeCl_2 . Not only does the catalyst nucleate Fe nanoparticles, but it readily dehydrogenates acetylene to form additional active C species for CNT growth (50). Moreover, HCl formed as a by-product of dehydrogenation can extend the life of active catalyst by either reacting with Fe to re-form FeCl_2 or even etching amorphous carbon away from catalyst particle surfaces. Adding chlorine gas to the reaction as a growth promoter has much the same effect as HCl (51). In fact, by adding only 100 ppm chlorine gas to the reaction the maximum array height increased from 2 mm to 3.5 mm. Additionally the amorphous content of chlorine-grown CNTs was significantly lower as confirmed by TEM (as shown in Figure 2.2) and Raman spectroscopy.

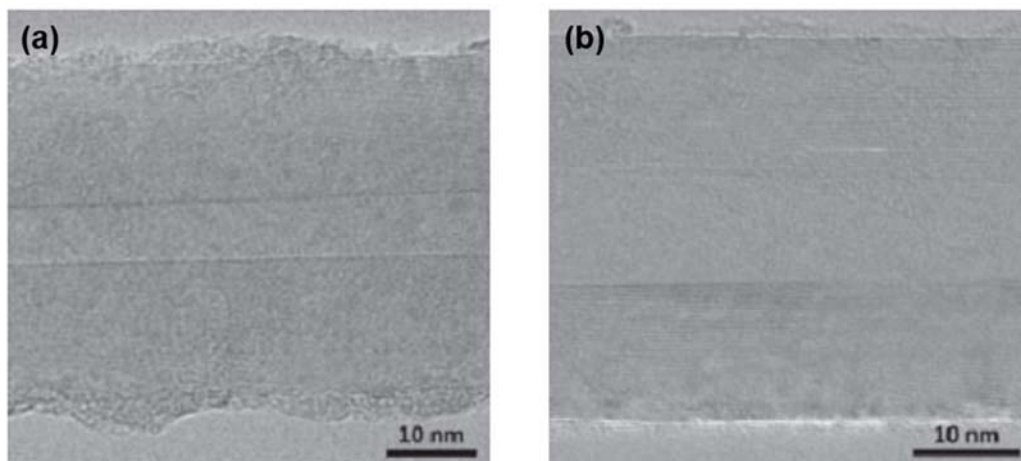


Figure 2.2 TEM images showing MWCNTs grown using chlorine mediated CVD with (a) no chlorine gas added, and (b) with chlorine gas. Reproduced from (51).

Besides Cl_2 , other oxidizing agents like CO_2 and O_2 have been used to treat spinnable arrays. Huang et al. demonstrated that free-standing spinnable arrays could be harvested from quartz substrates by weakening the array-substrate interactions via oxidation. Upon exposure

to CO₂, amorphous carbon and carbon surrounding the metallic catalyst particles was preferentially etched away, facilitating easier array removal (52).

It is obviously of great interest to grow the tallest spinnable CNT arrays possible, as increased CNT length will result in more enhanced physical properties in pure CNT assemblies as well as their composites (53). There is thought to be, however, an upper limit to the height which arrays can be grown and still remain highly spinnable (54, 55), though this limit differs among growth techniques. Lee et al. found that after 9 minutes of growth spinnability decreased sharply, at the same time when wavy CNT morphology became present (56). This waviness arises due to instabilities in the growth conditions which result in catalyst particle death, and thus a physical “pocket” of foreshortened growth. Locally, this pocket results in a change in CNT density and a loss of the mutually-supporting network which facilitates the growth of super-aligned arrays (40). Consequently, individual CNTs which have not yet died can occupy a larger radius of gyration before coming into contact with a neighboring CNT, thus creating the wavy CNT morphology seen in the SEM images in Figure 2.3.

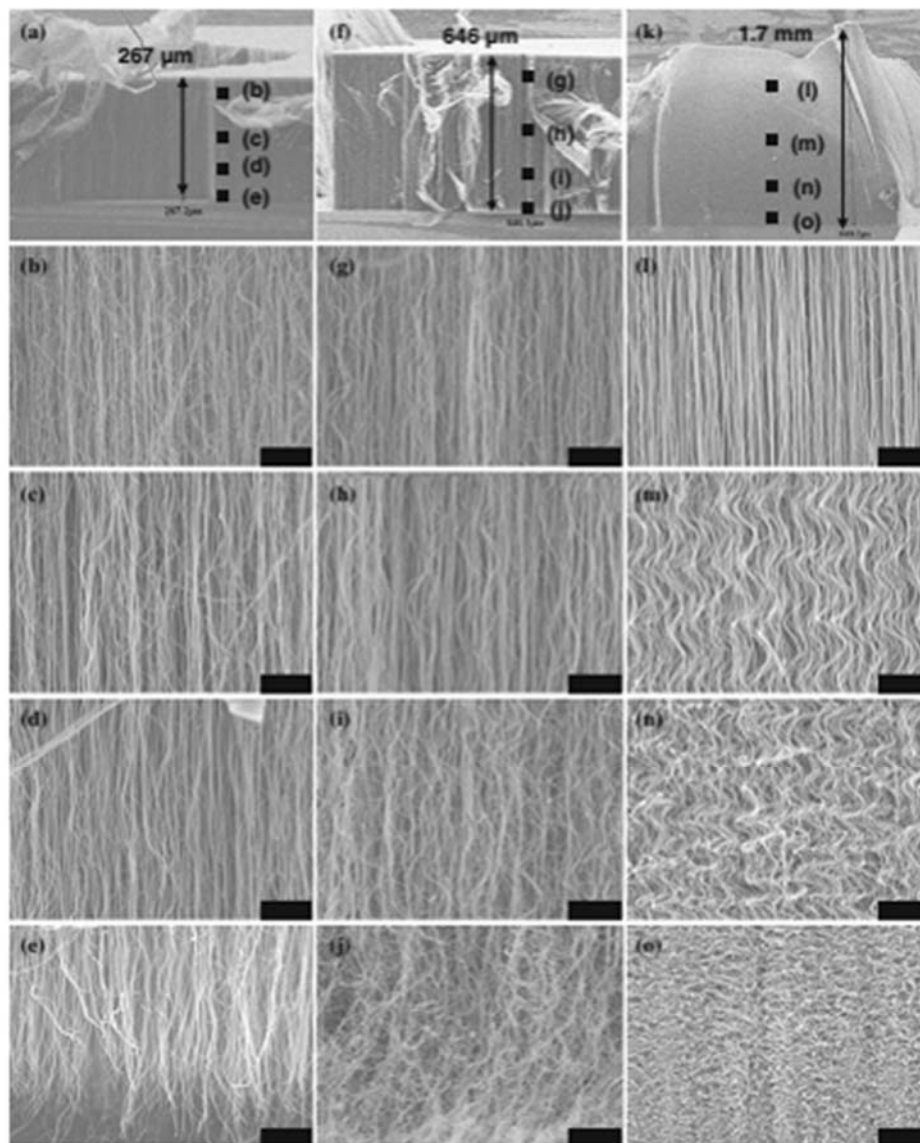


Figure 2.3 SEM images of CNT forests grown for 3 min (a-e), 9 min (f-j), and 60 min (k-o). All scale bars represent 1 μm . Reproduced from (56).

Furthermore, it was also determined in this study that the manner by which growth of the entire array is terminated has an effect on whether or not a particular array is spinnable. At the end of a growth run it is typical to turn off heat and carbon precursor sources. Lingering carbon molecules, however, were shown to decompose and react at non-ideal conditions

leading to a wavy array morphology at the bottom of the array near the substrate, yielding a non-spinnable sample. On the other hand, this was prevented by forcefully purging the CVD system with Ar gas following the end of growth, thus quickly removing carbon precursor from the chamber before reaction could occur (56).

2.1.1.4 Carbon Nanotube Assemblies Made from Spinnable Arrays

2.1.1.4.1 Thin Films and Ribbons

Thin films of CNTs are unique in that they are not only conductive, but also flexible and transparent. As such, they are an attractive alternative to indium tin oxide (ITO) as electrodes for electronic devices. Furthermore, due to their high surface area CNT thin films can act as conductive scaffolds for semiconductor materials in a variety of functional devices. These films have previously been fabricated through a series of complex processes relying on solution-based methods including acid purification, dispersion, ultrasonication, and eventually deposition (57–59).

Alternatively, CNT thin films can also be fabricated by dry-spinning from spinnable VACNT arrays. This technique circumvents the need for solution processing, and also protects the structural integrity of the CNTs. As-drawn films are free-standing, but can easily be transferred to the desired substrate for further processing, or collected on a rotating mandrel if thicker films or ribbons are desired. CNT thin films are characterized by their transparency and conductivity, with the goal generally being to maximize both. For flat panel displays it is necessary to achieve a sheet resistance of $\sim 100 \Omega \text{ sq}^{-1}$ and transparency of 80% at 550 nm (3). Conductivity can be enhanced by doping (60) or depositing metal coatings to the CNT films (61). Stretchable conductive films have been fabricated by embedding CNT films to extensible substrates like poly(dimethylsiloxane) (PDMS) (62). Resilience of these composite films can be enhanced by first pre-straining (63) or physically patterning (64) the PDMS prior to applying the CNT sheet.

CNT thin films have been utilized as electrodes and catalytic substrates in a variety of solar energy harvesting devices. Silicon hybrid solar cells can easily be fabricated by transferring the CNT film to a patterned Si wafer (65). In this scenario, the film acts as a charge

collector, and also as a Schottky junction for charge separation. Modest conversion efficiencies near 7.4% were achieved by a Si solar cell using as-spun CNT films. P-type doping of the CNTs via thermal oxidation or acid treatment improved the efficiency to 13.8% due to enhanced conductivity and also an increased barrier to charge recombination due to the formation of a thin oxide layer on the Si surface (66).

CNT thin films have also been utilized as catalytic components in dye-sensitized (67) and organic solar cells (68) to replace expensive platinum components. Compared to randomly oriented CNT films, aligned CNT films provided higher energy conversion efficiency on par with that of platinum-based cells. Aligned CNT sheets coated with TiO₂ were used as anode materials in photoelectrochemical water splitting cells (69). The aligned and interconnected morphology of the CNT film provided efficiency charge conduction pathways while the TiO₂ layer photogenerated and separated charges upon illumination.

Their high surface area and charge collection ability also makes CNT sheets a suitable scaffold for active materials in supercapacitors and lithium ion batteries. Aligned CNT sheets were electrodeposited with MnO_x to create a composite supercapacitor with high specific capacitance (~1250 F g⁻¹) and good cycling stability (70). Fu et al. recently reported the synthesis of core-shell CNT-Si and CNT-Si-amorphous carbon hybrids for flexible lithium ion electrodes with high columbic efficiency as well as good rate capability (71). Electrodes fabricated using solution techniques often still require aluminum or copper foil charge collectors due to high resistance from a lacking interconnected network. The low density and highly porous structure provide space for volume expansion and contraction which occurs during electrochemical cycling. The combination of these unique characteristics show promise for the manufacture of energy storage devices which are lightweight, flexible and small-scale—all of which are high attractive qualities for the consumer electronics industry.

CNTs drawn from spinnable arrays have also been investigated for actuators (72), thermoacoustic loudspeakers (73), organic light-emitting diodes (OLEDs) (74), substrates for CO₂ reduction (75), and reinforcement in high-performance polymer matrix composites (76).

2.1.1.4.2 *Fibers and Yarns*

As previously mentioned, dry-spun CNT sheets can easily be converted into fibers and yarns through densification techniques such as twisting (42) or solvent treatment (77). CNT yarns and their composites have been reported to have high strength, modulus, and electrical conductivity, and are therefore a desirable material for a wide variety of applications which are well documented in a recent review by Miao (78). A great deal of early work in this field focused on fabrication of high strength materials using CNT yarns as reinforcement in polymer matrix composite systems (79, 80). Composite yarns have also been created by drawing the spinnable sheet through a solvent droplet containing 1% poly(vinyl alcohol) (PVA) (81). After drying residual solvent the strength of the composite yarn more than doubled to 1.1 GPa compared to pristine CNT yarns.

Metal matrix composite yarns were synthesized via self-fuelled electrodeposition of Cu, Pt, Pd, and Ag onto the CNTs (82). Although metal-like electrical conductivities were achieved ($\sim 2.5 \times 10^5 \text{ S cm}^{-1}$), the tensile strength of the composite yarns was 30-50% lower than pristine CNT yarns. Using a novel biscrolling method, CNT hybrid yarns were fabricated where guest particles were deposited onto the CNT web using an electrostatic gun prior to yarn twisting and consolidation (83). By changing spinning conditions, drastically different morphologies were created including spiral and core-sheath structures, as shown in Figure 2.4.

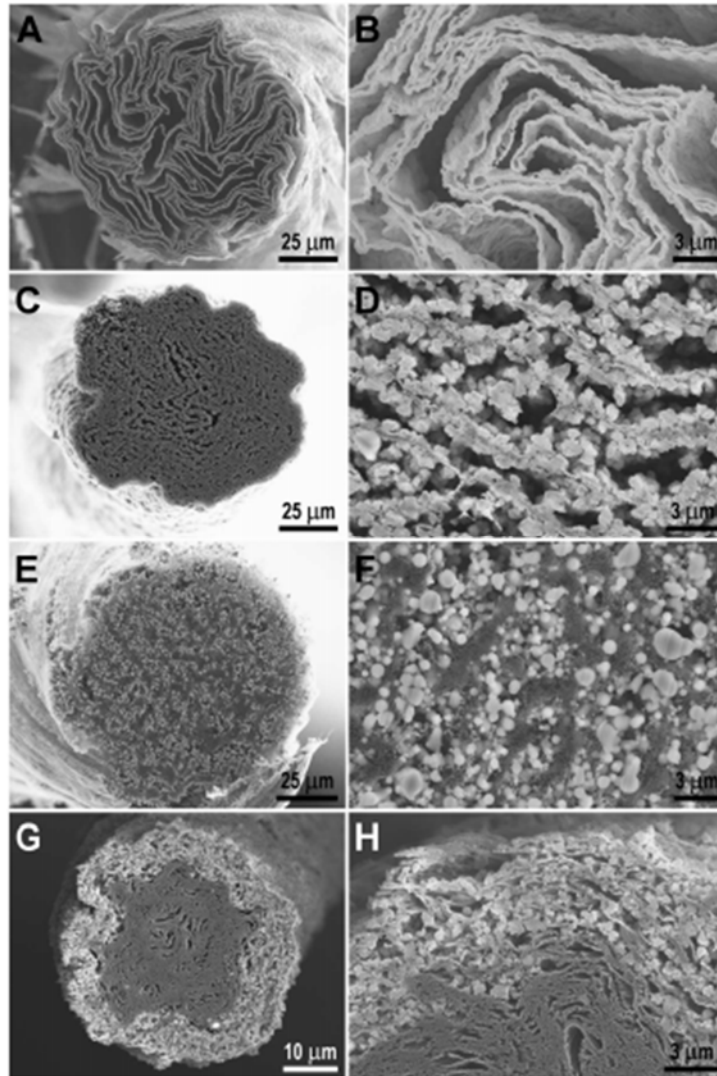


Figure 2.4 SEM images of the cross-sections of bisrolled yarns. (A, B) 70% Ti@MWNT yarn fabricated by electron beam evaporation and symmetrical twist insertion in liquid. (C, D) 93% TiO₂@MWNT yarn made by filtration based deposition and symmetrical twist insertion in liquid. (E, F) TiO₂@MWCNT yarn made by aerosol based deposition and twist insertion in air. (G, H) TiO₂@MWNT yarn made by patterned filtration-based deposition on MWNT sheets and asymmetrical twist insertion in liquid. Reproduced from (83).

Weng et al. recently reported the manufacture of coaxial fiber-based lithium ion batteries by winding the anode and cathode components onto a cotton yarn (84). To form the

anode, Si was electron beam deposited onto a CNT sheet. Then the CNT-Si sheet was sandwiched in between two pristine CNT sheets, after which the whole layered assembly was rolled together to form a scroll-structured yarn. The anode was fabricated by depositing lithium manganite particles to the CNT sheet, again followed by rolling to form a hybrid yarn. Finally, the individual anode and cathode yarns were wrapped onto the cotton yarn. The resulting battery was shown to have high specific capacity and good capacity retention. The fibers were also woven into a textile energy-storage structure which exhibited an areal energy density of 4.5 mW h cm^{-2} .

Fiber-based supercapacitors utilizing dry-spun CNT sheets have also recently been reported (85). CNT sheets were core-spun onto Pt filaments to form a core-sheath structure. CNTs, which are electrical double layer capacitors on their own, formed a thin layer on the fiber surface which could readily access the electrolyte. Surface generated charges were then quickly transported to the highly conductive core for efficient charge collection.

2.2 Carbon Nanotube – Inorganic Hybrid Materials

Carbon nanotube (CNT) – inorganic hybrids are a class of functional materials which have drawn widespread and increasing interest in recent years (2). As opposed to nanocomposites where the CNT and inorganic phases are combined via mechanical means, CNT-inorganic hybrids are characterized by CNTs which are coaxially coated with thin layers of inorganic material. Due to interfacial charge transfer processes and size domain effects, the CNT-inorganic hybrids are expected to exhibit a synergistic set of enhanced physical properties. CNTs are an interesting template for these hybrids as they possess superior mechanical, thermal, and electrical properties, while simultaneously being low density and of high surface area. There is considerable difficulty, however, in achieving smooth, conformal, and pin-hole free coatings on CNTs for three major reasons: 1) the inherent chemical inertness of high crystallinity and purity CNTs, 2) the tendency of CNTs to bundle and agglomerate due to large van der Waals forces, and 3) the lack of synthesis methods suitable for coating 3D and aligned CNT architectures. Before CNT-inorganic hybrid synthesis however, it is necessary to first address the issue of chemical inertness.

2.2.1 Functionalization

Functionalization of CNTs is a widely studied area of research due to the necessity of overcoming the inherently inert nature of CNTs before their use in virtually any application (86). CNTs may be functionalized covalently where attachment of the desired chemical groups occurs via bonding to the π -conjugated walls, or non-covalently where functional molecules are surface adsorbed or wrapped around the CNT structure. Perhaps the most common method of covalent functionalization is achieved by refluxing the CNTs in a mixture of strong acids, usually $\text{HNO}_3/\text{H}_2\text{SO}_4$, which results in the attachment of carboxyl and carbonyl groups to the CNT surface, thus improving solubility and chemical reactivity (87). Though effective, covalent functionalization methods inherently introduce structural defects and disrupts the delocalized electron system in CNT sidewalls due to the conversion of sp^2 carbon-carbon bonds to sp^3 bonds (88). As a result, CNT mechanical and electrical properties are altered which could degrade their performance in a hybrid material application.

Alternatively, plasma etching in an oxygen-rich atmosphere can be used to the same end (89). A benefit to using plasma treatment is the fact that it can be carried out in the vapor phase. This is particularly important for preserving the alignment, porosity, and low-density of CNT assemblies. In fact, oxygen plasma treatment was demonstrated as an effective means to improve wetting and chemical reactivity of CNT arrays by this researcher (90, 91), and others (92). To note, it was also shown by this researcher that CNT arrays made wetting via atmospheric pressure oxygen plasma treatment incurred less structural damage compared to those which were treated using thermal oxidation (91).

Non-covalent functionalization relies on hydrogen bonding and/or van der Waals forces to adsorb surfactant or polymer molecules to the CNT surface (93). Researchers have also demonstrated non-covalent attachment of aromatic compounds like porphyrins, relying on the π - π interactions to promote stacking of the aromatic rings on the CNT walls (94, 95). Though typically carried out using wet chemical processes, benzyl alcohol vapor was recently shown to effectively functionalize CNT yarns without destroying CNT alignment (96).

It is interesting to point out here an additional major difference between these methods. In terms of chemical reactivity, all parts of a CNT are not created equal. Areas of high reactivity

are present where there is a high degree of π -orbital mismatch caused by CNT curvature. These regions of high curvature are found at the CNT tips thus, CNT ends are more chemically reactive and are prone to preferential functionalization. This phenomenon is not seen in non-covalent techniques since the distribution of secondary interactions is uniform for CNT sidewalls and tips. Though weaker, non-covalent functionalization has the advantage of greater uniformity which could later improve coating uniformity as well (2).

2.2.2 Synthesis of CNT-Inorganic Hybrids

Many approaches for fabrication of CNT-inorganic hybrids exist, and they can generally be categorized into ex situ and in situ methods. In the case of the former, inorganic particles are first synthesized to have the desired structure and morphology, and are then attached to the CNT surface via covalent, non-covalent, or electrostatic interactions (97, 98). Though effective for the decoration of CNTs with nanoparticles or quantum dots, this technique is not suitable for applications where thin and continuous films are required. Furthermore, all ex situ approaches rely on wet chemical processing and are therefore incompatible with most low density CNT assemblies.

To contrast, continuous inorganic films can be directly synthesized on the CNT surface using in situ approaches. Because the CNT acts as a substrate it may promote or retard certain crystal structures or film compositions during film formation due to substrate-film interactions. Moreover, deposition may be carried out using wet chemical techniques such as sol-gel processing, electro or electroless deposition, electrochemical reduction, and hydrothermal treatment, or using gas phase methods including the gambit of physical deposition techniques (sputtering, evaporation, electron beam deposition, laser ablation), or chemical methods including CVD and ALD. The virtues of utilizing the ALD technique over the aforementioned gas phase methods will be discussed in greater detail in the following section.

2.2.3 Characteristics of Atomic Layer Deposition

ALD is a specialized subset of CVD that is capable of controllably depositing a variety of inorganic thin film materials onto substrates with complex shapes and micro and even nano-

sized architectures (99). It shares similarities in that film growth precursors are present in the gas phase. Whereas CVD precursors meet and react simultaneously in a reactor, ALD is unique in that the precursors remain completely separated from one another throughout the deposition process, thus preventing gas phase reaction. This results in a unique growth mechanism where substrates are saturated by alternating precursors. Chemical reactions are self-limiting due to the finite availability of reactive sites on a given substrate.

Due to the self-limiting and alternating precursor dose and purge cycles, the level of control over final film thickness is highly precise and accurate and lies simply in selecting the appropriate number of cycles as per desired thickness. ALD is particularly useful for coating rather high aspect ratio and high surface area substrates due to good step coverage characteristics and the lack of “line of sight” coating issues. In “line of sight” coating techniques like sputtering, preferential coating of areas of high substrate roughness is common. This results in the incorporation of many voids and defects, as well as non-conformal, non-uniform coating of nanostructured materials.

A typical ALD cycle, shown in Figure 2.5, proceeds by 6 characteristic steps which are as follows:

1. Exposure of a substrate to Precursor A;
2. Chemisorption of Precursor A to the substrate;
3. Inert gas purge to remove excess Precursor A;
4. Exposure of Precursor B to self-terminated substrate;
5. Surface reaction to produce monolayer of thin film;
6. Inert gas purge to remove gaseous by-products of reaction and excess Precursor B.

This reaction cycle results in a given amount of material deposited onto a substrate surface, and is commonly referred to as the growth per cycle (GPC). To grow a film of a desired thickness the reaction cycle is simply repeated until the desired amount of material has been deposited.

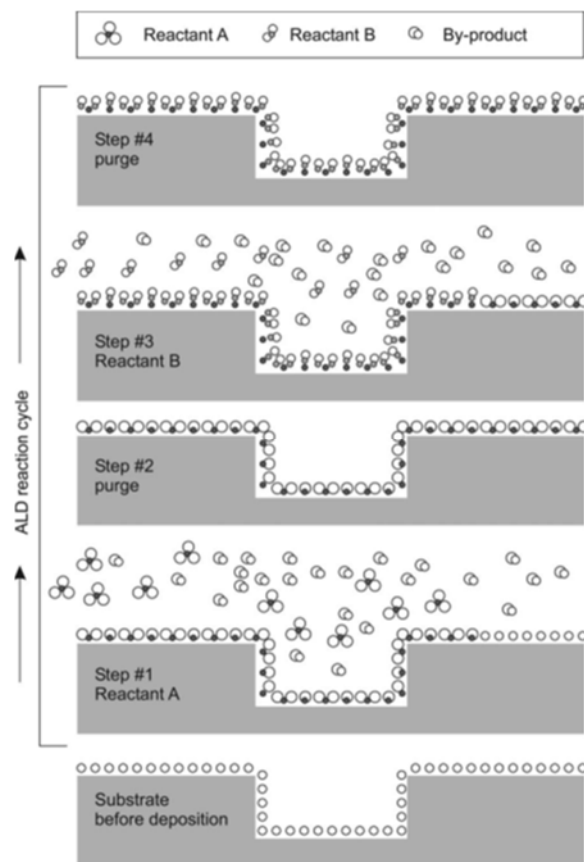


Figure 2.5 Schematic of ALD cycle. Step 1: Pulse of precursor A leading to its absorption on the substrate surface. Step 2: Purge of the unreacted precursor A and byproducts. Step 3: Pulse of precursor B, which reacts with the surface species created by precursor A. Step 4: Purge of the unreacted precursor B and byproducts. Reproduced from (100, 101).

Self-saturating ALD-type growth is said to occur in the regime where growth rate, GPC, is independent from precursor dose, given that there is an adequate flux of precursor molecules to coat all available active sites in the chamber and on the substrate. This means that GPC remains unchanged with respect to increasing precursor dose or pulse time, as illustrated in Figure 2.6a. This differs from CVD and other thin film deposition techniques in that increasing precursor dose usually results in additional material deposition.

In many self-limiting ALD precursor systems a temperature regime can be pin-pointed where deposition rate is constant. Below this window many precursors may either condense

on the sample and reactor walls or can also have so low thermal energy as to be non-reactive. Likewise, above the self-limiting window, ALD precursors are likely to thermally decompose, causing CVD-like growth or may possibly even desorb from the surface site before reaction takes place. A graph depicting the existence of an ALD window is shown in Figure 2.6b.

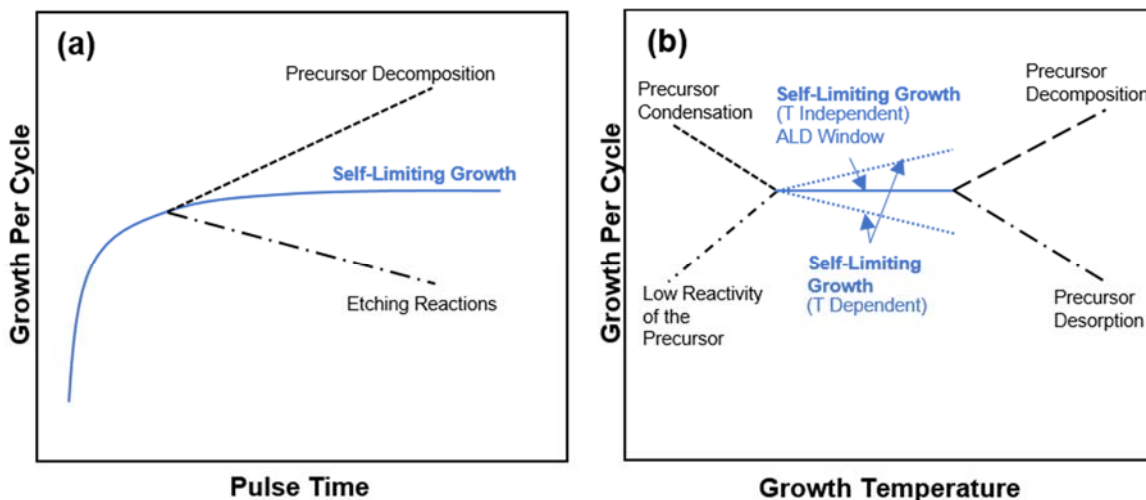


Figure 2.6 Growth per cycle as a function of (a) pulse time and (b) temperature for different growth modes.

There are of course drawbacks to the ALD technique. Compared to other film deposition techniques the typical ALD GPC is rather low, on the order of Å/cycle. In a highly optimized system a single cycle can take seconds, resulting in a monolayer of growth. In lab scale systems, or when depositing on high aspect ratio and/or high surface area substrates, the cycles times may be even longer, on the order of minutes. Luckily to alter the optical, thermal, or electrical properties of the substrate and impart the desired functionality, one needs only to deposit a few nanometers of the coating material. Additional shortcomings of ALD lie in the precursor chemistry. Though an active area of research, there are some technologically important materials such as Si, Ge, and Cu as well as many transition metals which do not

currently have a suitable precursor and/or ALD parameter space for the technique to be effective.

Additional difficulties may arise related to weak precursor-substrate reactivity. For nucleation to occur in ALD, reactive sites are required for precursor adsorption. During the initial cycles, GPC may not be perfectly constant, but instead may increase with cycle number until reaching a constant value. Substrates with few adsorption sites take longer to reach constant GPC compared to those with many. Therefore, it is only possible to deposit few nm-thick conformal films when dense nucleation occurs on the substrate surface. Poor nucleation results in discontinuous, rough, or even bead-like films. This is referred to as substrate-inhibited or island growth and has been shown to occur on H-terminated Si wafers (102). It is caused by weak interactions between the precursor molecules and the substrate terminations. If chemisorption does not occur, or if desorption of the precursor is favored, the substrate surface will not be densely saturated with precursor molecules following the first exposure. Subsequently, the islands of nucleated precursor will form islands of ALD film once Precursor B is introduced and reacted. If these islands are close enough together then only a few additional cycles will be required for the islands to grow and coalesce to form a continuous film. In substrate-inhibited growth however, the nucleation sites are distant from one another and instead of coalescing the islands tend to form particles or spheres of film on the substrate.

It is important to understand how ALD process and sample parameters may dictate film microstructure or crystallinity (103). Though each precursor system is unique and many parameters are interrelated, general trends do exist. Temperature is perhaps the most straightforward variable to control, since transitions from amorphous to crystalline polymorphs are known to occur at characteristic temperatures for a particular material. Increasing deposition temperature also typically results in the incorporation of fewer impurities. Impurities have also been shown to affect crystallinity. It is not uncommon to have residual Cl in TiO₂ films deposited from TiCl₄ at low temperature, though it is unclear whether this is the sole reason for the inability to obtain crystalline TiO₂ at low deposition temperatures (104). In the case of TiN ALD, crystalline films were found to contain up to 7.7 at% Cl and 16 at% H. However, incorporation of only a few at% of C resulted in only amorphous films (105, 106).

Similarly, researchers investigating ALD of V_2O_5 found that C impurities prevented the formation of crystalline films (107). It is also possible for the substrate to dictate whether a film is amorphous or crystalline. For instance, TiO_2 deposited at 300 °C on cleaned Si was found to be partly crystalline, while TiO_2 deposited on Al_2O_3 was amorphous (108). Crystalline ALD films will commonly exhibit columnar grains extending through the entire film thickness and perpendicular to the substrate. During the initial ALD cycles, dense nucleation will result in many smaller grains, while sparse nucleation yields fewer, but larger grains (103).

There has been a great deal of research done in the area of ALD in recent years, fueled particularly by the field of microelectronics. Exhaustive reviews (103, 109), books (110), and prospects (111) have been published which discuss the full gambit of ALD precursors, materials, substrates and applications—many which lie outside the scope of this dissertation.

2.2.3.1 Atomic Layer Deposition of Aluminum Oxide

Alumina (Al_2O_3) is considered an attractive material for thin film deposition due in part to its good barrier capabilities. In microelectronics it has been investigated as a dielectric material to replace SiO_2 due its wide band gap (9 eV), high permittivity ($\kappa = 9$), strong adhesion to a variety of materials, as well as good chemical and thermal stability (112, 113). Additionally, it has been investigated for use as passivation layers to inhibit gas diffusion for food packaging and plastic soda bottles (114, 115). Al_2O_3 ALD coatings on polymers could also be used as gas diffusion barriers for organic light emitting diodes or flexible electronic devices (116, 117).

The trimethylaluminum (TMA)/water ALD process for depositing Al_2O_3 is commonly chosen as a test system for ALD on new materials and substrates. This is due to the nearly “ideal” deposition characteristics at a wide variety of deposition parameters (temperature and pressure), due to favorable Gibbs free energy of formation between reactants and products in a relatively wide temperature range (30-300 °C) (114, 118, 119). Additionally, the gaseous by-product of reaction, in this case methane, is largely inert to a wide variety of substrate materials. As such, the process is highly optimized and the maximum growth rate of a half monolayer/cycle is able to be achieved, which equates to 0.9-1.1 Å/cycle (120).

Al₂O₃ coatings are deposited by the following two sequential chemical reactions where asterisks denote surface species (118, 119):



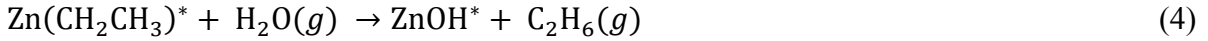
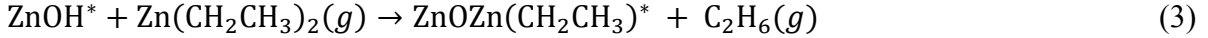
Though the TMA-H₂O process is by far the most common, other precursors for Al₂O₃ ALD have been studied including ozone and oxygen plasma for oxygen sources, and chloride, bromide, alkoxides, alkylamides, amidinates and mixed ligand compounds for aluminum sources (100). Regardless of precursor or substrate, all Al₂O₃ films deposited below 600 °C are amorphous (103). Post-deposition annealing treatments have been demonstrated as an effective means to crystallize films and improve their insulating properties. Jakschik et al. found that 5 nm thick films on SiO₂ could be crystallized at 900 °C. To note, thicker films could be crystallized at lower temperatures, possibly due to the greater likelihood of thicker films containing seeds to nucleate crystal growth (121). The deposition substrate can also determine the crystallization temperature and polymorph achieved (122, 123). Zhang et al. investigated the use of rapid thermal annealing to crystallize amorphous Al₂O₃ ALD films. At 1150 °C the full width half maximum (FWHM) of the Al₂O₃ (012) XRD peak was minimized, and the insulating properties of the film were maximized (124).

2.2.3.2 Atomic Layer Deposition of Zinc Oxide

Zinc oxide (ZnO) is a wide band gap semiconductor with great technical importance due to its many interesting properties such as transparency to visible light, controllable conductivity, low cost, ease of manufacture, high carrier mobility, and direct band gap of 3.37 eV. This combination of properties have given rise to applications in solar cells, thin film transistors, light emitting diodes, gas and UV sensors. Though it can be deposited using a variety of thin film techniques, the use of ALD to do so has grown significantly in popularity.

Though zinc acetate was historically the first precursor used for ZnO ALD (125), it has been superseded by diethyl zinc (DEZ) in recent years due to the ability to deposit at low

temperatures. DEZ reacts readily with water by the following reactions, where asterisks denote surface species (126, 127):



Typical deposition temperatures for the DEZ-H₂O system lie in the range of 100-200 °C, but deposition even at room temperature has been demonstrated (127–131). Though water is the most common oxygen source, more energetic species such as O₂ and/or H₂O in plasma enhanced ALD (PEALD) have been demonstrated. Oxygen species with higher reactivity result in the growth of highly stoichiometric films due to fewer oxygen vacancies. A high degree of stoichiometry is especially important for applications where the ZnO film must be insulating, such as in piezoelectric devices.

In a very recently published review article of ZnO ALD (132), the ALD window was estimated to lie in the range of 110-170 °C while the GPC was 1.8-2.0 Å/cycle, though these values depend greatly on the specific ALD system parameters. Deposition temperature is thought to be the most crucial factor in dictating ZnO GPC as well as resulting film properties.

Despite the fact that ALD is typically carried out at fairly low temperatures, ZnO still has a tendency to crystallize in the wurtzite structure quite readily. It has been observed that the growth temperature can influence the preferred crystal orientation of the resultant thin film. Generally, at deposition temperatures below 70 °C and above 220 °C the preferred grain orientation is along the c-axis, or (002) direction (133–135). When deposition temperature is increased above 70 °C the (101) crystal orientation likewise increases. In the range of 160-200 °C, the preferred grain orientation is fully along the a-axis (126, 128, 133, 135, 136). The effect of deposition temperature on preferred ZnO crystal orientation is shown in Figure 2.7. While deposition temperature is the main factor in determining the film crystal structure, it has also been shown that the oxygen source (137), as well as purging duration (138), may play a minor role.

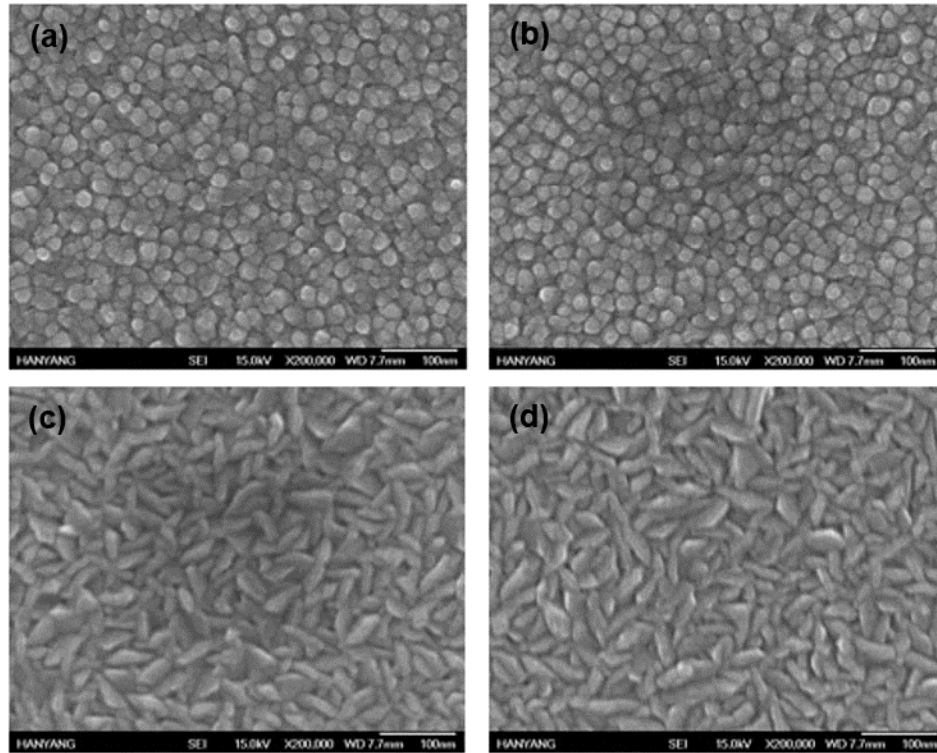


Figure 2.7 Top-view SEM images of ZnO films deposited on p-type Si(100) substrates at various temperatures of (a) 70, (b) 90, (c) 110, and (d) 150 °C. Films deposited at 70 and 90 °C have strong (002) *c*-axis preferred orientations due to the cylindrical and columnar structures oriented normal to the substrate. Films deposited at 110 and 150 °C show wedge-shaped crystal structures with *a*-axis directions parallel to the substrate. Reproduced from (128).

Besides crystal orientation, stoichiometry is another factor that can be controlled by deposition temperature. Film stoichiometry correlates directly to ZnO's electrical properties, and is therefore a technologically important parameter. As-deposited ZnO will typically demonstrate n-type conductivity due to the presence of defects and impurities in the crystal. Increasing the temperature of the ALD system alters the reactivity between precursor molecules and surface sites, which can lead to incomplete oxidation and therefore oxygen vacancies. In fact, a clear relationship exists between ALD growth temperature and free electron concentration in polycrystalline ZnO films. Guziewicz et al. determined that films grown at temperatures below 100 °C had an electron concentration of 10^{17} cm^{-3} , while it was

10^{20} cm^{-3} for films deposited at $200 \text{ }^\circ\text{C}$ which corresponded to film conductivities of 0.58 and $431 \text{ } \Omega^{-1} \text{ cm}^{-1}$, respectively (129). Films grown using PEALD generally result in highly stoichiometric films with very high resistivity due to the use of highly reactive O_2 plasma as the oxidation source (139–141).

2.2.3.3 Atomic Layer Deposition of Titanium Dioxide

Titanium dioxide (TiO_2) is another technologically important semiconductor which is utilized in a wide variety of applications including solar cells, photocatalysis, and sensors. It possesses excellent physical properties such as good chemical stability, high refractive index, and good visible and IR transmission. Titania's utility is enhanced by the fact that it can be deposited in a wide variety of polymorphs depending on the particular process conditions used. A great deal of work has focused on depositing anatase and rutile crystalline phases. However, amorphous TiO_2 is also an important material, especially for optical and photonic applications.

Especially for optical and optoelectronic applications, it is of utmost importance to maintain precise and accurate control over film thickness to ensure optimal device performance. One of the first comprehensive reports of using ALD, or atomic layer epitaxy (ALE) as it was called, to deposit TiO_2 was by Ritala et al. in 1993 (142). TiCl_4 and H_2O precursors were used to deposit films on a variety of substrates at growth temperatures between 150 and $600 \text{ }^\circ\text{C}$. The GPC varied as a function of temperature from $0.35 \text{ } \text{Å}/\text{cycle}$ at $200 \text{ }^\circ\text{C}$ to $0.56 \text{ } \text{Å}/\text{cycle}$ at $400 \text{ }^\circ\text{C}$. They also demonstrated that the substrate had an effect on GPC. At $500 \text{ }^\circ\text{C}$ the GPC on Corning 1733 was only $0.42 \text{ } \text{Å}/\text{cycle}$ while on soda lime the GPC was $0.52 \text{ } \text{Å}/\text{cycle}$. In the simplest case, ALD of TiO_2 can be described by the following ligand exchange reactions, where asterisks denote surface species:



Although earliest reports on ALD of TiO_2 used TiCl_4 and H_2O as precursors, films were also deposited using titanium isopropoxide (143) and titanium ethoxide (144) precursors, though

a self-limiting ALD temperature window was not found for the latter system. Detailed investigations on the structure and morphology of as-deposited TiO₂ films found that surface roughness increased as a function of increasing film thickness (145). This effect could be alleviated by incorporating thin Al₂O₃ interlayers among the thicker TiO₂ layers (146). Aarik et al. later determined that smooth amorphous films with some residual Cl content could be fabricated at deposition temperatures less than 165 °C, but roughness increased significantly above 165 °C (104). It was found that this surface roughening corresponded to the onset of crystallization. Furthermore, while films deposited above 165 °C were majorly anatase, the rutile content increased as a function of increasing temperature in the interval of 350 to 500 °C.

Triani et al. explored deposition of TiO₂ on polycarbonate (PC) films and Si wafers at temperatures ranging from 80-120 °C (147). While film thickness on Si increased linearly as a function of ALD cycles, they trend was somewhat scattered for PC films. It was inconclusive whether this could be attributed to the nature of TiO₂ nucleation and growth on PC or to film measurement difficulties. Chlorine concentration in the films was found to increase with decreasing deposition temperature. In fact, compared to similar measurements from a higher temperature study by Aarik et al. (148) the chlorine content increased drastically in films deposited below 160 °C. XRD analysis confirmed that films deposited on both Si and PC substrates were amorphous.

The effect of water plasma pre-treatment on the nucleation behavior of TiO₂ was evaluated using SEM. Interestingly, plasma treated PC exhibited island growth while as-received PC appeared smooth and featureless as shown in the images in Figure 2.8. Though water plasma treatment is known to increase hydroxyl group concentration (149), it was hypothesized that the treatment did not uniformly functionalize the PC surface, thus creating local nucleation sites with enhanced reactivity (147).

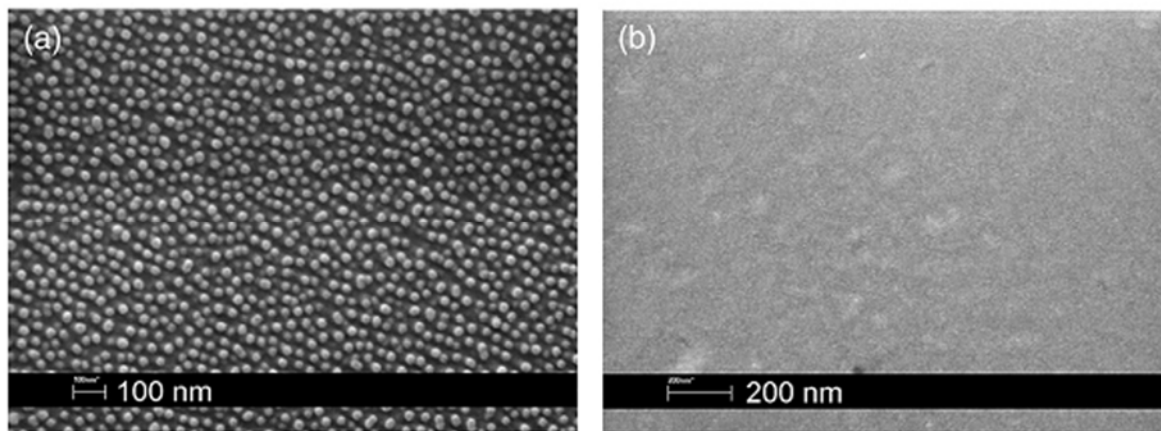


Figure 2.8 SEM images of TiO₂ films deposited on (a) water plasma treated and (b) as-received polycarbonate. Both films were deposited for 50 cycles at 80 °C. Reproduced from (147).

2.2.4 Coating Carbon Nanotubes Using Atomic Layer Deposition

ALD coating of CNTs was first reported by Javey et al. in 2002 (150). In this study SWCNTs supported on a SiO₂ substrate were coated with insulating ZrO₂ for the purpose of making a transistor. A variety of metal oxides and metals have since been deposited on CNTs including Al₂O₃ (151), HfO₂ (152), ZrO₂ (150), TiO₂ (153), SiO₂ (153), ZnO (154, 155), V₂O₅ (156), Pt (157, 158), Ru (159), and W (160) for a wide range of applications including catalysis (157, 158), Li-ion batteries (161), field-effect transistors (162), and many others (159). As ALD of Al₂O₃, ZnO, and TiO₂ on CNTs is of particular import for this research, discussion of their literature follows in the next sections.

2.2.4.1 Al₂O₃ Atomic Layer Deposition on Carbon Nanotubes

The first example of Al₂O₃ ALD on MWCNTs was in 2003 (151). Conformal and uniform deposition of amorphous Al₂O₃ was demonstrated on both the inner and outer surfaces of the MWCNT powders. The group cited that because MWCNTs should be primarily covered in sp² carbon orbitals, an alternate bonding mechanism must exist since conformal coatings were achieved. First they proposed that the hydrogen atoms of the water precursor (rather than

oxygen) could have bonded with the carbon surface. Alternately, they also hypothesized that the aluminum atoms from TMA could have bonded with the carbon.

Today it is common to attribute the facile nucleation and growth of Al_2O_3 on MWCNTs to the higher concentrations of defects found on MWCNT walls compared to SWCNTs. These defects can take on many forms and may or may not be oxygenated. Interestingly, the ordinal study by Lee et al. of Al_2O_3 on MWCNTs is the only one that proposes an actual bonding mechanism for non-functionalized CNTs. Since this particular study did not characterize the defect density or oxygen content in as-grown MWCNTs, it is impossible to determine whether or not these particular MWCNTs were inadvertently oxidized or defect-ridden.

Once coated with Al_2O_3 , CNTs are effectively functionalized since the surfaces are now densely covered with O-atoms. Herrmann et al. exploited this fact and coated MWCNTs with a seed layer of Al_2O_3 to provide a high concentration of $-\text{OH}$ functional groups to which they adsorbed and chemically bonded a functional hydrophobic monolayer (160). Additionally, by depositing alternating Al_2O_3 and W coatings on MWCNTs, this group demonstrated the manufacture of nanocoaxial cables.

In a similar study Al_2O_3 was deposited on MWCNTs as a seed layer to enable the subsequent conformal deposition of ZnO (154). Without the seed layer present, the ZnO was observed to be composed of non-uniform and discontinuous nanocrystals. It is interesting to note that the group could easily deposit Al_2O_3 conformally, but not ZnO. They hypothesized this was due to possible chemical reaction of ALD precursors with the CNT surface, though no additional experimentation or characterization was provided.

More recently MWCNTs were coated with Al_2O_3 for the purpose of improving the capacity of Li-ion battery anodes (161). In this particular study the group pointed to the high defect density, characterized using Raman spectroscopy, as the reason for achieving conformal coatings. In this case it was beneficial to have highly defective MWCNTs since defect sites increase surface area and intercalation sites on the tube surface. Anodes with a thin film of Al_2O_3 coating around the MWCNTs exhibited better performance than non-coated anodes. This was due to the additional mechanical integrity provided to the electrode by the coating, as well as increased intercalation sites for Li-ions. Additionally, the Al_2O_3 restricted unwanted

reactions between the electrolyte and carbon surface and thus stabilized the solid electrolyte interphase (SEI), which is a common source of inefficiency and failure in lithium-ion batteries.

Functionalization techniques were originally employed for the pre-treatment of SWCNTs prior to ALD. SWCNTs are known to have significantly fewer defects and impurities on their surfaces compared to MWCNTs, thus preventing adequate nucleation via precursor adsorption. The techniques can be categorized by their mechanism—covalent and non-covalent. Covalent functionalization was first demonstrated for Al₂O₃ ALD on SWCNTs in 2005 (163). Reactive diazonium species (nitroaniline) were allowed to react with SWCNT surfaces for 15 hours so that NO₂ functional groups could covalently attach to the sidewalls. The result was uniform and conformal Al₂O₃ thin films on functionalized, suspended SWCNTs.

Though –NO₂ chemical functionalization was shown to be an effective means for achieving conformal ALD films, there are some accompanying drawbacks. First, due to the liquid-based processing there are many impracticalities associated with potential scale-up. Furthermore, the nature of covalent functionalization dictates that the hybridization state of the CNTs be altered. This is problematic because the desirable optoelectronic properties are degenerated upon treatment.

As a result, Farmer and Gordon went on to publish a study one year later which explored gas-phase, non-covalent functionalization techniques (164). Suspended SWCNTs were subjected to alternating pulses of NO₂ gas and TMA vapor for the purpose of improving the nucleation behavior without altering the SWCNTs' physical properties. By monitoring the SWCNT conductivity, NO₂ molecules were shown to readily adsorb on SWCNT surfaces, but then quickly desorb during the purge step. To prevent desorption TMA was pulsed. The aluminum centers of TMA were attracted to the exposed oxygen ends of NO₂. A complex was formed which was difficult to desorb at room temperature, but not yet stable at typical Al₂O₃ ALD temperatures (>100 °C). This was alleviated by stabilizing the functional layer with 5 TMA/H₂O cycles at low temperature, before increasing the temperature to 225 °C for further coating. The resulting coatings were uniform, conformal and continuous. Other non-covalent functionalization techniques include the adsorption of surfactant molecules (165, 166) and

ethanol pre-treatment (166), though the latter does not ensure perfectly conformal coatings as the other techniques do.

Though the majority of studies on ALD on MWCNTs demonstrated facile coating without the need to functionalize, this is not always the case. In a study by Devine et al. multiple processing strategies were tested to effectively coat milligram quantities of CNT powders without the use of a fluidized bed reactor (167). CNT powders were placed inside polymer fiber “baskets”, which were then loaded into the ALD reactor. Long precursor dose (5 s) and soak (60 s) times were utilized to allow ample time for precursor molecules to permeate through the fiber basket and MWCNTs. Conformal coatings were achieved using this method. The experiment was repeated using conventional ALD process parameters (1 s/30 s/1 s/30 s), without the long soak period, and the coatings were not conformal or continuous.

Cavanagh et al. found that untreated MWCNTs coated in a fluidized bed ALD system exhibited nucleation difficulties which resulted in growth of nanospheres and bead-like Al₂O₃ structures (168). This atypical behavior was attributed to the supposedly lower defect density compared to MWCNTs used in previous studies. Utilizing gas-phase, non-covalent functionalization via NO₂/TMA exposure, an adhesion layer was deposited on the MWCNT surfaces allowing for conformal film growth.

2.2.4.2 ZnO Atomic Layer Deposition on Carbon Nanotubes

Given ZnO’s great potential in a variety of semiconducting applications, it was a natural material selection for coating CNTs. In 2007, Min and co-workers used ALD to synthesize ZnO nanoparticles on the surface of SWNTs for the purpose of improving the lifetime of SWCNT cold cathodes used for field emission applications (169). In this particular instance the selective nucleation and particle formation at nanotube defect and impurity sites was considered beneficial. Though pristine SWCNTs are considered to be superior field emitters due to their atomically sharp shape, large aspect ratio, and high electrical conductivity, concurrent ion bombardment during emission can drastically harm SWCNTs with defects, thus degrading performance and emission lifetime. To overcome this degradation, selective shielding provided by ZnO nanoparticles improved emission lifetime by 2.5 times compared

to pristine SWCNTs. This technique for ZnO nanoparticle deposition was later applied to SWCNT forests by the same group (170).

While the ZnO particle morphology was useful in the previous cases, smooth and conformal thin films are often desired for most other applications. This can be achieved by first depositing a thin buffer layer of Al₂O₃ to the CNT surface, followed by ZnO (154). Direct coating of CNTs without the use of a buffer layer is fundamentally important for many photoelectric and/or photochemical applications because it allows for charge transfer between the CNT and thin film. Li et al. directly coated plasma-enhanced CVD grown MWCNT arrays with conformal ZnO films without need for a buffer layer (171). They observed that, unlike the smooth amorphous films usually achieved via ALD of Al₂O₃, the ZnO films tended to be rough due to the polycrystalline texture. The continuous morphology was attributed to the high defect density of the as-grown CNTs. Figure 2.9 shows Raman spectra taken before (a) and after (b) ZnO ALD. The strong D band at ~ 1346 cm⁻¹ confirms the presence of many defects, while the additional low wavenumber peaks on curve (b) correspond to ZnO shells. In addition the group conducted photoluminescence (PL) measurements and found that the UV to visible emission ratio of their coated CNT array was significantly higher compared to previous reports (154). They attributed this to the high crystalline quality of the ALD-grown ZnO.

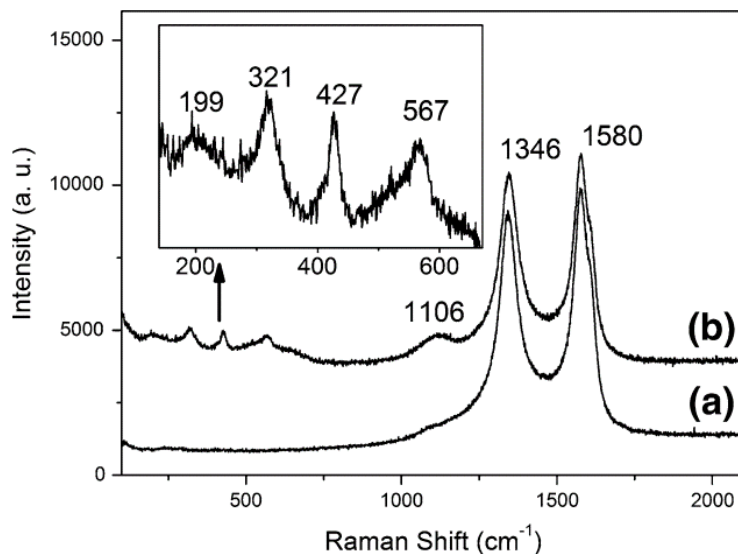


Figure 2.9 Raman spectrum of CNTs before (a) and after (b) ALD of ZnO. The inset depicts additional peaks due to presence of ZnO on ZnO-coated CNTs. Reproduced from (171).

In a similar experiment, Wen et al. also coated MWCNT arrays with ZnO for the purpose of studying the intensity of UV emission (172). The mechanism by which enhancement of UV emission occurred was determined by measuring the PL spectra of both ZnO coated arrays as well as ZnO coated Si wafers. They found that upon optical excitation light scattered between adjacent tubes within the array, and these multi-excitations improved the UV emission by 2.5 times over ZnO coated Si wafers with a simple planar morphology. Interestingly, XRD of ZnO coated CNTs found not only wurtzite ZnO, but also a secondary compound – ZnCO₃. No reflections from CNTs were measured due to suppression from the oxide coating. It was hypothesized that the ZnCO₃ formed as a result of C diffusion (from surface carbonaceous impurities), into the ZnO coating via substitution of Zn for C. This was verified by ab-initio calculations as well as the presence of a red-shifted PL spectrum which corresponded to the proposed doping state.

Hu et al. also demonstrated ZnO ALD coatings on MWCNT arrays for the purpose of creating flexible piezoelectronic generators (155). The top 60-65 μm of the MWCNT arrays appeared to be conformally coated with 30-35 nm of ZnO, while the rest of the array remained

uncoated. This was attributed to the finite diffusion depth of ALD precursor molecules into the array. They found with extended number of cycles, the ZnO grains grew preferentially along the c-axis. Silver electrodes were pasted on the ZnO coating and bare CNT sections, and generated current was measured upon application of strain. Due to the piezoelectric effect of ZnO, charges were generated and separated at the CNT-ZnO interface, thus creating current. The measured current was 3-6 orders of magnitude greater than previously reported data for ZnO nanowires.

Randomly oriented MWCNTs were uniformly coated with ZnO nanoparticles for application in UV photodetectors (173). After 50 ALD cycles, the MWCNTs were covered in uniformly dispersed ZnO nanoparticles. After 150 cycles however, the disparate particles coalesced to form a ZnO film with a thickness of 85 nm. Gold electrodes were sputtered onto the CNT-ZnO nanocomposites so current could be monitored upon exposure to UV light. The electrical resistance of the samples was found to be several orders of magnitude smaller than that of pure ZnO films, meaning that charges migrated along the conductive CNT network rather than through the ZnO particles. As shown in Figure 2.10, the sensing behavior of ZnO-CNT photodetectors switched from p-type to n-type with increasing ALD cycles due to an increased density of charge carriers in the case of the latter. Photodetectors fabricated from n-type nanocomposites also elicited faster response and recovery times due to the accelerated photochemical reactions on the thicker ZnO surface.

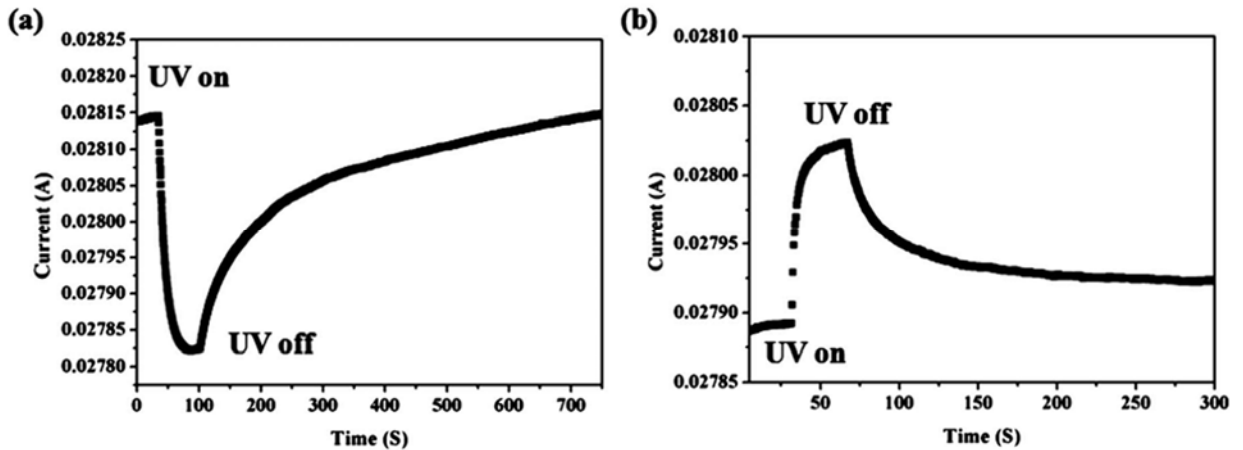


Figure 2.10 Photoresponse curves of MWCNT-ZnO UV photodetectors obtained after (a) 50 and (b) 150 ALD cycles. Reproduced from (173).

2.2.4.3 TiO₂ Atomic Layer Deposition on Carbon Nanotubes

In 2005 Gomathi et al. first demonstrated ALD of TiO₂ on SWCNTs and MWCNTs using TiCl₄ and H₂O precursors (153). To promote chemical bonding the CNTs were first acid treated to create hydroxyl groups on the CNT surface. EDX spectra showed that CNTs coated for 10 cycles at 80 °C contained residual chlorine due to incomplete hydrolysis of TiCl₄. Following calcination at 350 °C for 12 hours, the chlorine was removed and the oxide layer thickness measured 8-10 nm. MWCNT arrays have also been coated with TiO₂ using this precursor system (174). After 200 cycles at 150 °C the coating thickness was 5 nm, indicating a lower than normal GPC of 0.5 Å/cycles. Coated arrays were annealed in Ar at 450 °C for 2 hours which resulted in conversion from amorphous to anatase TiO₂ films. Unfortunately, neither the height of the arrays nor the coating uniformity throughout the array thickness was reported in this study.

Acid functionalized MWCNT networks (similar to thin buckypapers) have been coated using tetrakis dimethylamino titanium (TDMAT) and H₂O (175). After 200 cycles at 200 °C the MWCNTs within the network were conformally and uniformly coated with 10 nm thick films. To compare, TiO₂ was also deposited onto the MWCNT networks via spin-coating from

a sol-gel solution. Instead of conformal coatings, the TiO₂ was found to fill in the pores between the MWCNTs and the coating thickness varied greatly.

As an alternative to hydrolytic precursor systems, TiO₂ coatings were deposited on MWCNTs by reacting titanium isopropoxide (TIP) with carboxylic acid (176–178). As a result films were able to be deposited at temperatures as low as 20 °C, but the ALD window was found to occur between 150-200 °C with a GPC near 0.6 Å/cycle. EDX spectra showed that as-deposited films were highly pure without need for additional heat treatment. Marichy et al. used ALD of TiO₂ to characterize the density and distribution of nucleation sites on MWCNTs which had undergone a variety of functionalization treatments (179). In this case TIP was reacted with acetic acid, and the reaction was carried out at 200 °C. By varying the degree of functionalization via chemical and thermal treatments the TiO₂ coating morphology was found to change from bead-like to conformal corresponding to low and high densities of nucleation sites, respectively.

Recently TIP and H₂O precursors were used to deposit TiO₂ on MWCNTs (180). After 20 cycles at 220 °C, small nuclei (~2 nm) were formed on the MWCNT surface. Clusters of crystalline particles after 200 cycles, and conformal films were only achieved after 750 cycles. The authors suggested many interesting ideas for the characterization of the MWCNT-TiO₂ interface, but failed to report any results.

2.2.5 Properties and Applications of Carbon Nanotube – Metal Oxide Hybrids

To date, the majority of research on CNT-metal oxide hybrids has focused on their fabrication using methods besides ALD. Though other hybrid synthesis techniques are often used in the following examples, a recurring theme in the literature is the necessity for better control of coating thickness and uniformity. The following section outlines only a few of the numerous applications of CNT-metal oxide hybrids with special attention being focused on those applications where the unique capabilities of ALD (atomically thin and conformal coatings) are best suited.

2.2.5.1 Photocatalysis

The field of semiconductor photocatalysis is a booming one, as it encompasses technologies related to clean energy production as well as water and air purification. Solar energy conversion may be accomplished via photoelectrochemical electrolysis, or “water splitting” to produce hydrogen. Alternatively, dye-sensitized solar cells utilizing the photocatalytic activity of modified semiconductor nanostructures are another route to clean energy production. Heterogeneous photocatalytic oxidation and reduction of organic compounds or heavy metal ions in water is another interesting application of these materials. All of these technologies are realized through the same underlying mechanism. Electron-hole pairs are generated when a semiconductor is illuminated by photons having energies greater than the material’s band gap, E_G . In the case of water splitting, the electron-hole pairs are separated, and the electrons flow to a platinum counterelectrode where they reduce protons to form hydrogen. To contrast, in photocatalytic processes the photogenerated pairs act as reactive sites for oxidation (by holes) and/or reduction (by electrons) directly on the semiconductor surface.

TiO₂ is a commonly used material for these applications due to its low cost and ease of manufacture, as well as high photoactive efficiency and stability, inertness, and nontoxicity (181, 182). However, for a semiconductor to operate efficiently in solar illumination, a band gap near 1.35 eV is required. Anatase and rutile TiO₂ have band gaps of 3.25 and 3.0 eV, respectively, and therefore absorb only 3% of sunlight, instead operating most efficiently at near-UV wavelengths (181, 183). Extending the absorption of visible light and improving photocatalytic efficiency in TiO₂ is critically important to its effectiveness in devices, and although other techniques for doing so exist (2), the incorporation of CNTs is a particularly promising one.

2.2.5.1.1 Photocatalytic Oxidation and Reduction

The first example of enhanced photocatalytic activity of TiO₂-CNT hybrids demonstrated their use for oxidation degradation of phenol in 2004 (184). Composite catalysts with different MWCNT contents were fabricated using a modified sol-gel method. XRD

analysis showed that both neat and composite TiO₂ catalysts were anatase, where crystal size decreased with increasing MWCNT content. Pure MWCNTs, neat TiO₂, and composite catalysts were then evaluated for phenol decomposition under UV irradiation. Pure MWCNTs exhibited negligible decomposition activity. After 4 hours of exposure, however, TiO₂-MWCNT composite catalysts fully decomposed the phenol, while neat TiO₂ only reached 44.2% of phenol conversion for the same reaction time. The synergetic enhancement was found to be optimized at a MWCNT/TiO₂ weight ratio of 20%. Additionally, the sol-gel formed composite was shown to be more effective than a mechanically stirred mixture of the same composition. When evaluated in visible light instead of UV, 20% MWCNT/TiO₂ was also found to be the optimal ratio (185). Further studies have since demonstrated TiO₂-CNT hybrids for the decomposition of other organic molecules, including acetone (186) and propene (187). CNT-ZnO hybrids have shown enhanced photocatalytic oxidation of methylene blue (188) and indigo carmine (189).

MWCNT-TiO₂ composite catalysts were also shown to have enhanced photocatalytic activity for the reduction of CO₂ with H₂O (190). Fabrication via the sol-gel method resulted in MWCNTs coated with anatase TiO₂ nanoparticles, while hydrothermal processing resulted in rutile TiO₂ nanorod covered MWCNTs. Under UV irradiation sol-gel formed catalysts led to the formation of C₂H₅OH, while hydrothermal formed samples majorly produced HCOOH. Optimal photocatalyst enhancement was found to occur in lower concentrations of MWCNTs, supposedly caused by blocking or absorption of UV light by excessive CNTs. Recently, MWCNT-TiO₂ core-shell nanocomposites were fabricated to also study the photoreduction of CO₂ (191). Before coating, MWCNTs were acid treated to induce hydrophilicity and to functionalize the surfaces with carboxyl groups. Synthesis of the TiO₂ coating was carried out via hydrolysis of titanium butoxide (TBOT), followed by calcination in air. After calcination MWCNTs were coated in a network of densely packed, anatase TiO₂ nanoparticles with a thickness of 16.6 nm. UV-vis spectroscopy, which is shown in Figure 2.11, revealed that MWCNT-TiO₂ nanocomposites absorbed light in both visible and UV wavelength ranges, and as a result, exhibited superior photocatalytic activity for the photoreduction of CO₂ to CH₄ under visible light illumination.

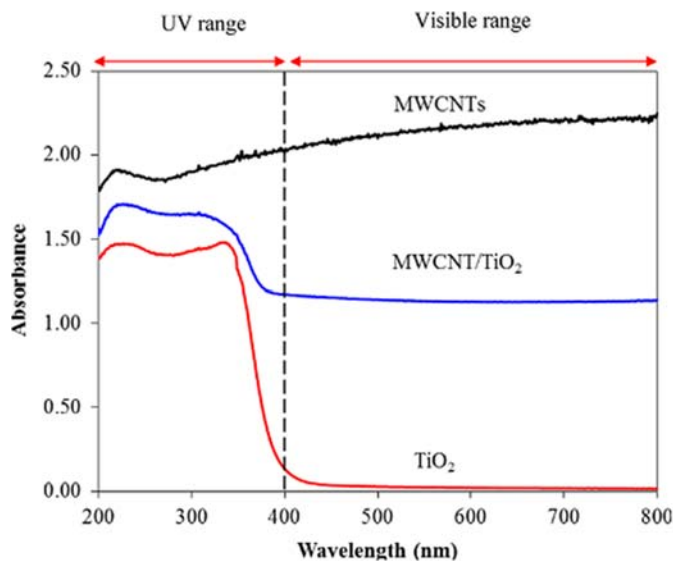


Figure 2.11 UV-vis spectra of core-shell MWCNT/TiO₂, acid-treated MWCNTs and anatase TiO₂. Reproduced from (191).

2.2.5.1.2 Photocatalytic Production of Hydrogen

Ou et al. first reported the use of MWCNT-TiO₂:Ni composite catalysts in photocatalytic water splitting. MWCNTs were grown via CVD directly on a NiO-TiO₂ support (192). For testing, composite catalyst powders were dispersed in methanol/water solutions, and then exposed to visible light. While pure NiO-TiO₂ catalysts were shown to be completely inactive for water splitting in visible light, the addition of 4.4 wt% MWCNTs produced significant amounts of H₂, with a reaction rate of 38 μmol g⁻¹ h⁻¹. Increasing MWCNT concentration beyond 4.4% resulted in worsened performance due to decreased light absorption.

Pure MWCNT-TiO₂ nanocomposite catalyst powders were produced hydrothermally using acid functionalized MWCNTs and titanium sulfate (193). UV-vis spectra showed extended wavelength absorption from the MWCNT-TiO₂ hybrids compared to pure TiO₂. Raman spectra confirmed the presence of anatase TiO₂ in the hybrid, though the Raman band corresponding to the E_g mode of the anatase phase was shifted to a lower energy. This indicates

a decrease in crystal lattice vibration energy, and thus a decrease in crystallinity. Interestingly, the G/D ratio for the MWCNTs did not change after acid treatment or deposition of TiO₂.

Hydrogen evolution was evaluated under visible light for hybrid catalysts, as well as pure MWCNTs, pure TiO₂, and a MWCNT-TiO₂ mechanical mixture. Only the hydrothermally formed hybrid exhibited hydrogen evolution under visible light with a reaction rate of 235.1 $\mu\text{mol g}^{-1}\text{h}^{-1}$. They proposed that good contact between MWCNTs and TiO₂ was crucial for effective transfer of visible light induced electrons on MWCNTs to TiO₂ nanoparticles. Unfortunately, no experimental results to prove bonding between MWCNT-TiO₂ phases was presented.

Additional experiments from the same group sought to optimize MWCNT pretreatment methods, MWCNT content, and hydrothermal temperature (194). While sonication in strong oxidizing acid (H₂SO₄/HNO₃) degraded the MWCNT structure and hydrogen evolution, stirring in nitrate solution provided highest photoactivity due to moderate oxidation without extensive MWCNT damage. Low concentrations of MWCNTs in the nanocomposite powders did not result in photoactivity enhancement due to lack of exposure to incident light. Highest photoactivity was measure for 5 wt% MWCNT-TiO₂ powders. Increasing hydrothermal temperature increased TiO₂ crystallinity, but also increased crystallite size. While high crystallinity is beneficial, large crystallites can lead to inadvertent electron-hole recombination. Therefore, the optimized hydrothermal temperature was found to be 140 °C.

2.2.5.1.3 Photovoltaic Devices

Photocatalytic activity of semiconductors has been widely demonstrated in solar cells, and some of the highest conversion efficiencies have been recorded for dye-sensitized solar cells (DSSCs) in particular. DSSCs utilize nanostructured semiconductor films modified with sensitizing dyes to improve photoconversion efficiency, but problems with electron-hole recombination remain (195). Specifically, photogenerated electrons in these nanostructured films must navigate a highly tortuous path of semiconductor particles and grain boundaries before being collected at the electrode (196, 197). One-dimensional nanowires and nanotubes have been synthesized in an attempt to control and direct the flow of photogenerated charge

carriers (198, 199), but these architectures still must have intimate contact with an electron acceptor to facilitate transport and collection.

For this reason, SWCNTs have been investigated as support scaffolds for TiO₂ and ZnO photoelectrochemical solar cells (200, 201). SWCNT-TiO₂ hybrids were formed by first refluxing the SWCNTs in acid, and then depositing them on a conductive carbon fiber electrode via electrophoretic deposition. TiO₂ nanoparticles were then dispersed on the SWCNT films and dried. The photon conversion efficiency for SWCNT-TiO₂ hybrids almost doubled compared to pure TiO₂, indicating improved charge collection. Photocurrent generation increased with larger TiO₂ loadings, up to 1.5 mg cm⁻³. Higher loadings resulted in saturation and eventual decrease of the photocurrent. Low concentrations of TiO₂ nanoparticles were easily dispersed by the SWCNTs, allowing for charge collection and transportation to the collecting electrode surface. On the other hand, higher loadings resulted in particle agglomeration, where many aggregates were not able to directly contact SWCNTs for charge transfer to occur (200).

The issue of particle agglomeration was solved altogether when Di et al. recently demonstrated vapor phase coating of continuous TiO₂ thin films on aligned MWCNT sheets for the manufacture of flexible and transparent photoanodes for light-harvesting devices (69). The continuous and interconnected network of MWCNTs was preserved in order to decrease contact resistance between the nanotubes and also enhance mechanical flexibility of the heterostructure film. MWCNT sheets were drawn and lightly fixed to transparent glass or polyethylene terephthalate (PET) film substrates. Oxide deposition was carried out by atmospheric vapor phase pyrolysis of titanium isopropoxide (TIP), in argon. TEM analysis, provided in Figure 2.12, showed that the coatings were formed by discrete crystalline (anatase) TiO₂ particles which coalesced to form a continuous coating with increased deposition time. This coating technique was previously demonstrated on MWCNT arrays, but was unsuccessful in fabricating continuous coatings (202). This is likely due to higher density and lower porosity within the array structure, which inhibits precursor diffusion.

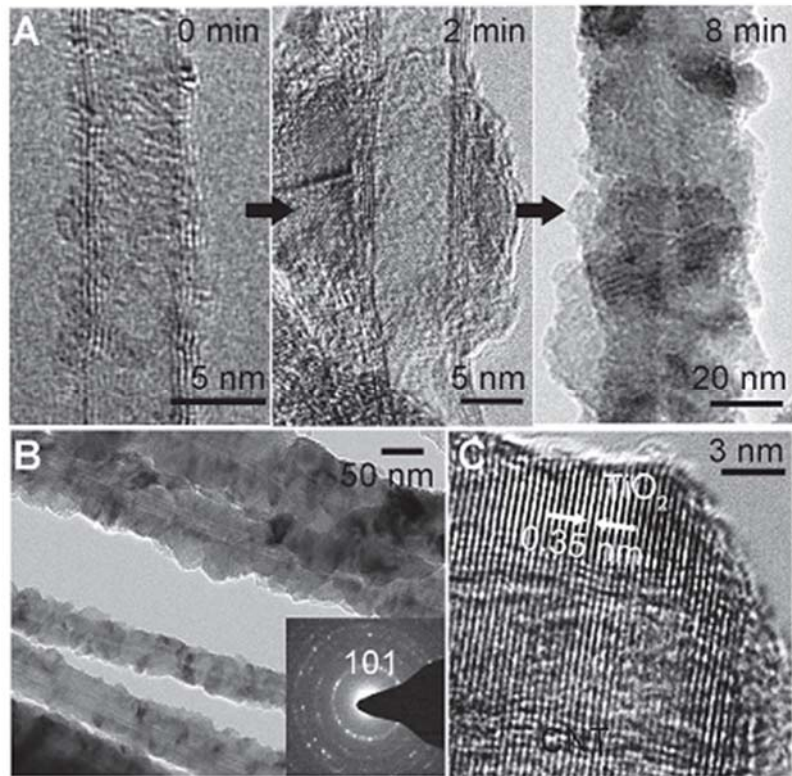


Figure 2.12 (A) A series of TEM images of CNT/TiO₂ coaxial nanocables with increasing deposition time, showing oxide behaviors on CNTs spun from nanotube arrays. (B) Low and (C) high resolution TEM images of the nanostructures in a CNT/TiO₂ film. Reproduced from (69).

Figure 2.13 shows analysis of Raman spectra which confirmed the presence of anatase TiO₂, and also showed that the TiO₂-MWCNT hybrid film had a lower G/D ratio than the pure MWCNT sheet. They hypothesized that this could be due to the reaction between the oxide and nanotubes (35). Further evidence of such a reaction was provided by comparison of XPS spectra of the TiO₂-MWCNT hybrid and pure TiO₂ films. They observed that the Ti2p and O1s peaks of the hybrid film shifted to higher binding energies compared to pure TiO₂, indicating strong interaction between MWCNTs and TiO₂, possibly by chemical bonding (203).

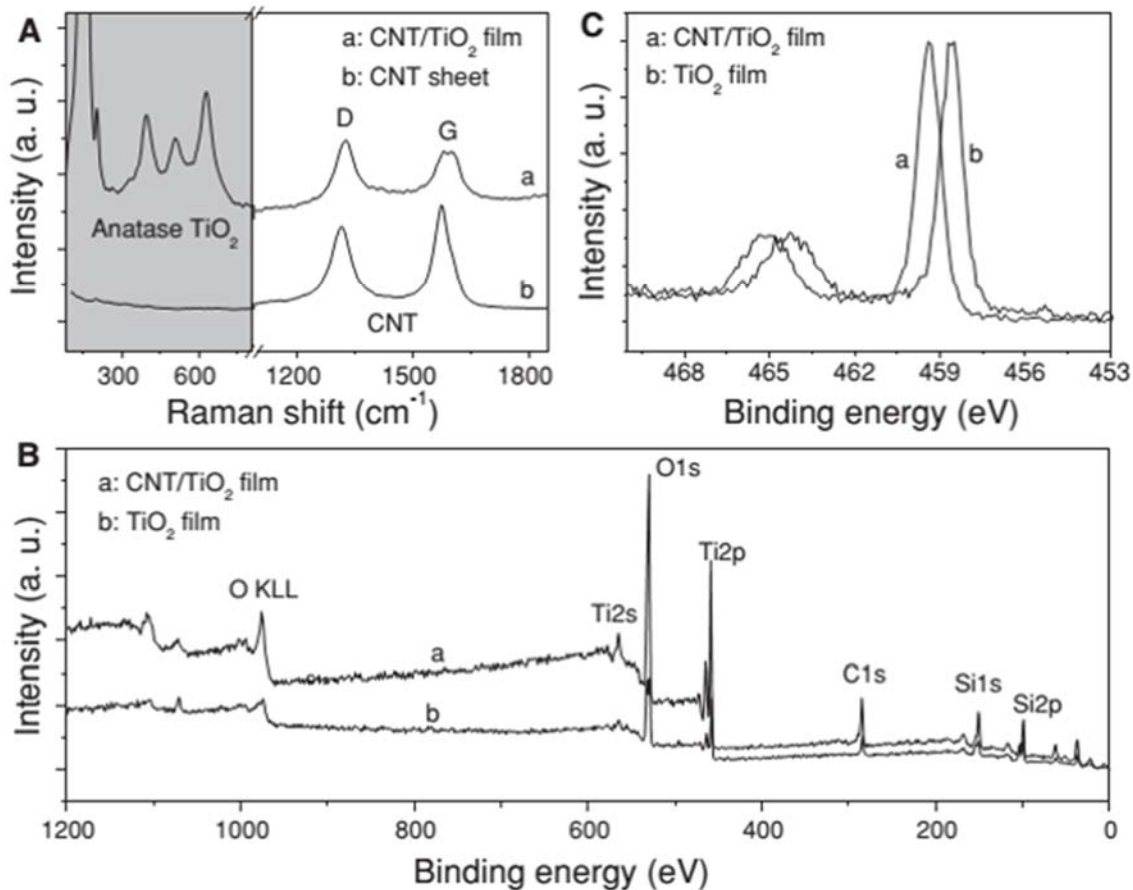


Figure 2.13 (A) Raman spectra of a CNT sheet (a) and a CNT/TiO₂ film (b). (B) XPS spectra of a 2 min deposited CNT/TiO₂ film (a) and a TiO₂ film prepared by oxidative removal of the CNTs in a CNT/TiO₂ film at 500 °C in air (b), and High-resolution XPS spectra of the Ti2p peaks for the two films. Reproduced from (69).

The effectiveness of the hybrid films in charge separation and transport was evaluated and compared against TiO₂ nanoparticles adhered to fluorine doped tin oxide (FTO) glass. They observed an incident photon-to-electron conversion efficiency of 32% for the hybrid films, vastly outperforming the controls. Photocurrent was found to increase with longer deposition times, up to 12 minutes, due to increased light absorption. Thicker coatings resulted in decreased photocurrent, possibly due to charge recombination. Finally, even after bending the hybrid film hundreds of times, a stable photocurrent could still be produced (69).

Due to their high aspect ratio and charge carrier mobility, MWCNTs have been utilized in organic photovoltaic cells (OPVCs) within bulk heterojunction (BHJ) structures to provide fast charge conduction pathways (204). Due to their metallic nature, however, they have no band gap for effective charge selection, which leads in inadvertent electron-hole recombination (205). Ultrathin ALD coatings of TiO_x on MWCNTs were investigated as charge selectivity barriers to improve the efficiency of OPCVs (175). Since TiO_x is an n-type material with a large band gap, it can act as a hole injection barrier, thus selectively providing electrons with an unobstructed pathway to the collection electrode (206).

Compared to sol-gel techniques, ALD proved superior for uniformly coating the CNT networks while also preserving their nanoporous structure. The power conversion efficiency (PCE) of ALD coated MWCNTs was enhanced by 30% due to increased surface area and preservation of the conductive interconnected MWCNT network. Though very thin (<10 nm) or inhomogeneous TiO_x coatings were shown to cause leakage currents, increasing coating thickness resulted in increased PCE due to effective hole blocking. TiO_x coatings thicker than 10 nm resulted in reduced PCE due to the overall increased resistance of the electrode.

2.2.5.1.4 Mechanisms for Photocatalytic Enhancement

There are a few possible explanations for the synergistic effects found in CNT-metal oxide hybrids. First, due to their high chemical and thermal stability, CNTs are an effective substrate for coated device morphologies. Their high surface area consequently provides high active surface area compared to coatings on planar, 2D substrates. Additionally, it has been shown that CNTs can influence particle and crystal size of metal oxide coatings (207). Upon addition of CNTs, Wang et al. demonstrated increased TiO_2 photocatalytic activity as a result of decreasing particle size and increasing active surface area (185). Second, there is evidence of carbon materials acting as photosensitizers for TiO_2 (208). Exposure of the hybrid to visible light may cause the injection of electrons from the CNT to the conduction band of TiO_2 , thus forming radicals which can participate in reaction. Finally, CNTs may aid in preventing electron-hole recombination. Carbon nanotubes act as electron acceptors, and once electron-hole pairs are formed, electrons can be transferred through the metal oxide-CNT interface to

the CNT, thus slowing recombination and improving photocatalytic efficiency. The validity of this hypothesis was supported in work by Wang et al. where photoluminescence (PL) emission spectroscopy was used to study the electron-hole recombination mechanisms of pure TiO₂ and TiO₂-coated CNTs. PL emission in TiO₂ is caused by radiative recombination of self-trapped excitations (209). The PL emission intensity of CNT hybrids decreased with increasing CNT concentration, meaning that the CNTs may inhibit electron-hole recombination (185).

Considerable debate remains, however, as to which mechanism is majorly responsible for photocatalytic enhancement. Optimization of device design relies on the deconvolution of these hypotheses to gain a more sound understanding. To illustrate, if CNTs act as charge sinks and retard electron-hole recombination an optimized device would maximize the surface area of TiO₂ exposed to incident photons, an example being TiO₂ nanoparticle covered CNTs. On the other hand, if CNTs act as photosensitizers, then a device which maximizes direct illumination of CNTs rather than TiO₂ would be optimal, such as CNTs grown on TiO₂ particles (210).

2.2.5.2 Gas Sensing

Metal oxide semiconductor (MOS) materials are widely used as the active material in gas sensors since their electrical conductivity is easily influenced by the surrounding gas environment. When an oxidizing or reducing gas molecule lands on a MOS surface, charges can be released or trapped, changing the concentration of oxygen vacancies, and creating a change in resistance. The performance of metal oxide sensing materials is inherently tied to morphological and structural parameters such as surface area, crystallinity, and chemical composition (including dopants and impurities). When the MOS particle size is close to that of the space-charge layer, the electron transport properties can be strongly affected by gas adsorption and desorption leading to greatly increased sensitivity. There is considerable difficulty, however, in achieving nanostructured metal oxides with small particle and/or grain sizes due to the high temperatures required by many synthesis techniques which lead to particle roughening and sintering. There is also a great deal of interest in being able to operate these

sensors at room temperature in order to reduce power consumption and to enable the safe detection of flammable gases.

Due to their high surface area, CNTs provide ample sites for gas adsorption. Additionally, their conductivity is highly sensitive to gas molecule adsorption and therefore can be utilized to detect resistance changes at low temperatures (211). For these reasons there has been considerable work on ALD coating CNTs with MOS materials for gas-sensing applications. In a study by Willinger et al. MWCNTs were homogeneously coated on both inner and outer surfaces with vanadium dioxide (V_2O_4) using a non-aqueous ALD method, and the coated tubes were tested as the active element in a NO_2 gas sensing device (212). Thin, amorphous vanadia films were able to be grown on nitric acid treated MWCNTs, and devices were fabricated by dispersing the coated MWCNTs in ethanol and drop-coating the suspension on alumina substrates with Pt interdigitated electrodes.

While pure MWCNTs were found to have p-type sensing behavior to NO_2 , V_2O_4 -MWCNT hybrids showed n-type sensing behavior with greatly enhanced sensitivity. Additionally, thinner coatings (2 vs. 4.5 nm) were found to have slightly higher responses. Simple electrical measurements on MWCNTs with different V_2O_4 coating thicknesses showed that resistance remained low, suggesting that current flows primarily through p-type MWCNTs, despite the fact that the device exhibited n-type response. The enhancement in sensitivity was therefore attributed to the creation of a p-n heterojunction in the core-shell structure, which was previously demonstrated on SnO_2 -MWCNT hybrids fabricated using other techniques (213) as well as ALD (214). Enhanced p-type sensing behavior to O_2 was demonstrated by TiO_2 -MWCNT hybrids also fabricated via ALD (215).

To elaborate more on the mechanism by which MWCNTs enhance room temperature sensing capabilities of MOS materials, various SnO_2 coating morphologies were controllably deposited on MWCNTs by varying surface functionalization (216). Following ALD coating, MWCNTs with a high density of functional groups were conformally coated with SnO_2 films, while graphitized MWCNTs were covered with small particles. The sensing properties of SnO_2 -MWCNT heterostructures was drastically affected by coating morphology. Continuous thin films resulted in enhanced sensing capabilities including high sensitivity for low NO_2

concentrations, as well as fast, reversible, and reproducible responses. To contrast, particle-covered MWCNTs exhibited p-type semiconductor responses, with poor sensitivity and slow response and recovery, much like pristine MWCNTs.

The discrepancy in behavior was explained by examining the physical junctions that exist in the hybrid materials and their influence on the path for conduction. In the continuous film condition, the sensing layer SnO₂, is an n-type semiconductor while the MWCNT core exhibits p-type behavior, thus creating an n-p heterojunction at the SnO₂-MWCNT interface. In this scenario electrical conduction must occur through the metal oxide-MWCNT interface. The barrier height of this junction is innately tied to the interaction of NO₂ molecules with the SnO₂ sensing layer, which explains the heightened sensitivity. On the other hand, when incomplete coatings are present, more carbon-carbon junctions exist which provide the path of least resistance, and thus p-type response. In short, it was found that carbon-carbon junctions should be avoided in the manufacture of high sensitivity gas sensors. This can be accomplished by ensuring continuous and conformal coatings via functionalization, and also by coating the MWCNTs prior to assembling the sensor on the electrode.

Though not for gas sensing, the same behavior was demonstrated by Lin et al. for ZnO-coated MWCNTs in UV photodetectors (173). Photodetectors coated for fewer ALD cycles with thin and discontinuous coatings exhibited p-type semiconductor behavior. Increasing the number of cycles yielded continuous and complete ZnO coating, and resulted in photodetectors with high sensitivity and n-type semiconductor character.

Porous networks of inorganic nanotubes and nanowires, synthesis using ALD, have also been investigated for use in gas sensors. SnO₂ nanotubes were formed by ALD coating a sacrificial template of electrospun polyacrylonitrile (PAN) nanofibers, followed by calcination (217). The nanostructured SnO₂ network was observed to have a fast and stable response for sensing of O₂, CO, NO₂, NH₃, and ethanol gases. Optimal response was measured for samples which had the thinnest wall thickness of 8 nm. Arrays of ZnO nanowires for sensing O₂ and CO were fabricated in a similar fashion, by ALD coating on a sacrificial patterned silicon oxide template (218). Additionally, porous alumina membranes have been investigated for DNA sensors (219, 220).

Very recently, ZnO aerogel-like materials with an interwoven hollow-sphere morphology were fabricated via ALD on sacrificial bacterial cellulose substrates (221). Calcination at faster heating rates and higher temperatures led to crystallization, grain growth, and changes to the nanostructural morphology, causing decreased specific surface area. Furthermore, the concentration of surface-bound hydroxyl groups decreased with increasing calcination temperature. The best ethanol sensing performance was measured for ZnO-550 (calcinated at 550 °C) due to multimodal porosity, high specific surface area, thin ZnO wall thickness, and high concentration of surface oxygen species.

2.2.5.3 Batteries and Capacitors

Electrochemical energy storage is a vital technology for handheld devices as well as conventional power generation and distribution. Though modest advancements in battery performance can be met by fine tuning of specific electrochemical systems and chemistries, major improvements require structurally and compositionally novel electrode materials. Performance demands include higher storage capacity and density, faster charging and discharging rates, and improved cycling stability (222).

Due to their high carrier mobility CNTs have been considered a promising material for improving the performance of electrochemical capacitors (223). Pristine CNTs have low specific capacitances, however, so they must be modified via doping or activation, or combined with an electroactive material to form a composite or hybrid (224). Transition metal oxides are commonly chosen due to their fast and electrochemically reversible Faradaic redox reactions to store charge in supercapacitors, resulting in high capacitance. Alone, these materials are typically high resistance and low surface area, which can also be solved through hybrid formation.

RuO₂ nanoparticle-MWCNT hybrids were synthesized by impregnation of Ru-ethoxide solution into films of pristine and acid-treated MWCNTs, followed by annealing at 200 °C for 10 hours (225). The specific capacitance for hybrids made with pristine and functionalized MWCNTs was 450 and 800 F g⁻¹, respectively. Rather than a particle morphology, 3 nm thick continuous films of RuO₂ were electrodeposited onto MWCNT films resulting in an even

higher specific capacitance of 1170 F g^{-1} , as well as improved rate capability (226). Improved performance was attributed to the very thin RuO_2 film, and the interconnected 3D nanoporous MWCNT architecture.

Though high performing, RuO_2 is also expensive to the point where its use in commercial applications is cost prohibitive. For this reason other transition metal oxides have been explored, including vanadium dioxide. Unlike RuO_2 , vanadia is highly insulating and therefore must be modified to obtain good performance. Vacuum filtration was used to combine vanadia nanowires and MWCNTs to form a binder-free electrode, but only moderate capacitances were obtained due to insufficient interface between the MWCNTs and vanadia (227). Electrodeposition was used to achieve a thin film morphology, yielding impressive capacitance values, but lack of film uniformity resulted in low capacitance retention at fast scan rates (228). To overcome these issues, ALD was used to conformally deposit VO_x films of various thicknesses on MWCNT electrodes (156). All VO_x -MWCNT electrodes had higher capacitances than pristine MWCNTs, but the sample with the thinnest coating of 10 nm had the best performance with a specific capacitance of the composite near 530 F g^{-1} . This result was explained by the combination of three mechanisms: (i) active redox sites are only present on the top layer of VO_x , so increased film thickness does not increase the amount of material participating in the reaction; (ii) there is limited access of the electrolyte ions to the bulk of the coating; and (iii) increased thickness of insulating coating impedes electron transport to active redox sites.

CNT-inorganic hybrids have been utilized as both anode and cathode materials in Li-ion batteries. Dispersed SnO_x on CNTs resulted in enhanced electrochemical performance over pure CNTs and pure SnO_x (229). This was due to improved electrical conductivity and mechanical ductility of the hybrid. ALD was used to deposit ultrathin alumina films on MWCNTs which were grown directly on copper foil (161). The binder-free anodes showed high specific capacity, good capacity retention, and good rate capability due to the synergetic effects of the Al_2O_3 -MWCNT hybrid. MWCNTs provided electron transport, sites for Li-ion intercalation, and structural integrity while the Al_2O_3 coating provided capacity enhancement.

High-density assemblies of V₂O₅-MWCNT hybrids were fabricated for Li-battery cathodes via ALD on MWCNT sponges (230). Due to their high electrical conductivity, porosity, and surface area the MWCNT sponges functioned as current collectors as well as mechanically robust, nanostructured substrates for V₂O₅ films. After coating, the sponge was compressed into a coin-cell battery for testing. SEM and TEM analysis revealed evidence of non-ideal ALD growth. After 1000 cycles the V₂O₅ film on MWCNTs measured 17 nm thick, while on the Si wafer it measured 30 nm. This suggests that there were significant barriers to nucleation of V₂O₅ on the MWCNTs, such as a lack of defects or functional groups. Additionally, it was determined that coating thickness was not uniform throughout the sponge structure as a result of limited precursor diffusion. The V₂O₅-MWCNT hybrid sponge provided high initial areal capacity, but cyclability was found to be poor. After cycling charge-transfer resistance increased due to the dissolution of V₂O₅ and the formation of a highly resistive solid-electrolyte interphase (SEI) layer on the hybrid structure. It is likely that these issues could be mitigated and performance enhanced by optimizing the coating conformality and uniformity throughout the sponge structure.

2.3 Cellular Solids

Cellular solids are a class of natural and synthetic materials comprised of hollow pores surrounded by an interconnected network of solid struts or ligaments. A foam is described as a cellular network where the cells are ordered or non-ordered polyhedral which are pack in three dimensions. If the cell faces are open to one another, the material is classified as an open-cell foam, were as a closed-cell foam contains cells which are isolated and separated from one another by solid cell walls. Though polymer foams are by far the most common, it also possible to make foams from ceramics, glasses, metals, and composites.

Density, and more specifically, relative density, is a defining characteristic of cellular materials. Relative density is calculated by ρ^*/ρ_s where ρ^* is the density of the cellular material and ρ_s is the density of the bulk material from which the foam is made. Of particular interest for this dissertation are ultralow density foams where $\rho^*/\rho_s < 0.001$. The physical properties of cellular materials differ from those of their bulk counterparts as a function of density. Many

natural cellular solids evolved to maximize modulus at a given density, and therefore exhibit superb structural efficiency attributed to good strut connectivity and efficient load transfer.

An additional characteristic of many natural cellular materials is their anisotropic properties. Wood and bone exhibit both structural anisotropy, derived from the shape and orientation of cells, as well as material anisotropy, where the material comprising the cell walls is preferentially arranged. Although commonly thought to be isotropic, polymer foams are in fact anisotropic as well as a result of the liquid precursors expanding in the mold during foaming, causing cell elongation in the direction of rise. There are varying degrees of anisotropy among these examples, which can be characterized by their shape-anisotropy ratio, R , calculated by the ratio of the largest cell dimension to the smallest. For isotropic materials, $R=1$, whereas $R=10$ for an anisotropic material like wood. This is an important factor to consider since foam properties such as modulus and strength are highly dependent on the degree of anisotropy.

2.3.1 Alumina-Based Aerogels and Foams

Aerogels, a sub-set of cellular solids, are synthetic, microporous, open-cell foams with high surface area and low density. Their solid skeletons are comprised of linked nanoparticles forming ligaments which are arranged in such a way to create a fractal or dendritic microstructure. As a result of their unique structure, aerogels have the lowest thermal conductivity, refractive index, sound velocity, and dielectric constant of any solid material (231). Although silica aerogels are the most widely produced (232), they can also be made from other metal oxides, like alumina (233), carbon-based materials (234, 235), and semiconducting chalcogenides (236), among others. Alumina and alumina-based materials are highly regarded for their high strength in addition to good chemical and thermal stability. Many of these properties have been shown to translate to low density alumina-based materials, making them attractive for high temperature catalysts and/or catalyst supports, sensors, thermal insulators, structural composites, and many other applications (233, 237, 238).

Until very recently, only materials derived from a wet gel via a sol-gel process were considered to be true aerogels. This manner of thinking began to change when new methods

of creating the characteristic structure were developed. Now, some suggest that the aerogel should be regarded as a state of matter which is typified by a gel-like structure with solid phase skeletons and gas phase pores (239). Even still, the majority of aerogels are synthesized via the sol-gel process, which is described in more detail below.

2.3.2 Sol-Gel Synthesis

The sol-gel method refers to a technique where a colloidal suspension of solid nanoparticles in a liquid (sol) are treated with a gelation agent which causes the particles to agglomerate together creating a continuously cross-linked three-dimensional network of solid skeleton within the liquid (gel). Successful creation of a gel requires very specific chemistries in order for crosslinking reactions to take place among the nanoparticles. Additionally, the reactions tend to be sensitive toward factors like pH, temperature, time, and use of catalyst. Once a liquid filled gel is formed, the task of removing liquid from the solid skeleton still remains before an aerogel can exist.

The history of aerogel preparation dates back to a bet made between Samuel Stephens Kistler and Charles Learned in 1931, who were debating on how to go about removing the liquid phase from a gel without changing the shape or volume of the original structure. Trouble arose when the liquid was evaporated from the gel, which caused large capillary pressures to accumulate in the pores resulting in catastrophic shrinkage and cracking. To mitigate these effects, Kistler developed an alternative drying procedure, relying on supercritical extraction (SCE) (240). Though successful in producing aerogels from a variety of materials with only minimal shrinkage, the process was tedious, expensive, and time-consuming. Furthermore, there were no useful applications for the aerogels at the time, other than to assuage scientific curiosity.

Decades later, renewed interest in the field came about from scientists studying high-energy physics and development of materials for Cerenkov detectors (241, 242). Successful detection of subatomic particle-generated Cerenkov radiation requires a medium which has an index of refraction ~ 1 , which aerogels are well-suited for. This demand fuelled the growth of aerogel processing and characterization of microstructure which exists today. While some

work has been done on development and optimization of gel formation, greater interest has been placed on drying processes, as this step tends to be the most critical in preserving porosity and preventing crack formation. Techniques include Kistler's supercritical extraction (240), supercritical CO₂ drying (243), ambient pressure drying (244, 245), and rapid supercritical extraction (246).

Sol-gel synthesis of alumina alkoxide-derived gels in water was demonstrated by Yoldas (247). Removal of water via heat treatment resulted in conversion to bayerite and boehmite powders. Mizushima and Hori first prepared monolithic alumina aerogels via supercritical drying of alumina gels prepared from the hydrolysis of alumina sec-butoxide and ethyl acetoacetate (248, 249). They also studied the effects of several additives on the heat resistance of produced aerogels. They determined that the addition of 10 mol% silica was the most effective, yielding an aerogel with specific surface area of 114.3 m² g⁻¹ at 1200 °C. Likewise, others have also demonstrated enhanced heat resistance of silica aerogels that were modified with alumina (250, 251). Keysar et al. investigated phase conversions, morphology changes, and temperature stability of fiber-like alumina aerogels undergoing high temperature heat treatment (252). While heating from 20-1300 °C in air the following conversions were found to occur: boehmite/pseudoboehmite → η-Al₂O₃ → θ-Al₂O₃ → η-Al₂O₃ → α-Al₂O₃. The specific surface area decreased from 350 m² g⁻¹ to 180 m² g⁻¹ ~800 °C, and η-Al₂O₃ was detected in XRD. In the temperature range of 1100-1220 °C, the η/θ occurred, accompanied by a decrease in specific surface area to 100 m² g⁻¹. Finally, the transition to α-Al₂O₃ occurred above 1220 °C, and specific surface area dropped significantly to 10-40 m² g⁻¹.

Poco et al. demonstrated the production of un-cracked monolithic aerogels with enhanced robustness and moisture stability using a novel two-step sol-gel synthesis technique followed by rapid supercritical extraction (233). As-produced aerogels exhibited a unique microstructure comprised of polycrystalline leaf-like particles, which is a departure from the typical amorphous spherical nanoparticle morphology seen in aerogels produced using other methods. This resulted in high porosity (> 98%), and high specific surface area (376 m² g⁻¹). The presence of crystallinity was attributed to sol-gel synthesis as well as supercritical drying steps being carried out at elevated temperatures. As a result, crystalline alumina aerogels were

more stable to sintering at high temperatures and had moduli 12-26% higher than silica aerogels with the same density. Mechanical enhancement was hypothesized to be due in part to the unique leaf-like morphology as well. Finally, aerogels produced in this study had thermal conductivities of 29 mW mK⁻¹ and 98 mW mK⁻¹ at temperatures of 30 °C and 400 °C, respectively. Kucheyev et al. further enhanced the mechanical properties of nanoleaflet alumina aerogels by controlling the crystallographic phase, shape, and size of ligaments via thermal processing (253). Heat treatment of as-produced aerogels resulted in curling of the nanoleaflets, promoting connectivity. This resulted in moduli an order of magnitude higher than both alumina and silica aerogels of the same density but with more typical “string of pearls” morphologies. Modulus was shown to decrease superlinearly as a function of density, with a slope of 2.8.

The mechanical properties and thermal stability of alumina aerogels have also been enhanced through the addition of various modification techniques to sol-gel and drying steps. Zu et al. developed a novel sol-gel route called the acetone in situ water formation (ISWF) method which resulted in better control of the hydrolysis reaction and formation of transparent gels with uniform microstructures (238). Removal of the liquid phase of the gel was carried out via supercritical fluid drying (SCFD) where high temperature and pressure caused the development of spherical and connected particles of boehmite crystals, resulting in high specific area and improvement in mechanical properties. Supercritical fluid modification (SCFM) was employed which led to conformal deposition and growth of a crosslinking agent on the surfaces of particles, leading to better connectivity and higher strength. Finally alumina aerogels were treated via hexamethyldisilazane (HMDS) gas phase modification resulting in the addition of methyl siloxyl groups on surface Al-OH sites. Upon heat treatment, these groups were converted to SiO₂ which served to prevent alumina nanoparticle sintering and growth, thus improving thermal stability. Ultimately, heat resistance was enhanced, resulting in alumina aerogels with specific surface areas of 125-136 m² g⁻¹ after two hours of treatment at 1300 °C. Moduli were shown to improve by 120% after utilization of the combined modification treatments.

The same group demonstrated similar improvement in heat resistance with trimethylsiloxane (TMEO) modification of alumina aerogels during employed during both sol-gel and SCFD processes (254). During sol-gel synthesis, TMEO again replaces Al-OH groups with methyl siloxyl groups, preventing condensation during drying. Additionally the small surface particles were shown to restrict growth of grain boundaries upon heat treatment. Further building on this work, the group went on to develop a synthesis technique to prepare nanostructured core-shell metal oxide aerogels (255). The structures created consisted of a pure alumina core, an alumina-silica intermediate layer, and finally a pure silica shell. First, alumina gels were prepared using the above-described method. After several days of aging and solvent exchange, wet gels were treated by alkoxides chemical liquid deposition (ACLD) to create the core-shell structure. In this process colloidal suspensions of partially hydrolysed metal alkoxides (basically pseudo-sols), were prepared into which wet gels were submerged. Specimens were removed after 12 hours and rinsed in ethanol for 4 hours. This process was repeated 6 times. Next, wet gels were submerged into an alumina and silica nanoparticle colloidal suspension for 12 hours to form the intermediate layer. This was followed by treatment in a pure silica colloidal suspension for 12 hours to form the outer shell. Finally, wet gels were dried using SCFD. The density and modulus of pure alumina aerogels increased from 93 mg cm^{-3} and 1.7 MPa to 143 mg cm^{-3} and 6.7 MPa following the core-shell fabrication route. Heat treatment of core-shell alumina-silica aerogels resulted in further increase of modulus to 11.2 MPa , but a decrease in specific surface area from $247 \text{ m}^2 \text{ g}^{-1}$ to $139 \text{ m}^2 \text{ g}^{-1}$.

2.3.3 Template-Based Methods

Alumina aerogels have historically been produced using sol-gel methods; though large-scale, un-cracked, and uniform monolithic aerogels are difficult to achieve (233, 238, 253). Furthermore, these techniques afford little control over cellular architecture such as pore size and distribution, particularly for very low densities ($\leq 20 \text{ mg cm}^{-3}$). There are significant challenges associated with producing low density, monolithic alumina aerogels that are mechanically robust and structurally uniform. Even at low strains, most non-silica aerogels, particularly alumina, are notoriously fragile (253). The mechanical properties of porous

materials are known to degrade significantly with decreasing density (256). They exhibit a scaling behavior between modulus and density as well as strength and density described by the relationship $E/E_s \sim (\rho/\rho_s)^n$ and $\sigma_y/\sigma_{ys} \sim (\rho/\rho_s)^n$, where E is Young's modulus, ρ is density, σ_y is yield strength, and s denotes the respective property value of the particular solid material. The power of n is microstructure-specific and describes the deformation mechanisms of the structural components within the cellular architecture (257). Superior mechanical properties can be attained using highly ordered lattices with stretching-dominated geometries which scale more linearly, where $1 \leq n \leq 2$ (256, 258, 259). Cellular geometries featuring either stochastic or periodic porosity that instead deform by bending-dominated mechanisms exhibit a steep scaling behavior, where $n \geq 2$ (260). Traditional aerogels are known to exhibit even higher scaling behaviors ($n \geq 3$) due to their fractal geometries and disconnected structures (261).

There has been growing interest in the development of novel methods to produce mesoporous metal oxide materials with ordered architectures (4). Many of these techniques rely on the use of a template onto which material is deposited, which may be followed by removal of the template leaving behind a material with large amounts of accessible surface area in the form of interconnected pores through which molecules can easily permeate, diffuse, and interact. Atomic layer deposition (ALD) has emerged as a preferred technique for template coating due to its ability to conformally deposit a wide variety of materials onto high aspect ratio and high surface area nanostructured substrates with continuous thin films at unprecedented levels of precision (110).

ALD was utilized to deposit alumina onto nanofibrillated cellulose (NFC) aerogel templates, prepared by either freeze drying or supercritical drying of NFC hydrogels (262). Supercritical drying of NFC hydrogels was found to be most effective for retaining volume and porosity, and samples as large as 12 mm in diameter and 10 mm in thickness were prepared. Template removal was achieved via calcination in air at 450 °C, leaving behind self-supporting alumina aerogels with a hollow nanotubular morphology. The group further demonstrated that the inorganic nanotubes could be crushed, made into a slurry, and then case into a thin film for use as a humidity sensor. Li et al. demonstrated similar results using swelling-induced porous block copolymers as sacrificial templates (263). Porosity of the

polymer films could be controlled by using a higher swelling temperature, but the maximum film thickness achieved was only tens of micrometers thick. Though useful for thin film applications such as humidity sensors, the limited ability to scale the templates to truly bulk dimensions limits their use for preparation of monolithic aerogels.

Biener et al. utilized nanoporous gold (NPG) templates formed via a self-organization process which have the unique ability to change ligament diameter by 2 orders of magnitude, from ~ 50 nm to ~ 30 μm , through template annealing (264). This resulted in templates with a wide range of densities with no change in porosity or ligament connectivity. After ALD, NPG templates were removed using a wet etch process, and then supercritically dried to prevent nanotube collapse. They demonstrated template removal with a 2 nm thick TiO_2 coating, resulting in a transparent monolith with a density of 150 mg cm^{-3} . The lowest density sample which retained its monolithic structure was a TiO_2 foam, with a density of 5 mg cm^{-3} , which is a significant decrease from the lowest densities readily achievable using sol-gel processes ($> 30 \text{ mg cm}^{-3}$). Nanoindentation testing showed that for any given density, values of modulus and hardness were up to an order of magnitude higher compared to silica and alumina aerogels of similar densities. Although they claimed bulk-scale dimensions, the largest monoliths prepared in this work were 200 μm thick disks with 5 mm diameters and 2 mm tall cylinders with 2 mm diameters. They also noted that while they did successfully etch away the NPG template from a sample with a 10 nm thick alumina coating, the etch rate slowed down significantly for coatings > 2 nm thick. These two drawbacks again limit the use of the processing route to applications geared toward thin films such as sensors and membranes.

Highly engineered micro and nanolattice geometries have been prepared using ALD to deposit alumina on digitally designed and lithographically fabricated sacrificial polymer templates (258, 259, 265, 266). Lithography-based template preparation, however, limits the minimum attainable feature size resulting in low volumetric surface area. Though proficient in creating optimized architectures, these templates are also limited in their ability to scale-up manufacturing for large-scale foams due to complexity and cost.

2.4 Critical Summary

Despite the fact that there is so much activity in the field of CNT-inorganic hybrids, ALD is only just being discovered as a viable route for fabrication. This is largely due to the fact that, until recently, CNT powders were the starting material. CNTs are an intriguing alternative to other template materials. Optimization of chemical vapour deposition (CVD) synthesis methods have made it possible to economically produce bulk-quantities of CNTs (267). Moreover, recent advances in processing technologies have led to the creation of various one, two, and three-dimensional large-scale and ordered assemblies including vertically aligned arrays, ribbons and sheets, yarns, and aerogels, sponges, or foams (3).

The advent of CNT assemblies, however, necessitates a re-examination of applicable devices as well as fabrication routes. By nature, CNTs which are able to be dry-spun into ribbons and yarns are well graphitized, have low defect densities, and small amounts of amorphous carbon on their surfaces. As such, they are highly inert and require functionalization prior to coating. Since CNT alignment can easily be disrupted by wet chemical methods, gas phase functionalization as well as deposition methods are required to preserve the interconnected structure. Therefore, it is necessary to develop these treatments with scalability in mind, validate their effectiveness in promoting conformal nucleation and growth of ALD films on CNTs, and examine the uniformity of coating throughout the bulk assembly. Furthermore, chemical and structural characterization of the treated CNTs, deposited films, as well as the interface between the two is necessary to understand the nature of the hybrid material and its associated properties.

Many applications dictate the optimal morphology of the thin film coating. For example, in supercapacitors it is desirable to minimize the loading of metal oxide since reactions only occur on the semiconductor surface and not the bulk. Furthermore metal oxides are dense and will add unnecessary mass to the device. Maximizing interfacial area between the metal oxide and CNT will also lead to better device performance due to enhanced charge transfer. The optimal device morphology in this scenario is an interconnected network of CNTs which are conformally coated with a thin layer of active material. This can easily be achieved using ALD to coat highly functionalized CNT assemblies.

On the other hand, high performance gas sensors do not rely on the existence of an interconnected network of CNTs, but instead rely on the existence of metal oxide-metal oxide junctions rather than CNT-CNT junctions. CNT assemblies can be utilized, however, as a sacrificial template for the formation of hollow inorganic nanotubes which exhibit enhanced sensing performance due to high surface area and a “flow-through” morphology. In this case, it is still important for the tube walls to be as thin as possible to increase sensitivity of the device.

To the best of this author’s knowledge, CNT arrays are the only CNT assembly to date that has been utilized as a sacrificial template for ALD. Much like a traditional aerogel, CNT foams (CNTFs) are porous, high surface area, ultralow density, and are composed of three-dimensionally interconnected networks of CNTs. Their use as a both a sacrificial and non-sacrificial template in conjunction with ALD has possible implications in a wide variety of applications where traditional aerogels fall short.

It is crucial to develop an understanding of the extent of the capabilities of ALD on CNT assemblies. Using other fabrication routes, researchers have demonstrated ability to control coating morphology in terms of crystal structure, crystal alignment, doping, and thickness. Due to the novelty of these two research areas—ALD and CNT assemblies—the same studies have not yet been undertaken. It is of critical importance to understand the structure-processing-property relationships of these hybrids in order to best understand their potential in new technologies.

3 Experimental

3.1 Materials and Methods

3.1.1 Aligned CNT Growth

VACNT arrays were grown on quartz substrates via chlorine mediated low-pressure chemical vapor deposition (CVD) using iron(II) chloride, anhydrous (99.5%, VWR) catalyst and acetylene carbon precursor (49). After 20 minutes of growth, the resulting arrays were 1.5 mm tall with an average MWCNT diameter of 43 nm, as measured from TEM images. While the MWCNT aspect ratio is $\sim 35,000$, the pore aspect ratio is $\sim 15,000$ corresponding to a MWCNT spacing of approximately 100 nm.

3.1.2 Growth of Spinnable CNT Arrays

Spinnable CNT arrays were synthesized using a process based on the chlorine-mediated low-pressure chemical vapor deposition technique (49). Arrays were grown on quartz substrates in a custom-built tube furnace at 760 °C and 3 Torr. Acetylene gas (600 sccm, 99.5%, Machine and Welding Supply Company), was used as the carbon source and FeCl₂ powder (anhydrous 99.5%, VWR) was the catalyst. Argon (398 sccm, 99.999%, Machine and Welding Supply Company), and chlorine (1.5 sccm, 99.99%, Custom Gas Solutions) gases were also flowed during the growth process. After 15 minutes, acetylene flow was stopped, and the arrays were left in the argon and chlorine gas flow for an additional 10 minutes. Finally the system was cooled to room temperature under a flow of argon. The resulting arrays were ~ 1.5 mm tall containing CNTs with an average diameter $\sim 29 \pm 8$ nm.

3.1.3 Fabrication of CNT Ribbons

Spinnable arrays could be easily drawn into thin aligned CNT sheets. Thicker samples were manufactured by continuously collecting aligned sheets on a rotating mandrel. After 20 rotations, the CNT ribbons were removed from the mandrel and transferred to a PET mesh substrate which acted as a supportive yet porous substrate.

3.1.4 Fabrication of CNT Foams

To manufacture thick foams, aligned CNT sheets were first drawn from the array and continuously collected around two parallel glass rods rotating at 13 rpm. Once the desired thickness was reached, winding was stopped, and the CNT structures were removed from the glass rods using a razor blade. The CNT assemblies were placed inside a tube furnace, where they were then coated with PyC via chemical vapor infiltration. This method, described in detail elsewhere (268, 269), proceeded by heating the CNT structures in vacuum. At 800 °C acetylene gas was flowed at 600 sccm while the system pressure was regulated at 30 Torr. After 60 min, the system was allowed to cool to room temperature while being purged with argon. After CVI treatment, the CNT foams were cut to the desired size using a laser cutter.

3.1.5 CNT Surface Modification

Three treatments were used to modify the as-grown VACNT surface chemistry, graphitic quality, and defect density. These included CVD of pyrolytic carbon (PyC), high-temperature graphitization (G), and O₂/CF₄ plasma functionalization (O₂). For PyC treatment, the VACNTs were conformally coated with PyC using CVD. Samples were heated in vacuum in a quartz tube furnace. At 800°C, C₂H₂ began to flow at 600 sccm, and the pressure of the system was maintained at 30 Torr. After 5 minutes, C₂H₂ flow was stopped and the system was cooled while being purged with Ar gas.

The O₂/CF₄ plasma treatment was conducted in a capacitively-coupled dielectric barrier discharge atmospheric pressure plasma system. The custom-built system consists of two parallel Cu plate electrodes (60x60 cm²), with a spacing of 3 cm. The plasma was operated by a 4.8 kW audio frequency power supply at 1.67 kHz. All treatments were carried out for 5 minutes in 1.0% oxygen + 1.0% CF₄ + 98% helium gas mixture (by mass).

Finally, the graphitization treatment (G) was carried out in a Red Devil Webb 124 high-temperature graphite furnace (R. D. Webb Company, Natick MA, USA). After removing the VACNT from the quartz substrate and loading it into the furnace, the chamber was evacuated with a vacuum pump. The sample was heated from 25 °C to 1500 °C at a rate of 25 °C per minute and then soaked at 1500 °C for 25 minutes. Following the dwell stage, the sample was

heated from 1500 °C to 2000 °C at a rate of 15 °C per minute. During this step, at 1750 °C, the chamber was refilled with argon, and kept there under a continuous flow of argon at 7.5 scfh. After dwelling at 2000 °C for 15 minutes, the temperature ramped up to 2150 °C at a rate of 3 °C per minute. Upon reaching 2150 °C, the program terminated and the furnace was left to cool, switching the chamber back to vacuum at ~1750 °C.

3.1.6 Atomic Layer Deposition

ALD of Al₂O₃, ZnO, and TiO₂ was performed in a custom built, hot-wall, viscous flow reactor at temperatures between 25 °C and 160 °C, and at operating pressures between 1 and 1.5 Torr. The metallorganic precursors used were trimethylaluminum (TMA) (98% Strem Chemicals, Inc.), diethylzinc (DEZ) (95% Strem Chemicals, Inc.), and titanium tetrachloride (TiCl₄) (99%, Gelest, Inc.), and the oxidizing agent was biotechnology performance certified grade high purity water (Sigma Aldrich). Ultra-high purity N₂ (Machine Welders) was used as the carrier gas for all precursors, and was further purified using a nickel catalyst filter (Gatekeeper ®, Entegris Inc., < 10 parts per trillion impurity). The pressure of the reactor was kept constant using an Alcatel 2021SD mechanical pump and an MKS (model PR4000B) flow controller with a N₂ gas flow rate of approximately 300-400 sccm.

The ALD process began with an N₂ purge of 300 seconds followed by a precursor (TMA/DEZ/TiCl₄) dose, N₂ purge, H₂O dose, and N₂ purge. The dosing sequence was repeated for the desired number of cycles, after which there was a final N₂ purge for 120 seconds. ALD cycle sequence of TMA/N₂/H₂O/N₂ = 0.2/30/0.2/45 sec which was repeated for the desired number of cycles. Separate experiments were carried out with the arrays oriented parallel and perpendicular to the flow of gas through the reactor. The MWCNT arrays were attached to the front of the sample stage via loops of thermally stable Kapton™ tape between the quartz substrate and the sample stage (for parallel orientation to the gas flow) or an angle bracket that was screwed into the front of the stage (for perpendicular orientation to the gas flow) and were then moved to the center of the ALD reactor.

3.2 Characterization

3.2.1 Microstructure Analysis

Scanning electron microscopy (SEM) was conducted on one of three tools: a JEOL JSM-6400F field-emission SEM with a beam voltage of 10 kV, and a Hitachi S3200 variable-pressure SEM with a beam voltage of 20 kV, or a FEI XHR-Verios 460L Field Emission SEM with a beam voltage of 1-2 kV. Transmission electron microscopy (TEM) images were either taken using a Hitachi HF2000 cold field emission TEM with a beam voltage of 200 kV or a JEOL 2010F field emission STEM. A probe sonicator was used to disperse 0.001 g of CNTs in 10 mL of ethanol. The mixture was pulse sonicated (1 second on, 0.3 seconds off) in an ice bath for 1 hour. Immediately following ultrasonication, a small amount of the dispersion was deposited on holey carbon mesh, Cu TEM grids and then allowed to dry.

X-ray diffraction (XRD) measurements were conducted on a Rigaku SmartLab Bragg-Brentano XRD with a Cu K α radiation source ($\lambda = 1.5418 \text{ \AA}$). Step scans were performed for $2\theta = 10\text{-}80^\circ$ with a step width of 0.5° and a scan speed of 3 seconds.

3.2.2 Chemical Analysis

Energy dispersive spectroscopy (EDS) measurements were gathered on the Hitachi S3200 VPSEM which was fitted with a 4Pi Isis EDS system. Elemental spectra were gathered over an acquisition time of 100 seconds. For quantitative elemental analysis, the collected spectra were compared to an Al₂O₃ standard.

Surface chemical composition of treated CNTs was completed using X-ray photoelectron spectroscopy (XPS) on a SPECS XPS system (SPECS Surface Nano Analysis) using a high-resolution PHOIBIS 150 hemispherical analyzer. Freshly post-treated arrays were transported and stored in non-outgassing Fluoroware containers to prevent surface contamination. Measurements were taken at a base pressure of 10^{-10} bar with an Mg K α excitation source (1254 eV). Survey scans were taken from 1200 – 1 eV and high-resolution scans were taken of the O 1s peak at 538 – 528 eV. Energy calibration was established by referencing to the carbon C 1s line at 285 eV binding energy.

The graphitic quality and defect density of the MWCNT arrays was analyzed using a Renishaw Ramascope with a laser wavelength of 514.5 nm focused to the sample using a Renishaw microscope with 50x objective. Five measurements were taken from different locations on each sample, and the collected data was averaged.

3.2.3 Thermal Analysis

Thermogravimetric analysis (TGA) experiments were conducted on a Perkin Elmer Pyris 1 TGA using 5-10 mg of each sample heated at a rate of 10°C/min in air to 900°C, and then isothermally soaked for 30 minutes.

3.2.4 Mechanical Analysis

The compressive properties were measured using an Instron 5544 mechanical tester operated in compression mode. Platens were custom-designed and fabricated to fit securely in the clamp holders to prevent unwanted instrument compliance. The top platen measured 3.175 cm diameter, while the bottom measured 5 cm, which allowed for total coverage of all arrays tested. For VACNT array nanocomposites the load rate was set to 0.1 mm/min, and a 2 kN load cell was used. For pure alumina and alumina/CNT composite foams the load rate was 5 mm/min, and a 100N load cell was used for all samples. Samples were loaded to 50% strain then unloaded, and this was repeated for a total of 5 cycles. Foams were tested in both transverse (nanotube axes perpendicular to load) and longitudinal (nanotube axes parallel to load) directions.

4 Conformal Atomic Layer Deposition of Alumina on Millimeter Tall, Vertically-Aligned Carbon Nanotube Arrays

*Kelly L. Stano^a, Murphy Carroll^a, Richard Padbury^a, Marian McCord^{a, b, c}, Jesse S. Jur^a, and Philip D. Bradford^{*a}*

^a Department of Textile Engineering, Chemistry and Science, North Carolina State University, Raleigh, NC, 27695-8301, USA. Fax: +1-919-515-6532; Tel: +1-919-515-1866; E-mail: philip_bradford@ncsu.edu

^b Joint Department of Biomedical Engineering, North Carolina State University, Raleigh, NC, 27695-7115, USA.

^c University of North Carolina, Chapel Hill, NC, 27599, USA.

ABSTRACT: Atomic layer deposition (ALD) can be used to coat high aspect ratio and high surface area substrates with conformal and precisely controlled thin films. Vertically aligned arrays of multi-walled carbon nanotubes (MWCNTs) with lengths up to 1.5 mm were conformally coated with alumina from base to tip. The nucleation and growth behaviors of Al₂O₃ ALD precursors on the MWCNTs were studied as a function of CNT surface chemistry. CNT surfaces were modified through a series of post-treatments including pyrolytic carbon deposition, high temperature thermal annealing, and oxygen plasma functionalization. Conformal coatings were achieved where post-treatments resulted in increased defect density as well as extent of functionalization, as characterized by X-ray photoelectron spectroscopy and Raman spectroscopy. Using thermogravimetric analysis it was determined that MWCNTs treated with pyrolytic carbon and plasma functionalization prior to ALD coating were more stable to thermal oxidation than pristine ALD coated samples. Functionalized and ALD coated arrays had a compressive modulus more than two times higher than a pristine array coated for the same number of cycles. Cross-sectional energy dispersive X-ray spectroscopy confirmed that Al₂O₃ could be uniformly deposited through the entire thickness of the vertically aligned MWCNT array by manipulating sample orientation and mounting techniques. Following the

ALD coating, the MWCNT arrays demonstrated hydrophilic wetting behavior, and also exhibited foam-like recovery following compressive strain.

KEYWORDS: carbon nanotube (CNT), atomic layer deposition (ALD), alumina, aligned carbon nanotube array, CNT – inorganic hybrid, plasma, functionalization

4.1 Introduction

Carbon nanotube (CNT) – inorganic hybrids are a class of functional materials which have drawn widespread and increasing interest in recent years (2). As opposed to nanocomposites where the CNT and inorganic phases are combined via mechanical means, CNT-inorganic hybrids are characterized by CNTs which are coaxially coated with thin layers of inorganic material. Due to interfacial charge transfer processes and size domain effects, the CNT-inorganic hybrids are expected to exhibit a synergistic set of enhanced physical properties. CNTs are an interesting template for these hybrids as they possess superior mechanical, thermal, and electrical properties, while simultaneously being low density and of high surface area. There is considerable difficulty, however, in achieving smooth, conformal, and pin-hole free coatings on CNTs for three major reasons: 1) the inherent chemical inertness of high crystallinity and purity CNTs, 2) the tendency of CNTs to bundle and agglomerate due to large van der Waals forces, and 3) the lack of synthesis methods suitable for coating 3D and aligned CNT architectures.

Atomic layer deposition (ALD) is a versatile technique used to conformally deposit a wide variety of multifunctional materials onto complex micro- and nano-sized structures with atomic scale precision. Using ALD, a variety of metal oxides and metals have been deposited on CNTs including Al_2O_3 (151), HfO_2 (152), ZrO_2 (150), TiO_2 (153), SiO_2 (153), ZnO (154, 155), V_2O_5 (156), Pt (157, 158), Ru (159), and W (160) for a wide range of applications including catalysis (157, 158), Li-ion batteries (161), field-effect transistors (162), and many others (159). The trimethylaluminum and water ALD process used to form Al_2O_3 nanoscale coatings has a favorable Gibbs free energy of formation between the reactants and products which allows for ‘ideal’ ALD growth behavior in a relatively wide temperature range from 30

°C to 300 °C (100, 114, 118, 119). Al₂O₃ is an attractive material to coat CNTs due to its excellent thermal stability and resistance to corrosion.

Several studies have demonstrated the ability to successfully coat multi-walled CNTs (MWCNTs) with Al₂O₃ via ALD without any post-treatment to activate the MWCNT surfaces (151, 154, 160, 161). In these instances the defect density in the MWCNT walls is high enough that they act as nucleation sites for deposition and growth. For many applications however, MWCNTs with large amounts of defects are highly undesirable as they degrade the MWCNTs' physical properties. Much like single-walled CNTs (SWCNTs), MWCNTs of high purity and low defect density will not readily nucleate the growth of conformal thin films due to their surfaces being non-reactive and chemically inert toward the ALD precursors (163, 166, 170). This leads to sparse nucleation and the development of a bead-like structure on the CNT surface instead of a uniform coating (152). This has been overcome through the development and application of covalent and non-covalent functionalization techniques which promote interaction between the CNT surface and precursor.

To promote conformal ALD coating, a common method of covalent functionalization of MWCNT surfaces is via refluxing in concentrated sulfuric and nitric acids (179). This results in the creation of carboxyl and hydroxyl groups on the MWCNT surfaces, which act as surface reaction sites for ALD precursors corresponding to conformal ALD growth (153, 156, 167). However, this method is aggressive and creates many defects on the MWCNT walls which degrades their physical properties. Additionally, this method is not suitable for the functionalization of aligned MWCNT arrays as wet-processing will disrupt the MWCNT alignment and cause bundling and agglomeration upon drying. Alternatively, gas-phase covalent functionalization via oxygen plasma treatment has been used on aligned MWCNT arrays as well as MWCNT powders to promote the ALD nucleation of Pt (157, 158). Though effective, covalent modification of MWCNTs and SWCNTs alters their intrinsic optical, electrical, and mechanical properties. For this reason non-covalent functionalization techniques have been explored as a method of weakly bonding the CNT surface to the ALD film via an adhesion layer. Farmer and Gordon accomplished this by adsorbing NO₂ molecules to the surfaces of suspended SWCNTs, and then reacting TMA with the adsorbed NO₂ to yield

a stable and uniform seed layer for subsequent coating with Al_2O_3 (164). Using this same method Cavanagh et al. conducted ALD on gram quantities of MWCNTs, but it was shown that the deposited Al_2O_3 coating was free to slide along MWCNTs due to the lack of covalent bonding between adjacent layers (168).

Despite the intense interest in his field, the application of ALD thin film techniques to 3D CNT architectures such as vertically aligned CNT arrays (VACNTs) have not been fully explored. Not only do arrays present a unique set of issues for functionalization, but due to their ultra-high aspect ratios and surface area, special considerations must be made regarding the ALD processing parameters. Adequate dosing and purging time must be provided for the full diffusion of precursor into and out of the array structure in order to ensure ideal ALD-type growth. Additionally, high aspect ratio structures are prone to non-uniformly distributed coatings due to gas flow effects in the reactor and within the sample (270–272). It is important to mitigate these effects so that property enhancement may be achieved via conformal coating along the entire length of the CNT rather than preferential accumulation at the top of the array.

In this work we present a systematic study of various gas-phase MWCNT surface modifications and their associated effects on the nucleation and growth of Al_2O_3 ALD coatings on high graphitic quality, low defect density VACNT arrays. Once the MWCNT surfaces were optimized to achieve conformal ALD coatings, sample orientation and mounting techniques were explored in order to promote full precursor infiltration and purging. As a result, 1.5 mm tall VACNT arrays were uniformly and conformally ALD coated with Al_2O_3 from base to tip without increasing precursor exposure time.

4.2 Materials and Methods

4.2.1 Aligned MWCNT Growth

VACNT arrays were grown on quartz substrates via chlorine mediated low-pressure chemical vapor deposition (CVD) using iron(II) chloride, anhydrous (99.5%, VWR) catalyst and acetylene carbon precursor (49). After 20 minutes of growth, the resulting arrays were 1.5 mm tall with an average MWCNT diameter of 43 nm, as measured from TEM images. While

the MWCNT aspect ratio is $\sim 35,000$, the pore aspect ratio is $\sim 15,000$ corresponding to a MWCNT spacing of approximately 100 nm.

4.2.2 MWCNT Surface Modification

Three treatments were used to modify the as-grown VACNT surface chemistry, graphitic quality, and defect density. These included CVD of pyrolytic carbon (PyC), high-temperature graphitization (G), and O_2/CF_4 plasma functionalization (O_2). For PyC treatment, the VACNTs were conformally coated with PyC using CVD. Samples were heated in vacuum in a quartz tube furnace. At 800°C , C_2H_2 began to flow at 600 sccm, and the pressure of the system was maintained at 30 Torr. After 5 minutes, C_2H_2 flow was stopped and the system was cooled while being purged with Ar gas.

The O_2/CF_4 plasma treatment was conducted in a capacitively-coupled dielectric barrier discharge atmospheric pressure plasma system. The custom-built system consists of two parallel Cu plate electrodes ($60 \times 60 \text{ cm}^2$), with a spacing of 3 cm. The plasma was operated by a 4.8 kW audio frequency power supply at 1.67 kHz. All treatments were carried out for 5 minutes in 1.0% oxygen + 1.0% CF_4 + 98% helium gas mixture (by mass).

Finally, the graphitization treatment (G) was carried out in a Red Devil Webb 124 high-temperature graphite furnace (R. D. Webb Company, Natick MA, USA). After removing the VACNT from the quartz substrate and loading it into the furnace, the chamber was evacuated with a vacuum pump. The sample was heated from 25°C to 1500°C at a rate of 25°C per minute and then soaked at 1500°C for 25 minutes. Following the dwell stage, the sample was heated from 1500°C to 2000°C at a rate of 15°C per minute. During this step, at 1750°C , the chamber was refilled with argon, and kept there under a continuous flow of argon at 7.5 scfh. After dwelling at 2000°C for 15 minutes, the temperature ramped up to 2150°C at a rate of 3°C per minute. Upon reaching 2150°C , the program terminated and the furnace was left to cool, switching the chamber back to vacuum at $\sim 1750^\circ\text{C}$.

The three post-treatments were used alone and in combination on the VACNT arrays to make five of the six distinct samples for these experiments: PyC, G, O_2 , PyC+ O_2 , and G+ O_2 . An as-grown sample was used as a control throughout the study and is referred to as “Pristine”.

4.2.3 ALD of Al₂O₃

Al₂O₃ ALD was performed in a custom hot wall viscous flow reactor at 100°C and 1 Torr using trimethylaluminum (TMA, 98% Strem Chemicals, Inc.) and biotechnology performance certified grade high purity water (Sigma Aldrich) as precursor and co-reactant, respectively. The pressure of the viscous flow reactor was kept constant at 1 Torr via an Alcatel 2021SD mechanical pump and an MKS (model PR4000B) flow controller with a nitrogen gas flow rate of approximately 400 sccm. The ALD process began with an N₂ purge of 300 seconds followed by an ALD cycle sequence of TMA/N₂/H₂O/N₂ = 0.2/30/0.2/45 sec which was repeated for the desired number of cycles. Separate experiments were carried out with the arrays oriented parallel and perpendicular to the flow of gas through the reactor. The MWCNT arrays were attached to the front of the sample stage via loops of thermally stable Kapton™ tape between the quartz substrate and the sample stage (for parallel orientation to the gas flow) or an angle bracket that was screwed into the front of the stage (for perpendicular orientation to the gas flow) and were then moved to the center of the ALD reactor. Photographs depicting sample mounting techniques are provided in Supplemental Information (Figure S4.10).

For the majority of experiments in this study, the VACNT arrays were coated with 100 cycles of alumina ALD. They are labeled as such: VACNT_100, PyC_100, G_100, O₂_100, PyC+O₂_100, and G+O₂_100. For compression testing and TGA samples were coated with 500 cycles of Al₂O₃ ALD and are labeled accordingly.

4.2.4 Characterization

Scanning electron microscopy (SEM) was conducted on a JEOL JSM-6400F field-emission SEM with a beam voltage of 10 kV, and a Hitachi S3200 variable-pressure SEM fitted with a 4Pi Isis energy dispersive spectrometer (EDS) system. Elemental spectra were gathered over an acquisition time of 100 seconds and accompanying images were taken with a beam voltage of 20 kV. For quantitative elemental analysis, the collected spectra were compared to an Al₂O₃ standard. Transmission electron microscopy (TEM) images were taken using a Hitachi HF2000 cold field emission TEM with a beam voltage of 200 kV. A probe sonicator was used to disperse 0.001 g of CNTs in 10 mL of ethanol. The mixture was pulse

sonicated (1 second on, 0.3 seconds off) in an ice bath for 1 hour. Immediately following ultrasonication, a small amount of the dispersion was deposited on holey carbon mesh, Cu TEM grids and then allowed to dry. The graphitic quality and defect density of the MWCNT arrays was analyzed using a Renishaw Ramascope with a laser wavelength of 514.5 nm focused to the sample using a Renishaw microscope with 50x objective. Five measurements were taken from different locations on each sample, and the collected data was averaged. Thermo-gravimetric analysis (TGA) experiments were conducted on a Perkin Elmer Pyris 1 TGA using 5-10 mg of each sample heated at a rate of 10°C/min in air to 900°C, and then isothermally soaked for 30 minutes. The compressive properties of MWCNT-Al₂O₃ nanocomposites were measured using an Instron 5544 mechanical tester operated in compression mode. Platens were custom-designed and fabricated to fit securely in the clamp holders to prevent unwanted instrument compliance. The top platen measured 3.175 cm diameter, while the bottom measured 5 cm, which allowed for total coverage of all arrays tested. The load rate was set to 0.1 mm/min, and a 2 kN load cell was used for all samples.

4.3 Results and Discussion

4.3.1 Conformal Coating of MWCNTs

An example VACNT array used in these experiments is shown in Figure S4.11. After 20 minutes of growth the arrays measured 1.5 mm tall with individual MWCNTs having an average diameter of 43 nm. The calculated aspect ratio of these MWCNTs was ~1:35,000 and the average specific surface area as measured by BET was 40 m²/g. An EDS spectrum (Figure S4.12) taken from an as-grown array detected only 0.96 at% and 0.42 at% O and Fe, respectively, indicating rather high purity.

Al₂O₃ ALD on as-grown VACNT arrays resulted in the surface nucleation and growth of beads or nanospheres as depicted in Figure 4.1a. TEM micrographs taken after 25, 75, and 100 cycles are shown in Figure S4.13. After 25 cycles, only sparse nucleation can be seen on the MWCNT surface. Increasing the number of cycles resulted in the growth of the nucleated Al₂O₃, with some local coalescence. After 100 cycles the MWCNT surface was covered with

large, monodisperse Al₂O₃ beads. The Al₂O₃ morphology was indicative of substrate-inhibited island growth where a lack of –OH functional sites for TMA reaction results in poor nucleation (273). Due to the lack of a conformal surface functionality, precursor molecules chemisorb at defect sites on the MWCNT surface and subsequently nucleated to grow disparate beads. This non-ideal growth mode has been demonstrated predominantly on SWNTs, (152, 163) which have comparatively fewer defects than MWCNTs. In fact, the majority of prior work in ALD coating of MWCNTs with Al₂O₃ has demonstrated facile and conformal coating on MWCNTs without any functionalization treatment (151, 154, 160, 161). Since the nucleation of Al₂O₃ relies on the presence of surface -OH groups and/or a high concentration of defects in the CNT walls, it is likely that the MWCNTs from previous studies had higher amounts of defects. Similar to the findings from Cavanagh et al., the MWCNTs grown and used for this study likely had a much lower defect density than those used in previous work, and thus did not readily nucleate and grow conformal Al₂O₃ films on unfunctionalized surfaces (168).

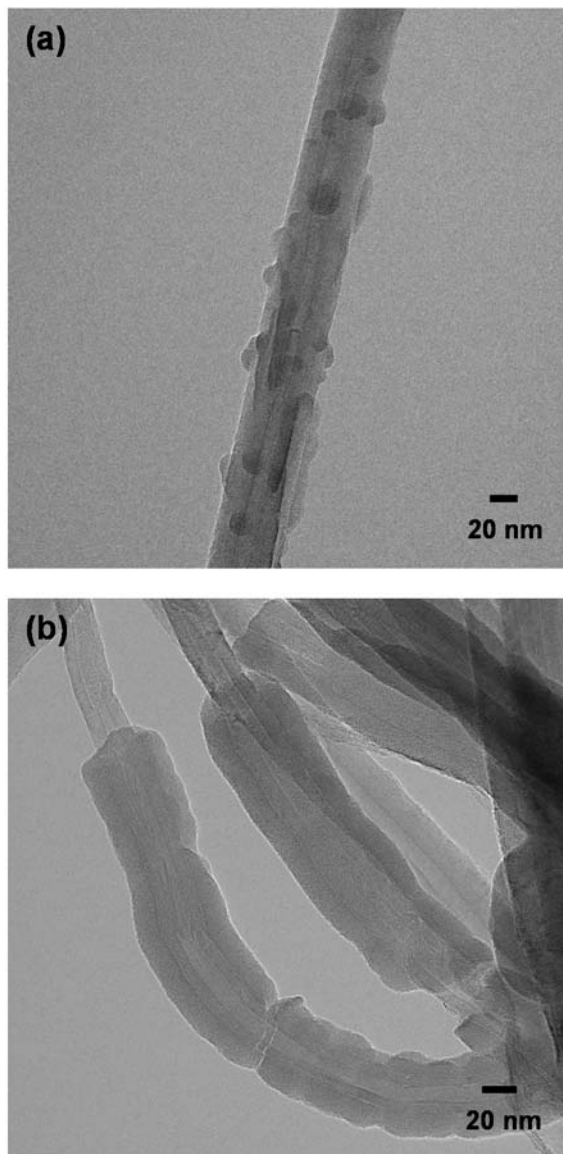


Figure 4.1 TEM micrographs taken after 100 cycles of Al₂O₃ ALD on (a) VACNT_100 and (b) PyC+O₂_100 (PyC deposited and plasma functionalized) MWCNTs.

Two additional control samples were synthesized in order to evaluate ALD coating uniformity on MWCNTs with a variety graphitic qualities and amorphous contents. This was achieved via post-treatment of as-grown MWCNTs with high temperature graphitization and PyC deposition. TEM micrographs of samples G_100 and PyC_100 after 100 Al₂O₃ ALD

cycles are shown in Figure S4.14. The Al₂O₃ morphology on graphitized MWCNTs appears similar to that seen on as-grown CNTs with coverage of monodisperse beads. During high temperature annealing of MWCNTs, amorphous and graphitic defects can be healed (268, 274). Long soak times at high temperature in an inert atmosphere allows disordered carbon atoms at defect sites to rearrange, thus increasing the degree of graphitization but also decreasing nucleation sites for Al₂O₃ growth.

The nucleation and growth behavior of ALD Al₂O₃ on PyC coated MWCNTs appeared different compared to the other controls. The particles were no longer monodisperse, instead having a wide range of diameters. Additionally, the deposited material formed both smooth, round beads as well as angular and plate-like morphologies. This can be attributed to the increased surface roughness created during PyC deposition. PyC formed via thermal decomposition of C₂H₂ is a mixture of sp²-sp³ hybridized carbon molecules. This technique has been used to radially grow MWCNTs, where additional walls are deposited in a layer-by-layer fashion (41, 275). Characteristic of this mechanism, the roughness of the film increases as a partial layer is formed, only decreasing once the layer is complete. The areas of roughness resemble high surface energy MWCNT wall defects, and thus act as sites for nucleation. Jensen et al. demonstrated conformal Al₂O₃ coatings on MWCNT arrays using amorphous carbon pre-treatment (276). In our case however, PyC deposition alone was not enough to achieve smooth films.

To enhance Al₂O₃ nucleation and coating uniformity, functionalization treatment was employed to modify the MWCNT surface chemistry and thus MWCNT-TMA reactivity. Pristine, PyC coated, and graphitized VACNT arrays were treated for 5 minutes in O₂/CF₄ plasma before being deposited with 100 cycles of Al₂O₃. All plasma treated samples exhibited a significant improvement in conformality of the Al₂O₃ coating compared to the non-functionalized controls. TEM images taken at low magnification (Figure S4.15a,c,e), show many Al₂O₃-coated MWCNTs, which was exemplary of the entire grid. The smoothest and most conformal Al₂O₃ coatings were formed for PyC+O₂_100, as shown in Figure Figure 4.1b. The average deposition rate of Al₂O₃ on each sample was calculated to be within 1.0-1.3

Å/cycle, using measurements taken from high-magnification TEM micrographs. This deposition rate is typical for the ALD parameters used (114, 118, 119).

Improvement in Al₂O₃ film quality is attributed to increased nucleation site density from surface activation. Defects are incurred to MWCNTs upon plasma treatment due to ion bombardment and breakage of sp² bonds. When treated in an oxidizing environment like O₂, defects and dangling bonds can be satisfied by an oxygenated species. Oxygen-containing functional groups react with TMA to nucleate Al₂O₃ (100). A higher concentration of reactive sites results in dense nucleation along the MWCNT surface. These nuclei quickly grow and coalesce due to favorable surface energy to form smooth films. O₂ plasma treatment has also been shown to be an effective means for improving the uniformity of Pt nanoparticle distribution on MWCNT surfaces deposited via ALD (157). In the TEM micrographs there are obvious areas where it appears that the Al₂O₃ film has cracked and slid along the length of the MWCNTs. This “macaroni on a string” morphology has been previously reported by Cavanagh et al. (168), and it is suspected that ultrasonication caused the deposited film to break, slip, and even be completely removed in areas of the MWCNTs.

XPS spectra, shown in Figure 4.2, confirm the presence of oxygen-containing functional groups on PyC deposited and plasma treated arrays. Before any treatment only the C 1s peak was visible (~285 eV), indicating that the concentrations of oxygen or other impurities are below the detection limit of the instrument. After 5 minutes of PyC deposition, the XPS spectrum remained unchanged. Following the 5 minute O₂/CF₄ plasma treatment O 1s and F 1s peaks became apparent in the survey scan, each comprising ~5 at%. The high resolution O 1s scan for plasma treated MWCNTs is majorly symmetric and centered over 533 eV, corresponding to carbon atoms with single oxygen bonds (O-C) (277). Despite the presence of oxygen however, high resolution spectra collected for arrays with and without plasma treatment show no change in the shape of the C 1s peak. This indicates that there is no significant change in the nature of carbon-carbon bonding on the MWCNT surface, whether in the form of defects, functional groups, or other sp³ carbon species. This is reasonable due to the low concentrations of O₂ and CF₄ (1%) in He and the short duration of the plasma treatment (5 minutes). O₂/CF₄ plasmas are commonly used to modify the surface chemistry of polymer

films to affect surface energy and adhesion properties, but there are competing reactions between the plasma species generated from O₂ and CF₄ (278). While oxygen species are used to make surfaces more wetting, atomic fluorine and molecules consisting of fluorine may act as etchants or can react with the substrate to make surfaces hydrophobic, non-wetting to polar solvents, and non-sticking. The ratio of O₂:CF₄ gases in the plasma will greatly affect the surface modification imparted to the substrate (279). In fact, in gas ratios as low as 40:60 (O₂:CF₄), oxidation of the substrate is preferentially accelerated, thus creating a more hydrophilic surface (280). Since the gas ratio used in these treatments was 1:1:98 (O₂:CF₄:He), the MWCNT arrays were oxidized and made fully wetting.

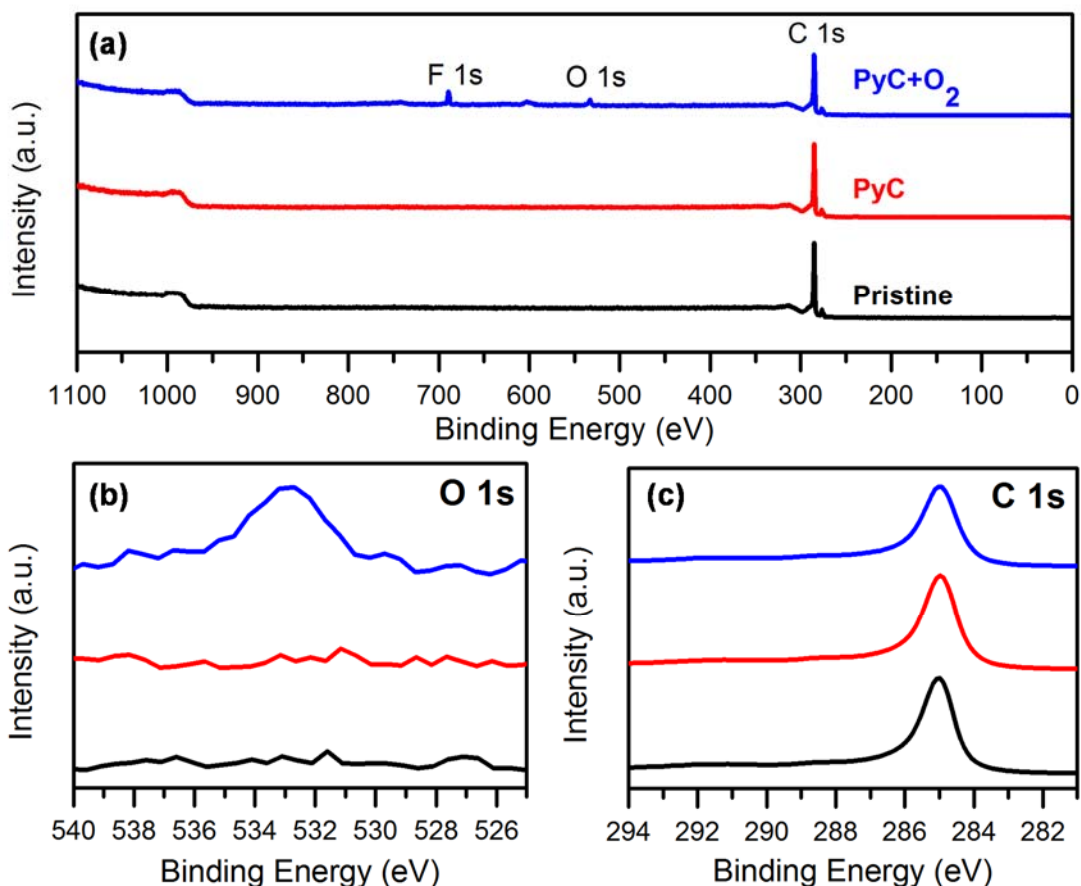


Figure 4.2 XPS spectra (a) survey and high resolution scans of the (b) O 1s and (c) C 1s collected for pristine, PyC deposited, and plasma treated MWCNT arrays. Only the C 1s peak is visible for non-plasma treated arrays, but O 1s and F 1s peaks are found in PyC+O₂.

Pristine and functionalized MWCNT arrays were characterized with Raman spectroscopy to elucidate changes in the MWCNT structure and defect density. In sp²-bonded carbon materials it is common to compare the ratio of intensities of the G-band (~1580 cm⁻¹), which arises from in-plane vibrations of graphite and the material disorder induced D-band (~1350 cm⁻¹). Predominance of the G-band over the D-band corresponds to a highly graphitic sample with a relatively small presence of disorder due to chemical impurities, structural defects, or amorphous material. Representative spectra for all samples are plotted in Figure

4.3. Though all arrays had predominantly higher G-bands, they exhibited varying degrees of defect density based on surface treatment. Pristine arrays had an average G:D ratio of 2.06 which confirms that the as-grown samples have a low defect density. The ratio nearly doubled after graphitization, with an average of 3.78 attributed to healing of defects. Additionally, the D-band peak width decreases, which signifies the removal of amorphous carbon. PyC deposition results in a decreased of the average G:D ratio to 1.7 and a broadening of the D-band width, resulting from coating the MWCNTs with disordered sp^3 -rich carbonaceous material. After O_2/CF_4 plasma functionalization, all G:D ratios is observed to decrease due to incurred defects in the form of broken and dangling bonds plus incorporation of oxygen-containing functional groups.

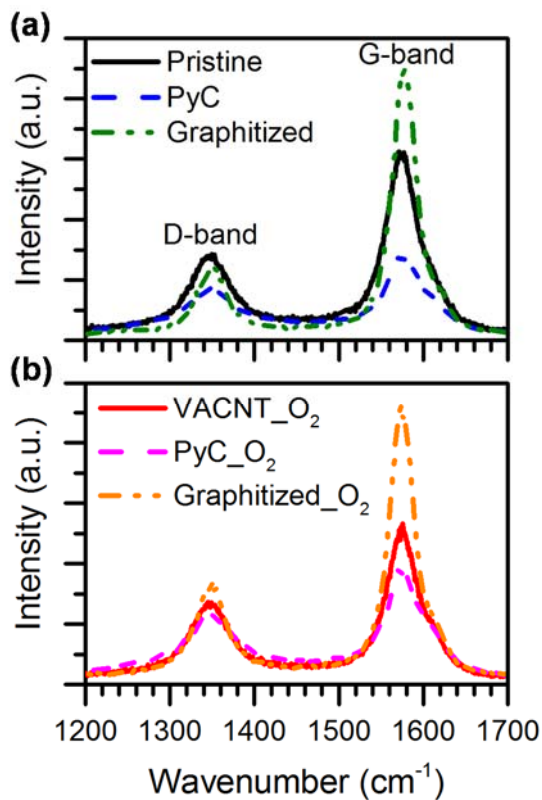


Figure 4.3 Raman spectra were collected from post-treated VACNT arrays with (b) and without (a) plasma functionalization treatments to characterize changes in defect density.

Prior research has shown that after an ALD coating, the G:D ratio and peak intensities will decrease due to the inability of coated CNTs to resonate at the same magnitude as uncoated CNTs (152, 167). This was generally true for these samples with the exception of G_100, O₂_100 and G+ O₂_100 arrays. For these samples, G:D ratio increased after ALD coating, especially for the latter. Though the exact reason for this behavior is unclear, we suspect that the increasing G:D ratio is the result of a shielding effect caused by preferential grafting of nucleated alumina to functional defect sites on the MWCNT surfaces. This effect has been previously observed in the grafting of metal nanoparticles to CNT surfaces (281).

4.3.2 Al₂O₃ Distribution in VACNT Arrays

Cross-sectional SEM analysis of sections located in the center of the ALD coated arrays, shown in Figure 4.4a, reveal an uneven distribution of Al₂O₃ through the array thickness. A visible gradient from top to bottom caused by charging induced bright field contrast indicates an accumulation of insulating Al₂O₃ material. This effect was especially apparent in the cross-section of samples which were plasma treated prior to ALD, which are presented in Figure S4.16-Figure **S4.18**. The uneven distribution was further confirmed using EDS spectral analysis acquired at the top, middle, and bottom of each ALD coated array, and the change in Al concentration was quantified using an Al₂O₃ standard. All samples were observed to have a higher concentration of Al at the top of the array. This disparity was maximized for plasma treated samples, the highest top surface concentration being 34.4 at%, followed by 28.6 at%, and 28 at% for O₂_100, G+O₂_100, and PyC+O₂_100, respectively. Plasma treatment can preferentially functionalize the top of VACNT arrays due to increased bombardment by energetic species. Furthermore, as these arrays are known to grow via base growth, the MWCNT tips are likely to have many defects. These defects would have an affinity for oxidation during plasma treatment in the O₂ atmosphere.

Generally, the Al concentration decreases through the thickness of the array. As shown in Figure S4.16, this effect was somewhat mitigated for graphitized samples which had higher Al concentrations at the top and bottom of the array, with a depleted region in the middle. Prior to high temperature heat treatment, these VACNTs were removed from the quartz growth

substrate to prevent melting. By removing the quartz, ALD precursors were able to diffuse into the array from the top and bottom, creating the unique concentration profile.

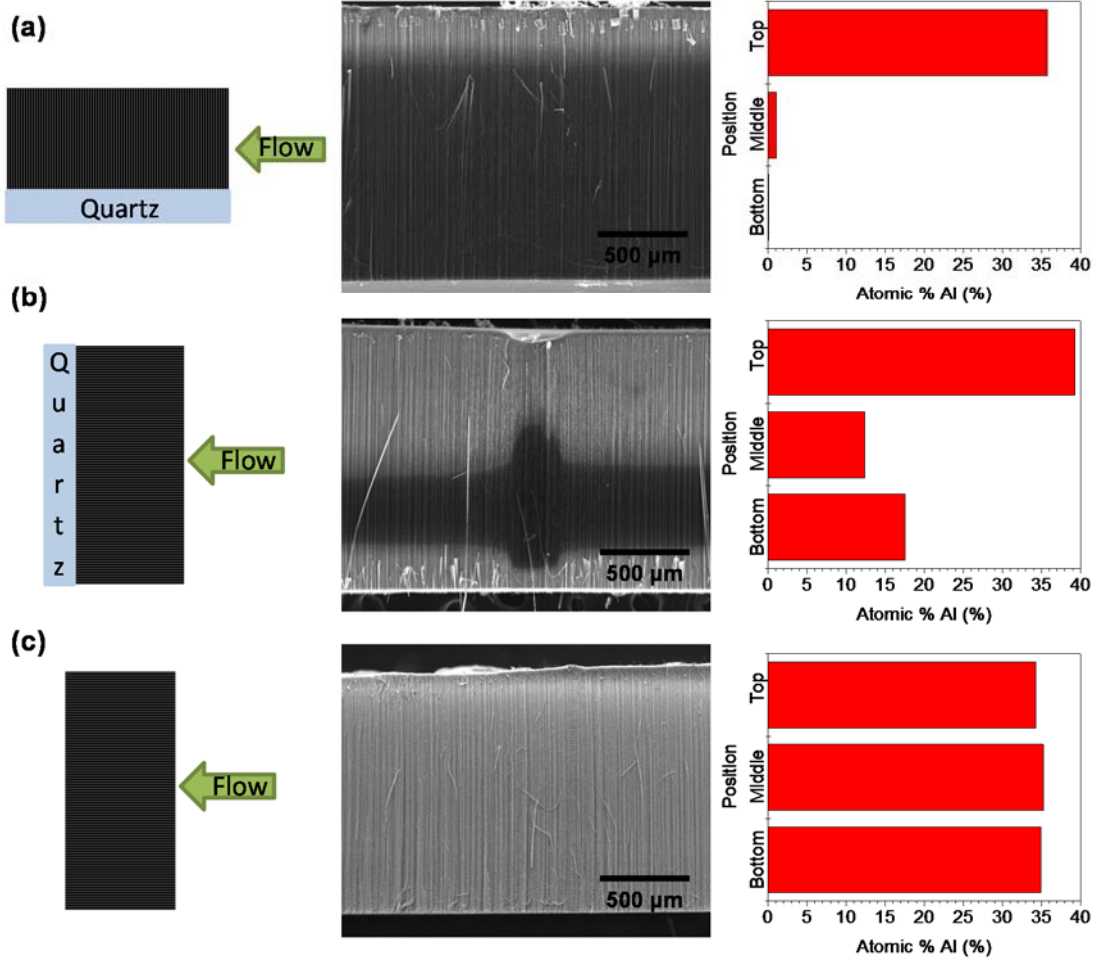


Figure 4.4 EDS analysis at the top, middle, and bottom of each ALD coated array and the atomic % of Al was measured through the thickness as a function of experimental set up. In (a), the MWCNT axes were aligned perpendicular to the flow of ALD precursor and the array remained on the quartz growth substrate. This resulted in a high concentration of Al at the top of the array, which rapidly decreased through the thickness. (b) The array mounted to the quartz was then rotated 90° so that the MWCNT axes were oriented parallel to precursor flow. (c) Finally, Al was homogeneously dispersed throughout the MWCNT array which was both removed from the quartz growth substrate and rotated.

A similar concentration profile was found to occur when arrays still mounted to the quartz were turned 90° so that the MWCNT axes were parallel to the precursor flow, as can be seen in Figure 4.4b. It is suspected that the quartz substrate causes a gas turbulence within the array and extending outward from the sample surface. This turbulence prevents satisfactory purging and delivery of reactants to the VACNT array. As a result, CVD-like growth occurred at the array surface, further inhibiting adequate product removal and prohibiting ideal ALD nucleation and growth throughout the sample cross-section. In previous studies of ALD on high aspect ratio materials, this non-ideal behavior has been attributed to site-blocking by reaction by-products (282). Only by both rotating the array as well as removing it from the quartz substrate could a uniform Al distribution be achieved, as shown in Figure 4.4c. A sample holder was fabricated to carefully sandwich the array between two pieces of PET mesh screen and suspend it in the middle of the ALD reactor cross-section. This technique was used to produce all arrays for mechanical testing and thermal analysis. These samples included Pristine and PyC+O₂ arrays coated for 100 cycles (VACNT_100 and PyC+O₂_100, respectively) as well as PyC+O₂ coated for 500 cycles (PyC+O₂_500). SEM micrographs showing the thick conformal coatings for samples coated for 500 cycles are shown in Figure 4.5.

It is generally accepted that the aligned nature of VACNT arrays is beneficial in promoting ideal ALD-type growth compared to more dense, randomly oriented CNT structures such as buckypapers (171). Aligned structures have more free space between adjacent CNTs, which allows for easier precursor diffusion and purging. This alone, however, does not guarantee uniform coating thickness through the array cross-section. Non-uniform coating thickness as a function of precursor penetration depth has been demonstrated by other researchers working with VACNT arrays (155, 158). It has been theoretically and experimentally determined that this is caused by the decreasing pore diameter with additional ALD cycles which hinders the diffusion of precursor molecules (109, 272). Additionally, with more ALD cycles, the surface area of the VACNT array increases, meaning more precursor molecules and/or longer exposures are required with each subsequent cycle to satisfy all available active sites on the CNT surfaces. In the case of ALD on anodic alumina, another high aspect ratio structure, large precursor dose (120 seconds) and purging times (240 seconds) were

required to uniformly coat the anodic alumina membrane through the whole thickness (270). None of these prior studies investigated the effect of rotating the long pore axis parallel to the direction of precursor flow. Though longer purge times were used in this current study (30 and 45 seconds for TMA and H₂O, respectively), a uniform coating thickness was achieved without increasing the overall exposure despite the ever-decreasing pore diameter.

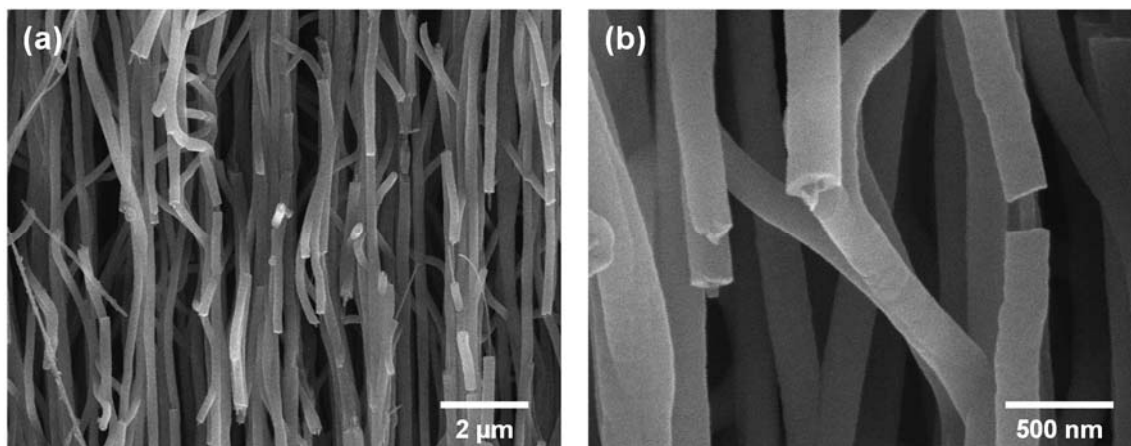


Figure 4.5 SEM micrographs of pre-treated VACNT arrays after 500 cycles of Al₂O₃ ALD at (a) low and (b) high magnification. Both images were taken from the middle section of the coated array.

TGA and dTGA curves for coated and uncoated arrays, with and without surface treatments, are shown in Figure 4.6. The large drop in mass above 600 °C corresponds to the decomposition of the MWCNTs due to thermal oxidation. The onset of this decomposition (T_{onset}), is shifted toward higher temperatures for all ALD coated samples, though by varying amounts. Without any surface pre-treatment, T_{onset} increased significantly from 670 °C to 730 °C following 100 cycles of Al₂O₃ ALD. Additionally, the mass remaining following a 30 minute isothermal soak at 900 °C increased from 0.52 wt% to 24.1 wt% after ALD treatment, corresponding to the weight of deposited alumina. The addition of PyC deposition and plasma treatment did not significantly change the thermal behavior of pristine arrays, but after 100 ALD cycles, the T_{onset} increased to 744 °C with almost 36 wt% remaining. The higher onset

and increased mass remaining are a result of more uniform nucleation and coating on the MWCNT array. The greatest improvement in thermal stability was measured for surface pre-treated samples coated with 500 cycles of Al_2O_3 , with $T_{\text{onset}} = 763\text{ }^\circ\text{C}$. The decomposition rate was significantly lower than others tested, only $0.9\text{ } \%/ \text{min}$ as a result of the thick Al_2O_3 coatings that uniformly coat and protect the MWCNTs from oxidation. Interestingly a small increase in mass was repeatedly observed around $500\text{ }^\circ\text{C}$ for samples coated with 500 cycles of Al_2O_3 . We suspect that this is a result of the incorporation of oxygen from the atmosphere into the amorphous Al_2O_3 as it is heated. Aksel and Eder investigated the oxidation resistance of many metal oxide-CNT hybrids, including Al_2O_3 , fabricated via a modified sol-gel technique (283). They found that Al_2O_3 -CNT hybrids exhibited improved resistance to thermal oxidation by almost $100\text{ }^\circ\text{C}$, which agrees well with our results.

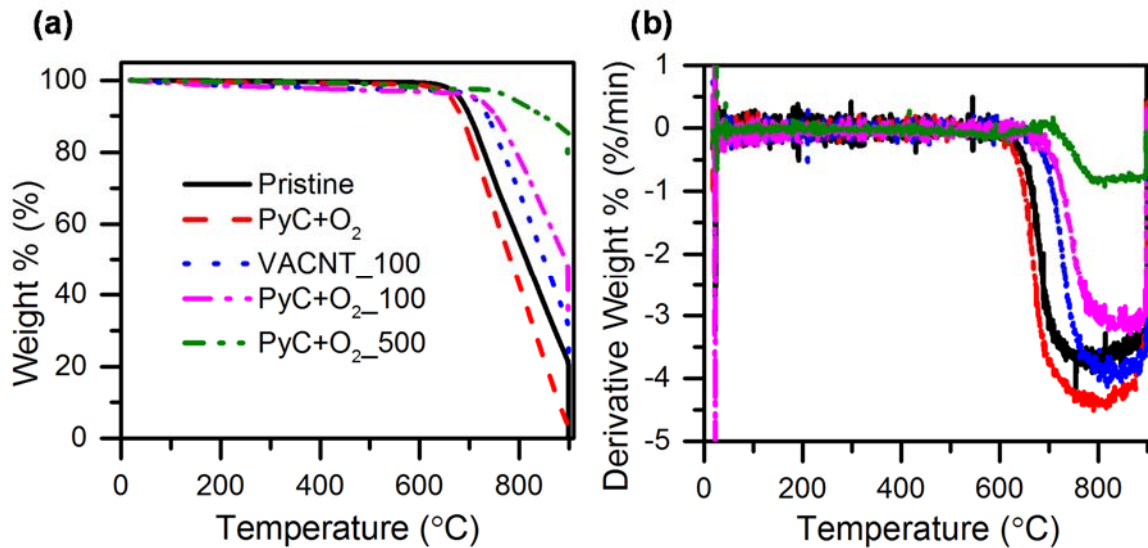


Figure 4.6 (a) TGA and (b) dTGA plots show improvement in oxidation resistance of all alumina ALD coated CNT samples compared to as-grown.

All samples were fully calcined after TGA testing, leaving behind arrays of vertically aligned Al₂O₃ nanotubes, which are shown in Figure 4.7. The Al₂O₃ arrays were found to be continuous through the thickness with high porosity and surface area. The porosity is likely a product of CO₂ gas release upon thermal oxidation of the MWCNT walls. Al₂O₃ nanotubes have previously been produced by coating CNTs using solution methods followed by CNT removal via oxidation, and though the resulting structure was high surface area (60 m² g⁻¹) it was also discontinuous and highly fragmented (284). The creation of aligned Al₂O₃ nanotubes using the ALD technique is straightforward and can be easily controlled by varying the height of the MWCNT array and the thickness of the ALD coating.

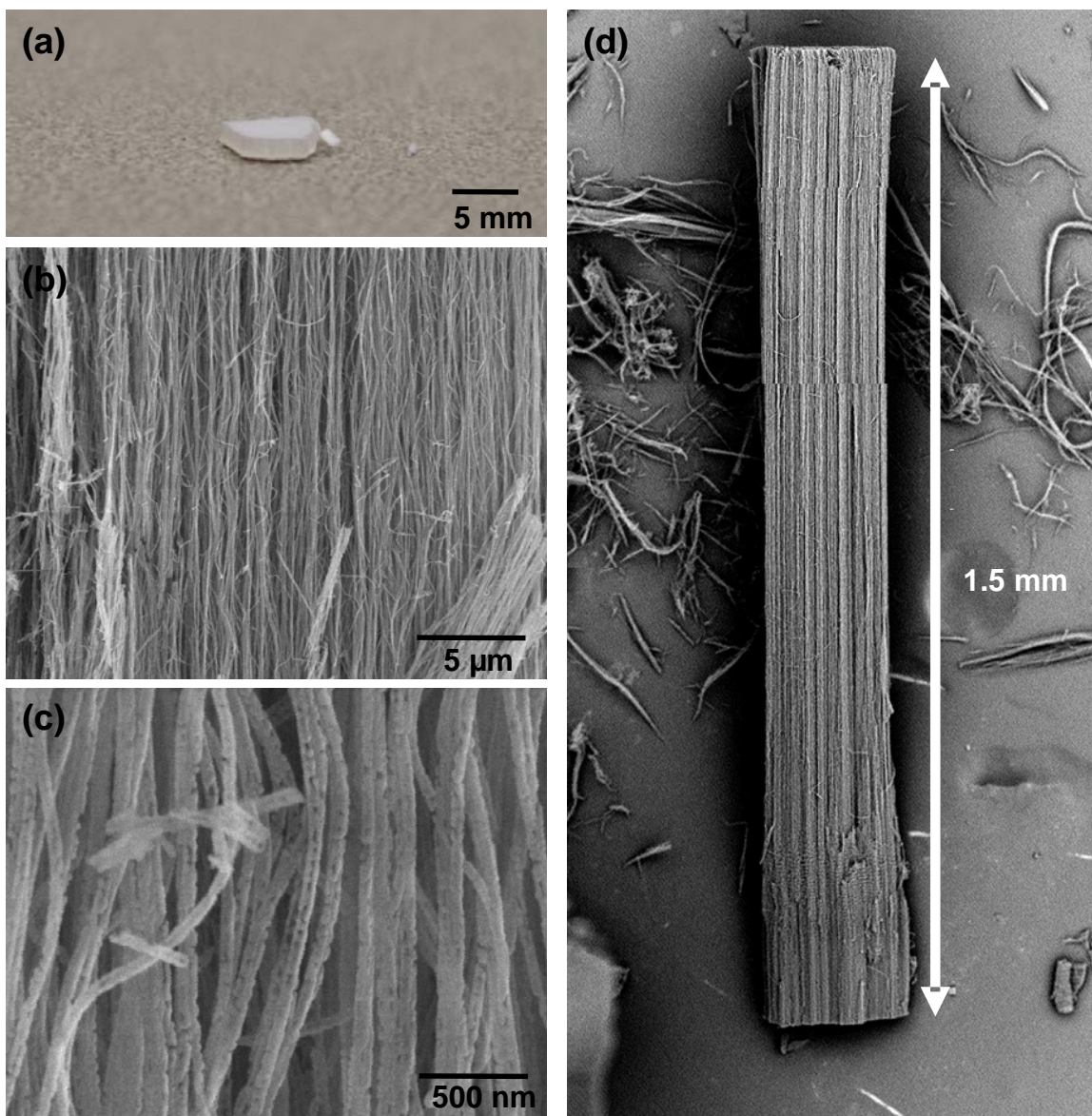


Figure 4.7 VACNTs were removed via oxidation to leave behind a vertically aligned network of alumina nanotubes with high porosity and high surface area.

Compression testing was carried out on pristine and functionalized VACNT arrays to compare the mechanical responses of the arrays with and without ALD coatings. Due to their ultra-low density, as-grown VACNT arrays have poor mechanical properties, as can be seen from the stress-strain plots in Figure 4.8. The modulus is observed to increase from 0.83 MPa

for the pristine arrays to 3.24 MPa simply after ALD coating. Even more significant is the increase in the compressive modulus of functionalized arrays after ALD coating (PyC+O₂_100), which nearly triples to 11.11 MPa. This large increase is attributed to the uniform coating of the VACNTs throughout the entire array rather than sparse nucleation that was found to occur on pristine, non-functionalized VACNTs. In the case of the latter, nucleated Al₂O₃ beads on the MWCNT surface does not participate in load transfer in the same manner than a concentric, conformal Al₂O₃ coating would. Another explanation could also be that the strong presence of functional groups on the MWCNT surfaces can improve interfacial bonding between the MWCNT surface and Al₂O₃ film. It is also interesting to note that these particular samples exhibited foam-like recovery of nearly 100% after the compressive load was removed. In earlier work, this researcher and others have fabricated VACNT sponges via PyC deposition (41, 90). It is impressive that the foam properties can be maintained and even enhanced with the addition of a 12 nm thick alumina coating. The modulus was further improved to 12.81 MPa by coating the functionalized arrays for 500 cycles. The compressive strengths at 20% and 60% strain for each array was also measured. At low strains the compressive strength is also low due to buckling of the VACNT forest structure. An increase was observed for higher strains however, as the samples were densified and consolidated during compression. At 60% strain, the compressive strength increased from 0.15 MPa to 2.16 MPa after only adding 100 cycles of alumina ALD. After 500 cycles, the compressive strength further increased to 6.32 MPa. These values are especially impressive when one considers the low density of even the ALD coated VACNT arrays. The average compressive moduli and strength values are summarized in Table 1.

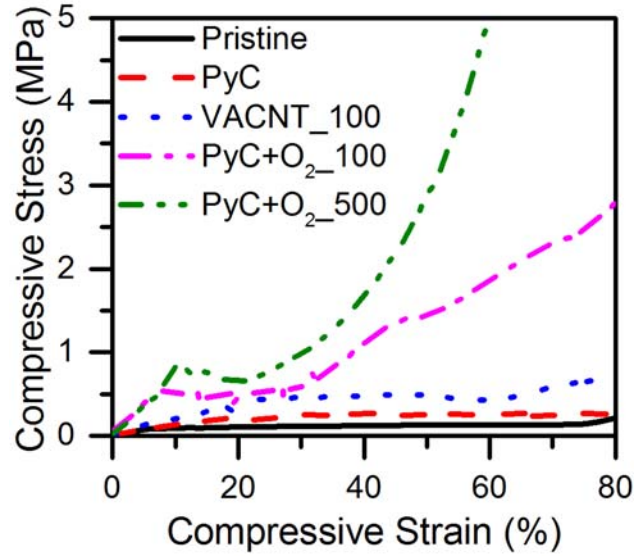


Figure 4.8 Compressive stress – strain curves for ALD coated and uncoated VACNTs. Arrays which underwent surface activation prior to ALD coating (PyC+O₂_100 and PyC+O₂_500) exhibited a larger enhancement in compressive properties compared to uncoated and non-functionalized arrays (Pristine, PyC, VACNT_100).

Table 1. Average compressive modulus and strength values for ALD coated and uncoated VACNTs.

Sample	Modulus (MPa)	Strength @ 20% (MPa)	Strength @ 60% (MPa)
Pristine	0.83 ± 0.16	0.11 ± 0.002	0.15 ± 0.01
PyC	1.34 ± 0.29	0.24 ± 0.05	0.37 ± 0.11
VACNT_100	3.24 ± 0.60	0.44 ± 0.07	0.56 ± 0.10
PyC_O ₂ _100	11.11 ± 3.42	0.61 ± 0.10	2.16 ± 0.18
PyC_O ₂ _500	12.81 ± 3.27	0.71 ± 0.22	6.32 ± 0.96

An additional benefit to coating the MWCNT arrays with Al₂O₃ is their improved ability to be processed into ceramic composites. One common route for the manufacture of toughened ceramic composites is the addition of CNTs to ceramic powders prior to consolidating and sintering (285). There are several issues with this method however. First,

CNTs are prone to agglomeration due to mutual van der Waals attractions. Second, due to large differences in density between the ceramic powders and CNTs it is difficult to achieve a uniform dispersion of CNTs in the matrix which results in a worsening in properties. Additionally, because pristine CNTs are for the majority inert they will exhibit little to no interfacial bonding with the surrounding matrix. Finally, due to the presence of oxygen during many sintering techniques, CNTs are prone to degradation from thermal oxidation. The ALD Al_2O_3 coated MWCNTs fabricated in this study have the potential to resolve these issues due to the observed improvements in thermal stability and mechanical robustness. In addition, the coated MWCNT surfaces are effectively surface functionalized by their being conformally coated in oxygen-rich Al_2O_3 . As shown in Figure 4.9, arrays coated for 100 cycles are easily wettable by water and other aqueous solutions where pristine arrays are typically hydrophobic due to high hierarchical micro- and nanoscale surface roughness.

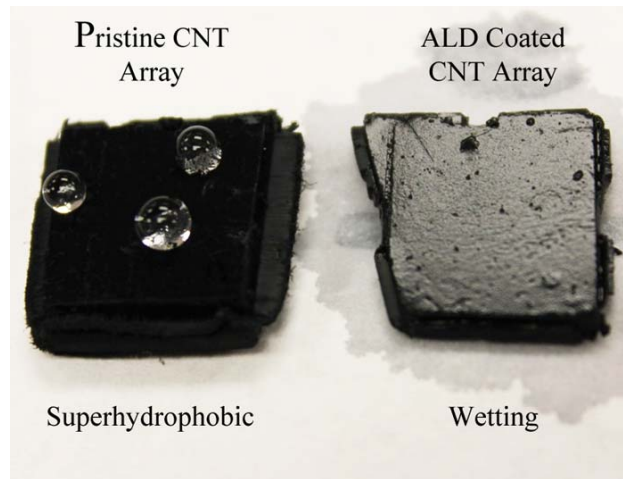


Figure 4.9 Pristine VACNT arrays are superhydrophobic due to high surface roughness and low CNT density in the array. After 100 cycles of Al_2O_3 ALD, the surface energy of the coating dominates over the physical structure and the arrays wet.

4.4 Conclusions

ALD is a useful technique for the uniform and conformal coating of high surface area and high aspect ratio VACNT arrays, but not without first optimizing the sample and process parameters for best results. The surface chemistry of high graphitic quality, low defect density MWCNTs was optimized for Al₂O₃ nucleation via PyC deposition and oxygen plasma functionalization. The combination of these two surface pre-treatments provided a high concentration of oxygen-containing functional groups that could complex with TMA upon dosing, thus creating a high nucleation density of Al₂O₃ on the MWCNT surface which then quickly spread and coalesced into a thin film. Furthermore, a uniform distribution of Al₂O₃ through the thickness of the array was achieved by removing the MWCNTs from their growth substrate and orienting the MWCNT axes parallel to the flow of the reactor. It was determined that the Al₂O₃ coated MWCNTs not only exhibited greatly enhanced compressive properties, but also improved thermal stability to oxidation by delaying onset by nearly 100 °C. To the best of the authors' knowledge, this is the first demonstration of conformal ALD coating of 1.5 mm long VACNTs with a pore aspect ratio ~15,000.

Acknowledgements

The authors acknowledge the use of the Analytical Instrumentation Facility (AIF) at North Carolina State University, which is supported by the State of North Carolina and the National Science Foundation. This material is based upon work supported by the National Science Foundation Graduate Research Fellowship Program under Grant No. DGE-0946818. The authors thank Prof. Yuntian Zhu for time on the Raman Microscope.

4.5 Supplemental Information

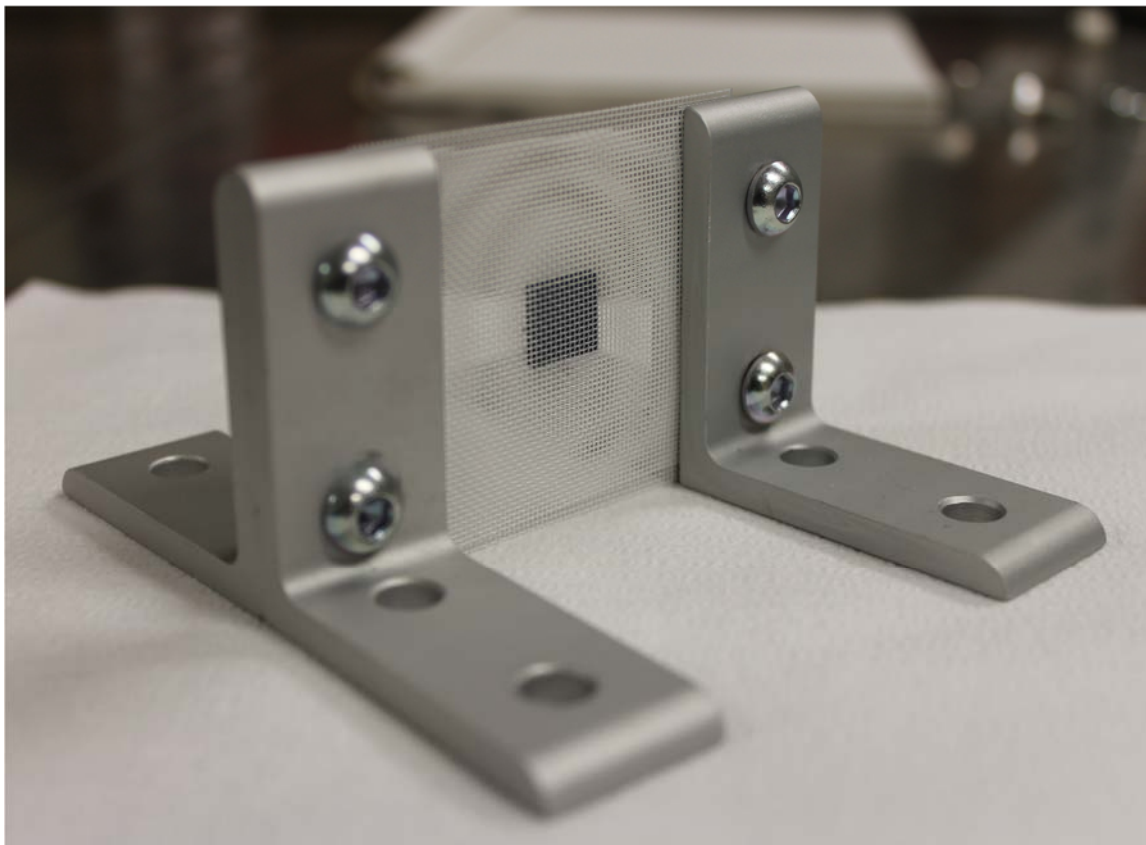


Figure S4.10 Experimental apparatus used to mount MWCNT array with CNT axes parallel to precursor flow in ALD chamber.

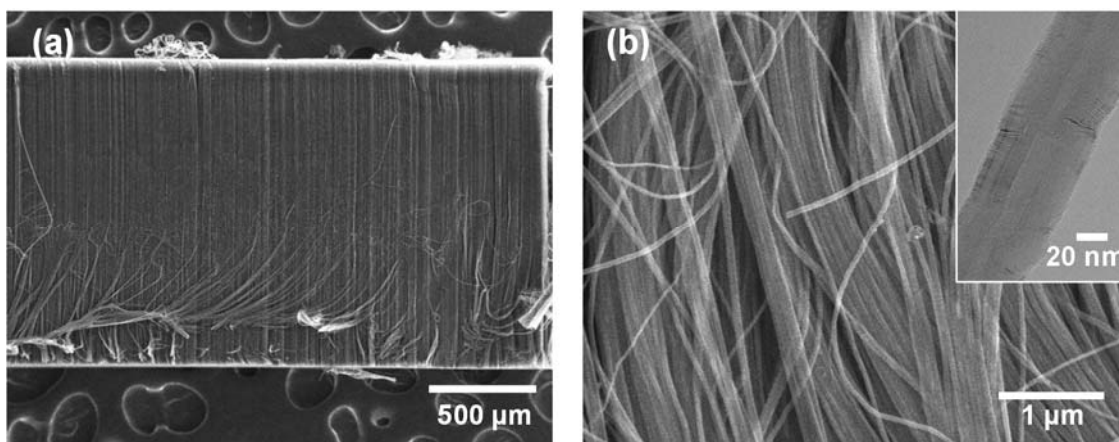


Figure S4.11 SEM images of VACNT array cross section at (a) low and (b) high magnification. Inset shows TEM image of typical MWNT used in experiments.

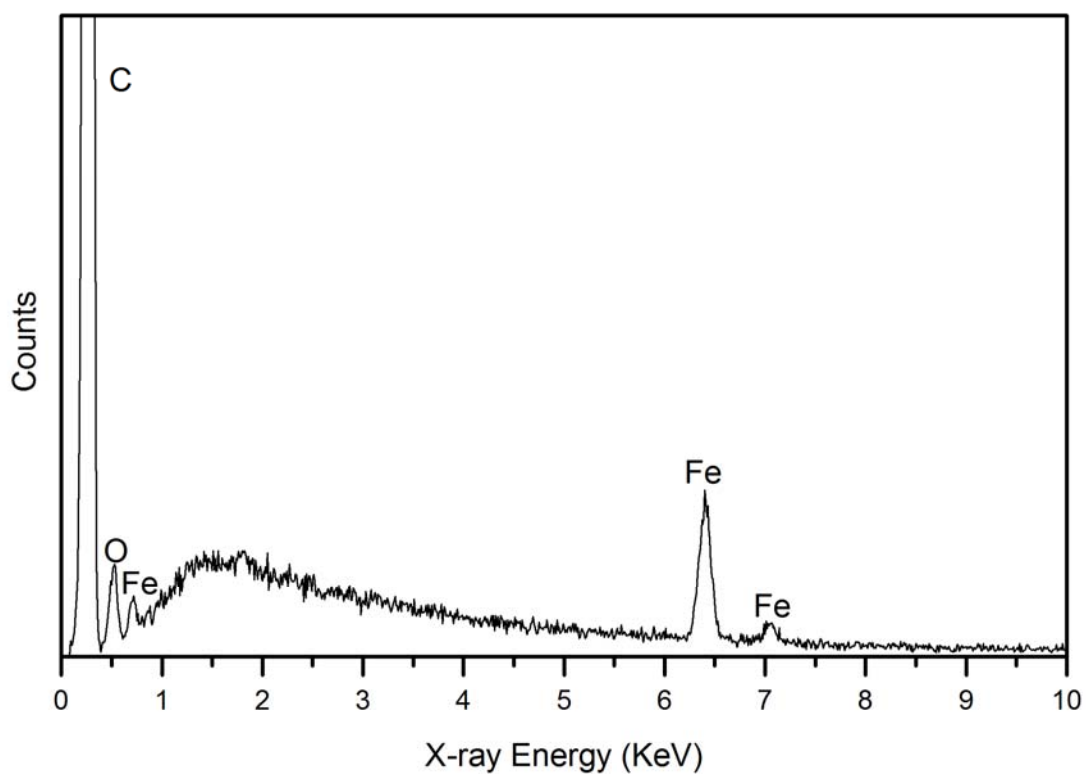


Figure S4.12 EDS spectrum from an as-grown array shows that the level of impurity is very low, with only 0.96 at% and 0.42 at% oxygen and iron, respectively.

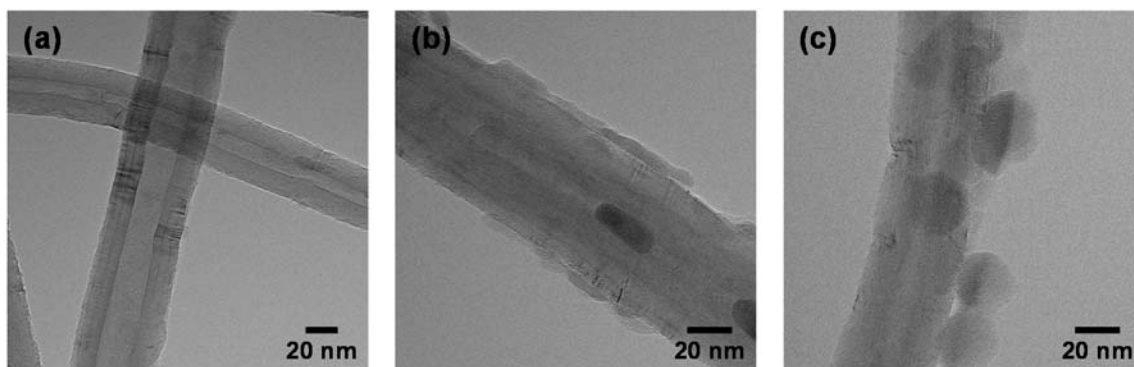


Figure S4.13 TEM images of alumina nucleation on as-grown CNTs after (a) 25, (b) 75, and (c) 100 ALD cycles.

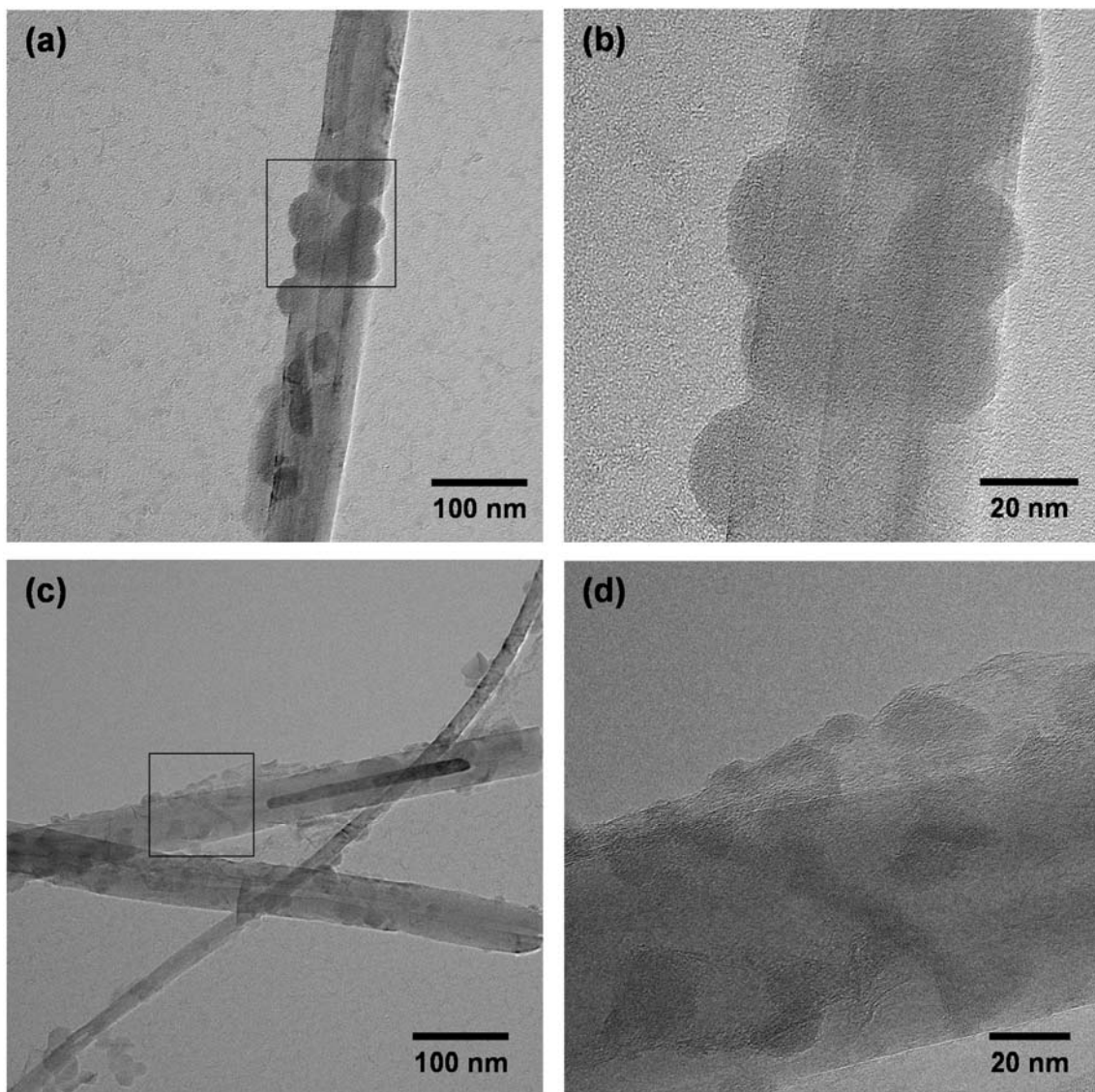


Figure S4.14 TEM images after 100 cycles of alumina ALD on (a,b) graphitized and (c,d) PyC coated CNTs.

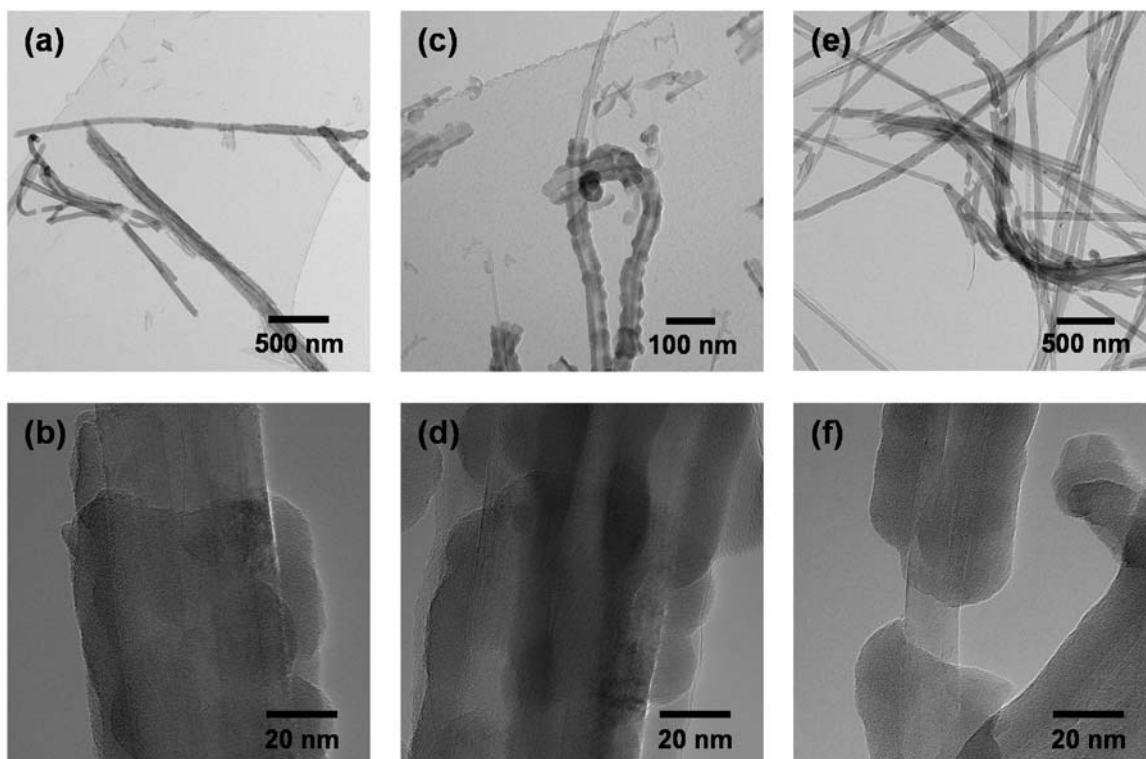


Figure S4.15 TEM images after 100 cycles alumina ALD on (a,b) VACNT+O₂/CF₄, (c,d) VACNT+G+O₂/CF₄, and VACNT+PyC+O₂/CF₄ (e,f).

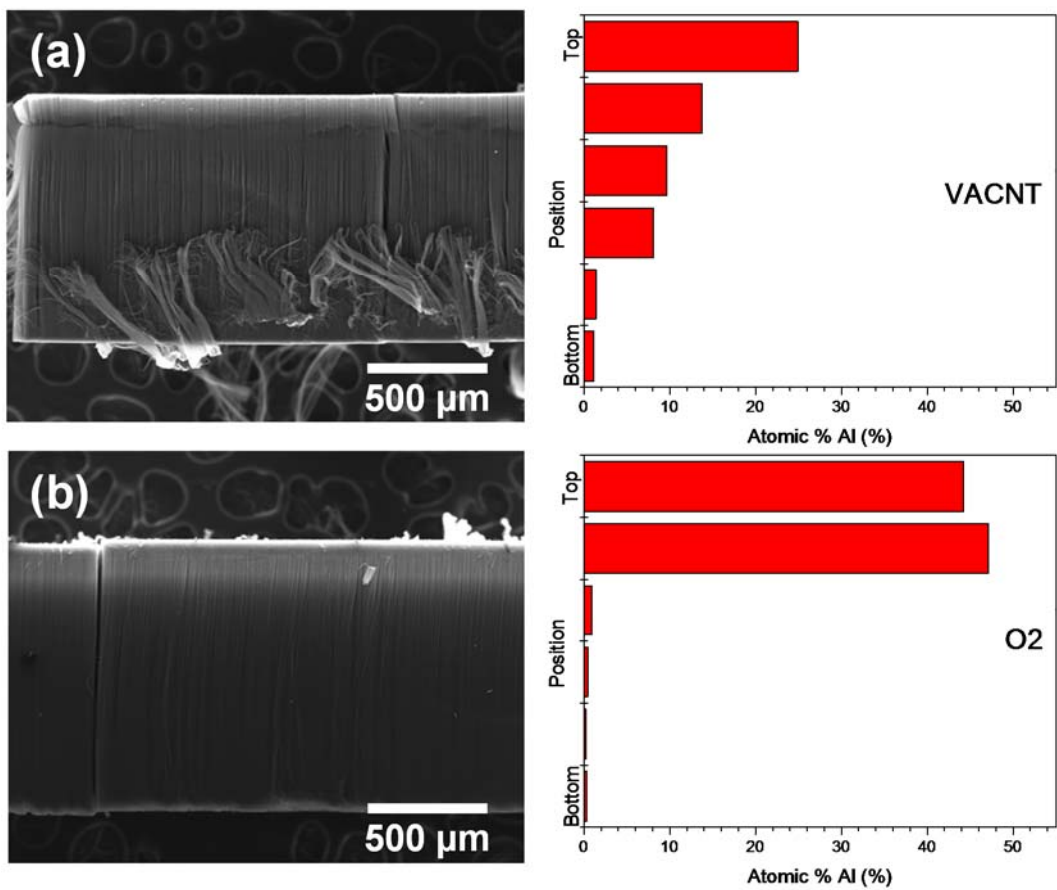


Figure S4.16 Cross-sectional SEM and accompanying EDS measurements taken from top to bottom throughout the ALD-coated array for (a) pristine VACNTs and (b) VACNT+O₂/CF₄.

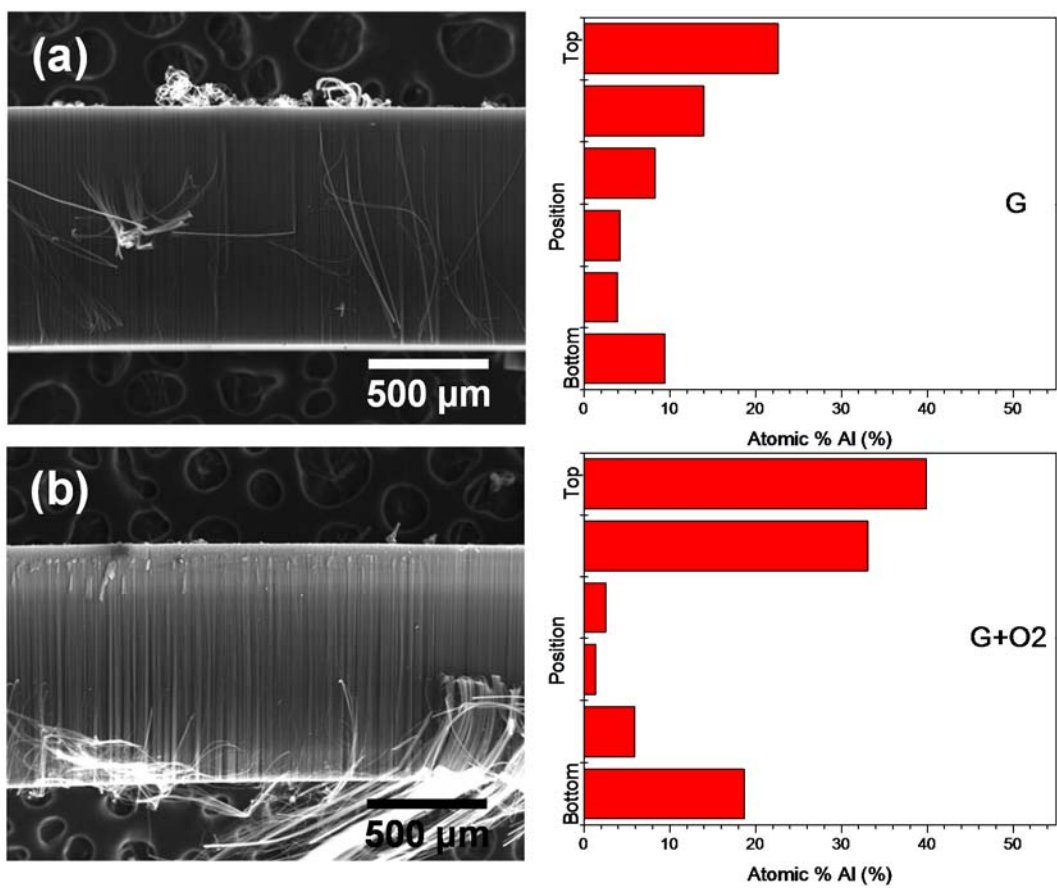


Figure S4.17 Cross-sectional SEM and accompanying EDS measurements taken from top to bottom throughout the ALD-coated array for (a) graphitized VACNTs and (b) G+O₂/CF₄.

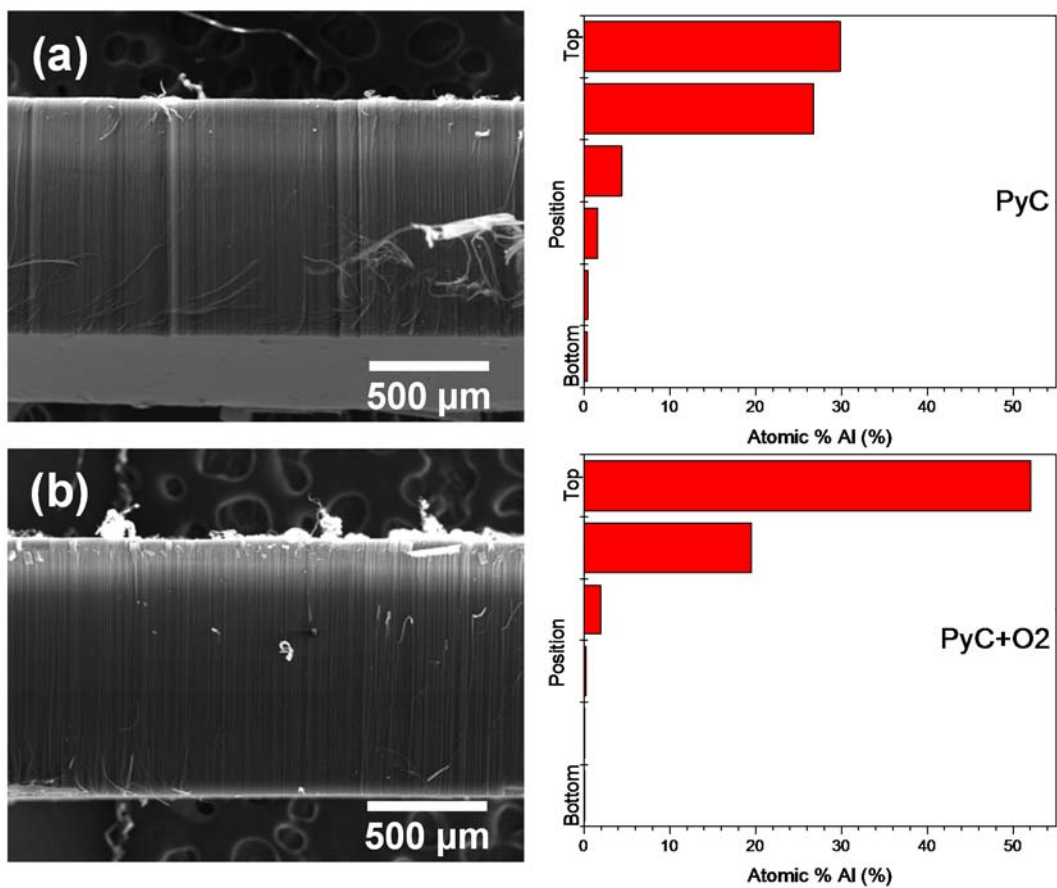


Figure S4.18 Cross-sectional SEM and accompanying EDS measurements taken from top to bottom throughout the ALD-coated array for (a) PyC deposited VACNTs and (b) PyC+O₂/CF₄.

5 Chemical and Structural Characterization of ALD-Deposited Alumina on Carbon Nanotube Foams

5.1 Introduction

Aluminum oxide, or alumina, is a technologically important material utilized in applications ranging from structural composites to catalysis to thermal insulators. There has been extensive research on the deposition of alumina via ALD on a variety of substrates (111). As with any material deposition technique, processing parameters such as temperature, pressure, and substrate material (among countless others), play a significant role in determining the structure of the deposited material, and hence, its properties (114, 118, 119). Regardless of parameters, alumina is generally known to deposit in the amorphous phase (103). Differences arise, however, in the growth rate, film density, and stoichiometry as a function of processing conditions. Generally, films deposited at lower temperatures are further away from stoichiometric equilibrium due to lower precursor reactivity. Chemical characterization often reveals oxygen deficient films with O/Al ratios < 1.5 caused by insufficient oxidation of TMA (100). This can be overcome by increasing reactor temperature (if parameter space permits), using plasma-enhanced ALD, or using a more reactive oxidizing agent such as ozone (286). On the other hand, alumina films with O/Al ratios > 1.5 are also possible (287).

Understanding the nature of as-deposited material is important as it determines the physical properties of the film such as density, index of refraction, and catalytic behavior (112). In addition, this information is useful when studying phase transformation behavior during annealing. For example, γ -AlO(OH) (boehmite) and α -Al(OH)₃ (bayerite) are known to undergo difference sequences during crystallization, with unique metastable polymorphs formed at difference temperatures in route to becoming fcc α -Al₂O₃. In fact, the packing of oxygen in the amorphous state will determine whether hcp or fcc α -Al₂O₃ will be formed (288).

The substrate material may also influence the behavior of coatings during deposition as well as annealing (122). CNTs have previously been shown to stabilize the formation of rutile TiO₂, and also limit the extent of grain growth during heat treatment (2, 207).

Furthermore, unique interfacial compounds have been identified for highly carboxylated CNTs coated with ZnO using ALD (172, 289). Despite the prevalence of alumina and its widespread use in coating CNTs, there is little information on post-deposition processing of alumina to promote crystallization by annealing. In this study XPS and XRD techniques were utilized to gain insight on the nature of alumina on CNTFs in the as-deposited state as well as upon annealing in inert and oxidizing atmospheres.

5.2 Experimental

5.2.1 Materials and Methods

CNTF templates were prepared using procedures outlined in Section 3.1. XRD samples were coated for 500 cycles to ensure there was an adequate quantity of material for characterization.

5.2.2 Characterization

SEM was conducted on a FEI XHR-Verios 460L field emission SEM. Samples were not sputter-coated prior to imaging. For TEM, a JEOL 2010F field emission STEM was used. Micrographs were recorded using a Gatan Orius digital camera. XRD measurements were conducted on a Rigaku SmartLab Bragg-Brentano XRD with a Cu K α radiation source ($\lambda = 1.5418 \text{ \AA}$). Step scans were performed for $2\theta = 10\text{-}80^\circ$ with a step size of 0.05° and scan speed of 3 seconds. Surface chemical composition of treated CNTs was completed using X-ray photoelectron spectroscopy (XPS) on a SPECS XPS system (SPECS Surface Nano Analysis) using a high-resolution PHOIBIS 150 hemispherical analyzer. Freshly post-treated arrays were transported and stored in non-outgassing Fluoroware containers to prevent surface contamination. Measurements were taken at a base pressure of 10^{-10} bar with an Mg K α excitation source (1254 eV). Survey scans were taken from 1200 – 1 eV and high-resolution scans were taken of the O1s peak (538 – 528 eV), C1s peak (291 - 283 eV), and Al2p peak (80 – 70 eV). Energy calibration was established by referencing to the carbon C 1s line at 285 eV binding energy.

5.3 Results and Discussion

5.3.1 Analysis of As-Deposited and Calcinated Alumina

XRD spectra, shown in Figure 5.1a, showed that as-deposited alumina was amorphous which is typical for deposition at low temperatures (100). After calcination in air at 800 °C peaks corresponding to the metastable polymorph, η -Al₂O₃, were found to evolve (288). This is in agreement with high-resolution TEM images which also showed evidence of lattice fringes from crystallites forming post-calcination (Figure 5.1b).

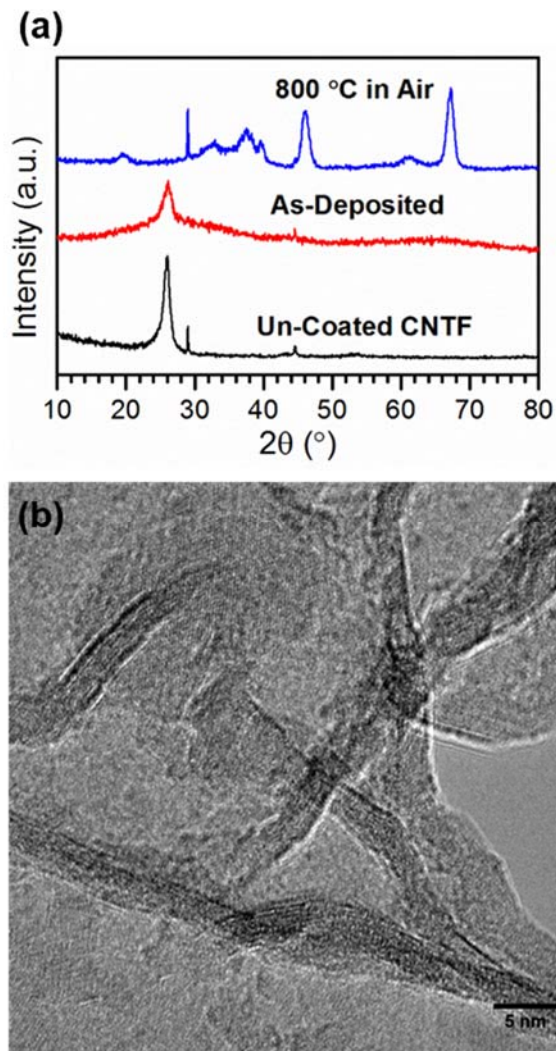


Figure 5.1 (a) XRD spectra of pure CNTFs, as-deposited alumina on CNTFs, and calcinated alumina nanotubes. The peak signature of the alumina nanotubes, along with (b) TEM showing lattice fringes in alumina walls indicates that crystallization began during calcination, to form metastable η - Al_2O_3 .

High resolution O1s and Al2p XPS scans are shown in Figure 5.2 for alumina coated CNTFs with varying film thicknesses as well as calcinated alumina. As-deposited alumina was found to be oxygen rich, with an O/Al ratio of 2.42, which indicates that rather than stoichiometric Al_2O_3 being deposited, the material is more likely an aluminum hydroxide with

the form $\text{Al}(\text{OH})_{2-3}$. Following calcination, the O/Al ratio drops to 1.86, which correlates with the evolution of $\eta\text{-Al}_2\text{O}_3$ shown by XRD and TEM analyses.

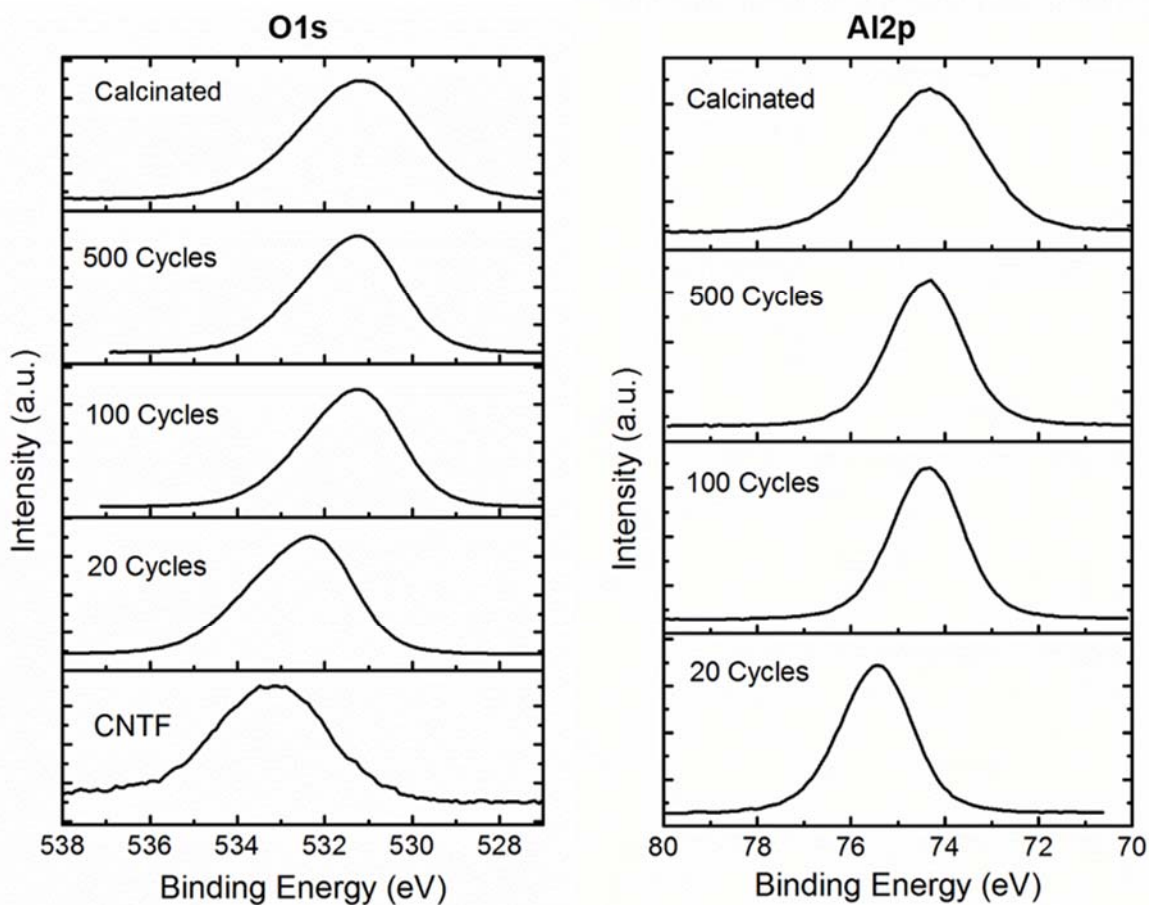


Figure 5.2 High resolution XPS spectra of the O1s and Al2p peaks taken from pure CNTFs (only O1s), and CNTFs coated with alumina for 20, 100, and 500 cycles, as well as calcinated alumina nanotubes.

Examination of the high resolution O1s peak provides information on the changing nature of oxygen bonding with increasing coating thickness. In the case of un-coated CNTFs, the largely symmetric peak is attributed to single-bonded C-O functional groups (532.7 eV)

resulting from oxygen plasma treatment (290). Upon coating with alumina, the O1s peak for CNTF+20AO becomes asymmetric and shifts to higher energy. These changes arise from the combined contributions of the aforementioned surface functional groups as well as the evolution of new oxygen bonding states from Al-O-Al and Al-O-C bonds, located at 531.2 eV and 532.4 eV, respectively (286, 291).

Increasing the number of ALD cycles causes the signal to gradually shift to higher energies while peak asymmetry is maintained. Now, because the alumina coating is in excess of 60 nm thick, we can be confident that we are not receiving signal from the CNT surfaces. Therefore, this asymmetry can be also attributed to the presence of Al-O-H bonds (531.8 eV) for all coated samples, which agrees well with the high O/Al atomic concentrations mentioned before (292). Additionally, Figure 5.2 provides high resolution Al2p spectra which further confirm these findings. The downward shift of the Al2p peak from 75.4 eV to 74.4 eV with increasing cycles is a result of the presence of Al-O-C bonds (75.4 eV) in the 20 cycle samples which are not visible in thicker coatings with signals dominated by Al-O-Al or Al-O-H bonds (74.4 eV).

Following removal of CNTFs via calcination, the O1s peak energy is unchanged but symmetry is restored indicating the disappearance of Al-O-H bonds and their replacement with Al-O-Al bonds (293). This result agrees well with the measured decrease in O/Al concentration (2.42 → 1.86) as well as XRD and TEM analyses which showed crystallization of alumina after calcination.

5.3.2 High Temperature Thermal Annealing

Due to their high thermal stability, particularly in non-oxidizing environments, CNTs are an interesting template for studying the crystallization behavior of alumina thin films at high temperatures. As mentioned previously, as-deposited alumina was determined to be amorphous, and one hour of low temperature heat treatment (in air) resulted in oxidative removal of CNTs as well as crystallization of alumina to form η -Al₂O₃.

To preserve the CNTs and elucidate their effect on alumina crystallization, high temperature heat treatments were instead performed in argon. SEM and TEM micrographs

depicting the crystallized morphology are shown in Figure 5.3. XRD analysis on annealed samples is provided in Figure 5.4. After 1 hour of treatment at 1200 °C the alumina had crystallized to form a mixture of metastable θ -Al₂O₃ and α -Al₂O₃ polymorphs. Annealing the sample for 2 hours resulted in the full conversion to α -Al₂O₃. Following treatment the coated CNTFs exhibited no signs of shrinkage or cracking. Typically, high temperature annealing of alumina aerogels leads to drastic shrinkage due to particle sintering (238, 249, 254). Sintering takes place at points of contact between adjacent particles, or “necks”. Traditional aerogels are comprised by ligaments made of nanoparticles in a morphology commonly referred to as “pearls on a string”. As there are many necks, there is also a large driving force for sintering to occur. Conversely, the ligaments within our materials are continuously connected CNTs covered in thin and smooth films of alumina. Not only is there a lower driving force for sintering, the presence of the CNT substrate also inhibits drastic shrinkage which normally occurs in alumina aerogels at high temperatures. Furthermore, calcination in air still permits the removal of CNTs from the foam, leaving behind a highly crystallized α -Al₂O₃ aerogel.

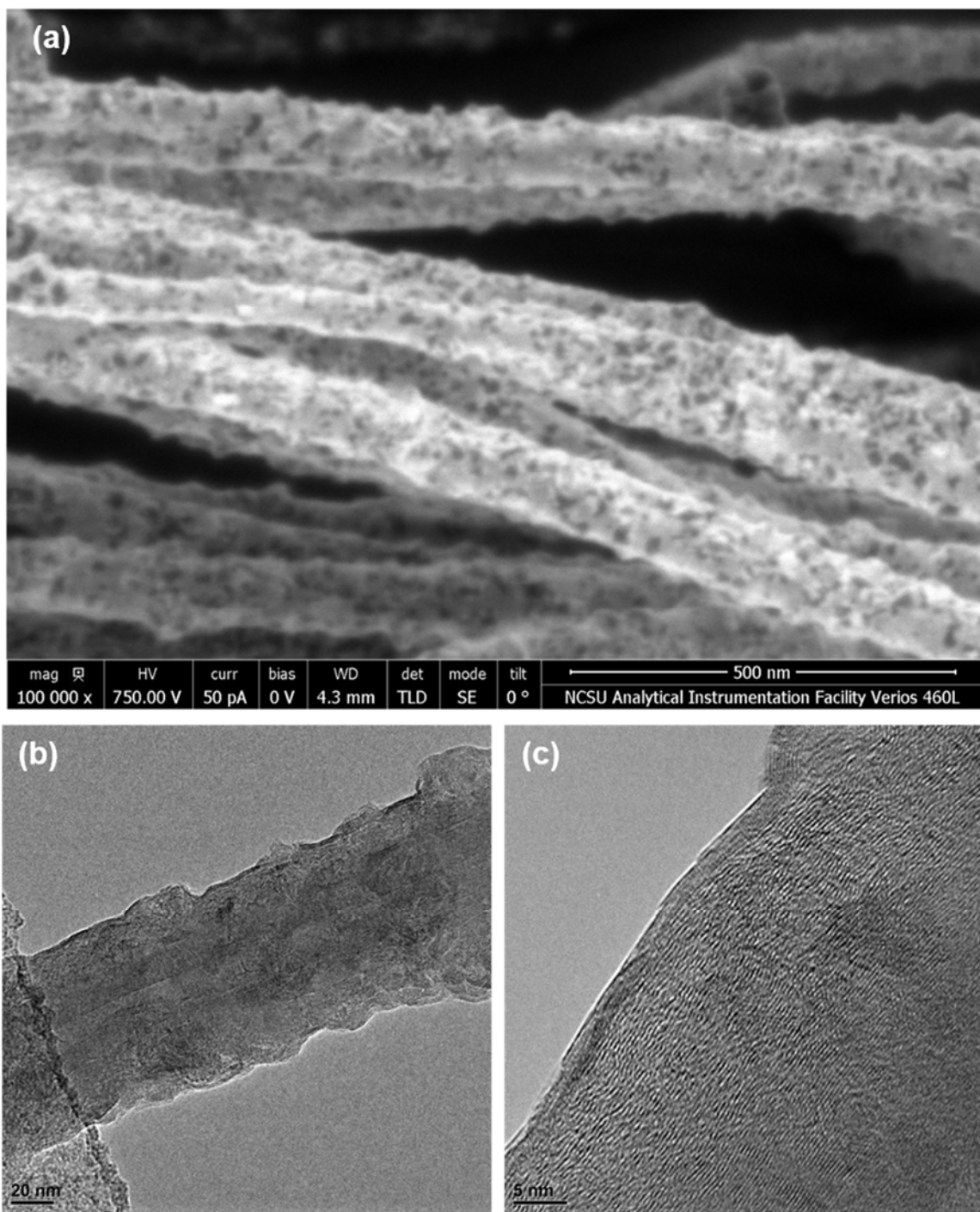


Figure 5.3 (a) SEM and (b,c) TEM micrographs of CNTF coated for 20 ALD cycles with alumina, and then annealed for 1 hour in Ar at 1200 °C. The alumina coating was found to remain intact during heat treatment, and evidence of lattice fringes shown in (c) indicate crystallization.

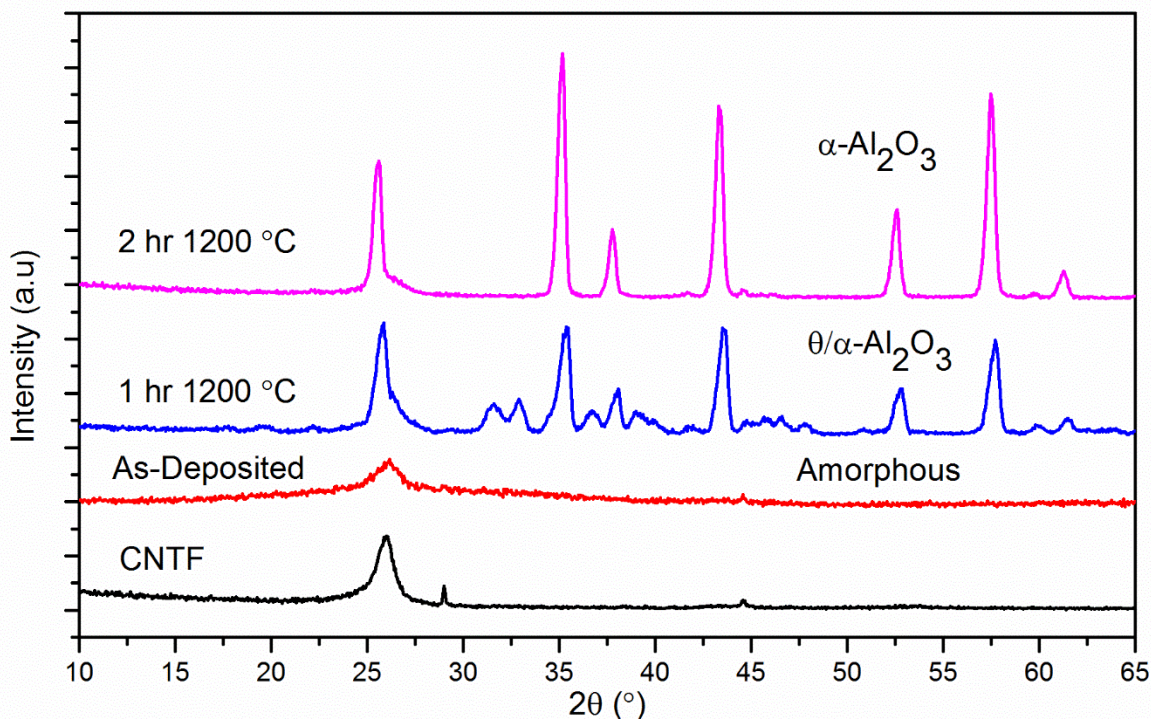


Figure 5.4 XRD spectra of pure CNTF, as-deposited alumina on CNTF, and alumina-coated CNTFs after high temperature annealing in Ar gas after 1 and 2 hours. While as-deposited alumina was found to be amorphous, 1 hour of annealing yielded a mixture of θ and α - Al_2O_3 polymorphs. After 2 hours of treatment, all alumina was fully converted to α - Al_2O_3 .

5.4 Conclusions

Alumina deposited via ALD on plasma functionalized CNTFs was determined to be amorphous, though calcination in air at 800 °C resulted in oxidation and removal of carbon as well as alumina phase transformation to η - Al_2O_3 . High temperature annealing of CNT-alumina hybrids in argon preserved the CNTFs and showed the following phase transitions: amorphous alumina \rightarrow θ/α - Al_2O_3 \rightarrow α - Al_2O_3 . Characterization of the specimens using XPS indicated that as-deposited alumina was oxygen rich, likely with the form $\text{Al}(\text{OH})_{2-3}$ corresponding to boehmite and bayerite aluminum hydroxides. The relative oxygen concentration decreased after crystallization due to formation of stoichiometrically balanced Al_2O_3 . Analysis of high-resolution XPS spectra from O1s and Al2p peaks provided evidence indicating the presence of

Al-O-C bonding near the interface of CNTFs and alumina. To the best knowledge of this author, this is the first time that evidence of interfacial bonding between CNTs and ALD-deposited alumina has been presented.

6 Interconnected Metal Oxide Nanotube Networks for Ultralight Aerogels

*Kelly L. Stano, Shaghayegh Faraji, Ryan Hodges, Ozkan Yildiz, Brian Wells, Halil Akyildiz, Junjie Zhao, Jesse Jur, and Philip D. Bradford**

6.1 Introduction

Synthesis of multifunctional materials that are simultaneously ultralow density, high surface area, yet mechanically robust is a topic of intense interest for researchers in catalysis, energy harvesting, filtration, and gas sensing (4, 294, 295). These applications dictate that the material have large amounts of accessible surface area in the form of interconnected pores through which molecules can easily permeate, diffuse and interact with the active material. Nanoscale architectures are often desired due to their high surface area to volume ratio, but methods to controllably fabricate three-dimensional and large-scale (dimensions ≥ 1 cm) nanostructured materials are rare. In this work, we present a method for the fabrication of large, ultralow density (1.2 mg cm^{-3}) and anisotropic metal oxide foams with high porosity and surface area using aligned carbon nanotube foams (CNTFs) as a novel and customizable template. The resulting three-dimensional architecture is unique in that it is comprised by a continuous network of aligned, interconnected, and hollow Al_2O_3 nanotubes. Additionally, these materials can be fabricated in large-scale dimensions with highly customizable form-factors. Despite the fact that its density is the lowest ever reported for an Al_2O_3 aerogel, the material is mechanically robust, exhibiting elastic recovery response after compression.

Ultralight materials ($\rho \leq 10 \text{ mg cm}^{-3}$) have recently gained widespread attention, and have been realized in many forms including silica (295), and carbon-based aerogels (235, 296), as well as engineered structures such as inorganic micro- and nanolattices (258–260). Porous metal oxides, particularly alumina, are desirable due to their semiconducting and dielectric properties as well as thermal, mechanical, and chemical stability. Historically, monolithic alumina aerogels have been fabricated using sol-gel processes (233, 237, 253). Although this

and other self-assembly methods can produce very high surface area aerogels, they have a moderate low density ($\geq 30 \text{ mg cm}^{-3}$), and little to no control over pore size and structure. To overcome this, templating methods have been developed where sacrificial scaffolds are utilized in conjunction with various deposition techniques to create unique materials with hollow and interconnected pores (4).

A promising templating technique is atomic layer deposition (ALD), which has the unique ability to conformally deposit materials with angstrom-level precision onto large-scale substrates. ALD has been demonstrated to be suitable for coating materials with large surface areas and high aspect ratio features such as aerogels (297, 298). ALD on sacrificial templates including mesoporous block copolymer (263), nanofibrillated cellulose aerogels (262), CNT-based aerogels (5), and nanoporous gold (264), has been demonstrated as a viable means for the production of high surface area films. Following removal of the templates, porous networks of inorganic nanotubes remain, though with random orientation. Aligned networks have been fabricated by ALD of TiO_2 (299), and Al_2O_3 (300), onto vertically aligned carbon nanotube (CNT) arrays or forests, subsequently followed by their oxidative removal, but only in the case of the latter study was the tubular nature of the Al_2O_3 coating preserved after CNT removal. In both cases the final form factor is limited by the dimensions of the CNT array template and the depth to which ALD precursors can diffuse into the high aspect ratio structures. Due to limited precursor diffusion, penetration depth is typically limited to 10s or 100s of micrometers for reasonable process times (38, 272), though infiltration to over 1 mm has been demonstrated (300). Achieving large-scale foams with tunable nanostructure remains a primary challenge.

In the present study, we have employed aligned CNTFs as unique sacrificial templates for the formation of anisotropic, large-scale inorganic nanotube architectures that exhibit the combined characteristics of high surface area, ultralow density, and mechanical robustness. Using ALD, very thin yet conformal coatings were deposited onto the CNTFs, followed by their removal via calcination in air to leave behind an interconnected network of thin-walled and aligned nanotubes. A schematic illustrating the novel processing method is provided in Figure 6.1.

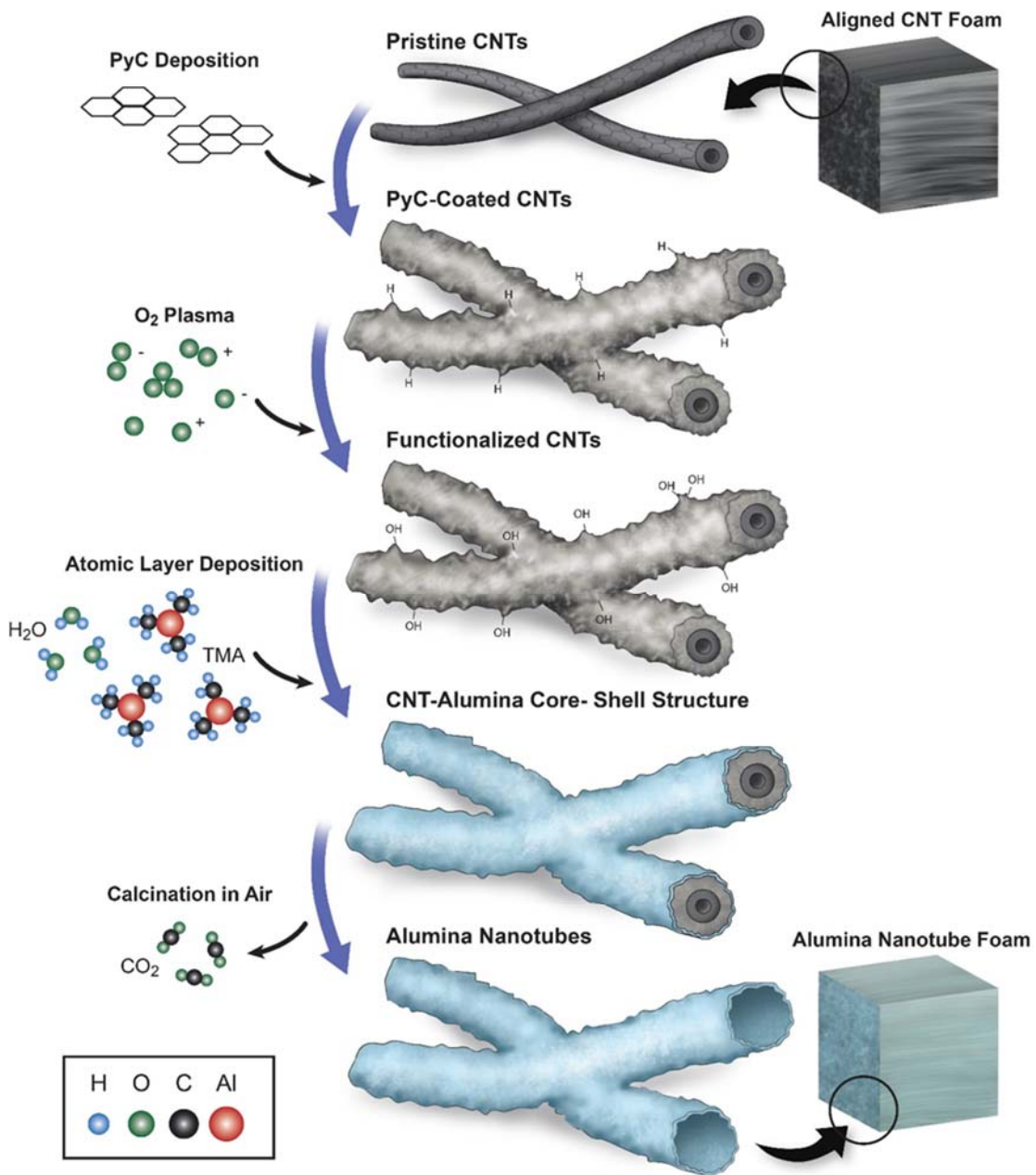


Figure 6.1 Illustration of the processing steps used to synthesize ultralow density aligned Al_2O_3 aerogels. PyC coating of CNTs creates physical crosslinks at CNT junctions which provide elastic response. Oxygen plasma treatment functionalizes the CNTF surface, which allows for very thin yet conformal Al_2O_3 films to be deposited, creating a core-shell structure. The CNTF is easily removed from the Al_2O_3 shell via calcination in air, to leave behind an interconnected network of aligned Al_2O_3 nanotubes.

6.2 Experimental

6.2.1 Materials and Methods

6.2.1.1 Growth of Spinnable CNT Arrays

Spinnable CNT arrays were synthesized using a process based on the chlorine-mediated low-pressure chemical vapor deposition technique.⁽⁴⁹⁾ Arrays were grown on quartz substrates in a custom-built tube furnace at 760 °C and 3 Torr. Acetylene gas (600 sccm, 99.5%, Machine and Welding Supply Company), was used as the carbon source and FeCl₂ powder (anhydrous 99.5%, VWR) was the catalyst. Argon (398 sccm, 99.999%, Machine and Welding Supply Company), and chlorine (1.5 sccm, 99.99%, Custom Gas Solutions) gases were also flowed during the growth process. After 15 minutes, acetylene flow was stopped, and the arrays were left in the argon and chlorine gas flow for an additional 10 minutes. Finally the system was cooled to room temperature under a flow of argon. The resulting arrays were ~1.5 mm tall containing CNTs with an average diameter $\sim 29 \pm 8$ nm.

6.2.1.2 Preparation of Aligned CNT Foam Templates

Spinnable arrays could be easily drawn into thin aligned CNT sheets. To manufacture thick foams, aligned CNT sheets were first drawn from the array and continuously collected around two parallel glass rods rotating at 13 rpm (see Figure S6.6). Once the desired thickness was reached, winding was stopped, and the CNT structures were removed from the glass rods using a razor blade. The CNT assemblies were placed inside a tube furnace, where they were then coated with PyC via chemical vapor infiltration. This method, described in detail elsewhere (268, 269), proceeded by heating the CNT structures in vacuum. At 800 °C acetylene gas was flowed at 600 sccm while the system pressure was regulated at 30 Torr. After 60 min, the system was allowed to cool to room temperature while being purged with argon. After CVI treatment, the CNT foams were cut to the desired size using a laser cutter.

6.2.1.3 CNT Foam Functionalization

Atmospheric pressure oxygen plasma treatment was utilized to functionalize the surface of PyC-coated CNTs, which has been previously shown to enhance nucleation of ALD precursors thus enabling conformal coating (300). The plasma treatment was conducted in a capacitively-coupled dielectric barrier discharge atmospheric pressure plasma system. The custom-built system consists of two parallel Cu plate electrodes (60x60 cm²), with a spacing of 3 cm. The plasma was operated by a 4.8 kW audio frequency power supply at 1.67 kHz. All treatments were carried out for 5 minutes in 1.0% oxygen + 1.0% CF₄ + 98% helium gas mixture (by mass).

6.2.1.4 Synthesis of Metal Oxide Nanotube Foam

ALD of Al₂O₃ was performed in a custom built, hot-wall, viscous flow reactor at a temperature of 120 °C, and an operating pressure of 1 Torr. The metallorganic precursor used was trimethylaluminum (TMA) (98% Strem Chemicals, Inc.), and the oxidizing agent was high purity water (Sigma Aldrich). Ultra-high purity N₂ was used as the carrier gas. The dose and purge times were TMA/N₂/H₂O/N₂ = 0.2/30/0.2/45 sec. This sequence was repeated for 20 cycles, after which there was a final N₂ purge for 120 seconds. Coated foams were converted to pure Al₂O₃ nanotube foams by calcination. Samples were heated to 800 °C in air and allowed to dwell isothermally for 2 hours.

6.2.2 Characterization

6.2.2.1 Structure and Morphology

SEM was conducted on a FEI XHR-Verios 460L field emission SEM. Samples were not sputter-coated prior to imaging. For TEM, a JEOL 2010F field emission STEM was used. Micrographs were recorded using a Gatan Orius digital camera. Bulk density (ρ) was calculated by $\rho = M/V$, where M and V are bulk mass and bulk volume of the specimens. Bulk volume was calculated by $V = l \times w \times h$, where l, w, and h are length, width, and height of the specimens, respectively. Sample dimensions were taken using digital calipers and averaged over three measurements. Masses were measured using a Denver Instrument M-220D balance

with 0.01 mg accuracy. XRD measurements were conducted on a Rigaku SmartLab Bragg-Brentano XRD with a Cu K α radiation source ($\lambda = 1.5418 \text{ \AA}$). Step scans were performed for $2\theta = 10\text{-}80^\circ$ with a step size of 0.05° and scan speed of 3 seconds. Quantachrome Autosorb-1C surface area and pore size analyzer was used for characterizing the BET surface area. All samples were dried in vacuum at 60°C for 12 ~ 38 hours to reach a degassing rate $< 10 \mu\text{mHg/min}$. N₂ adsorption and desorption isotherms were measured at 77 K, and BET surface area was calculated based on the adsorption data within the relative pressure ranging from 0.05 to 0.30. Thermo-gravimetric analysis (TGA) experiments were conducted on a Perkin Elmer Pyris 1 TGA using 5-10 mg of each sample heated at a rate of 10°C/min in air to 800°C , and then isothermally soaked for 30 minutes.

6.2.2.2 Humidity Sensing

Air flows with varying humidity levels were created using the system shown in Figure 6.2. Lab air was filtered and compressed using a ZAG6-1 zero-air generator manufactured by F-DGS. This generator provided the system with a compressed air source with a relative humidity (RH) less than 1% and CH₄, CO, NO_x contaminants less than 50 ppb. Dry, contaminant free air was then supplied at 40 psi to three mass flow controllers (MFCs) and an Owlstone OHG-4 humidity generator.

The OHG-4 consisted of an MFC and bubbler containing distilled water. A split flow and makeup flow, controlled by MFC1 and MFC2, respectively, were connected to the output of the OHG-4 and the relative volume flow rates were adjusted to allow for the generation of air flows with RH levels between 7% - 80% while a constant volume flow rate was maintained. MFC3 was used to control the volume flow rate of the dry air.

The humid and dry air flows were connected to a computer-controlled air switch manifold which routed the air flows to either the sensor chamber or exhaust. The sensor chamber was a milled PTFE. The sensor was placed inside the PTFE chamber and resistance was measured using an Agilent 34410A multimeter. A SHT21 (Sensirion, accuracy $\pm 2\%$ RH) humidity sensor was also placed in the chamber to collect control measurements.

Stability Testing: Dry air with a relative humidity of 8% was allowed to flow into the sensor chamber at 500 mL/min for a period of 3 minutes followed by humid air at 500 mL/min with a relative humidity of 30% for 3 minutes. This was repeated 3 times to measure the repeatability of the sensor.

Response to RH Range: Dry air with a relative humidity of 8% was allowed to flow into the sensor chamber at 500 mL/min for a period of 3 minutes followed by humid air at 500 mL/min with a relative humidity of 20% for 2 minutes. This was repeated 7 times and each iteration, the relative humidity of the humid air was increased by 10% to measure the sensor response to increasing RH.

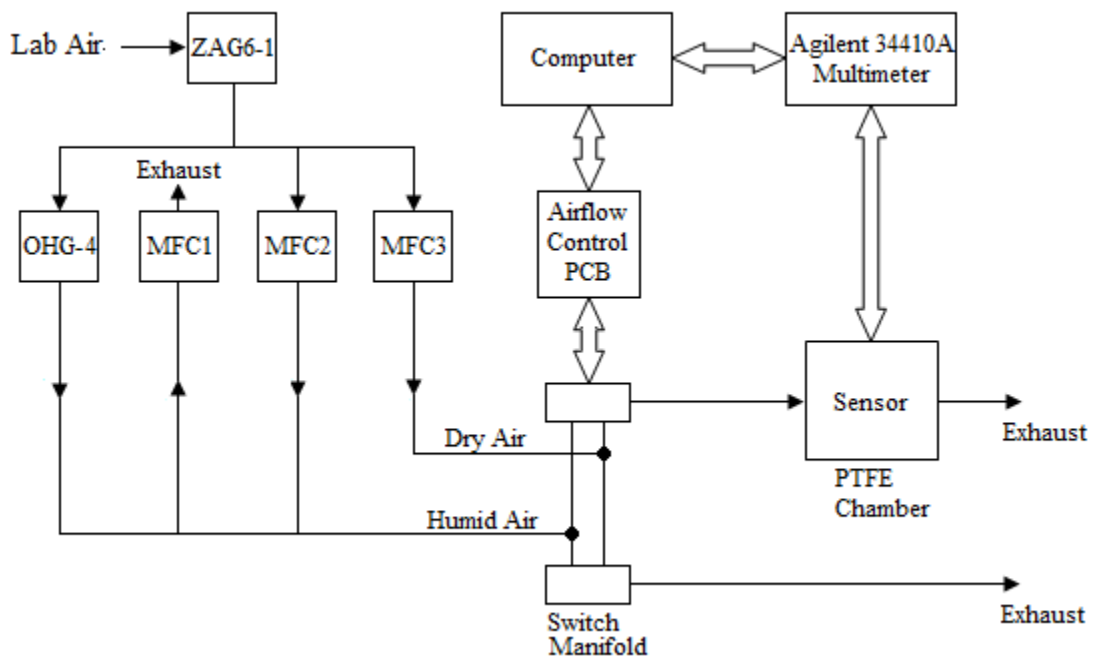


Figure 6.2 Schematic of humidity sensor testing apparatus.

6.2.2.3 Flame Testing

Thermal resistance of the alumina aerogel was measured on a Thermal Protective Performance experimental set-up at the Textile Protection and Comfort Center at North Carolina State University (Raleigh, NC). The aerogel (25 mm (l) x 25 mm (w) x 12 mm (h)) was mounted in a sample holder which consisted of two ceramic plates equipped with adjustable spacers to ensure thickness and density of the aerogel was unaffected. The holder assembly was placed on a stand above the heat source and was protected by a water-cooled shutter before and after the test run. Heat exposure was generated by a flame from two laboratory burners, and was calibrated to 1000 °C.

Heat transferred through the sample was measured by two thermocouples that were placed at the top and bottom (flame-side) surfaces of the aerogel inside the sample holder assembly. Temperature measurements were acquired on a computer interface using a LabView software program at a sampling interval of 0.25 seconds. At the start of the test, the protective-shutter was removed and the sample was continuously fired for 5 minutes before the shutter was closed.

6.3 Results and Discussion

Synthesis of aligned CNTFs, covered in recent work (269), was achieved via chemical vapor infiltration (CVI) of pyrolytic carbon (PyC) onto thick stacks of aligned CNT sheets drawn from spinnable CNT arrays. After 60 minutes of PyC deposition, the average CNT diameter increased from 31 to 78 nm, and the once smooth CNTs were highly roughened due to the thick PyC coating shown in Figure 6.3b,c. Accordingly, the specific surface area (SSA) increased from 40 m² g⁻¹ to 59 m² g⁻¹. The CNTFs exhibit fully recoverable elastic properties, as shown in Figure 6.4a, due to the creation of “physical crosslinks” within the structure which serve to provide a recovery force to compression. Despite their low density (6 mg cm⁻³), they could be easily handled and cut into the desired form-factor by simply using a razor blade or laser cutter.

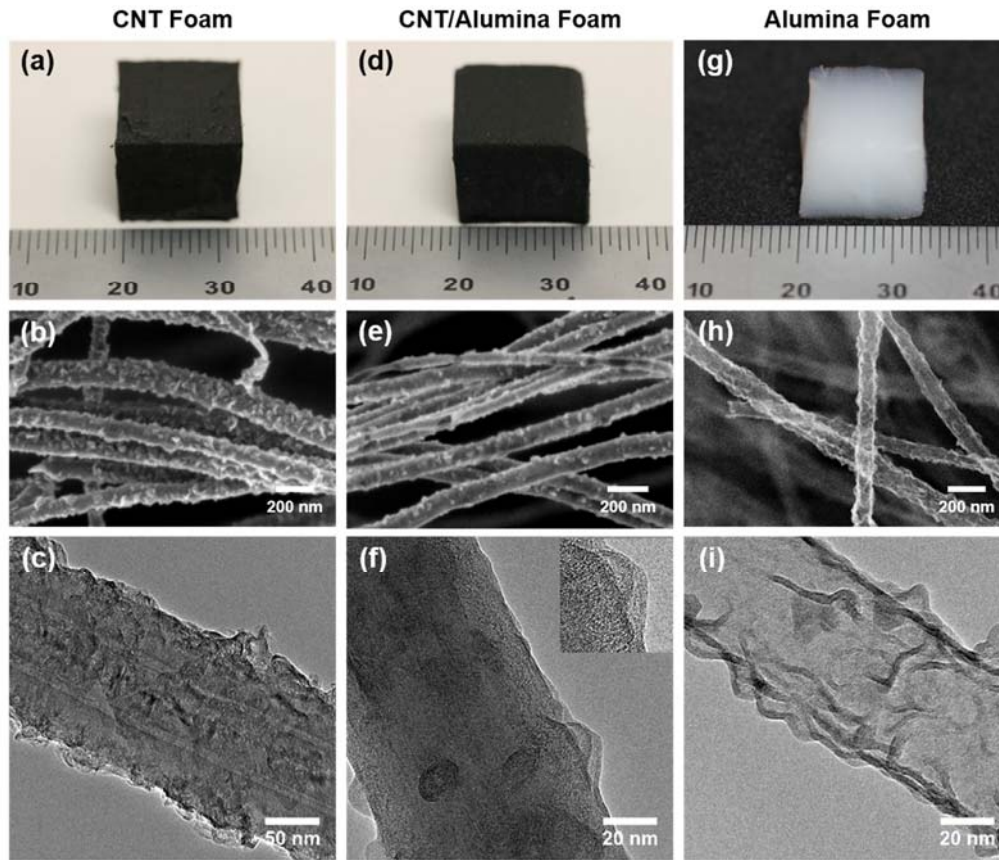


Figure 6.3 Analysis of sample morphology. Photographs, SEM, and TEM micrographs of a-c) CNTF template with significant surface roughness from PyC coating, d-f) CNTF template with 2.5 nm thick Al_2O_3 coating, and g-i) Al_2O_3 aerogel and hollow Al_2O_3 nanotubes following removal of CNTF template via calcination.

Following O_2 plasma functionalization, alumina was deposited on the CNTFs via ALD. After 20 cycles, CNTs were conformally coated with 2.5 nm Al_2O_3 which can be observed in the high resolution TEM images in Figure 6.3f. This thickness correlates well with film thickness measured on a control Si wafer, showing an expected ALD deposition rate of 1.2 $\text{\AA}/\text{cycle}$. ALD coating resulted in a decrease of SSA to $34 \text{ m}^2 \text{ g}^{-1}$, and slight increase in density to 7 mg cm^{-3} . Interestingly, ALD coated CNTFs still exhibited a resilient foam-like recovery after compression, with no apparent permanent deformation.

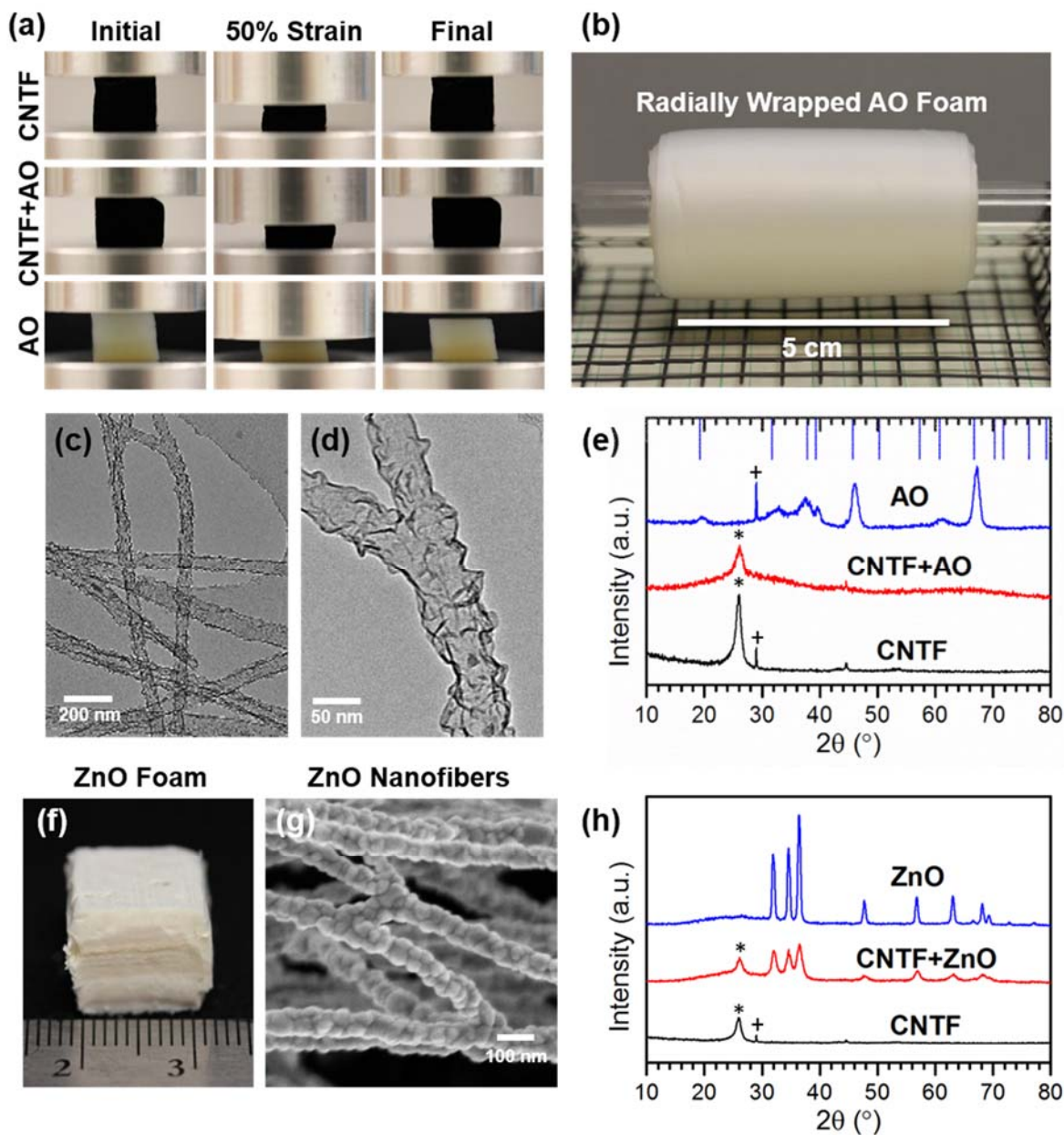


Figure 6.4 Structural characterization and translation of process to other materials. a) Photographs of foams before, during and after compression to 50% strain. Al_2O_3 foams exhibit slight permanent deformation, but all samples recover elastically due to c,d) encapsulation of junctions by ALD coating. b) CNTF wound on quartz rod creates low density insulating layer following ALD coating and calcination. e) XRD spectra showing amorphous nature of ALD alumina and crystallization following calcination. f,g) Photograph and SEM micrograph of ZnO nanofiber foam, made using same process. h) XRD spectra showing as-deposited wurtzite ZnO on CNTF and improvement in crystal structure and grain growth that occurs during calcination. For XRD plots, peaks corresponding to the CNTF and sample holder are depicted by * and + symbols, respectively.

CNTFs were removed via calcination in air, leaving behind a free-standing network of aligned alumina nanotubes, as shown in Figure 6.3g-i. The resulting material had an average density of 1.2 mg cm^{-3} , which is ~ 16 times lower than the previously reported lowest density for an alumina aerogel (5), and among the lowest reported for any inorganic aerogel. Due to the good conformality of the alumina coating and full removal of the CNTF template, the resulting nanotubes had a greatly increased surface area, $265 \text{ m}^2 \text{ g}^{-1}$. Despite the wall thickness only measuring 2.5 nm, the tubular structure and interconnected network of the foam was preserved during calcination. Consistent with traditional aerogels, the alumina nanotube structures were highly translucent (Figure S6.7) due to their low density and nanoscale feature size.

XRD spectra, shown in Figure 6.4e, showed that as-deposited alumina was amorphous which is typical for deposition at low temperatures (100). After calcination in air at $800 \text{ }^\circ\text{C}$ peaks corresponding to the metastable polymorph, $\eta\text{-Al}_2\text{O}_3$, were found to evolve. This is in agreement with TEM images which also showed evidence of lattice fringes from crystallites forming post-calcination (Figure S6.8). Thermogravimetric analysis (provided in Figure S6.9) on coated and uncoated CNTFs showed minimal mass loss before $650 \text{ }^\circ\text{C}$, where the oxidation of CNTs began. The onset of decomposition increased after only 20 cycles of ALD, indicating good conformality of the coating. The final mass remaining at the end of the test was 16%, which correlated well with mass of alumina measured before and after ALD.

Aligned CNTFs make an interesting preform for creating aerogel-like materials. Rather than being cast on a planar substrate or poured into a mold, the CNT sheets can be continuously collected on a mandrel of any size or shape. This processing technique allows for preferential alignment of the CNTs in the foam, and also dictates not only the alignment but also the form-factor of the eventual aerogel following ALD and calcination, as is shown in Figure 6.4b. Because the CNTFs are ultralow density and highly porous, it is possible to conformally coat very large samples ($>10 \text{ cm}$), while still maintaining the nanostructured architecture.

The ALD technique offers additional flexibility as it is capable of depositing a multitude of different materials, including pure metals, other metal oxides, or combinations of layered materials for added multifunctionality. As such, this processing technique can be used

to create aligned nanotube foams out of any material available for ALD. To demonstrate this, a ZnO nanofiber foam was fabricated, and is shown in Figure 6.4f,g. As-deposited films were found to be polycrystalline wurtzite ZnO as shown in the XRD plot in Figure 6.4h. CNTFs were removed during calcination and grain growth occurred, causing the tubular structure to collapse, leaving behind a ZnO foam comprised by aligned and interconnected ZnO nanofibers.

The wetting behavior of the foams is shown in Figure 6.5a-c. As-produced CNTFs exhibit hydrophobic wetting behavior due to their hierarchical surface roughness as well as inert surface chemistry (301). After 20 ALD cycles, the CNTFs becomes wettable, as shown in Figure 6.4b, which can be attributed to the hydroxyl-terminated alumina coating. Rather than the droplet spreading radially across the surface of the ALD coated CNTF, the droplet was instead transported preferentially in the direction of the CNT axis. This wetting behavior and anisotropic transport was also seen for alumina foams, though their macroscopic structure collapsed from the capillary forces created by wetting. Interestingly, the interconnected nanotube network was maintained after wetting, and when the liquid was let to evaporate a thin paper made of aligned Al₂O₃ nanotubes remained.

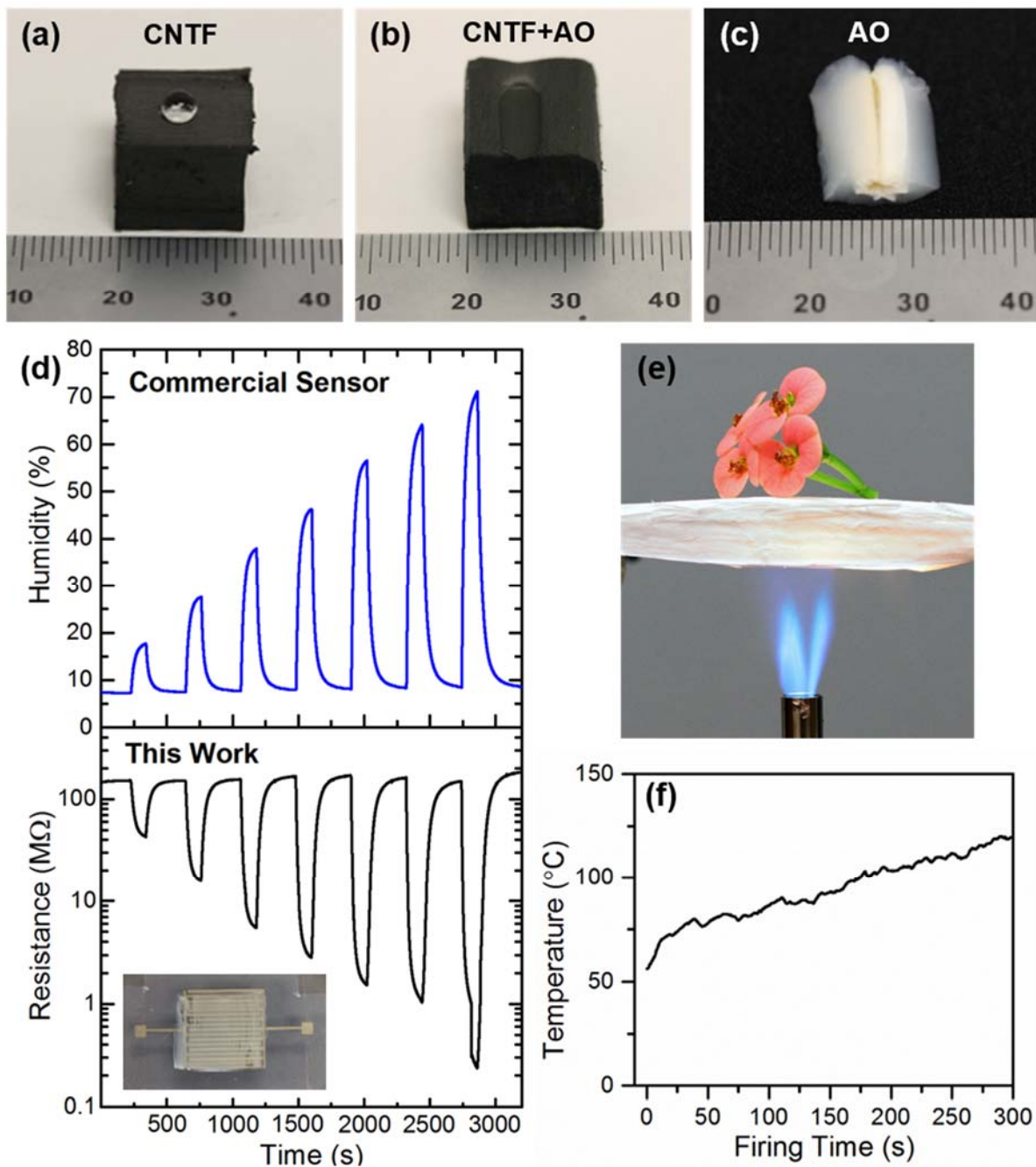


Figure 6.5 Demonstrations of multifunctionality. a-c) Photographs showing different wetting behaviors among un-coated, coated and calcinated foams. d) Humidity-time (top) and Resistance-time (bottom) plots for a commercial humidity sensor and Al_2O_3 nanotube sensor (shown in inset), respectively. e) Photograph depicting high temperature insulating ability of Al_2O_3 aerogel which effectively protects the flower from a propane flame. f) Plot describing temperature rise of the top surface of the Al_2O_3 aerogel over time.

Humidity-sensing devices were fabricated and tested to demonstrate the functionality of the densified alumina nanotube papers and their interconnected tubular structure. Metal oxides are widely utilized as active materials in resistive/capacitive-based sensing technologies due to their ability to operate at high temperatures and harsh environments (302). In particular, alumina is a desirable sensing material due to its high sensitivity at low humidity levels as well as a broad temperature independence (303). In general, surface adsorbed water lowers the impedance or resistance of the sensing material, thus allowing ionic conduction to occur. Using a simple solvent transfer technique, alumina foams were adhered to an inkjet printed interdigitated electrode such that the alumina nanotubes were oriented perpendicular to the electrode fingers. The aerogel sensor was placed in the test chamber and was exposed to different relative humidity levels while resistance across the sensor was measured. A commercially available humidity sensor (SHT21, Sensirion), was also placed in the chamber at the same time for control humidity measurements. As shown in Figure 6.5d, the aerogel sensor resistance response mirrors that of the commercial sensor nearly identically. The overall resistance change from 8-70% humidity spanned over three orders of magnitude, while even for low level humidity changes (8-18%), the resistance was shown to decrease from 152 M Ω to 45 M Ω . The sensor exhibited good stability with little baseline drift and repeatable switching ability, as shown in Figure S6.10.

The nanostructured Al₂O₃ nanotube sensor is desirable due to the large quantity of accessible surface area. Furthermore, the thin-walled alumina nanotube networks exhibit high porosity, which allows for easier diffusion throughout the structure. Interconnected nanotubes which can span across electrodes also aid in performance due to the ability to achieve a continuous water layer for conduction rather than a system with dead-ends. Compared to other metal oxide-based nanostructured sensors, the aerogel sensor exhibited impressive sensitivity to changes in low level humidity (262, 263).

Alumina aerogels are sought after for their high stability and stellar thermal insulation capabilities (233, 238, 255). Flame tests were carried out to evaluate the high temperature insulation capability of the aligned alumina nanotube aerogels. As a demonstration of the thermal insulation, Figure 6.5e shows a fresh flower placed on top of a 10 mm thick aerogel,

suspended over a propane torch. Even after several seconds the flower exhibited no signs of wilting. Despite the fact that the aerogel was fired repeatedly, the alumina aerogel was visibly unchanged with no signs of shrinkage or cracking, indicating superb heat resistance. To quantify this behavior, thermocouples were placed above and below the aerogel to measure the temperature rise through the sample over time. The plot, shown in Figure 6.5f, illustrates that after exposure to a 1000 °C flame for 5 minutes the temperature on the top of the foam increased from 56 °C to 120 °C. Similar tests on mullite fiber felt, a traditional refractory insulator, resulted in a temperature rise of ~250 °C (238).

6.4 Conclusions

In conclusion, we have successfully fabricated free-standing Al₂O₃ nanotube aerogels with an average density of 1.2 mg cm⁻³, which is the lowest reported density for an alumina aerogel to date. ALD of Al₂O₃ on sacrificial CNTF templates followed by calcination yielded a microstructure unique from traditional alumina aerogels. The network of aligned and interconnected nanotubes with high porosity and surface area exhibited elastic deformation behavior, and structural robustness even after wetting. The multifunctionality of the novel material was demonstrated by its utilization as the active material in a sensitive humidity sensor, and also as an effective high temperature thermal insulation material.

Acknowledgements

The authors acknowledge the use of the Analytical Instrumentation Facility (AIF) at North Carolina State University, which is supported by the State of North Carolina and the National Science Foundation. This material is based upon work supported by the National Science Foundation Graduate Research Fellowship Program under grant no. DGE-0946818. The authors would like to thank Dr. Marian McCord for use of plasma equipment, and Dr. Greg Parsons for BET measurements. Finally, the authors would also like to thank Amanda Padbury for assistance with photography and Liz Bradford for scientific illustration of the process schematic.

6.5 Supplemental Information

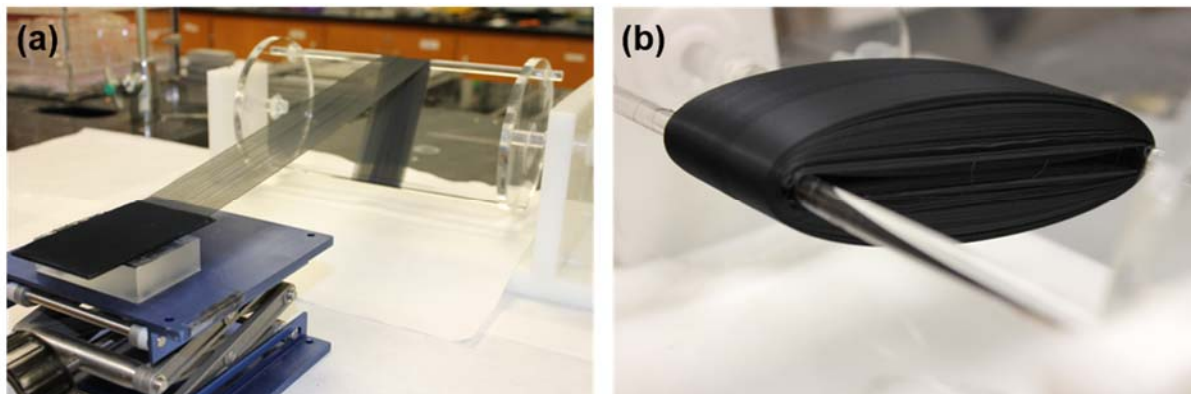


Figure S6.6 Photographs depicting (a) drawing of aligned CNT sheets from a spinnable array which are continuously collected on rotating parallel glass rods. (b) Many layers of stacked CNT sheets accumulated on glass rods.



Figure S6.7 Photograph illustrating the translucent optical behavior of a thick Al_2O_3 nanotube aerogel due to its nanoscale features and high porosity.



Figure S6.8 TEM micrograph of hollow Al₂O₃ nanotubes after CNTF removal. Lattice fringes seen in the tube walls indicate that the amorphous Al₂O₃ began to crystallize during calcination.

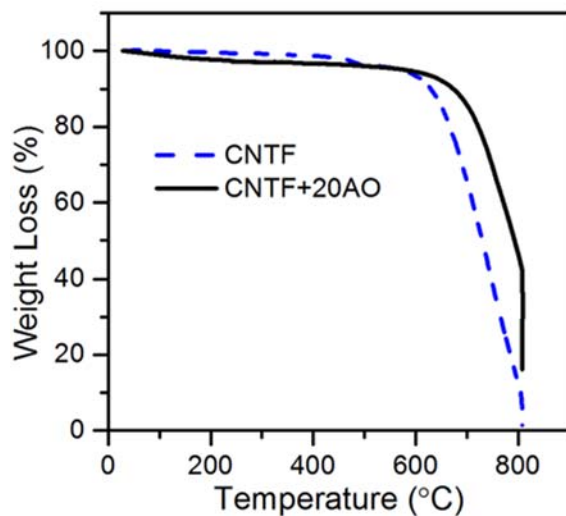


Figure S6.9 Thermogravimetry plot shows that minimal mass loss occurs in either foam until 650 °C, when un-coated CNTFs begin to oxidize. The onset of decomposition for ALD coated foams is shifted slightly higher, indicating good conformality of the coating.

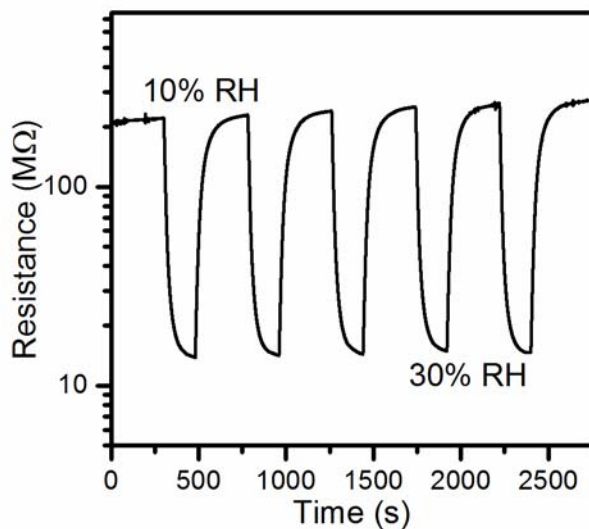


Figure S6.10 Resistance-time curve of the Al₂O₃ nanotube sensor exposed to 5 cycles of switching relative humidity from 10% to 30%.

7 Strong and Resilient Alumina Nanotube and CNT/Alumina Hybrid Foams with Tuneable Elastic Properties

Kelly L. Stano, Shaghayegh Faraji, Ozkan Yildiz, Halil Akyildiz, Jesse Jur, and Philip D. Bradford

ABSTRACT: Excellent chemical and heat resistance combined with the attractive properties of aerogels, including large surface area and low density makes alumina aerogels an attractive material for high temperature catalysis, thermal insulation, and vibration damping. Brittle behaviour, a high propensity to sinter, and poor moisture stability, however, have drastically inhibited the practical use of alumina aerogels produced using traditional methods. Herein, we report the scalable fabrication of low density, anisotropic carbon nanotube (CNT)/alumina hybrid foams synthesized via atomic layer deposition (ALD) on aligned carbon nanotube foams (CNTFs). Calcination of the hybrid foams in air resulted in removal of the CNTFs, leaving behind a free-standing three-dimensional network of interconnected alumina nanotubes. Both CNT/alumina hybrid foams and pure alumina nanotube foams exhibit unprecedented elastic recovery following 50% compression, and possess values for strength and Young's moduli which exceed those of aerogels with similar densities. The scaling behaviour of Young's modulus to foam density for pure alumina foams exhibits a power-law dependence of $n \approx 1.9$, attributed to superb ligament connectivity. These unique structures remain stable to the large capillary forces induced upon liquid infiltration and removal, and can absorb up to 100 times their own weight in water. Furthermore, alumina nanotube foams demonstrate enhanced thermal insulation capabilities at temperature of 1000 °C with no evidence of shrinkage.

7.1 Introduction

Aerogels and related cellular materials are characteristically unique from their solid counterparts due to their high porosity, low density, and large specific surface area. These properties make them desirable for a multitude of applications (304). As a structural ceramic,

alumina and alumina-based materials are highly regarded for their high strength in addition to good chemical and thermal stability. Many of these properties have been shown to translate to low density alumina aerogels, with the exception of mechanical resilience. In particular, studies on the preparation of mechanically robust monolithic alumina aerogels with high heat resistance are limited. Although alumina aerogels are known to have superior heat resistance compared to silica, which sinters above 600 °C (305), their fragility has limited their practical use. High temperature stability and chemical resistance combined with durability would make alumina aerogels attractive for high temperature catalysts and/or catalyst supports, sensors, thermal insulators, structural composites, and many other applications (233, 237, 238).

There are significant challenges, however, associated with producing low density, monolithic alumina aerogels that are mechanically robust and structurally uniform. Even at low strains, most non-silica aerogels, particularly alumina, are notoriously fragile (253). The mechanical properties of porous materials are known to degrade significantly with decreasing density (256). They exhibit a scaling behaviour between modulus and density as well as strength and density described by the relationship $E/E_s \sim (\rho/\rho_s)^n$ and $\sigma_y/\sigma_{ys} \sim (\rho/\rho_s)^n$, where E is Young's modulus, ρ is density, σ_y is yield strength, and s denotes the respective property value of the particular solid material. The power of n is microstructure-specific and describes the deformation mechanisms of the structural components within the cellular architecture (257). Superior mechanical properties can be attained using highly ordered lattices with stretching-dominated geometries which scale more linearly, where $1 \leq n \leq 2$ (256, 258, 259). Cellular geometries featuring either stochastic or periodic porosity that instead deform by bending-dominated mechanisms exhibit a steep scaling behaviour, where $n \geq 2$ (260). Traditional aerogels are known to exhibit even higher scaling behaviours ($n \geq 3$) due to their fractal geometries and disconnected structures (261).

Alumina aerogels have historically been produced using sol-gel methods; though large-scale, un-cracked, and uniform monolithic aerogels are difficult to achieve (233, 238, 253). Furthermore, these techniques afford little control over cellular architecture such as pore size and distribution, particularly for very low densities ($\leq 20 \text{ mg cm}^{-3}$). Alternatively, there has been growing interest in the development of novel methods to produce mesoporous metal oxide

materials with ordered architectures (4). Many of these techniques rely on the use of a template onto which material is deposited, which may be followed by removal of the template.

Atomic layer deposition (ALD) has emerged as a preferred technique for template coating due to its ability to conformally coat high aspect ratio and high surface area nanostructured substrates with continuous thin films at unprecedented levels of precision (110). ALD of alumina on sacrificial templates such as nanocellulose aerogels (262), mesoporous block copolymers (263), and nanoporous gold (264), has resulted in high surface area specimens with unique interconnected nanotubular morphologies, but the resulting aerogels are fragile and have film-like thicknesses. Highly engineered micro and nanolattice geometries have been prepared using ALD to deposit alumina on digitally designed and lithographically fabricated sacrificial polymer templates (258, 259, 265, 266). Lithography-based template preparation, however, limits the minimum attainable feature size resulting in low volumetric surface area. Though proficient in creating optimized architectures, these templates are also limited in their ability to scale-up manufacturing for large-scale foams due to complexity and cost.

Carbon nanotubes (CNTs) are an intriguing alternative to other template materials. Optimization of chemical vapour deposition (CVD) synthesis methods have made it possible to economically produce bulk-quantities of CNTs (267). Moreover, recent advances in processing technologies have led to the creation of various one, two, and three-dimensional large-scale and ordered assemblies including vertically aligned arrays, ribbons and sheets, yarns, and aerogels, sponges, or foams (3). CNT foams (CNTFs) have been manufactured via single-step CVD (301), and multi-step aqueous gel and critical point drying synthesis techniques (234). The resulting foams are porous and high surface area, and are composed of randomly oriented 3D networks of CNTs. Though elastic and compressible, these foams are often low stiffness due to the weak van der Waals interactions at CNT-CNT junctions as well as poor alignment of CNTs in the direction of loading.

In our lab, we have recently developed a technique to produce ultralow density, large-scale, and aligned CNTFs that demonstrate anisotropic mechanical, electrical, and thermal properties (269). This was achieved via chemical vapour infiltration (CVI) of pyrolytic carbon

(PyC) into thick stacks of aligned CNT sheets drawn from spinnable arrays and continuously collected on a rotating mandrel. Varying the duration of CVI treatment allowed for tuning of mechanical properties due to radial growth and thickening of CNT struts, and also encapsulation of CNT-CNT junctions with PyC. This effectively created physical crosslinks in the foam structure which provided a collective restoring force to reverse the compressive strain. The unique properties of these aligned CNTFs make them an interesting template for fabrication of metal oxide foams.

Herein, we report on the fabrication of large-scale pure alumina and CNT/alumina hybrid foams via ALD on aligned CNTFs. The mechanical properties of these foams were investigated as a function of density (controlled by alumina coating thickness), and nanotube alignment. All foams were found to exhibit unprecedented elastic recovery after being compressed to 50% strain, with total apparent recovery for thin-walled specimens. The Young's moduli for these foams exceeded that of any other aerogel with similar density. The scaling behaviour of Young's modulus to foam density for CNT/alumina hybrid foams was found to follow that of CNT aerogels, where $n \approx 2.6$. Pure alumina foams, however, exhibited a power-law dependence of $n \approx 1.9$, attributed to enhanced ligament connectivity and efficient load-transfer.

7.2 Experimental

7.2.1 Materials and Methods

7.2.1.1 Preparation of ACNT Foam Templates

CNT foams were prepared via chemical vapor infiltration (CVI) on ~ 1.3 cm thick stacks of aligned CNTs drawn from spinnable CNT arrays (269). Samples were coated with pyrolytic carbon (PyC) for 60 min at 800 °C and 30 Torr under acetylene gas flow. After CVI treatment, the CNT foams were cut to the desired size using a laser cutter. Atmospheric pressure oxygen plasma treatment was utilized to functionalize the surface of PyC-coated CNTs, which has been previously shown to enhance nucleation of ALD precursors thus enabling conformal coating (300). The plasma treatment was conducted in a capacitively-

coupled dielectric barrier discharge atmospheric pressure plasma system. The custom-built system consists of two parallel Cu plate electrodes (60x60 cm²), with a spacing of 3 cm. The plasma was operated by a 4.8 kW audio frequency power supply at 1.67 kHz. All treatments were carried out for 5 minutes in 1.0% oxygen + 1.0% CF₄ + 98% helium gas mixture (by mass).

7.2.1.2 Synthesis of Alumina/CNT Hybrid Foams

ALD of Al₂O₃ was performed in a custom built, hot-wall, viscous flow reactor at a temperature of 120 °C, and an operating pressure of 1 Torr. The metallorganic precursor used was trimethylaluminum (TMA) (98% Strem Chemicals, Inc.), and the oxidizing agent was high purity water (Sigma Aldrich). Ultra-high purity N₂ was used as the carrier gas. The ALD process began with an N₂ purge of 900 seconds followed by a TMA dose, N₂ purge, H₂O dose, and N₂ purge. The dosing sequence was repeated for the desired number of cycles after which there was a final N₂ purge for 120 seconds. The dose and purge times used in this particular study were TMA/N₂/H₂O/N₂ = 0.2/30/0.2/45 sec. CNTFs were coated for 20, 100, 300, and 500 ALD cycles and samples were designated as CNTF+20AO, CNTF+100AO, CNTF+300AO, and CNTF+500AO, respectively.

7.2.1.3 Synthesis of Pure Alumina Nanotube Foams

CNT foams coated by varying numbers of ALD cycles were converted to pure Al₂O₃ nanotube foams by calcination. Samples were heated to 800 °C in air and allowed to dwell isothermally for 2 hours. Alumina nanotube foams were created from CNTFs coated with 20, 100, 300, and 500 ALD cycles followed by the calcination step. These samples were designated as 20AO, 100AO, 300AO, and 500AO.

7.2.2 Characterization

SEM was conducted on a FEI XHR-Verios 460L field emission SEM. Samples were not sputter-coated prior to imaging. For TEM, a JEOL 2010F field emission STEM was used. Micrographs were recorded using a Gatan Orius digital camera. Bulk density (ρ) was calculated by $\rho = M/V$, where M and V are bulk mass and bulk volume of the specimens. Bulk

volume was calculated by $V = l \times w \times h$, where l , w , and h are length, width, and height of the specimens, respectively. Sample dimensions were taken using digital calipers and averaged over three measurements. Masses were measured using a Denver Instrument M-220D balance with 0.01 mg accuracy. Thermogravimetric analysis (TGA) experiments were conducted on a Perkin Elmer Pyris 1 TGA using 5-10 mg of each sample heated at a rate of 10°C/min in air to 800°C, and then isothermally soaked for 30 minutes. Cyclic uniaxial compression testing was conducted on an Instron 5544 mechanical tester. The load rate was 5 mm/min, and a 100N load cell was used for all samples. Samples were loaded to 50% strain then unloaded, and this was repeated for a total of 5 cycles. Foams were tested in both transverse (nanotube axes perpendicular to load) and longitudinal (nanotube axes parallel to load) directions.

7.3 Results and Discussion

Pristine stacks of aligned CNTs were easily and permanently deformed due to limited ligament connectivity and insufficient energy to overcome the van der Waals adhesion forces generated from compression and increased CNT-CNT contact area. In contrast, PyC deposition on CNT stacks resulted in radial growth of CNTs and encapsulation of CNT bundles and CNT-CNT junctions, essentially creating a three-dimensional interconnected network of aligned CNTs. Foam-like recovery observed in these samples was attributed to the newly created physical crosslinks which provided increased capacity for energy storage upon compression which provided a recovery force larger than accumulated van der Waals adhesion forces (269). Additionally, CNTFs featured enhanced processability and could be easily cut to the desired dimensions using a razor blade or laser cutter. The ability to precisely machine the templates in the manner is a highly unique feature of this process, as complex sub-millimetre architectures with controlled depth profiling can be generated.

Atmospheric pressure oxygen plasma treatment was employed to functionalize the inert CNTF surface, and encourage dense nucleation of ALD precursor molecules. As a result, continuous alumina films measuring only 2.5 nm thick were found on the CNTF surfaces after only 20 ALD cycles (Figure 7.1a,b, and g). Additionally, due to good conformality of the coating CNT-CNT junctions were also coated and preserved in the structure. The use of ALD,

combined with highly porous ultralow density CNTF templates allowed for large-scale samples to be fabricated without sacrificing uniformity. Due to its sequential and self-limiting reactions, ALD is highly regarded for producing precisely thick coatings on high aspect ratio and high surface area substrates. Nanoporous templates with very high aspect ratios, however, have an upper limit for practically achievable dimensions (on the order of 10s – 100s of micrometres) due to limited precursor diffusion within their highly tortuous structures (263, 264, 306). Although the largest samples we have currently produced measure ~ 13 cm (l) x 8 cm (w) x 1.5 cm (h), commercial CVI and ALD equipment could readily scale our method for the production of truly bulk quantities.

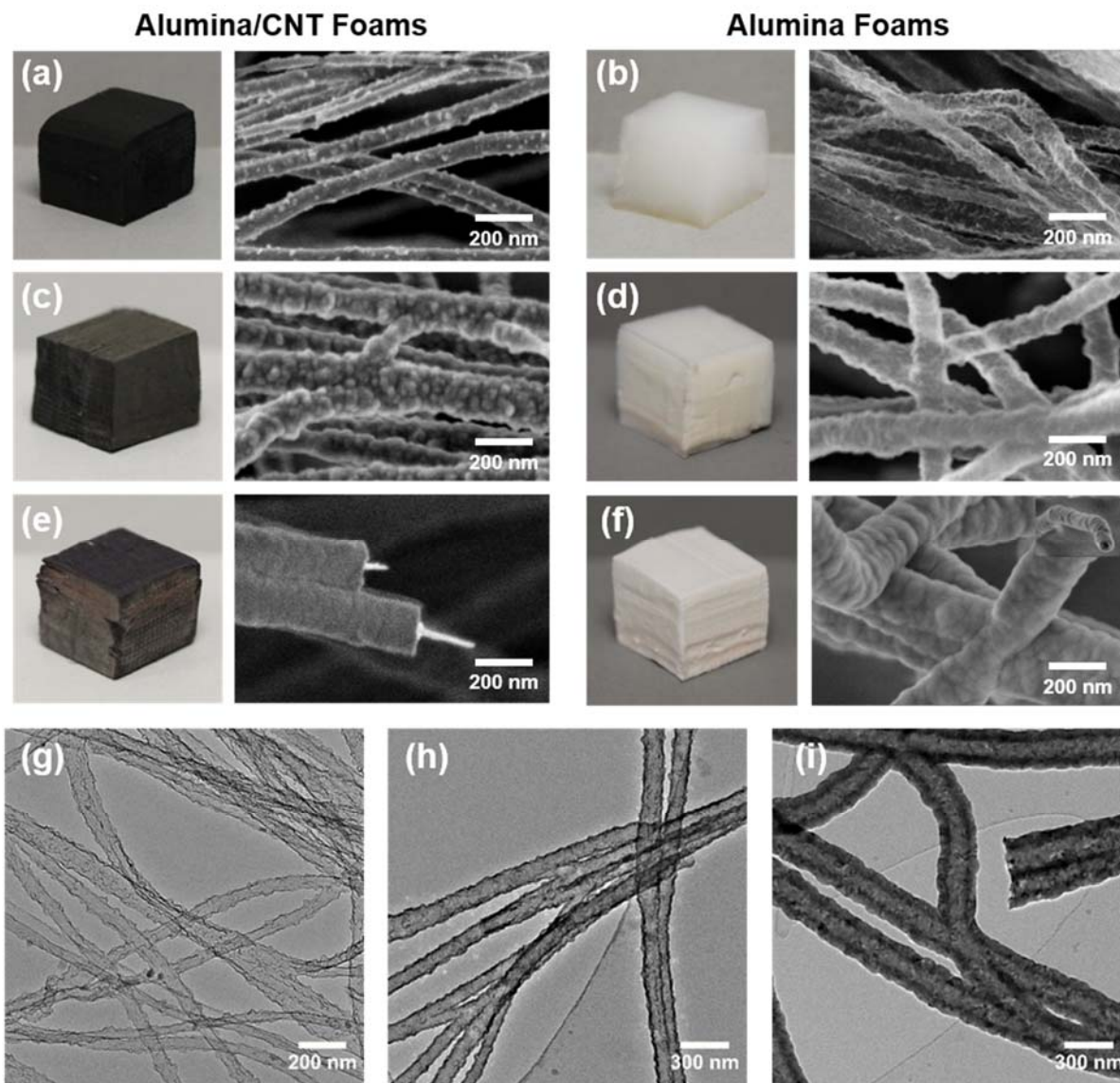


Figure 7.1 Analysis of sample morphology. Photographs and SEM micrographs of (a) CNTF+20AO, (b) 20AO, (c) CNTF+100AO, (d) 100AO, (e) CNTF+500AO, and (f) 500AO. TEM micrographs depicting hollow and interconnected alumina nanotube structures for (g) 20AO, (h) 100AO, and (i) 500AO.

The thickness of alumina was easily controlled by varying the number of cycles as shown in the SEM micrographs provided in Figure 7.1. Alumina film thicknesses measured 12 and 63 nm for 100 and 500 cycles, respectively, corresponding to a growth rate of 1.2 Å/cycle which correlated well with the film thickness measured from a control Si wafer using ellipsometry. CNTFs were oxidatively removed via calcination in air, leaving behind an interconnected network of hollow alumina nanotubes. The tubular morphology as well as coated junctions were maintained for all coating thicknesses studied, which is visible in the TEM micrographs provided in Figure 7.1g-i. As-deposited alumina was determined to be amorphous while removal of CNTFs through calcination resulted in crystallization of the alumina to form η -Al₂O₃ (307).

The plot in Figure 7.2 illustrates that the density of alumina/CNT foams and pure alumina foams increased linearly with the number of ALD cycles and spanned ranges of ~ 6-45 and ~ 1-40 mg cm⁻³, respectively. The lowest density achieved, 1.2 mg cm⁻³, is the lowest for an alumina aerogel reported to date, and is among the lowest overall for any inorganic material (260, 295). Even the highest density demonstrated in this work (39 mg cm⁻³), is lower than that of alumina aerogels fabricated using sol-gel methods (233, 238, 253). Thermogravimetric analysis, provided in Figure 7.2, revealed that alumina coated CNTFs exhibited good thermal stability with minimal weight loss at low temperature. The onset of decomposition from CNT oxidation increased with coating thickness, confirming conformal coverage. Additionally, the mass % remaining at the end of testing for each sample correlated well with the actual mass of ALD added as measured by a microbalance.

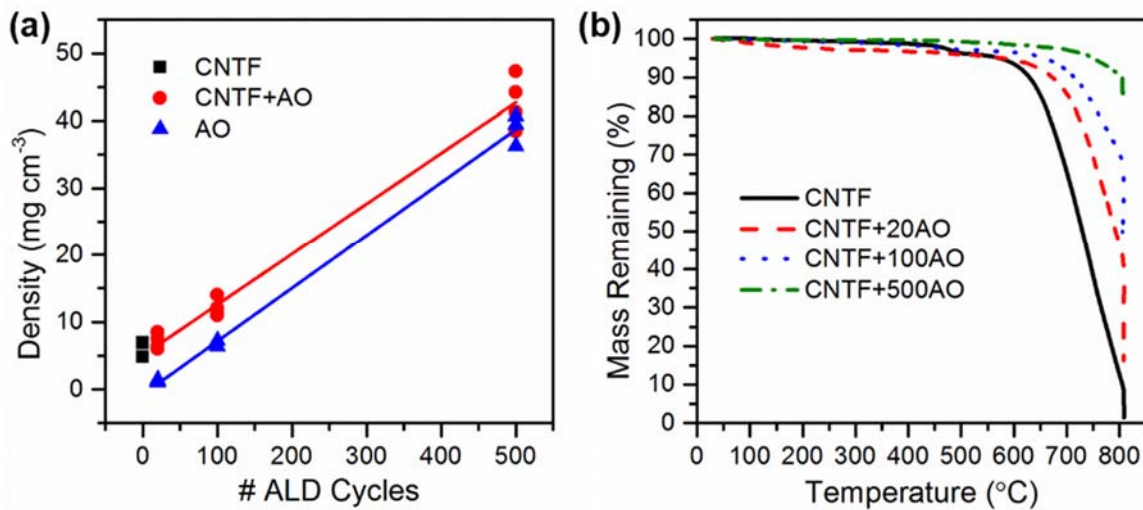


Figure 7.2 (a) Linear dependence of CNTF/alumina and alumina foam density on # of ALD cycles. (b) Mass loss as a function of temperature for CNTFs coated for 0, 20, 100, and 500 cycles of ALD.

7.3.1 Compression Testing

Pure alumina nanotube and CNT/alumina composite foams were compressed in transverse and longitudinal directions to characterize their mechanical properties. Representative stress-strain curves for each sample are provided in Figure 7.3. The mechanical response transitioned from elastomeric for thin-walled and hybrid foams to elastic-brittle behaviour for thick-walled and pure alumina foams. Low density foams demonstrated super-compressibility and tuneable elastic behaviour. During transverse compression, the nanotube axes were oriented perpendicular to the direction of loading. All samples tested in this orientation, including composite foams and pure alumina nanotube foams, exhibited some degree of elastic recovery following compression, though recovery was maximized for thin-walled CNT/alumina nanotube foams.

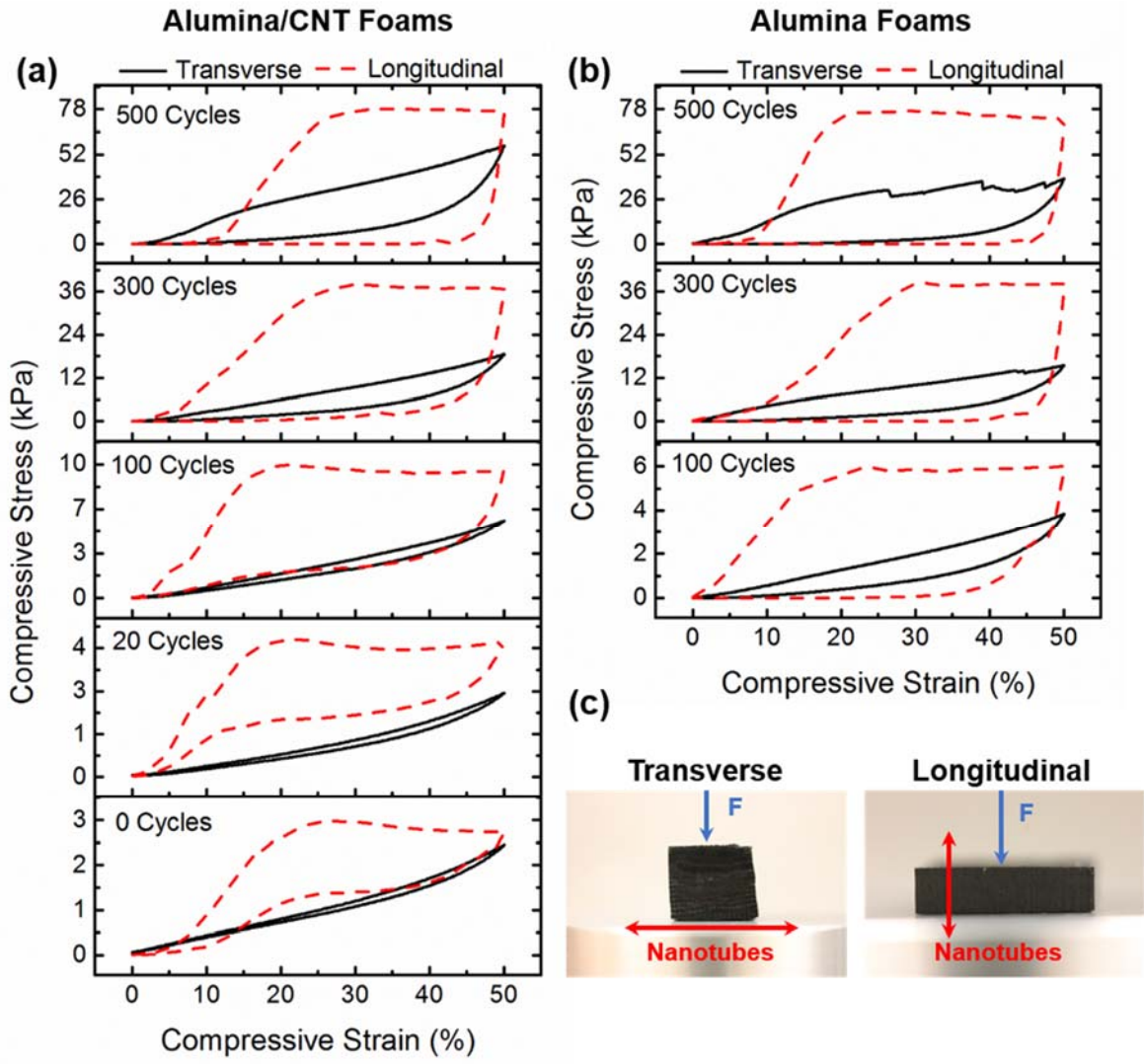


Figure 7.3 Compressive stress – strain curves from first cycle of testing (a) alumina/CNT foams and (b) alumina nanotube foams in both transverse and longitudinal directions. Schematic provided in (c) to illustrate nanotube alignment relative to direction of compressive load.

This is an interesting result, because elastic recovery behavior in a pure ceramic foam or aerogel is unprecedented. Typically, aerogels must be modified through the addition of flexible organic polymers to the surface to provide mechanical reinforcement (232). For a material which may find application in high temperature environments, this is obviously not the best solution. CNT/alumina foams coated for 20, 100, and 300 cycles as well as pure

alumina 100 cycle foams deformed elastically up to 50% strain. The stress-strain curves from 300AO and 500AO displayed evidence of “strain bursts” which correlate to brittle failure events leading to permanent deformation. Larger strain bursts were measured for thicker-walled samples likely due to their increased capacity for storage of elastic strain energy compared to thinner-walled samples.

In longitudinal compression the nanotube axes were oriented parallel to the direction of loading. All samples initially exhibited linearly elastic deformation until yield. Thin-walled CNT/alumina nanotube foams coated for 20 and 100 cycles underwent ductile-like deformation characterized by the plateau region of the stress-strain curve. These samples exhibited total elastic recovery after 50% compressive strain, indicating that the additional deformation after yield was accommodated by elastic modes such as tube bending and wrinkling (258). Even CNT/alumina foams coated for 300 cycles recovered to 85% of their original height. In contrast, thick-walled CNT/alumina nanotube foams (500 cycles) and all pure alumina nanotube foams behaved in a more brittle manner with only moderate recovery after longitudinal compression. Following yield, these foams plastically deformed through non-recoverable node breakage and tube fracture.

The fatigue behavior of the foams was evaluated from cyclic compression tests, and representative stress-strain curves for 100 cycle alumina and CNT/alumina foams are presented in Figure 7.4 (cyclic compression tests for other samples may be found in

of Supplemental Information). Curves from subsequent compression cycles, particularly for denser foams, exhibited a pseudo hardening behavior where slope rapidly increased with small strain. This can be attributed to the densification of the structure upon deformation. Although energy absorption degraded quite significantly for most samples following the initial cycle, moduli and maximum stress decreased only slightly. For the remainder of testing, however, all mechanical properties were shown to stabilize.

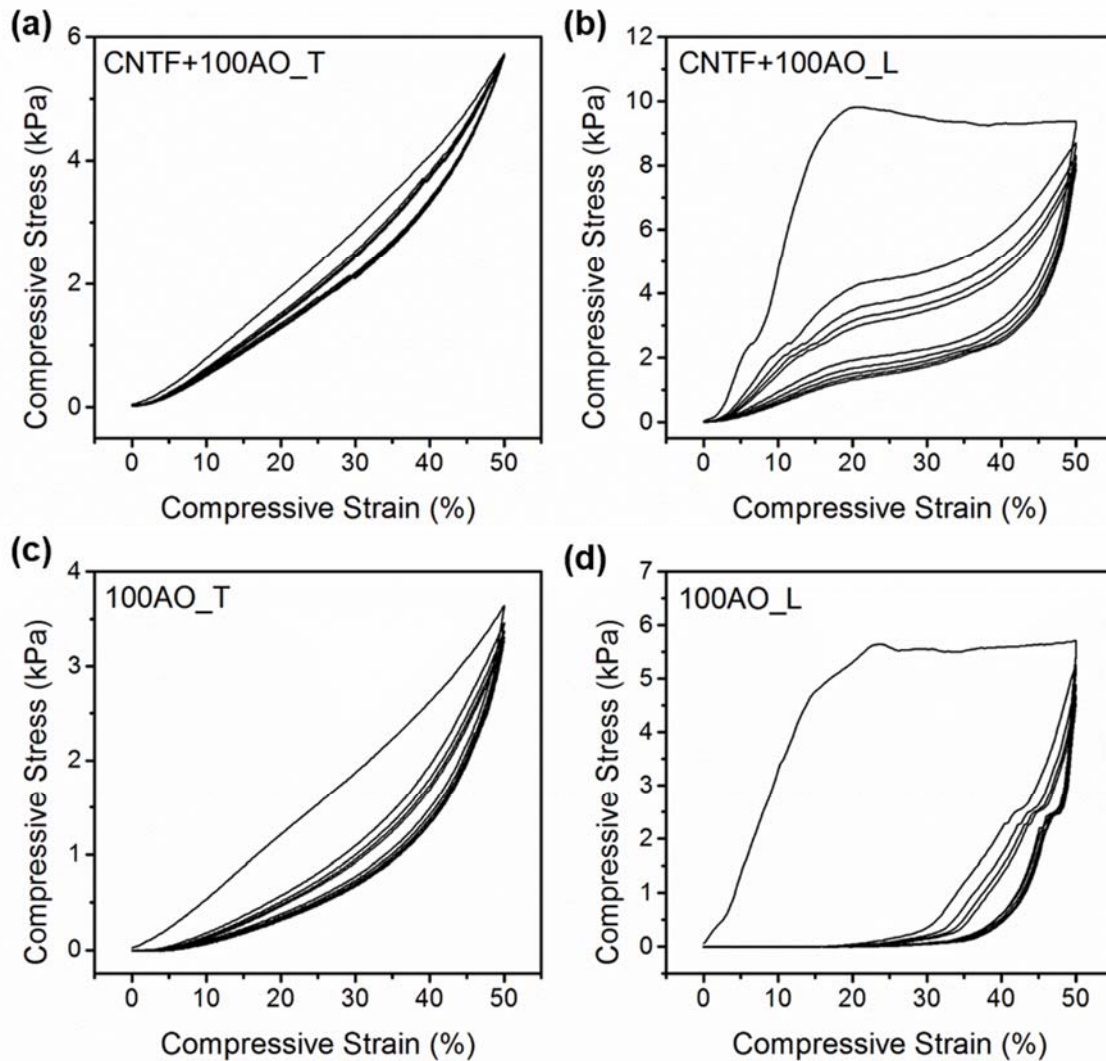


Figure 7.4 Cyclic compression behavior for CNTF+100AO in (a) transverse, and (b) longitudinal directions as well as 100AO in (c) transverse, and (d) longitudinal directions.

For quantification of mechanical properties, E was calculated from the initial slope of the unloading curve and strength was determined to be the maximum value of stress on the stress-strain plot. For all samples, modulus increased with the number of ALD cycles. The moduli of pure alumina and CNT/alumina composite foams were the same for a given coating thickness. Specific modulus, however, was higher for all alumina foams due to their lower

density from CNT removal. This effect was much less pronounced upon increasing the number of ALD cycles since the CNTs make up a smaller fraction of the total density for thicker alumina coatings.

The log-log plots provided in Figure 7.5 examine the relationships between compressive modulus, compressive strength, and density. We discovered that alumina nanotube foams exhibited power law scaling behaviors of $E_T \sim \rho^{1.7}$ and $E_L \sim \rho^{1.9}$. For cellular geometries with bending-dominated deformation mechanisms a scaling factor of 2 indicates perfect connectivity of the ligaments, and thus efficient load transfer (257). Aerogels typically exhibit scaling factors greater than 3 attributed to their “pearls on a string” microstructure which provides poor ligament connectivity (261). The scaling behavior of CNT/alumina composite foams was steeper, with $E_T \sim \rho^{2.2}$ and $E_L \sim \rho^{2.5}$. Similar scaling factors have been reported for both pure CNT (308, 309), and composite CNT aerogels (5), as well as alumina coated CNT arrays (310). As the scaling exponent is related to ligament connectivity, it is possible that pure alumina foams possess enhanced connectivity as a result of film sintering and crystallization which occurs during calcination. SEM images of 100 cycle coated samples before and after CNT removal show that as-deposited alumina is rough and nodular, whereas calcinated films are smooth due to particle sintering.

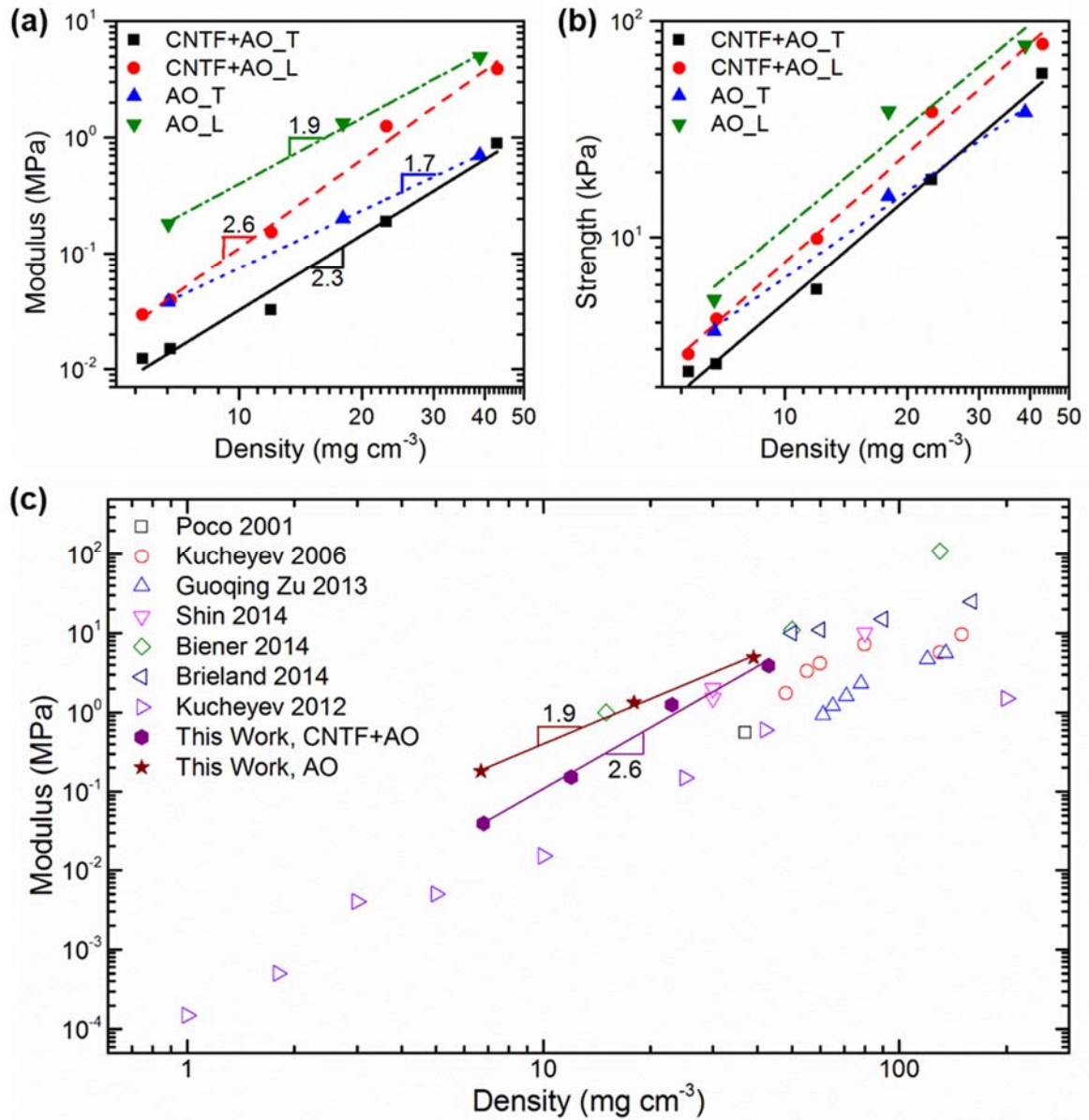


Figure 7.5 Evaluation of mechanical properties. (a) Modulus and (b) strength as a function of density for CNT/alumina and alumina nanotube samples in transverse and longitudinal directions. (c) To benchmark the materials produced in this study, modulus as a function of density for other foams with similar densities was also plotted.

Figure 7.5c provides the modulus-density relationships from data published on other aerogels and foams with similar densities. All of our foams match or exceed the other moduli, particularly in the ultralow density regime where our 100 cycle alumina foam had a modulus one order of magnitude higher than that from a silica aerogel of similar density (295). Strength-density relationships were equally impressive. 500 cycle pure alumina and CNT/alumina hybrid foams with densities less than 40 mg cm^{-3} had strengths near 80 kPa, whereas a commercially available isotropic aluminium foam with twice the density only had strength of 20 kPa (311).

7.3.2 Wetting Behavior and Liquid Absorption Capacity

A benefit to the fabrication of mechanically robust CNT/alumina and alumina foams is the added stability to moisture and heat. Metal oxide aerogels typically possess hydroxylated surfaces which result in their being extremely hydrophilic. For many materials this would not be an issue except that, in the case of an aerogel, the strong capillary forces generated upon wetting are often enough to cause catastrophic rupture (312). One route to overcome this deficiency is to make the aerogels hydrophobic, which is commonly accomplished by modification of the sol-gel chemistry, or by coating the aerogel with a polymer.

Instead, we demonstrate here that both hybrid and pure alumina foams can be wet without harming their structure. Photographs in Figure 7.6 illustrate the wetting behaviors of the foams. Due to their anisotropy, a water droplet placed on the surface spreads preferentially in the direction of the nanotube axes. This response was observed in all samples, but most visibly apparent in Figure 7.6a,b. Despite the fact that the lowest density sample (20AO, Figure 7.6c) was densified by the droplet, it was found that a gel network formed where the previously existing interconnects were maintained. Upon drying, an alumina nanotube paper was formed. Higher density alumina foams made from 100 and 500 cycle samples remained structurally stable upon wetting. The 100AO foam initially flattened where wet, but as more droplets were added, the foam gradually expanded until it regained its full volume. Photographs in Figure 7.6d,e depict fully saturated CNTF+100AO and 100AO foams. Finally, after drying in an oven the foams retained their structural integrity with minimal shrinkage.

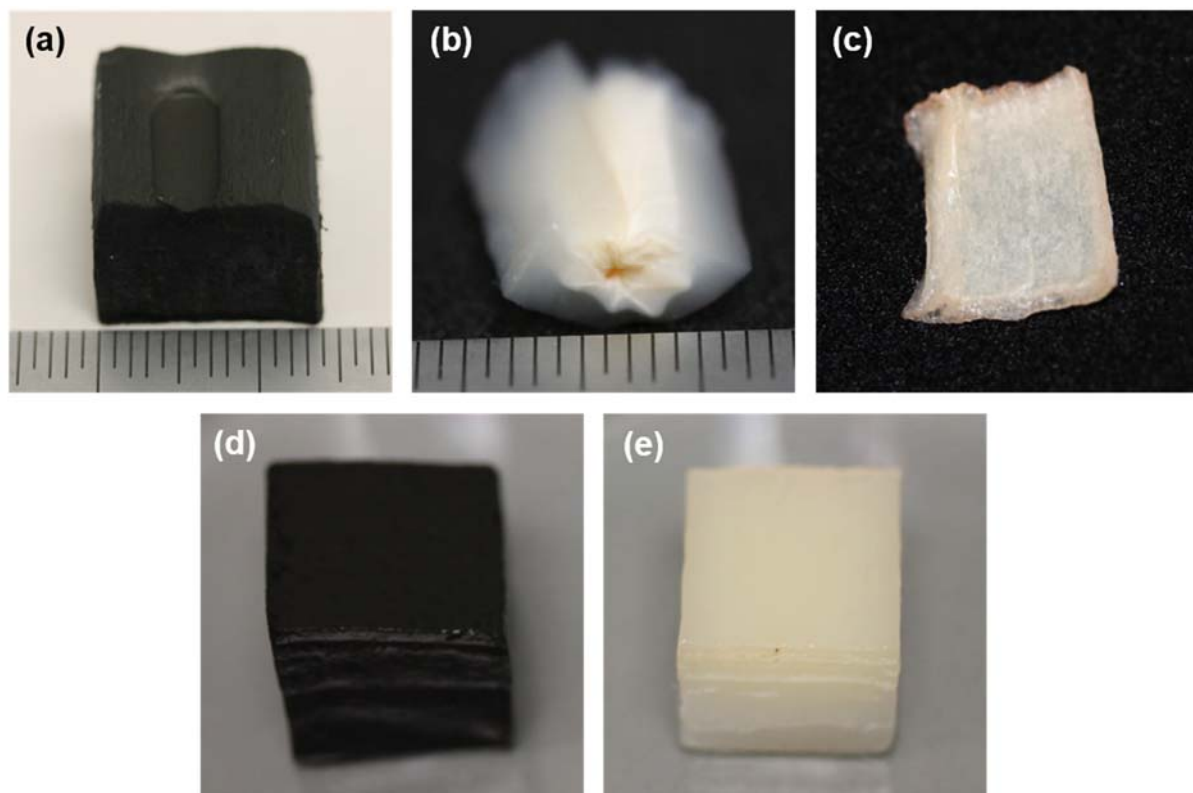


Figure 7.6 Anisotropic wetting behavior is shown for (a) CNTF+20AO and (b) 20AO foams. (c) Densified 20AO foam remains intact and forms a film. Fully saturated (d) CNTF+100AO and (e) 100AO foams.

The liquid absorption capacity of 100 and 500 cycle CNT/alumina hybrid and pure alumina foams was measured by weighing them dry, and then gradually adding water until they became saturated. The 100AO foam had the largest absorption capacity, holding almost 100 times its own weight in water. This was followed by CNTF+100AO which held 77 times its weight. Likely due to decreased free volume, both 500 cycle samples only absorbed about 27 times their weight in water. This ability for these foams to retain stability upon wetting has implications for liquid filtration as well as aqueous-based processing routes like solution infiltration or electrochemical deposition.

7.3.3 Thermal Stability

Following the removal of CNTFs via calcination in air at 800 °C, sample dimensions were measured to check for shrinkage. While the width and height did not change, there was some shrinkage along the direction of the nanotube axis. Though not perceptible by eye, the foam lengths decreased by 2, 6, and 3 % for 20AO, 100AO, and 500AO foams, respectively. The thermal insulating ability of alumina foams was evaluated using a flame test. Foam blocks were placed over a flame source and then continuously fired for 5 minutes with a 1000 °C flame. Temperature rise on the top surface of the foams was measured with a thermocouple, and was plotted as function of time, as shown in Figure 7.7. The 500AO foam demonstrated the best performance with a total temperature rise of 45 °C. 20AO and 100AO foams rose 63 and 69 °C, respectively. Furthermore, the alumina foams exhibited no signs of damage caused by shrinkage or sintering from continuous high temperature exposure.

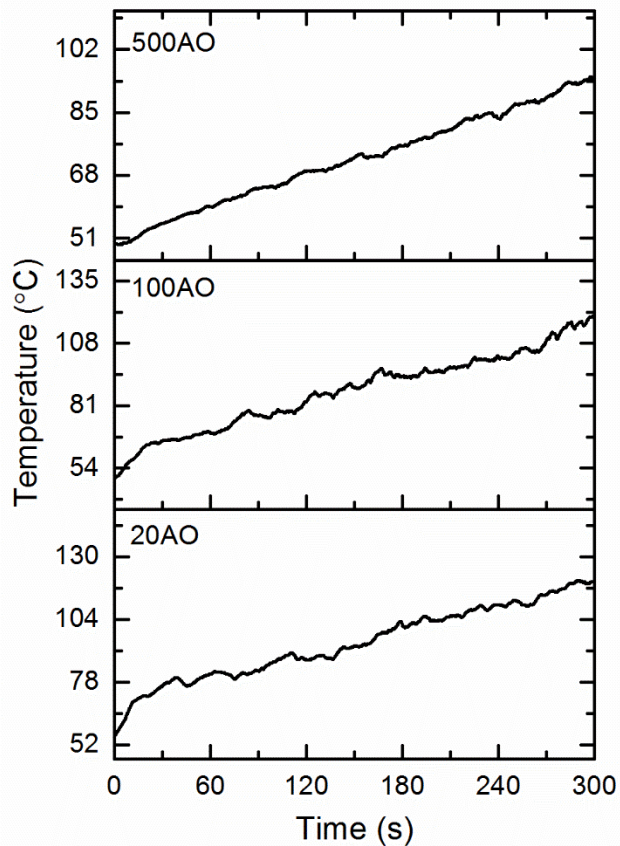


Figure 7.7 Thermal insulating performance was evaluated by measuring the temperature rise over time for 20, 100, and 500 cycle alumina nanotube foams subjected to 5 minutes of continuous firing from a 1000 °C flame.

7.4 Conclusions

Hybrid alumina/CNT and pure alumina nanotube foams with ultralow densities were produced via ALD on CNTF templates. The foams exhibited unique anisotropic mechanical properties due to a high level of alignment among the nanotubes. Foams demonstrated unprecedented elastic recovery following compression and exceed some of the highest strength and modulus values for any type of foam with similar density. Pure alumina foams were shown

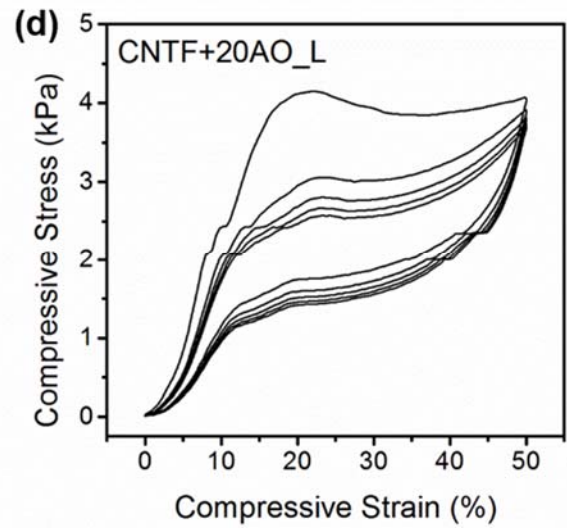
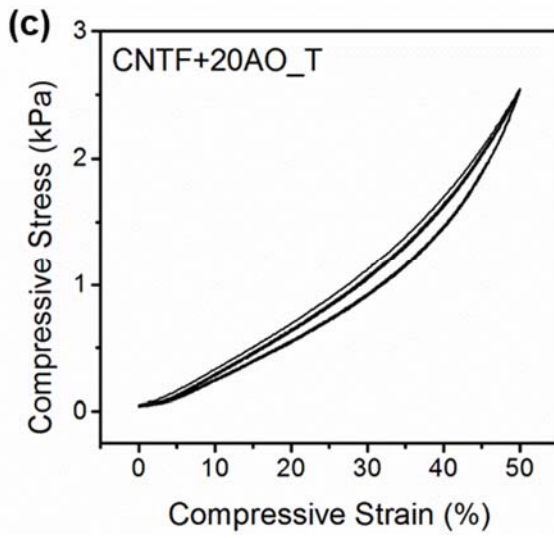
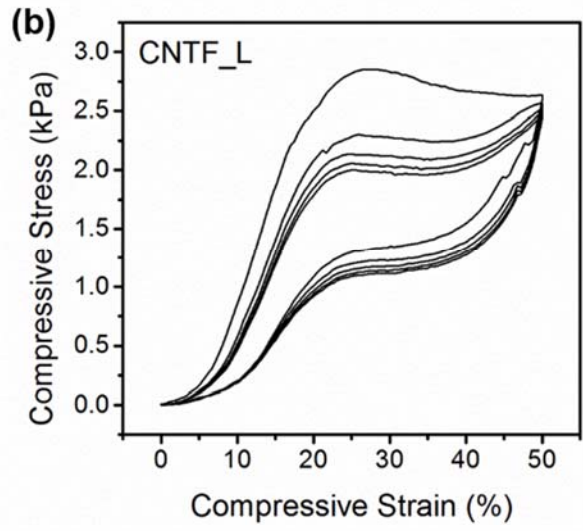
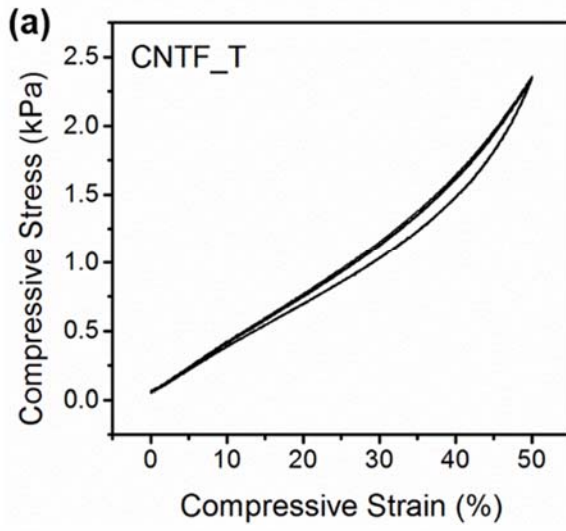
to have a density-modulus scaling dependence of 2, indicating superior ligament connectivity and efficient load transfer. Finally, foams exhibited impressive thermal stability and insulating properties as well as high durability for liquid filtration and drying.

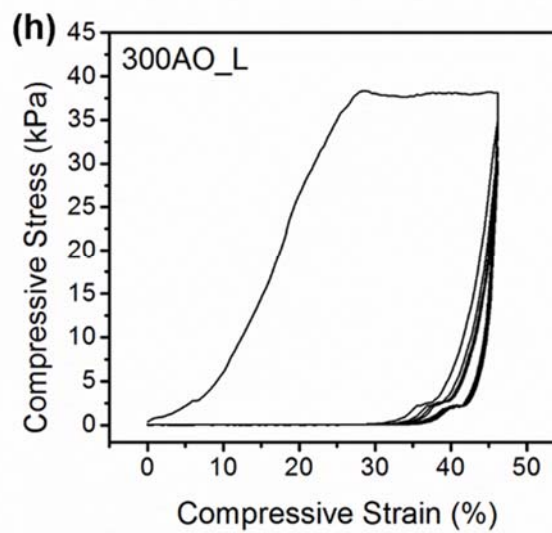
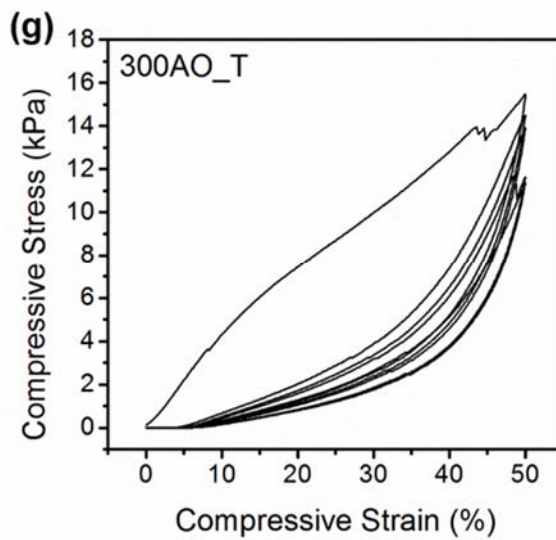
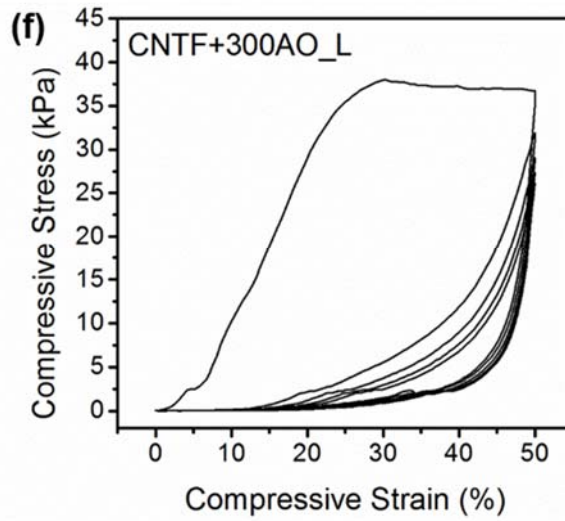
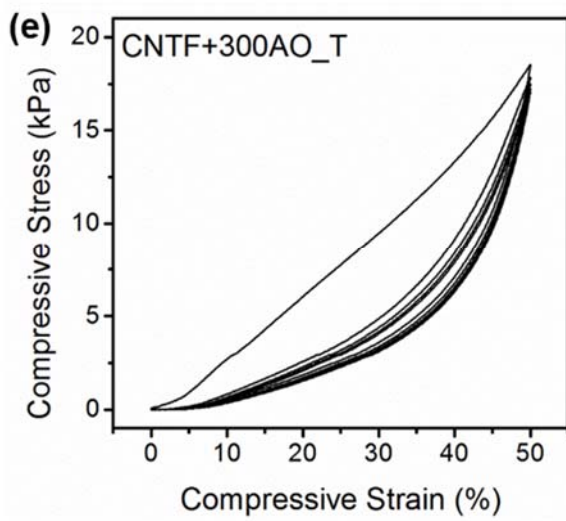
Acknowledgements

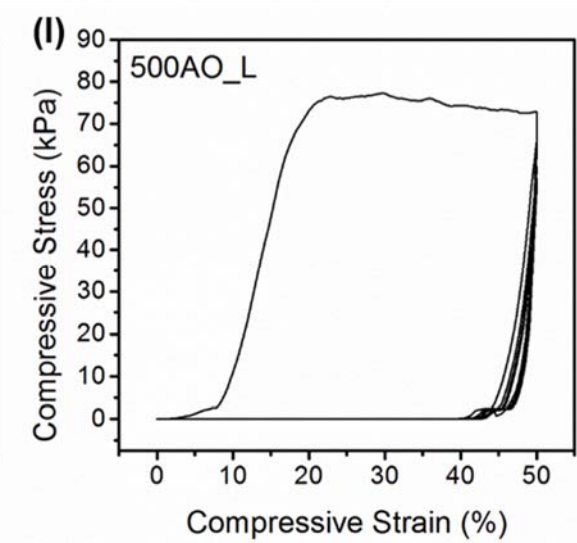
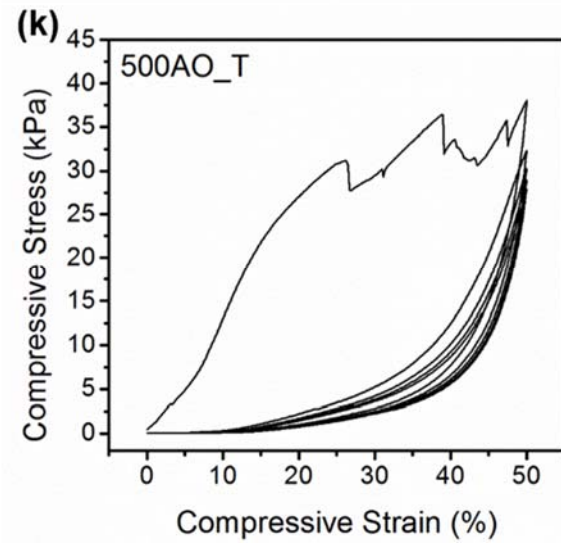
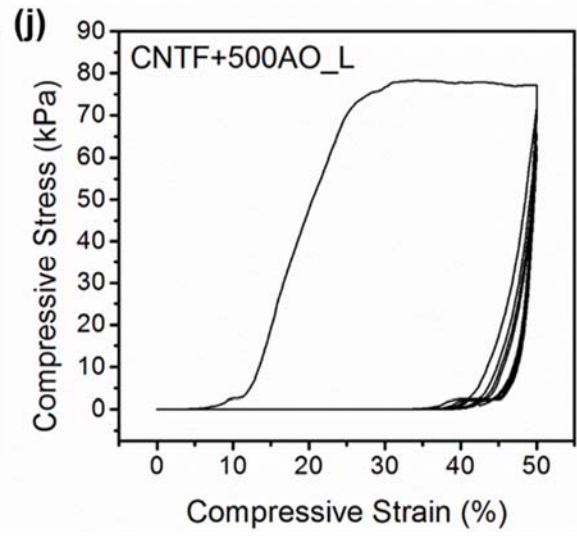
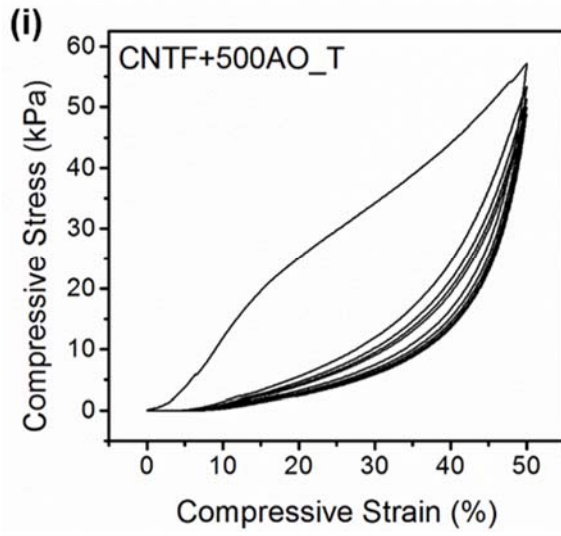
The authors acknowledge the use of the Analytical Instrumentation Facility (AIF) at North Carolina State University, which is supported by the State of North Carolina and the National Science Foundation. This material is based upon work supported by the National Science Foundation Graduate Research Fellowship Program under grant no. DGE-0946818. The authors would like to thank Dr. Marian McCord (NCSU) for use of the plasma equipment, Dr. Russell Gorga (NCSU) for use of the Instron.

Supplemental Information

Figure S7.8 Cyclic compression behavior for CNTF in (a) transverse, and (b) longitudinal directions, CNTF+20AO in (c) transverse, and (d) longitudinal directions, CNTF+300AO in (e) transverse and (f) longitudinal directions, 300AO in (g) transverse and (h) longitudinal directions, CNTF+500AO in (i) transverse and (j) longitudinal directions, and 500AO in (k) transverse and (l) longitudinal directions.







8 Final Conclusions

Research discoveries surrounding the intersection of two technologies—the assembly of CNTs into large-scale architectures, and the application of ALD to create CNT-inorganic hybrids—have only begun to be explored. The ability to economically scale production of CNT assemblies has expanded the potential realm of applications for CNT-inorganic hybrids beyond the nanoscale. The objectives of this research were to explore the use of ALD on novel CNT assemblies, prepare CNT-metal oxide hybrid materials, and critically evaluate their structure-property relationships in order to develop an understanding of the applications for which they are best suited. Conclusions generated from the body of this work follows:

- ALD is a useful technique for the uniform and conformal coating of high surface area and high aspect ratio CNT arrays, but not without first optimizing the sample and process parameters for best results. The surface chemistry of high graphitic quality, low defect density CNTs was optimized for Al₂O₃ nucleation via PyC deposition and oxygen plasma functionalization. The combination of these two surface pre-treatments provided a high concentration of oxygen-containing functional groups that could complex with TMA upon dosing, thus creating a high nucleation density of Al₂O₃ on the CNT surface which then quickly spread and coalesced into a thin film. Furthermore, a uniform distribution of Al₂O₃ through the thickness of the array was achieved by removing the CNTs from the growth substrate and orienting the CNT axes parallel to the flow of the reactor. It was determined that the Al₂O₃ coated CNTs not only exhibited greatly enhanced compressive properties, but also improved thermal stability to oxidation by delaying onset nearly 100 °C.
- Alumina deposited via ALD on plasma functionalized CNTFs was determined to be amorphous, though calcination in air at 800 °C resulted in oxidation and removal of carbon as well as alumina phase transformation to η-Al₂O₃. High temperature annealing of CNT-alumina hybrids in argon preserved the CNTFs and showed the following phase transitions: amorphous alumina → θ/α-Al₂O₃ → α-Al₂O₃. Characterization of the specimens using XPS indicated that as-deposited alumina was oxygen rich, likely with the form Al(OH)₂₋₃ corresponding to boehmite and bayerite aluminum hydroxides. The relative oxygen

concentration decreased after crystallization due to formation of stoichiometrically balanced Al_2O_3 . Analysis of high-resolution XPS spectra from O1s and Al2p peaks provided evidence indicating the presence of Al-O-C bonding near the interface of CNTFs and alumina.

- ALD of Al_2O_3 on sacrificial CNTF templates followed by their removal via calcination in air yielded a microstructure unique from traditional alumina aerogels. Free-standing Al_2O_3 nanotube aerogels with an average density of 1.2 mg cm^{-3} were demonstrated. The network of aligned and interconnected nanotubes with high porosity and surface area exhibited elastic deformation behavior, and structural robustness even after wetting. The multifunctionality of the novel material was demonstrated by its utilization as the active material in a sensitive humidity sensor, and also as an effective high temperature thermal insulation material.
- Hybrid alumina/CNT and pure alumina nanotube foams with ultralow densities were produced via ALD on CNTF templates. The foams exhibited unique anisotropic mechanical properties due to a high level of alignment among the nanotubes. Foams demonstrated unprecedented elastic recovery following compression and exceed some of the highest strength and modulus values for any type of foam with similar density. Pure alumina foams were shown to have a density-modulus scaling dependence of 2, indicating superior ligament connectivity and efficient load transfer. Finally, foams exhibited impressive thermal stability and insulating properties as well as high durability for liquid filtration and drying.

9 Items of Interest and Future Work

9.1 Resilient and Hydrophobic PyC-Alumina Nanotube Foams

Alumina nanotube aerogels produced from 20 cycle foams possessed some of the most intriguing properties: optical translucence, high surface area, record-breaking density, etc. However, they were also unstable to moisture and highly compressible at low force. Not being an uncommon issue in the field of ultralow density materials, several studies have demonstrated methods for improving the mechanical properties and moisture stability of aerogels. Most typically this is accomplished by depositing polymer to the aerogel surfaces by way of vapor deposition or plasma polymerization (232).

Not having either of these techniques readily available, the aerogels were instead coated with PyC for 30 minutes using the previously described CVI technique. A stainless steel basket, shown in Figure 9.1a, was fabricated to contain the sample and prevent it from moving when pumping out the CVD reactor. After deposition the samples turned black (Figure 9.1b) as a result of carbon deposition. The samples were mechanically resilient, demonstrating full elastic recovery after being completely flattened repeatedly (by various and sundry lab mates and advisors). The PyC-coated alumina also exhibited stable hydrophobicity, shown in Figure 9.1c, a stark contrast to the alumina foams from before.

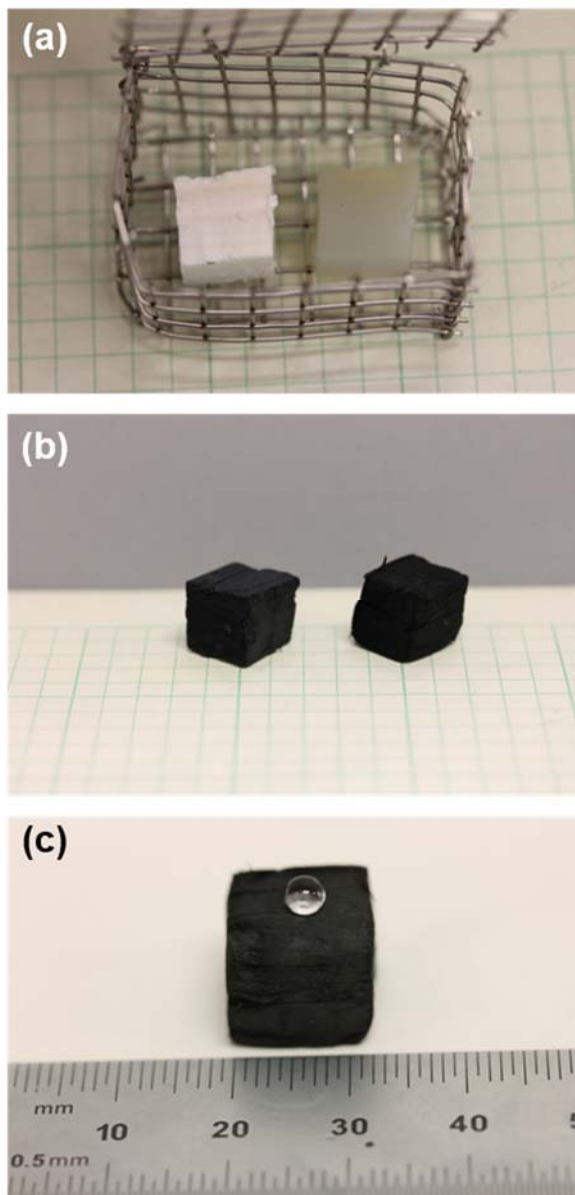


Figure 9.1 (a) Alumina nanotube foams made from 500 ALD cycles (left) and 20 cycles (right) before PyC deposition. (b) After 30 minutes of PyC treatment, the foams turned black from deposition of carbon. (c) PyC coated alumina foams exhibited hydrophobic wetting behavior and mechanical resilience.

Figure 9.2 shows SEM and TEM images which provided some insight on the interesting behavior. First, and most surprisingly, numerous webs of tangled CNTs were found throughout the alumina foam growing from residual Fe left inside the alumina nanotubes after the CNTFs were removed via calcination. The “new” CNTs were much smaller diameter than what is typically grown in our lab, and in some cases, were long enough to span across the gaps between alumina nanotubes. TEM revealed that PyC had conformally deposited in a laminar fashion along the length of the alumina nanotubes. The coating had a complex morphology, exhibiting both classic graphitic layers with $\sim 3.4 \text{ \AA}$ spacing and also other discernable layers with much larger spacing. The new CNTs were also very apparent and still attached to the alumina despite having been sonicated while preparing the TEM grid.

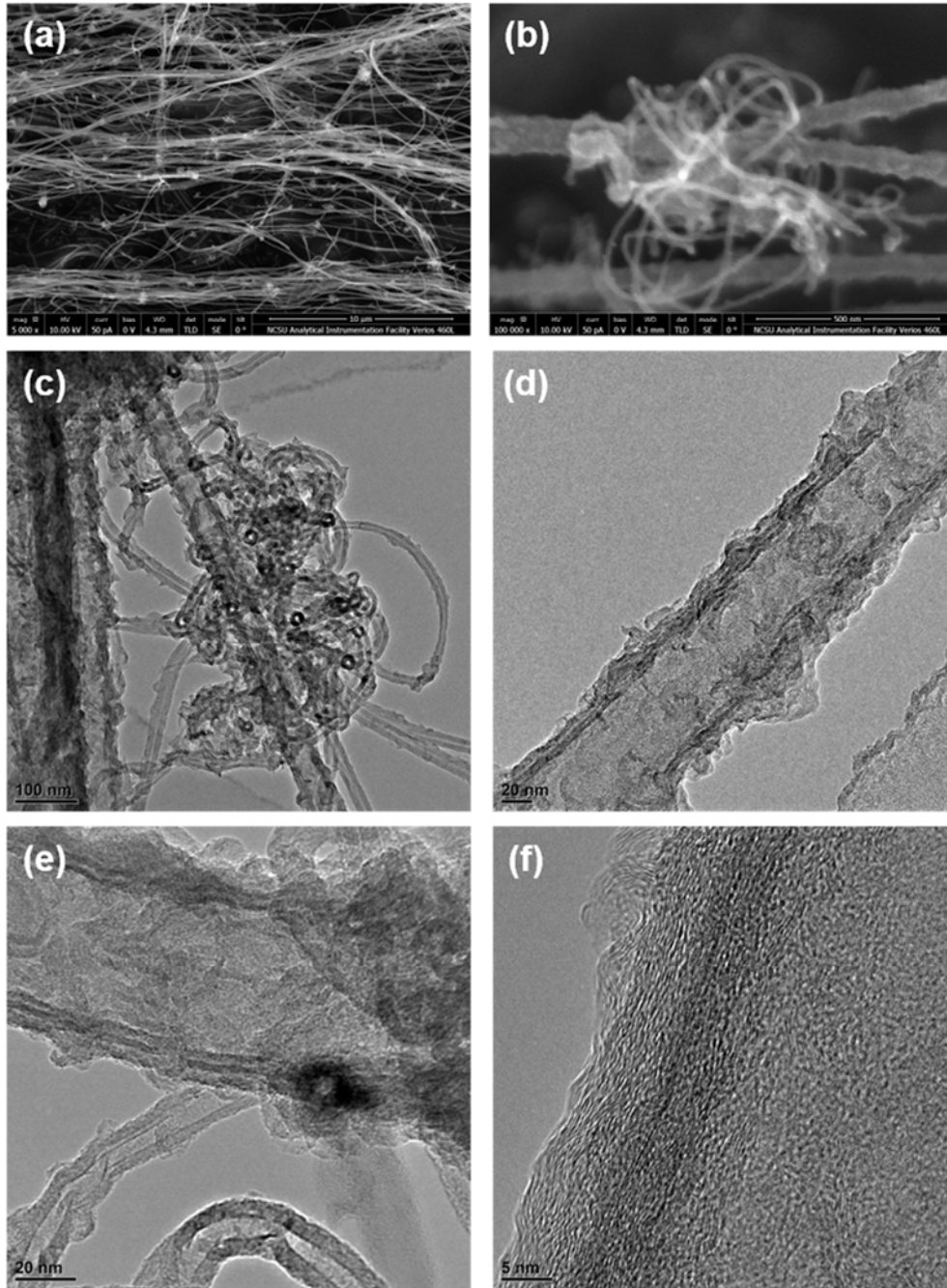


Figure 9.2 (a,b) SEM and (c-f) TEM micrographs showing morphology of CNTs grown on thin-walled alumina nanotubes. Graphitic PyC layers deposited on alumina nanotubes are particularly visible in images d-f.

It is hypothesized that, much like with the CNT foams, the addition of PyC to the alumina nanotubes creates a more robust network through thickening of struts and reinforcement of tube-tube junctions. While it is possible that the new CNTs play a role in the mechanical response by providing physical entanglements, further experimentation will be required to elucidate their role.

9.2 Synthesis of Carbon Nanotubes on Alumina-Coated CNTFs

Alumina is a well-known buffer layer material used for the growth of CNTs, primarily on planar substrates like Si (313). Recently, however, researchers have used various thin film deposition techniques, including ALD, to deposit alumina onto unique non-planar substrates such as glass and carbon fibers to promote CNT growth. We also found it possible to grow CNTs within and on our CNT/alumina hybrid foams. After ALD coating with 10 nm of alumina, samples were placed in the CVD reactor along with FeCl₂ catalyst, and then pumped down to vacuum. The furnace was heated to 760 °C, at which time 500 sccm of H₂ gas was flowed for 1 minute, and then replaced with 600 sccm C₂H₂, 398 sccm argon, and 1.5 sccm Cl₂ gases regulated at 3 Torr. After 20 minutes the reactor was purged with argon and left to cool.

The resulting samples exhibited drastically different mechanical properties compared to typical 100 cycle CNT/alumina foams, particularly along the outermost edges. Specimens collected from the edge and middle of the foam were analyzed using SEM, the images from which are shown in Figure 9.3. Although tangled clusters of long and thin CNTs were found throughout the entire foam there was a particularly high concentration at the edges. This was likely caused by a combination of non-uniform Fe catalyst reduction and limited diffusion of the growth gases into the bulk of the foam's interior.

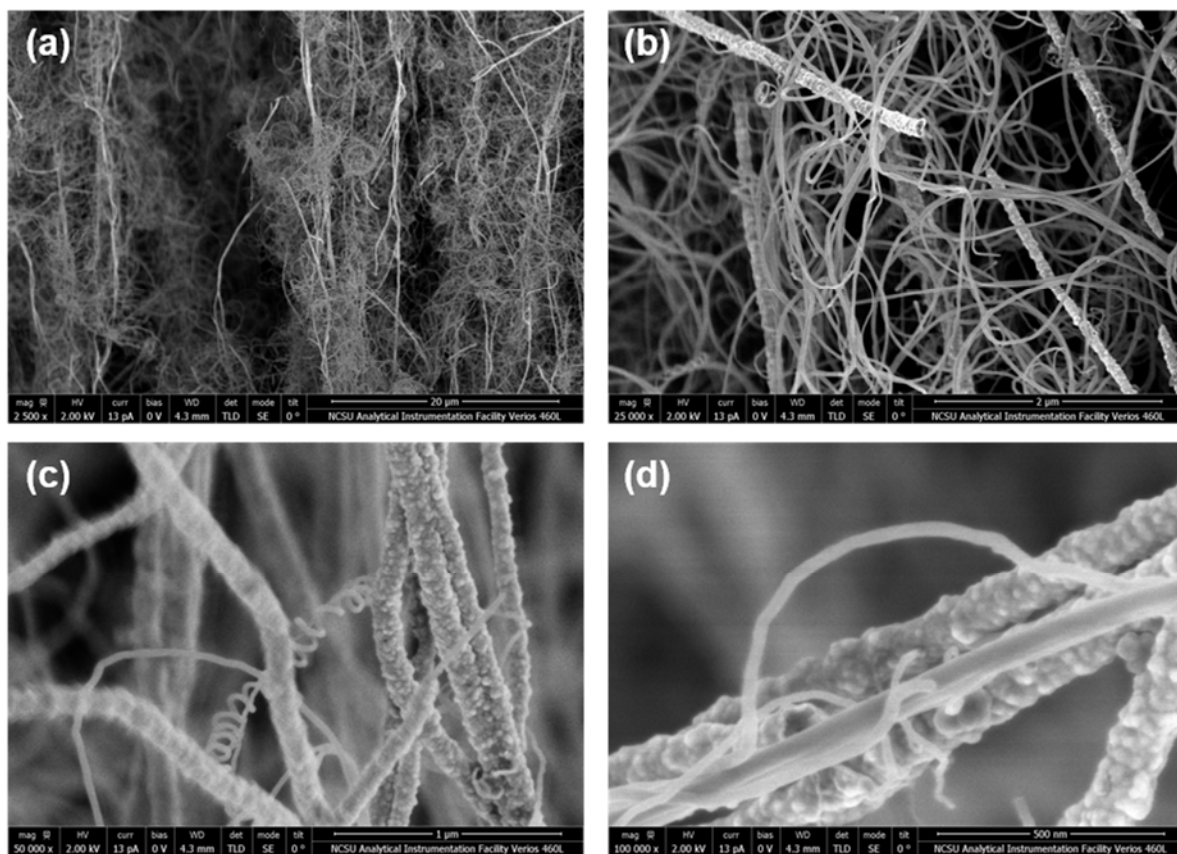


Figure 9.3 SEM characterization of CNTs grown on CNTFs coated with 100 cycles of alumina.

Nevertheless, these are issues that may be solved with further experimentation and process optimization. The outlines process is a unique route for the production of CNT-based foams which are a topic of considerable interest as of late (235, 269, 301, 314). Not to be discounted, however, is the further potential for this technique to be applied to other CNT assemblies such as ribbons, arrays, yarns, and buckypapers.

9.3 Future Work

The vast majority of this work focused on understanding the nucleation, growth, chemical, and structural morphology of alumina deposited via ALD onto CNT assemblies and characterization of the physical properties of the produced hybrid. Alumina is one of many

technologically useful materials able to be deposited via ALD, and a great deal of what has been learned in this work can be directly translated and applied to alternate precursor chemistries for an even wider breadth of applications. Additionally, the ALD technique can be used to easily create complex layered structures or doped films on the CNT templates.

Vapor phase surface modification techniques developed in Chapter 4 have far-reaching implications for CNT-inorganic hybrids derived from CNT assemblies. Though some applications may require complete and conformal coating of the CNTs—as in the preparation of aerogel-like materials—CNTs decorated with nanoparticles may be advantageous for others such as catalysis where the surface area of the active material should be maximized. The ability to precisely tune the surface chemistry of the CNTs to promote the desired morphology while also preserving the CNT assembly structure and alignment is important for future development.

In Chapter 5 evidence indicating the presence of interfacial Al-O-C bonding was presented. Hybrid materials, with their nanoscale sized domains, exhibit properties unique from either constituent phase as a result of the vast interfacial surface area which dominates the overall volume of the material. It is therefore necessary to investigate the effects of interfacial bonding on charge, heat, and stress transfer between CNT and inorganic phases, as this will influence the electrical, thermal, and mechanical properties of the hybrid.

The preparation of hybrid CNT/alumina and alumina nanotube aerogels presented in Chapters 6 & 7 shows promise in applications where traditional metal oxide aerogels are lacking; namely mechanical robustness, thermal stability, and ease of processing. Some of the literature reviewed for this dissertation made claims of “bulk production” and presented samples only 2 mm thick, or “high strength” and yet neither measured nor reported actual values of strength. The truly large-scale alumina aerogels presented in this work (which are capable of being produced in less than a day from CNT growth to calcination), with a density of only 39 mg cm^{-3} had a modulus of 5 MPa and exhibited good thermal stability. To contrast, core-shell alumina-silica aerogels which took well over a week to synthesize and had a density more than three times higher (143 mg cm^{-3}), had only a slightly higher modulus of 6.7 MPa (255). Further work to develop and optimize the synthetic method outlined in this research should be undertaken to maximize mechanical and thermal performance. For example, pre-

compression followed by high temperature annealing would allow for synthesis of higher density structures without having to increase the thickness of the ALD coating. This would also result in the creation of additional CNT-CNT junctions, therefore decreasing the distance between interconnects. Greater control of the structure, improved ligament connectivity, and enhancement of strength and stiffness are potential benefits to exploration in this area.

REFERENCES

1. G. Kickelbick, *Hybrid Materials: Synthesis, Characterization, and Application* (Wiley-VCH, Weinheim, Germany, 2007).
2. D. Eder, Carbon Nanotube-Inorganic Hybrids. *Chem. Rev.* **110**, 1348–85 (2010).
3. J. Di *et al.*, Dry-Processable Carbon Nanotubes for Functional Devices and Composites. *Small*, 1–20 (2014).
4. Y. Ren, Z. Ma, P. G. Bruce, Ordered mesoporous metal oxides: synthesis and applications. *Chem. Soc. Rev.* **41**, 4909 (2012).
5. S. J. Shin *et al.*, Robust nanoporous alumina monoliths by atomic layer deposition on low-density carbon-nanotube scaffolds. *Carbon N. Y.* **73**, 443–447 (2014).
6. H. W. Zhu *et al.*, Direct synthesis of long single-walled carbon nanotube strands. *Science.* **296**, 884–6 (2002).
7. Y.-L. Li, I. A. Kinloch, A. H. Windle, Direct spinning of carbon nanotube fibers from chemical vapor deposition synthesis. *Science.* **304**, 276–8 (2004).
8. K. K. K. Koziol *et al.*, High-performance carbon nanotube fiber. *Science.* **318**, 1892–5 (2007).
9. K. L. Stano *et al.*, Direct spinning of carbon nanotube fibres from liquid feedstock. *Int. J. Mater. Form.* **1**, 59–62 (2008).
10. R. M. Sundaram, K. K. K. Koziol, A. H. Windle, Continuous Direct Spinning of Fibers of Single-Walled Carbon Nanotubes with Metallic Chirality. *Mater. Sci.*, 1–5 (2011).
11. K. Jiang, Q. Li, S. Fan, Spinning continuous carbon nanotube yarns. *Nature.* **419**, 801 (2002).
12. M. Zhang *et al.*, Strong, transparent, multifunctional, carbon nanotube sheets. *Science.* **309**, 1215–9 (2005).
13. J. Sehested *et al.*, Atomic-scale imaging of carbon nanofibre growth. *Nature.* **427** (2004), doi:10.1038/nature02308.1.

14. M. Stadermann *et al.*, Mechanism and kinetics of growth termination in controlled chemical vapor deposition growth of multiwall carbon nanotube arrays. *Nano Lett.* **9**, 738–44 (2009).
15. W. Z. Li *et al.*, Large-Scale Synthesis of Aligned Carbon Nanotubes. *Science.* **274**, 1701–3 (1996).
16. Z. Pan, S. Xie, B. Chang, C. Wang, L. Lu, Very long carbon nanotubes. *Nature.* **394**, 631–632 (1998).
17. S. Fan *et al.*, Self-Oriented Regular Arrays of Carbon Nanotubes and Their Field Emission Properties. *Science.* **283**, 512–514 (1999).
18. Z. F. Ren *et al.*, Synthesis of Large Arrays of Well-Aligned Carbon Nanotubes on Glass. *Science.* **282**, 1105–1107 (1998).
19. R. Vander Wal, T. Tichich, V. Curtis, Substrate–support interactions in metal-catalyzed carbon nanofiber growth. *Carbon N. Y.* **39**, 2277–2289 (2001).
20. P. B. Amama *et al.*, Influence of alumina type on the evolution and activity of alumina-supported Fe catalysts in single-walled carbon nanotube carpet growth. *ACS Nano.* **4**, 895–904 (2010).
21. C. Mattevi *et al.*, In-situ X-ray Photoelectron Spectroscopy Study of Catalyst–Support Interactions and Growth of Carbon Nanotube Forests. *J. Phys. Chem. C.* **112**, 12207–12213 (2008).
22. T. de los Arcos *et al.*, Influence of iron–silicon interaction on the growth of carbon nanotubes produced by chemical vapor deposition. *Appl. Phys. Lett.* **80**, 2383 (2002).
23. K. Hata *et al.*, Water-assisted highly efficient synthesis of impurity-free single-walled carbon nanotubes. *Science.* **306**, 1362–4 (2004).
24. T. Yamada *et al.*, Revealing the Secret of Water-Assisted Carbon Nanotube Synthesis by Microscopic Observation of the Interaction of Water on the Catalysts. *Nano Lett.* (2008), doi:10.1021/nl801981m.
25. S. Yasuda *et al.*, Improved and large area single-walled carbon nanotube forest growth by controlling the gas flow direction. *ACS Nano.* **3**, 4164–70 (2009).
26. R. Guzmán de Villoria *et al.*, High-yield growth of vertically aligned carbon nanotubes on a continuously moving substrate. *Nanotechnology.* **20**, 405611 (2009).

27. R. Guzmán de Villoria, A. J. Hart, B. L. Wardle, Continuous high-yield production of vertically aligned carbon nanotubes on 2D and 3D substrates. *ACS Nano*. **5**, 4850–7 (2011).
28. W. Lin, R. Zhang, K.-S. Moon, C. P. Wong, Synthesis of High-Quality Vertically Aligned Carbon Nanotubes on Bulk Copper Substrate for Thermal Management. *IEEE Trans. Adv. Packag.* **33**, 370–376 (2010).
29. H. Huang, C. H. Liu, Y. Wu, S. Fan, Aligned Carbon Nanotube Composite Films for Thermal Management. *Adv. Mater.* **17**, 1652–1656 (2005).
30. Y. Chai, K. Zhang, M. Zhang, P. C. H. Chan, M. M. F. Yuen, Carbon Nanotube/Copper Composites for Via Filling and Thermal Management. *2007 Proc. 57th Electron. Components Technol. Conf.*, 1224–1229 (2007).
31. B. L. Wardle *et al.*, Fabrication and Characterization of Ultrahigh-Volume- Fraction Aligned Carbon Nanotube-Polymer Composites. *Adv. Mater.* **20**, 2707–2714 (2008).
32. K. L. Stano *et al.*, Copper-encapsulated vertically aligned carbon nanotube arrays. *ACS Appl. Mater. Interfaces*. **5**, 10774–81 (2013).
33. R. H. Poelma *et al.*, Tailoring the Mechanical Properties of High-Aspect-Ratio Carbon Nanotube Arrays using Amorphous Silicon Carbide Coatings. *Adv. Funct. Mater.* **24**, 5737–5744 (2014).
34. H. Zhang, G. Cao, Y. Yang, Carbon nanotube arrays and their composites for electrochemical capacitors and lithium-ion batteries. *Energy Environ. Sci.* **2**, 932 (2009).
35. Y. Zhao *et al.*, Super-long aligned TiO₂/carbon nanotube arrays. *Nanotechnology*. **21**, 505702 (2010).
36. C. L. Pint *et al.*, Three dimensional solid-state supercapacitors from aligned single-walled carbon nanotube array templates. *Carbon N. Y.* **49**, 4890–4897 (2011).
37. Z. Yang *et al.*, A Facile and General Approach for the Direct Fabrication of 3D, Vertically Aligned Carbon Nanotube Array/Transition Metal Oxide Composites as Non-Pt Catalysts for Oxygen Reduction Reactions. *Adv. Mater.* **26**, 3156–3161 (2014).
38. C. J. Hu *et al.*, ZnO-coated carbon nanotubes: flexible piezoelectric generators. *Adv. Mater.* **23**, 2941–5 (2011).

39. A. Cao, P. L. Dickrell, W. G. Sawyer, M. N. Ghasemi-Nejhad, P. M. Ajayan, Super-compressible foamlike carbon nanotube films. *Science*. **310**, 1307–10 (2005).
40. Y. Zhang *et al.*, Tailoring the morphology of carbon nanotube arrays: from spinnable forests to undulating foams. *ACS Nano*. **3**, 2157–62 (2009).
41. P. D. Bradford, X. Wang, H. Zhao, Y. T. Zhu, Tuning the compressive mechanical properties of carbon nanotube foam. *Carbon N. Y.* **49**, 2834–2841 (2011).
42. M. Zhang, K. R. Atkinson, R. H. Baughman, Multifunctional Carbon Nanotube Yarns by Downsizing an Ancient Technology. *Science*. **306**, 1358–61 (2004).
43. K. Liu *et al.*, Controlled growth of super-aligned carbon nanotube arrays for spinning continuous unidirectional sheets with tunable physical properties. *Nano Lett.* **8**, 700–705 (2008).
44. X. Zhang *et al.*, Spinning and Processing Continuous Yarns from 4-Inch Wafer Scale Super-Aligned Carbon Nanotube Arrays. *Adv. Mater.* **18**, 1505–1510 (2006).
45. C. P. Huynh, S. C. Hawkins, Understanding the synthesis of directly spinnable carbon nanotube forests. *Carbon N. Y.* **48**, 1105–1115 (2010).
46. J.-H. Kim, H.-S. Jang, K. H. Lee, L. J. Overzet, G. S. Lee, Tuning of Fe catalysts for growth of spin-capable carbon nanotubes. *Carbon N. Y.* **48**, 538–547 (2010).
47. J.-T. Di, Z.-Z. Yong, X.-J. Yang, Q.-W. Li, Structural and morphological dependence of carbon nanotube arrays on catalyst aggregation. *Appl. Surf. Sci.* **258**, 13–18 (2011).
48. T. Laude *et al.*, in *Fullerene-Nanotubes General Symposium* (Tokyo, 2004).
49. Y. Inoue *et al.*, One-step grown aligned bulk carbon nanotubes by chloride mediated chemical vapor deposition. *Appl. Phys. Lett.* **92**, 213113 (2008).
50. T. Laude, H. Kuwahara, K. Sato, FeCl₂-CVD production of carbon fibres with graphene layers nearly perpendicular to axis. *Chem. Phys. Lett.* **434**, 78–81 (2007).
51. C. Ghemes, A. Ghemes, Study of Growth Enhancement of Multiwalled Carbon Nanotubes by Chlorine-Assisted Chemical Vapor Deposition. *Jpn. J. Appl. Phys.* **52**, 035202–1–6 (2013).
52. J.-Q. Huang, Q. Zhang, M.-Q. Zhao, F. Wei, The release of free standing vertically-aligned carbon nanotube arrays from a substrate using CO₂ oxidation. *Carbon N. Y.* **48**, 1441–1450 (2010).

53. J. Jia *et al.*, A comparison of the mechanical properties of fibers spun from different carbon nanotubes. *Carbon N. Y.* **49**, 1333–1339 (2011).
54. A. A. Kuznetsov, A. F. Fonseca, R. H. Baughman, A. A. Zakhidov, Structural model for dry-drawing of sheets and yarns from carbon nanotube forests. *ACS Nano.* **5**, 985–93 (2011).
55. Q. W. Li *et al.*, Sustained Growth of Ultralong Carbon Nanotube Arrays for Fiber Spinning. *Adv. Mater.* **18**, 3160–3163 (2006).
56. J. Lee *et al.*, The reason for an upper limit to the height of spinnable carbon nanotube forests. *J. Mater. Sci.* **48**, 6897–6904 (2013).
57. Z. Wu *et al.*, Transparent, conductive carbon nanotube films. *Science.* **305**, 1273–6 (2004).
58. B. Dan, G. C. Irvin, M. Pasquali, Continuous and scalable fabrication of transparent conducting carbon nanotube films. *ACS Nano.* **3**, 835–43 (2009).
59. F. Mirri *et al.*, High-performance carbon nanotube transparent conductive films by scalable dip coating. *ACS Nano.* **6**, 9737–44 (2012).
60. A. Kaskela *et al.*, Aerosol-synthesized SWCNT networks with tunable conductivity and transparency by a dry transfer technique. *Nano Lett.* **10**, 4349–55 (2010).
61. C. Feng *et al.*, Flexible, Stretchable, Transparent Conducting Films Made from Superaligned Carbon Nanotubes. *Adv. Funct. Mater.* **20**, 885–891 (2010).
62. Y. Zhang *et al.*, Polymer-embedded carbon nanotube ribbons for stretchable conductors. *Adv. Mater.* **22**, 3027–31 (2010).
63. F. Xu, X. Wang, Y. Zhu, Y. Zhu, Wavy Ribbons of Carbon Nanotubes for Stretchable Conductors. *Adv. Funct. Mater.* **22**, 1279–1283 (2012).
64. J.-H. Lee *et al.*, Highly Stretchable Piezoelectric-Pyroelectric Hybrid Nanogenerator. *Adv. Mater.* **26**, 765–769 (2014).
65. Y. Jia *et al.*, Nanotube-Silicon Heterojunction Solar Cells. *Adv. Mater.* **20**, 4594–4598 (2008).
66. Y. Jia *et al.*, Strong and reversible modulation of carbon nanotube-silicon heterojunction solar cells by an interfacial oxide layer. *Phys. Chem. Chem. Phys.* **14**, 8391–6 (2012).

67. F. Hao *et al.*, Highly catalytic cross-stacked superaligned carbon nanotube sheets for iodine-free dye-sensitized solar cells. *J. Mater. Chem.* **22**, 22756 (2012).
68. Z. Yang *et al.*, Aligned carbon nanotube sheets for the electrodes of organic solar cells. *Adv. Mater.* **23**, 5436–9 (2011).
69. J. Di *et al.*, Robust and aligned carbon nanotube/titania core/shell films for flexible TCO-free photoelectrodes. *Small.* **9**, 148–55 (2013).
70. J. Kim, K. H. Lee, L. J. Overzet, G. S. Lee, Synthesis and Electrochemical Properties of Spin-Capable Carbon Nanotube Sheet/MnO, 2611–2617 (2011).
71. K. Fu *et al.*, Aligned Carbon Nanotube-Silicon Sheets: A Novel Nano-architecture for Flexible Lithium Ion Battery Electrodes. *Adv. Mater.* **25**, 5109–5114 (2013).
72. A. Aliev, J. Oh, M. Kozlov, A. Kuznetsov, Giant-stroke, superelastic carbon nanotube aerogel muscles. *Science.* **323**, 1575–1578 (2009).
73. L. Xiao *et al.*, Flexible, stretchable, transparent carbon nanotube thin film loudspeakers. *Nano Lett.* **8**, 4539–45 (2008).
74. C. D. Williams *et al.*, Multiwalled carbon nanotube sheets as transparent electrodes in high brightness organic light-emitting diodes. *Appl. Phys. Lett.* **93**, 183506 (2008).
75. Y. Koo *et al.*, Aligned carbon nanotube/copper sheets: a new electrocatalyst for CO₂ reduction to hydrocarbons. *RSC Adv.* **4**, 16362 (2014).
76. X. Wang *et al.*, Ultrastrong, Stiff and Multifunctional Carbon Nanotube Composites. *Mater. Res. Lett.* **1**, 19–25 (2013).
77. K. Liu *et al.*, Carbon nanotube yarns with high tensile strength made by a twisting and shrinking method. *Nanotechnology.* **21**, 045708 (2010).
78. M. Miao, Yarn spun from carbon nanotube forests: Production, structure, properties and applications. *Particuology.* **11**, 378–393 (2013).
79. A. E. Bogdanovich, P. D. Bradford, Carbon nanotube yarn and 3-D braid composites. Part I: Tensile testing and mechanical properties analysis. *Compos. Part A Appl. Sci. Manuf.* **41**, 230–237 (2010).
80. M. Zu *et al.*, The effective interfacial shear strength of carbon nanotube fibers in an epoxy matrix characterized by a microdroplet test. *Carbon N. Y.* **50**, 1271–1279 (2012).

81. Y. Zhu, P. Arendt, X. Zhang, Q. Li, Carbon nanotube fiber spun from wetted ribbon. *US Pat. 8,709,372*. **19** (2009), pp. 1719–1723.
82. L. K. Randeniya, A. Bendavid, P. J. Martin, C.-D. Tran, Composite yarns of multiwalled carbon nanotubes with metallic electrical conductivity. *Small*. **6**, 1806–11 (2010).
83. M. D. Lima *et al.*, Biscrolling nanotube sheets and functional guests into yarns. *Science*. **331**, 51–5 (2011).
84. W. Weng *et al.*, Winding aligned carbon nanotube composite yarns into coaxial fiber full batteries with high performances. *Nano Lett.* **14**, 3432–8 (2014).
85. D. Zhang, M. Miao, H. Niu, Z. Wei, Core Spun Carbon Nanotube Yarn Supercapacitors for Wearable Electronic Textiles. *ACS Nano*. **8**, 4571–4579 (2014).
86. K. L. Klein *et al.*, Surface characterization and functionalization of carbon nanofibers. *J. Appl. Phys.* **103**, 061301 (2008).
87. D. Tasis, N. Tagmatarchis, V. Georgakilas, M. Prato, Soluble carbon nanotubes. *Chemistry*. **9**, 4000–8 (2003).
88. C. G. Salzmann *et al.*, The Role of Carboxylated Carbonaceous Fragments in the Functionalization and Spectroscopy of a Single-Walled Carbon-Nanotube Material. *Adv. Mater.* **19**, 883–887 (2007).
89. K. S. Han *et al.*, Atmospheric-pressure plasma treatment to modify hydrogen storage properties of multiwalled carbon nanotubes. *Appl. Phys. Lett.* **86**, 263105 (2005).
90. K. L. Stano *et al.*, Copper Encapsulated Vertically Aligned Carbon Nanotube Arrays. *ACS Appl. Mater. Interfaces*. **5**, 10774–10781 (2013).
91. K. L. Stano, thesis, North Carolina State University (2012).
92. S. C. Ramos *et al.*, Wettability control on vertically-aligned multi-walled carbon nanotube surfaces with oxygen pulsed DC plasma and CO₂ laser treatments. *Diam. Relat. Mater.* **19**, 752–755 (2010).
93. X. Xie, Y. Mai, X. Zhou, Dispersion and alignment of carbon nanotubes in polymer matrix: A review. *Mater. Sci. Eng. R Reports*. **49**, 89–112 (2005).

94. S. Giordani *et al.*, Debundling of single-walled nanotubes by dilution: observation of large populations of individual nanotubes in amide solvent dispersions. *J. Phys. Chem. B.* **110**, 15708–18 (2006).
95. S. Cambré *et al.*, Characterisation of nanohybrids of porphyrins with metallic and semiconducting carbon nanotubes by EPR and optical spectroscopy. *Chemphyschem.* **9**, 1930–41 (2008).
96. S. Neocleus, S. W. Pattinson, A. M. Moisala Motta, A. H. Windle, D. Eder, Hierarchical Carbon Nanotube-Inorganic Hybrid Structures Involving CNT Arrays and CNT Fibers. *Funct. Mater. Lett.* **04**, 83–89 (2011).
97. V. Georgakilas *et al.*, Decorating carbon nanotubes with metal or semiconductor nanoparticles. *J. Mater. Chem.* **17**, 2679 (2007).
98. G. G. Wildgoose, C. E. Banks, R. G. Compton, Metal nanoparticles and related materials supported on carbon nanotubes: methods and applications. *Small.* **2**, 182–93 (2006).
99. J. Antson, T. Suntola, Method for producing compound thin films. *US Pat. 4,058,430* (1977) (available at <http://www.google.com/patents/US4058430>).
100. R. L. Puurunen, Surface chemistry of atomic layer deposition: A case study for the trimethylaluminum/water process. *J. Appl. Phys.* **97**, 121301 (2005).
101. C. Marichy, M. Bechelany, N. Pinna, Atomic Layer Deposition of Nanostructured Materials for Energy and Environmental Applications. *Adv. Mater.* **24**, 1017–1032 (2012).
102. M. Copel, M. Gribelyuk, E. Gusev, Structure and stability of ultrathin zirconium oxide layers on Si(001). *Appl. Phys. Lett.* **76**, 436 (2000).
103. V. Miikkulainen, M. Leskelä, M. Ritala, R. L. Puurunen, Crystallinity of inorganic films grown by atomic layer deposition: Overview and general trends. *J. Appl. Phys.* **113**, 021301 (2013).
104. J. Aarik, A. Aidla, T. Uustare, V. Sammelselg, Morphology and structure of TiO₂ thin films grown by atomic layer deposition. *J. Cryst. Growth.* **148**, 268–275 (1995).
105. M. Juppo *et al.*, Atomic Layer Deposition of Titanium Nitride Thin Films Using tert-Butylamine and Allylamine as Reductive Nitrogen Sources. *Electrochem. Solid-State Lett.* **5**, C4 (2002).

106. M. Juppo, M. Ritala, M. Leskelä, Use of 1,1-Dimethylhydrazine in the Atomic Layer Deposition of Transition Metal Nitride Thin Films. *J. Electrochem. Soc.* **147** (2000), p. 3377.
107. J. Musschoot *et al.*, Comparison of Thermal and Plasma-Enhanced ALD/CVD of Vanadium Pentoxide. *J. Electrochem. Soc.* **156**, P122 (2009).
108. D. R. G. Mitchell *et al.*, Atomic layer deposition of TiO₂ and Al₂O₃ thin films and nanolaminates. *Smart Mater. Struct.* **15**, S57–S64 (2006).
109. S. M. George, Atomic Layer Deposition: An Overview. *Chem. Rev.* **110**, 111–31 (2010).
110. N. Pinna, M. Knez, Eds., *Atomic Layer Deposition of Nanostructured Materials* (Wiley-VCH Verlag GmbH & Co., Weinheim, 2012).
111. G. N. Parsons, S. M. George, M. Knez, Progress and future directions for atomic layer deposition and ALD-based chemistry. *MRS Bull.* **36**, 865–871 (2011).
112. M. D. Groner, J. W. Elam, F. H. Fabreguette, S. M. George, Electrical characterization of thin Al₂O₃ films grown by atomic layer deposition on silicon and various metal substrates. *Thin Solid Films.* **413** (2002), pp. 186–197.
113. S. Elliott, J. Greer, Simulating the atomic layer deposition of alumina from first principles. *J. Mater. Chem.* **14**, 3246–3250 (2004).
114. M. D. Groner, F. H. Fabreguette, J. W. Elam, S. M. George, Low-Temperature Al₂O₃ Atomic Layer Deposition. *Chem. Mater.* **16**, 639–645 (2004).
115. M. Benmalek, H. Dunlop, Inorganic coatings on polymers. *Surf. coatings Technol.* **77**, 821–826 (1995).
116. P. E. Burrows *et al.*, Reliability and degradation of organic light emitting devices. *Appl. Phys. Lett.* **65**, 2922 (1994).
117. M. S. Weaver *et al.*, Organic light-emitting devices with extended operating lifetimes on plastic substrates. *Appl. Phys. Lett.* **81**, 2929 (2002).
118. A. C. Dillon, A. W. Ott, J. D. Way, S. M. George, Surface chemistry of Al₂O₃ deposition using Al(CH₃)₃ and H₂O in a binary reaction sequence. *Surf. Sci.* **322**, 230–242 (1995).

119. A. W. Ott, J. W. Klaus, J. M. Johnson, S. M. George, Al₂O₃ thin film growth on Si(100) using binary reaction sequence chemistry. *Thin Solid Films*. **292**, 135–144 (1997).
120. G. S. Higashi, C. G. Fleming, Sequential surface chemical reaction limited growth of high quality Al₂O₃ dielectrics. *Appl. Phys. Lett.* **55**, 1963 (1989).
121. S. Jakschik, U. Schroeder, T. Hecht, M. Gutsche, H. Seidl, Crystallization behavior of thin ALD-Al₂O₃ films. **425**, 216–220 (2003).
122. J. Huang, S. Liu, Y. Wang, Z. Ye, Fabrication of ZnO/Al₂O₃ core–shell nanostructures and crystalline Al₂O₃ nanotube. *Appl. Surf. Sci.* **254**, 5917–5920 (2008).
123. C. M. Tanner, J. Lu, H.-O. Blom, J. P. Chang, Growth of Epitaxial γ -Al₂O₃ Dielectrics on 4H-SiC. *Mater. Res. Soc. Symp.* **911**, 3–7 (2006).
124. L. Zhang, H. C. Jiang, C. Liu, J. W. Dong, P. Chow, Annealing of Al₂O₃ thin films prepared by atomic layer deposition. *J. Phys. D: Appl. Phys.* **40**, 3707–3713 (2007).
125. M. Tammenmaa, T. Koskinen, L. Hiltunen, Zinc chalcogenide thin films grown by the atomic layer epitaxy technique using zinc acetate as source material. *Thin Solid Films*. **124**, 125–128 (1985).
126. E. B. Yousfi, J. Fouache, D. Lincot, Study of atomic layer epitaxy of zinc oxide by in-situ quartz crystal microgravimetry. *Appl. Surf. Sci.* **153**, 223–234 (2000).
127. E. Guziewicz *et al.*, Extremely low temperature growth of ZnO by atomic layer deposition. *J. Appl. Phys.* **103**, 033515 (2008).
128. S. Jeon *et al.*, Structural and Electrical Properties of ZnO Thin Films Deposited by Atomic Layer Deposition at Low Temperatures. *J. Electrochem. Soc.* **155**, H738 (2008).
129. E. Guziewicz, M. Godlewski, T. A. Krajewski, Ł. Wachnicki, G. Łuka, ZnO by ALD — Advantages of the Material Grown at Low Temperature. **116** (2009).
130. I. A. Kowalik *et al.*, Structural and optical properties of low-temperature ZnO films grown by atomic layer deposition with diethylzinc and water precursors. *J. Cryst. Growth*. **311**, 1096–1101 (2009).

131. J. Malm, E. Sahramo, J. Perälä, T. Sajavaara, M. Karppinen, Low-temperature atomic layer deposition of ZnO thin films: Control of crystallinity and orientation. *Thin Solid Films*. **519**, 5319–5322 (2011).
132. T. Tynell, M. Karppinen, Atomic layer deposition of ZnO: a review. *Semicond. Sci. Technol.* **29**, 043001 (2014).
133. S.-Y. Pung, K.-L. Choy, X. Hou, C. Shan, Preferential growth of ZnO thin films by the atomic layer deposition technique. *Nanotechnology*. **19**, 435609 (2008).
134. Y. Kawamura, N. Hattori, N. Miyatake, Y. Uraoka, Comparison between ZnO films grown by plasma-assisted atomic layer deposition using H₂O plasma and O₂ plasma as oxidant. *J. Vac. Sci. Technol. A Vacuum, Surfaces, Film*. **31**, 01A142 (2013).
135. N. Y. Yuan *et al.*, The influence of deposition temperature on growth mode, optical and mechanical properties of ZnO films prepared by the ALD method. *J. Cryst. Growth*. **366**, 43–46 (2013).
136. H. Makino, A. Miyake, T. Yamada, N. Yamamoto, T. Yamamoto, Influence of substrate temperature and Zn-precursors on atomic layer deposition of polycrystalline ZnO films on glass. *Thin Solid Films*. **517**, 3138–3142 (2009).
137. S. K. Park, Y. Lee, Controlling preferred orientation of ZnO thin films by atomic layer deposition. *J. Mater. Sci.* **9**, 2195–2197 (2004).
138. A. Wójcik, M. Godlewski, E. Guziewicz, R. Minikayev, W. Paszkowicz, Controlling of preferential growth mode of ZnO thin films grown by atomic layer deposition. *J. Cryst. Growth*. **310**, 284–289 (2008).
139. S.-H. K. Park, C.-S. Hwang, H.-S. Kwack, J.-H. Lee, H. Y. Chu, Characteristics of ZnO Thin Films by Means of Plasma-Enhanced Atomic Layer Deposition. *Electrochem. Solid-State Lett.* **9**, G299 (2006).
140. D. Kim, H. Kang, J.-M. Kim, H. Kim, The properties of plasma-enhanced atomic layer deposition (ALD) ZnO thin films and comparison with thermal ALD. *Appl. Surf. Sci.* **257**, 3776–3779 (2011).
141. M. A. Thomas, J. B. Cui, Highly tunable electrical properties in undoped ZnO grown by plasma enhanced thermal-atomic layer deposition. *ACS Appl. Mater. Interfaces*. **4**, 3122–8 (2012).
142. M. Ritala, M. Leskelä, E. Nykänen, P. Soininen, L. Niinistö, Growth of titanium dioxide thin films by atomic layer epitaxy. *Thin Solid Films*. **225**, 288–295 (1993).

143. M. Ritala, M. Leskela, Titanium isopropoxide as a precursor in atomic layer epitaxy of titanium dioxide thin films. *Chem. Mater.* **5**, 1174–1181 (1993).
144. M. Ritala, M. Leskela, E. Rauhala, Atomic layer epitaxy growth of titanium dioxide thin films from titanium ethoxide. *Chem. Mater.* **6**, 556–561 (1994).
145. M. Ritala, M. Leskelä, L. Johansson, L. Niinistö, Atomic force microscopy study of titanium dioxide thin films grown by atomic layer epitaxy. *Thin Solid Films.* **228**, 32–35 (1993).
146. M. Ritala, M. Leskelä, L. Niinistö, Surface roughness reduction in atomic layer epitaxy growth of titanium dioxide thin films. *Thin Solid Films.* **249**, 155–162 (1994).
147. G. Triani *et al.*, Low temperature atomic layer deposition of titania thin films. *Thin Solid Films.* **518**, 3182–3189 (2010).
148. J. Aarik, A. Aidla, A.-A. Kiisler, T. Uustare, V. Sammelselg, Effect of crystal structure on optical properties of TiO₂ films grown by atomic layer deposition. *Thin Solid Films.* **305**, 270–273 (1997).
149. K. S. Finnie *et al.*, Influence of Si(100) surface pretreatment on the morphology of TiO₂ films grown by atomic layer deposition. *Thin Solid Films.* **440**, 109–116 (2003).
150. A. Javey *et al.*, High-k dielectrics for advanced carbon-nanotube transistors and logic gates. *Nat. Mater.* **1**, 241–6 (2002).
151. J. S. Lee *et al.*, Al₂O₃ nanotubes and nanorods fabricated by coating and filling of carbon nanotubes with atomic-layer deposition. *J. Cryst. Growth.* **254**, 443–448 (2003).
152. L. S. Liyanage *et al.*, Atomic layer deposition of high-k dielectrics on single-walled carbon nanotubes: a Raman study. *Nanotechnology.* **24**, 245703 (2013).
153. A. Gomathi, S. R. C. Vivekchand, A. Govindaraj, C. N. R. Rao, Chemically Bonded Ceramic Oxide Coatings on Carbon Nanotubes and Inorganic Nanowires. *Adv. Mater.* **17**, 2757–2761 (2005).
154. D. S. Kim *et al.*, Synthesis and optical properties of ZnO and carbon nanotube based coaxial heterostructures. *Appl. Phys. Lett.* **93**, 103108 (2008).
155. C. J. Hu *et al.*, ZnO-Coated Carbon Nanotubes: Flexible Piezoelectric Generators. *Adv. Mater.* **23**, 2941–5 (2011).

156. S. Boukhalfa, K. Evanoff, G. Yushin, Atomic layer deposition of vanadium oxide on carbon nanotubes for high-power supercapacitor electrodes. *Energy Environ. Sci.* **5**, 6872 (2012).
157. Y.-C. Hsueh, C.-C. Wang, C. Liu, C.-C. Kei, T.-P. Perng, Deposition of platinum on oxygen plasma treated carbon nanotubes by atomic layer deposition. *Nanotechnology*. **23**, 405603 (2012).
158. A. A. Dameron *et al.*, Aligned carbon nanotube array functionalization for enhanced atomic layer deposition of platinum electrocatalysts. *Appl. Surf. Sci.* **258**, 5212–5221 (2012).
159. Y.-S. Min *et al.*, Ruthenium Oxide Nanotube Arrays Fabricated by Atomic Layer Deposition Using a Carbon Nanotube Template. *Adv. Mater.* **15**, 1019–1022 (2003).
160. C. F. Herrmann, F. H. Fabreguette, D. S. Finch, R. Geiss, S. M. George, Multilayer and functional coatings on carbon nanotubes using atomic layer deposition. *Appl. Phys. Lett.* **87**, 123110 (2005).
161. I. Lahiri *et al.*, Ultrathin alumina-coated carbon nanotubes as an anode for high capacity Li-ion batteries. *J. Mater. Chem.* **21**, 13621 (2011).
162. L. Fu *et al.*, Carbon Nanotubes Coated with Alumina as Gate Dielectrics of Field-Effect Transistors. *Adv. Mater.* **18**, 181–185 (2006).
163. D. B. Farmer, R. G. Gordon, ALD of High- κ Dielectrics on Suspended Functionalized SWNTs. *Electrochem. Solid-State Lett.* **8**, G89 (2005).
164. D. B. Farmer, R. G. Gordon, Atomic layer deposition on suspended single-walled carbon nanotubes via gas-phase noncovalent functionalization. *Nano Lett.* **6**, 699–703 (2006).
165. D. M. King, J. A. Spencer, X. Liang, L. F. Hakim, A. W. Weimer, Atomic layer deposition on particles using a fluidized bed reactor with in situ mass spectrometry. *Surf. Coatings Technol.* **201**, 9163–9171 (2007).
166. G.-D. Zhan *et al.*, Atomic Layer Deposition on Bulk Quantities of Surfactant-Modified Single-Walled Carbon Nanotubes. *J. Am. Ceram. Soc.* **91**, 831–835 (2008).
167. C. K. Devine, C. J. Oldham, J. S. Jur, B. Gong, G. N. Parsons, Fiber Containment for Improved Laboratory Handling and Uniform Nanocoating of Milligram Quantities of Carbon Nanotubes by Atomic Layer Deposition. *Langmuir*. **27**, 14497–507 (2011).

168. A. S. Cavanagh, C. A. Wilson, A. W. Weimer, S. M. George, Atomic layer deposition on gram quantities of multi-walled carbon nanotubes. *Nanotechnology*. **20**, 255602 (2009).
169. Y.-S. Min *et al.*, ZnO nanoparticle growth on single-walled carbon nanotubes by atomic layer deposition and a consequent lifetime elongation of nanotube field emission. *Appl. Phys. Lett.* **90**, 263104 (2007).
170. Y.-S. Min, I. H. Lee, Y. H. Lee, C. S. Hwang, Botryoidal growth of crystalline ZnO nanoparticles on a forest of single-walled carbon nanotubes by atomic layer deposition. *CrystEngComm*. **13**, 3451 (2011).
171. X. L. Li *et al.*, Atomic Layer Deposition of ZnO on Multi-walled Carbon Nanotubes and Its Use for Synthesis of CNT-ZnO Heterostructures. *Nanoscale Res. Lett.* **5**, 1836–1840 (2010).
172. H.-C. Wen *et al.*, ZnO-coated carbon nanotubes: an enhanced and red-shifted emission band at UV-VIS wavelength. *J. Mater. Chem.* **22**, 13747 (2012).
173. Y.-H. Lin *et al.*, Atomic Layer Deposition of Zinc Oxide on Multiwalled Carbon Nanotubes for UV Photodetector Applications. *J. Electrochem. Soc.* **158**, K24 (2011).
174. C.-Y. Hsu *et al.*, Supersensitive, ultrafast, and broad-band light-harvesting scheme employing carbon nanotube/TiO₂ core-shell nanowire geometry. *ACS Nano*. **6**, 6687–92 (2012).
175. S. H. Jin, G. H. Jun, S. H. Hong, S. Jeon, Conformal coating of titanium suboxide on carbon nanotube networks by atomic layer deposition for inverted organic photovoltaic cells. *Carbon N. Y.* **50**, 4483–4488 (2012).
176. M.-G. Willinger *et al.*, The controlled deposition of metal oxides onto carbon nanotubes by atomic layer deposition: examples and a case study on the application of V₂O₄ coated nanotubes in gas sensing. *Phys. Chem. Chem. Phys.* **11**, 3615–3622 (2009).
177. E. Rauwel, G. Clavel, M.-G. Willinger, P. Rauwel, N. Pinna, Non-Aqueous Routes to Metal Oxide Thin Films by Atomic Layer Deposition. *Angew. Chemie*. **120**, 3648–3651 (2008).
178. E. Rauwel *et al.*, Carboxylic Acids as Oxygen Sources for the Atomic Layer Deposition of High- κ Metal Oxides. *J. Phys. Chem. C*. **112**, 12754–12759 (2008).

179. C. Marichy *et al.*, Labeling and monitoring the distribution of anchoring sites on functionalized CNTs by atomic layer deposition. *J. Mater. Chem.* **22**, 7323 (2012).
180. Y. Zhang *et al.*, Growth and characterization of CNT-TiO₂ heterostructures. *Beilstein J. Nanotechnol.* **5**, 946–55 (2014).
181. O. Carp, Photoinduced reactivity of titanium dioxide. *Prog. Solid State Chem.* **32**, 33–177 (2004).
182. U. Diebold, The surface science of titanium dioxide. *Surf. Sci. Rep.* **48**, 53–229 (2003).
183. M. R. Hoffmann, S. T. Martin, W. Choi, D. W. Bahnemann, Environmental Applications of Semiconductor Photocatalysis, 69–96 (1995).
184. W. Wang, P. Serp, P. Kalck, J. L. Faria, Photocatalytic degradation of phenol on MWNT and titania composite catalysts prepared by a modified sol–gel method. *Appl. Catal. B Environ.* **56**, 305–312 (2005).
185. W. Wang, P. Serp, P. Kalck, J. L. Faria, Visible light photodegradation of phenol on MWNT-TiO₂ composite catalysts prepared by a modified sol–gel method. *J. Mol. Catal. A Chem.* **235**, 194–199 (2005).
186. Y. Yu *et al.*, Enhancement of photocatalytic activity of mesoporous TiO₂ by using carbon nanotubes. *Appl. Catal. A Gen.* **289**, 186–196 (2005).
187. N. Bouazza, M. Ouzzine, M. A. Lillo-Ródenas, D. Eder, A. Linares-Solano, TiO₂ nanotubes and CNT–TiO₂ hybrid materials for the photocatalytic oxidation of propene at low concentration. *Appl. Catal. B Environ.* **92**, 377–383 (2009).
188. L. Jiang, L. Gao, Fabrication and characterization of ZnO-coated multi-walled carbon nanotubes with enhanced photocatalytic activity. *Mater. Chem. Phys.* **91**, 313–316 (2005).
189. K. Byrappa *et al.*, Hydrothermal preparation of ZnO:CNT and TiO₂:CNT composites and their photocatalytic applications. *J. Mater. Sci.* **43**, 2348–2355 (2008).
190. X.-H. Xia *et al.*, Preparation of multi-walled carbon nanotube supported TiO₂ and its photocatalytic activity in the reduction of CO₂ with H₂O. *Carbon N. Y.* **45**, 717–721 (2007).

191. M. M. Gui, S.-P. Chai, B.-Q. Xu, A. R. Mohamed, Enhanced visible light responsive MWCNT/TiO₂ core-shell nanocomposites as the potential photocatalyst for reduction of CO₂ into methane. *Sol. Energy Mater. Sol. Cells*. **122**, 183–189 (2014).
192. Y. Ou, J. Lin, S. Fang, D. Liao, MWNT–TiO₂:Ni composite catalyst: A new class of catalyst for photocatalytic H₂ evolution from water under visible light illumination. *Chem. Phys. Lett.* **429**, 199–203 (2006).
193. K. Dai, T. Peng, D. Ke, B. Wei, Photocatalytic hydrogen generation using a nanocomposite of multi-walled carbon nanotubes and TiO₂ nanoparticles under visible light irradiation. *Nanotechnology*. **20**, 125603 (2009).
194. K. Dai, X. Zhang, K. Fan, P. Zeng, T. Peng, Multiwalled Carbon Nanotube-TiO₂ Nanocomposite for Visible-Light-Induced Photocatalytic Hydrogen Evolution. *J. Nanomater.* **2014**, 1–8 (2014).
195. M. Grätzel, Solar energy conversion by dye-sensitized photovoltaic cells. *Inorg. Chem.* **44**, 6841–51 (2005).
196. M. Grätzel, Conversion of sunlight to electric power by nanocrystalline dye-sensitized solar cells. *J. Photochem. Photobiol. A Chem.* **164**, 3–14 (2004).
197. T. A. Heimer, E. J. Heilweil, C. A. Bignozzi, G. J. Meyer, Electron Injection, Recombination, and Halide Oxidation Dynamics at Dye-Sensitized Metal Oxide Interfaces. *J. Phys. Chem. A*. **104**, 4256–4262 (2000).
198. D. J. Sirbuly, M. Law, H. Yan, P. Yang, Semiconductor nanowires for subwavelength photonics integration. *J. Phys. Chem. B*. **109**, 15190–213 (2005).
199. M. Law, L. E. Greene, J. C. Johnson, R. Saykally, P. Yang, Nanowire dye-sensitized solar cells. *Nat. Mater.* **4**, 455–9 (2005).
200. A. Kongkanand, R. M. Domínguez, P. V. Kamat, Single wall carbon nanotube scaffolds for photoelectrochemical solar cells. Capture and transport of photogenerated electrons. *Nano Lett.* **7**, 676–80 (2007).
201. F. Vietmeyer, B. Seger, P. V. Kamat, Anchoring ZnO Particles on Functionalized Single Wall Carbon Nanotubes. Excited State Interactions and Charge Collection. *Adv. Mater.* **19**, 2935–2940 (2007).
202. H. Yu, X. Quan, S. Chen, H. Zhao, TiO₂ - Multiwalled Carbon Nanotube Heterojunction Arrays and Their Charge Separation Capability. *J. Phys. Chem. B*. **111**, 12987–12991 (2007).

203. X.-X. Zou *et al.*, Light-Driven Preparation, Microstructure, and Visible-Light Photocatalytic Property of Porous Carbon-Doped TiO₂. *Int. J. Photoenergy*. **2012**, 1–9 (2012).
204. T. Dürkop, S. A. Getty, E. Cobas, M. S. Fuhrer, Extraordinary Mobility in Semiconducting Carbon Nanotubes. *Nano Lett.* **4**, 35–39 (2004).
205. L. Liu, W. E. Stanchina, G. Li, Effects of semiconducting and metallic single-walled carbon nanotubes on performance of bulk heterojunction organic solar cells. *Appl. Phys. Lett.* **94**, 233309 (2009).
206. J. H. Lee, S. Cho, A. Roy, H.-T. Jung, A. J. Heeger, Enhanced diode characteristics of organic solar cells using titanium suboxide electron transport layer. *Appl. Phys. Lett.* **96**, 163303 (2010).
207. D. Eder, A. H. Windle, Morphology control of CNT-TiO₂ hybrid materials and rutile nanotubes. *J. Mater. Chem.* **18**, 2036 (2008).
208. H.-C. Huang, G.-L. Huang, H.-L. Chen, Y.-D. Lee, Immobilization of TiO₂ nanoparticles on carbon nanocapsules for photovoltaic applications. *Thin Solid Films*. **511-512**, 203–207 (2006).
209. D. A. Tryk, A. Fujishima, K. Honda, Recent topics in photoelectrochemistry: achievements and future prospects. *Electrochim. Acta*. **45** (2000), pp. 2363–2376.
210. K. Woan, G. Pyrgiotakis, W. Sigmund, Photocatalytic Carbon-Nanotube-TiO₂ Composites. *Adv. Mater.* **21**, 2233–2239 (2009).
211. J. Kong *et al.*, Nanotube Molecular Wires as Chemical Sensors. *Science*. **287**, 622–625 (2000).
212. M.-G. Willinger *et al.*, Vanadium oxide sensing layer grown on carbon nanotubes by a new atomic layer deposition process. *Nano Lett.* **8**, 4201–4 (2008).
213. B.-Y. Wei *et al.*, A novel SnO₂ gas sensor doped with carbon nanotubes operating at room temperature. *Sensors Actuators B Chem.* **101**, 81–89 (2004).
214. C. Marichy *et al.*, Tin Dioxide Sensing Layer Grown on Tubular Nanostructures by a Non-Aqueous Atomic Layer Deposition Process. *Adv. Funct. Mater.* **21**, 658–666 (2011).
215. C. Marichy, N. Pinna, Carbon-nanostructures coated/decorated by atomic layer deposition: Growth and applications. *Coord. Chem. Rev.* **257**, 3232–3253 (2013).

216. C. Marichy, P. Russo, Tin Dioxide–Carbon Heterostructures Applied to Gas Sensing: Structure-Dependent Properties and General Sensing Mechanism. *J. Phys. Chem. C.* **117**, 19729–19739 (2013).
217. W.-S. Kim *et al.*, SnO₂ nanotubes fabricated using electrospinning and atomic layer deposition and their gas sensing performance. *Nanotechnology.* **21**, 245605 (2010).
218. H.-W. Ra, K.-S. Choi, J.-H. Kim, Y.-B. Hahn, Y.-H. Im, Fabrication of ZnO nanowires using nanoscale spacer lithography for gas sensors. *Small.* **4**, 1105–9 (2008).
219. B. M. Venkatesan *et al.*, Highly Sensitive, Mechanically Stable Nanopore Sensors for DNA Analysis. *Adv. Mater.* **21**, 2771–2776 (2009).
220. B. M. Venkatesan, A. B. Shah, J. M. Zuo, R. Bashir, DNA Sensing using Nanocrystalline Surface Enhanced Al₂O₃ Nanopore Sensors. *Adv. Funct. Mater.* **20**, 1266–1275 (2010).
221. P. Wang *et al.*, Zinc oxide aerogel-like materials with an intriguing interwoven hollow-sphere morphology for selective ethanol sensing. *RSC Adv.* **4**, 21815 (2014).
222. M. S. Whittingham, R. F. Savinell, T. Zawodzinski, Introduction: batteries and fuel cells. *Chem. Rev.* **104**, 4243–4 (2004).
223. C. Niu, E. K. Sichel, R. Hoch, D. Moy, H. Tennent, High power electrochemical capacitors based on carbon nanotube electrodes. *Appl. Phys. Lett.* **70**, 1480 (1997).
224. G. Lota, K. Lota, E. Frackowiak, Nanotubes based composites rich in nitrogen for supercapacitor application. *Electrochem. commun.* **9**, 1828–1832 (2007).
225. J. H. Park, J. M. Ko, O. Ok Park, Carbon Nanotube/RuO₂ Nanocomposite Electrodes for Supercapacitors. *J. Electrochem. Soc.* **150**, A864 (2003).
226. I.-H. Kim, J.-H. Kim, Y.-H. Lee, K.-B. Kim, Synthesis and Characterization of Electrochemically Prepared Ruthenium Oxide on Carbon Nanotube Film Substrate for Supercapacitor Applications. *J. Electrochem. Soc.* **152**, A2170 (2005).
227. S. D. Perera *et al.*, Vanadium Oxide Nanowire-Carbon Nanotube Binder-Free Flexible Electrodes for Supercapacitors. *Adv. Energy Mater.* **1**, 936–945 (2011).
228. I.-H. Kim, J.-H. Kim, B.-W. Cho, Y.-H. Lee, K.-B. Kim, Synthesis and Electrochemical Characterization of Vanadium Oxide on Carbon Nanotube Film Substrate for Pseudocapacitor Applications. *J. Electrochem. Soc.* **153**, A989 (2006).

229. M. H. Chen *et al.*, Synthesis and characterization of SnO–carbon nanotube composite as anode material for lithium-ion batteries. *Mater. Res. Bull.* **38**, 831–836 (2003).
230. X. Chen *et al.*, MWCNT/V₂O₅ Core/Shell Sponge for High Areal Capacity and Power Density Li-Ion Cathodes. *ACS Nano.* **6**, 7948–7955 (2012).
231. J. Fricke, T. Tillotson, Aerogels: production, characterization, and applications. *Thin Solid Films.* **297**, 212–223 (1997).
232. H. Maleki, L. Durães, A. Portugal, An overview on silica aerogels synthesis and different mechanical reinforcing strategies. *J. Non. Cryst. Solids.* **385**, 55–74 (2014).
233. J. Poco, J. H. Satcher, L. Hrubesh, Synthesis of high porosity, monolithic alumina aerogels. *J. Non. Cryst. Solids.* **285**, 57–63 (2001).
234. M. B. Bryning *et al.*, Carbon nanotube aerogels. *Adv. Mater.* **19**, 661–664 (2007).
235. Q. Peng *et al.*, Graphene nanoribbon aerogels unzipped from carbon nanotube sponges. *Adv. Mater.* **26**, 3241–3247 (2014).
236. J. L. Mohanan, I. U. Arachchige, S. L. Brock, Porous semiconductor chalcogenide aerogels. *Science.* **307**, 397–400 (2005).
237. G. Zu *et al.*, Preparation and characterization of monolithic alumina aerogels. *J. Non. Cryst. Solids.* **357**, 2903–2906 (2011).
238. G. Zu *et al.*, Nanoengineering super heat-resistant, strong alumina aerogels. *Chem. Mater.* **25**, 4757–4764 (2013).
239. A. Du, B. Zhou, Z. Zhang, J. Shen, A Special Material or a New State of Matter: A Review and Reconsideration of the Aerogel. *Materials (Basel).* **6**, 941–968 (2013).
240. S. S. Kistler, Coherent Expanded Aerogels. *Rubber Chem. Technol.* **5** (1932), pp. 600–603.
241. G. Poelz, R. Riethmüller, Preparation of silica aerogel for Cherenkov counters. *Nucl. Instruments Methods Phys. Res.* **195**, 491–503 (1982).
242. S. Henning, L. Svensson, Production of Silica Aerogel. *Phys. Scr.* **23**, 697–702 (2007).
243. M. J. van Bommel, A. B. de Haan, Drying of silica aerogel with supercritical carbon dioxide. *J. Non. Cryst. Solids.* **186**, 78–82 (1995).

244. S. Hæreid, M. A. Einarsrud, G. W. Scherer, Mechanical strengthening of TMOS-based alcogels by aging in silane solutions. *J. Sol-Gel Sci. Technol.* **3**, 199–204 (1994).
245. D. M. Smith, D. Stein, J. M. Anderson, W. Ackerman, Preparation of low-density xerogels at ambient pressure. *J. Non. Cryst. Solids.* **186**, 104–112 (1995).
246. L. Hrubesh, J. Poco, Processing and characterization of high porosity aerogel films. *MRS Proc.* (1994) (available at http://journals.cambridge.org/abstract_S1946427400526980).
247. B. E. Yoldas, Hydrolysis of aluminium alkoxides and bayerite conversion. *J. Appl. Chem. Biotechnol.* **23**, 803–809 (1973).
248. Y. Mizushima, M. Hori, Alumina aerogel for support of a methane combustion catalyst. *Appl. Catal. A Gen.* **88**, 137–148 (1992).
249. Y. Mizushima, M. Hori, I. Introduction, Preparation of heat-resistant alumina aerogels. **8** (1993).
250. R. Saliger, T. Heinrich, T. Gleissner, J. Fricke, Sintering behaviour of alumina-modified silica aerogels. *J. Non. Cryst. Solids.* **186**, 113–117 (1995).
251. B. Himmel, H. Biiirger, G. Holzhufter, A. Olbertz, Structural characterization of SiO₂-Al₂O₃ aerogels. *J. Non. Cryst. Solids.* **186**, 149–158 (1995).
252. S. Keysar, G. E. Shter, Y. de Hazan, Y. Cohen, G. S. Grader, Heat Treatment of Alumina Aerogels. *Chem. Mater.* **9**, 2464–2467 (1997).
253. S. O. Kucheyev *et al.*, Nanoengineering mechanically robust aerogels via control of foam morphology. *Appl. Phys. Lett.* **89**, 041911 (2006).
254. W. Wang *et al.*, Trimethylethoxysilane-modified super heat-resistant alumina aerogels for high-temperature thermal insulation and adsorption applications. *RSC Adv.* **4**, 54864–54871 (2014).
255. G. Zu *et al.*, Robust, Highly Thermally Stable, Core–Shell Nanostructured Metal Oxide Aerogels as High-Temperature Thermal Superinsulators, Adsorbents, and Catalysts. *Chem. Mater.* **26**, 5761–5772 (2014).
256. H. Fan *et al.*, Modulus-density scaling behaviour and framework architecture of nanoporous self-assembled silicas. *Nat. Mater.* **6**, 418–423 (2007).

257. L. J. Gibson, M. F. Ashby, *Cellular Solids: Structure and Properties* (Cambridge University Press, Cambridge, ed. 2, 1999).
258. L. R. Meza, S. Das, J. R. Greer, Strong, Lightweight and Recoverable Three - Dimensional Ceramic Nanolattices. *Science*. **345**, 1322–1326 (2014).
259. X. Zheng *et al.*, Ultralight, ultrastiff mechanical metamaterials. *Science*. **344**, 1373–7 (2014).
260. T. A. Schaedler *et al.*, Ultralight Metallic Microlattices. *Science*. **334**, 962–965 (2011).
261. T. Woignier, J. Phalippou, Scaling Law Variation of the Mechanical Properties of Silica Aerogels. *Le J. Phys. Colloq.* **24**, C4–179–C4–184 (1989).
262. J. T. Korhonen *et al.*, Inorganic hollow nanotube aerogels by atomic layer deposition onto native nanocellulose templates. *ACS Nano*. **5**, 1967–74 (2011).
263. F. Li *et al.*, Highly porous metal oxide networks of interconnected nanotubes by atomic layer deposition. *Nano Lett.* **12**, 5033–5038 (2012).
264. M. M. Biener *et al.*, Ultra-strong and low-density nanotubular bulk materials with tunable feature sizes. *Adv. Mater.* **26**, 4808–4813 (2014).
265. D. Jang, L. R. Meza, F. Greer, J. R. Greer, Fabrication and deformation of three-dimensional hollow ceramic nanostructures. *Nat. Mater.* **12**, 893–8 (2013).
266. J. Bauer, S. Hengsbach, I. Tesari, R. Schwaiger, O. Kraft, High-strength cellular ceramic composites with 3D microarchitecture. *Proc. Natl. Acad. Sci. U. S. A.* **111**, 2453–8 (2014).
267. M. F. L. De Volder, S. H. Tawfick, R. H. Baughman, a J. Hart, Carbon nanotubes: present and future commercial applications. *Science*. **339**, 535–9 (2013).
268. S. Faraji *et al.*, Structural annealing of carbon coated aligned multi-walled carbon nanotube sheets. *Carbon N. Y.* **79**, 113–122 (2014).
269. S. Faraji *et al.*, “Multifunctional Anisotropic Foams from Layered Aligned Carbon Nanotube Sheets” (2015).
270. J. Elam, D. Routkevitch, P. P. Mardilovich, S. M. George, Conformal coating on ultrahigh-aspect-ratio nanopores of anodic alumina by atomic layer deposition. *Chem. Mater.*, 3507–3517 (2003).

271. J. W. Elam, J. A. Libera, T. H. Huynh, H. Feng, M. J. Pellin, Atomic Layer Deposition of Aluminum Oxide in Mesoporous Silica Gel. *J. Phys. Chem. C*. **114**, 17286–17292 (2010).
272. N. Yazdani *et al.*, Modeling and optimization of atomic layer deposition processes on vertically aligned carbon nanotubes. *Beilstein J. Nanotechnol.* **5**, 234–44 (2014).
273. R. L. Puurunen *et al.*, Island growth in the atomic layer deposition of zirconium oxide and aluminum oxide on hydrogen-terminated silicon: Growth mode modeling and transmission electron microscopy. *J. Appl. Phys.* **96**, 4878 (2004).
274. R. Andrews, D. Jacques, D. Qian, E. C. Dickey, Purification and structural annealing of multiwalled carbon nanotubes at graphitization temperatures. *Carbon N. Y.* **39**, 1681–1687 (2001).
275. G.-B. Zheng, H. Sano, Y. Uchiyama, A layer-by-layer deposition mechanism for producing a pyrolytic carbon coating on carbon nanotubes. *Carbon N. Y.* **57**, 267–273 (2013).
276. D. S. Jensen *et al.*, Stable, microfabricated thin layer chromatography plates without volume distortion on patterned, carbon and Al₂O₃-primed carbon nanotube forests. *J. Chromatogr. A*. **1257**, 195–203 (2012).
277. C. Hontoria-Lucas, A. J. López-Peinado, J. de D. López-González, M. L. Rojas-Cervantes, R. M. Martín-Aranda, Study of oxygen-containing groups in a series of graphite oxides: Physical and chemical characterization. *Carbon N. Y.* **33**, 1585–1592 (1995).
278. S. Kanazawa, M. Kogoma, S. Okazaki, T. Moriwaki, Glow plasma treatment at atmospheric pressure for surface modification and film deposition. *Nucl. Instruments Methods Phys. Res.* **38**, 842–845 (1989).
279. M. Kogoma, H. Kasai, K. Takahashi, T. Moriwaki, S. Okazaki, Wettability control of a plastic surface by CF₄-O₂ plasma and its etching effect. *J. Phys. D. Appl. Phys.* **20**, 147–149 (1987).
280. E. Occhiello, M. Morra, F. Gardassi, J. Bargon, On the application of XPS, SSIMS and QCM to study the surface of a CF₄/O₂ plasma treated polycarbonate. *Appl. Surf. Sci.* **36**, 285–295 (1989).
281. R. Mohan, A. M. Shanmugaraj, R. H. Sung, An efficient growth of silver and copper nanoparticles on multiwalled carbon nanotube with enhanced antimicrobial activity. *J. Biomed. Mater. Res. B Appl. Biomater.* **96B**, 119–126 (2011).

282. S. O. Kucheyev *et al.*, Mechanisms of atomic layer deposition on substrates with ultrahigh aspect ratios. *Langmuir*. **24**, 943–8 (2008).
283. S. Aksel, D. Eder, Catalytic effect of metal oxides on the oxidation resistance in carbon nanotube–inorganic hybrids. *J. Mater. Chem.* **20**, 9149 (2010).
284. B. C. Satishkumar, A. Govindaraj, E. M. Vogl, L. Basumallick, C. N. R. Rao, Oxide nanotubes prepared using carbon nanotubes as templates. *J. Mater. Res.* **12**, 604–606 (2011).
285. J. Cho, A. R. Boccaccini, M. S. P. Shaffer, Ceramic matrix composites containing carbon nanotubes. *J. Mater. Sci.* **44**, 1934–1951 (2009).
286. J. Haerberle *et al.*, Ellipsometry and XPS comparative studies of thermal and plasma enhanced atomic layer deposited Al₂O₃-films. *Beilstein J. Nanotechnol.* **4**, 732–742 (2013).
287. L. Zhang, H. C. Jiang, C. Liu, J. W. Dong, P. Chow, Annealing of Al₂O₃ thin films prepared by atomic layer deposition. *J. Phys. D: Appl. Phys.* **40**, 3707–3713 (2007).
288. I. Levin, D. Brandon, Metastable Alumina Polymorphs: Crystal Structures and Transition Sequences. *J. Am. Ceram. Soc.* **81**, 1995–2012 (1998).
289. C.-I. Hung *et al.*, *ChemPhysChem*, in press, doi:10.1002/cphc.201402736.
290. T. Gougousi, D. Barua, E. D. Young, G. N. Parsons, Metal Oxide Thin Films Deposited from Metal Organic Precursors in Supercritical CO₂ Solutions. *Chem. Mater.* **17**, 5093–5100 (2005).
291. K. Lee, J. S. Jur, D. H. Kim, G. N. Parsons, Mechanisms for hydrophilic/hydrophobic wetting transitions on cellulose cotton fibers coated using Al₂O₃ atomic layer deposition. *J. Vac. Sci. Technol. A Vacuum, Surfaces, Film.* **30**, 01A163 (2012).
292. J. T. Klopogge, L. V. Duong, B. J. Wood, R. L. Frost, XPS study of the major minerals in bauxite: Gibbsite, bayerite and (pseudo-)boehmite. *J. Colloid Interface Sci.* **296**, 572–576 (2006).
293. G. Krautheim, T. Hecht, S. Jakschik, U. Schröder, W. Zahn, Mechanical stress in ALD-Al₂O₃ films. *Appl. Surf. Sci.* **252**, 200–204 (2005).
294. L. Qiu, J. Z. Liu, S. L. Y. Chang, Y. Wu, D. Li, Biomimetic superelastic graphene-based cellular monoliths. *Nat. Commun.* **3**, 1241 (2012).

295. S. O. Kucheyev *et al.*, Super-compressibility of ultralow-density nanoporous silica. *Adv. Mater.* **24**, 776–780 (2012).
296. M. Mecklenburg *et al.*, Aerographite: ultra lightweight, flexible nanowall, carbon microtube material with outstanding mechanical performance. *Adv. Mater.* **24**, 3486–90 (2012).
297. S. O. Kucheyev *et al.*, Atomic layer deposition of ZnO on ultralow-density nanoporous silica aerogel monoliths. *Appl. Phys. Lett.* **86**, 083108 (2005).
298. J. Biener *et al.*, Ruthenium/aerogel nanocomposites via atomic layer deposition. *Nanotechnology.* **18**, 055303 (2007).
299. S. Deng *et al.*, Atomic layer deposition-based synthesis of photoactive TiO₂ nanoparticle chains by using carbon nanotubes as sacrificial templates. *RSC Adv.* **4**, 11648 (2014).
300. K. L. Stano *et al.*, Conformal Atomic Layer Deposition of Alumina on Millimeter Tall, Vertically-Aligned Carbon Nanotube Arrays. *ACS Appl. Mater. Interfaces.* **6**, 19135–19143 (2014).
301. X. Gui *et al.*, Carbon nanotube sponges. *Adv. Mater.* **22**, 617–21 (2010).
302. O. K. Varghese, C. A. Grimes, Metal oxide nanoarchitectures for environmental sensing. *J. Nanosci. Nanotechnol.* **3**, 277–293 (2003).
303. Z. Chen, C. Lu, Humidity Sensors: A Review of Materials and Mechanisms. *Sens. Lett.* **3**, 274–295 (2005).
304. J. L. Gurav, I.-K. Jung, H.-H. Park, E. S. Kang, D. Y. Nadargi, Silica Aerogel: Synthesis and Applications. *J. Nanomater.* **2010**, 1–11 (2010).
305. A. Emmerling *et al.*, Isothermal sintering of SiO₂-aerogels. *J. Non. Cryst. Solids.* **125**, 230–243 (1990).
306. J. W. Elam *et al.*, Atomic Layer Deposition for the Conformal Coating of Nanoporous Materials. *J. Nanomater.* **2006**, 1–5 (2006).
307. K. L. Stano *et al.*, “Interconnected Metal Oxide Nanotube Networks for Ultralight Aerogels” (2015).
308. S. J. Shin, S. O. Kucheyev, M. A. Worsley, A. V. Hamza, Mechanical deformation of carbon-nanotube-based aerogels. *Carbon N. Y.* **50**, 5340–5342 (2012).

309. K. H. Kim, Y. Oh, M. F. Islam, Mechanical and thermal management characteristics of ultrahigh surface area single-walled carbon nanotube aerogels. *Adv. Funct. Mater.* **23**, 377–383 (2013).
310. A. Brieland-Shoultz *et al.*, Scaling the Stiffness, Strength, and Toughness of Ceramic-Coated Nanotube Foams into the Structural Regime. *Adv. Funct. Mater.* **24**, 5728–5735 (2014).
311. E. Andrews, W. Sanders, L. J. Gibson, Compressive and tensile behaviour of aluminum foams. *Mater. Sci. Eng. A.* **270**, 113–124 (1999).
312. P. B. Wagh, S. V. Ingale, Comparison of some physico-chemical properties of hydrophilic and hydrophobic silica aerogels. *Ceram. Int.* **28**, 43–50 (2002).
313. B. T. Quinton *et al.*, Influence of oxide buffer layers on the growth of carbon nanotube arrays on carbon substrates. *Carbon N. Y.* **87**, 175–185 (2015).
314. M. A. Worsley, S. O. Kucheyev, J. H. Satcher, A. V. Hamza, T. F. Baumann, Mechanically robust and electrically conductive carbon nanotube foams. *Appl. Phys. Lett.* **94**, 073115 (2009).